Optimisation of plasma sprayed hydroxyapatite coatings using a design of experiments approach

David Atter Kuntin

PhD

University of York

Department of Biology

February 2020

Abstract

Hip revision surgery, where a failed hip replacement is replaced and damage is repaired, presents a significant socioeconomic burden. Improved fixation and longevity of hip stems can alleviate this problem, thereby improving patient quality of life. This is achieved by modulating hydroxyapatite (HA) surfaces to provide a more favourable environment for regeneration *in situ* by resident mesenchymal stromal cells (MSCs). By changing the variables that go into application of the HA surface by plasma spraying, material properties can be changed and a model to predict material changes can be created using Design of Experiments (DoE).

Plasma spraying is a highly complex, multifactorial technique working on the principle of introducing HA powder into a high temperature plasma jet, propelling molten and partially molten particles of HA onto a substrate. Five factors (A-E) were explored using a DoE approach to assess the effect of each on crystallinity and roughness. A model of crystallinity and roughness response to changing factor settings was created, allowing for prediction of material properties in response to changing plasma sprayer settings.

MSC response to different surfaces was assessed in terms of proliferation, osteogenic response, and Wnt signalling. Depending on the surface, Wnt signalling and proliferation can be enhanced, and HA can have osteoinductive properties. Optimal plasma sprayer settings for maximising proliferation, osteogenic response, and Wnt signalling were determined and material properties for each predicted, enabling the production of HA-coated hip stems with fine-tuneable MSC responses and material properties.

The use of foetal bovine serum (FBS) in biomaterial studies brings with it ethical and scientific issues, chiefly among them the undefined nature of protein adsorption to biomaterial surfaces. A chemically defined medium was developed using DoE, which supported growth of MSCs on biomaterial surfaces, as well MSC expansion and extracellular vesicle production in a clinical grade perfusion bioreactor.

Table of Contents

List of Figures

List of Tables

List of Equations

List of Appendices

Acknowledgements

I would like to thank my supervisors Paul Genever, David Wood, and Niki Gosling for their advice and support throughout this project. I would especially like to thank Paul for his endless patience with my statistics.

My PhD has been made easier by the friends made along the way, including members of the J0 and Genever lab groups. Special thanks (in alphabetical order) go to Amanda Barnes, Alasdair Kay, Dimi Kioumourtzoglou, Dave Mentlak, and Andrew Stone, without whom the PhD experience would have been particularly dull, and whose company and tolerance of board games made an especially positive impact on my mental wellbeing. Also, thanks to Alison Wilson, whose advice about regulatory issues around medical devices always gave me fresh perspective and made for excellent conversation.

I have received a lot of very valuable technical assistance from the Technology Facility staff – particular thanks go to Meg Stark, who prepared a large number of samples for me when I had an injury and was not able to do so myself. The JEOL Nanocentre staff, Chris Reardon above all, have also supported my work tremendously by training and supporting me in using profilometry equipment.

Finally, I would like to thank my family for their boundless support and love, even when the stresses of the project rendered me insufferable.

Declaration

I declare that this thesis is a presentation of original work performed between September 2015 and February 2020. All experiments were performed by the author except for the isolation, quantification, and characterisation of extracellular vesicles, which was carried out by Savvas Ioannou. Furthermore, crystallinity DoEs are based on data collected previously collected by DePuy Synthes in Cork, Ireland. This work has not previously been presented for an award at this, or any other, university. All sources are acknowledged as references.

1 Chapter 1: Introduction

1.1 Joint disease demographics in the UK

90% of patients undergoing total hip replacement do so due to late stage osteoarthritis[1]. Musculoskeletal disease presents a vast socioeconomic burden in the UK, as incidence increases with increasing age, and the UK's over-65 population being projected to increase to 26.4% of the population by 2041[2]. It is estimated that a total of 8.75 million people over the age of 45 have sought advice for osteoarthritis in the UK. Currently, 2.9 million people suffer from osteoarthritis of the hip in Scotland, England, and Wales, 838,000 of whom suffer from severe osteoarthritis[1].

Osteoarthritis can affect any joint, but is most commonly affects the most load-bearing joints, such as hips, knees, and joints in the feet. Clinically, osteoarthritis may initially present itself with increasing, progressive pain, with mechanical symptoms following as the joint space reduces. Osteophytes, subchondral sclerosis, and cysts may also occur, contributing to reduced range of motion and joint pain, significantly reducing patients' quality of life[3]. Osteoarthritis has been documented as the indication for hip joint replacement in 91.7% of cases between 2004 and 2018, with the annual number of primary hip replacements more than doubling in this time (42,796 in 2004 versus 92,874 in 2018). Of 1,091,892 primary hip replacements recorded in the National Joint registry between 2004 and 2018, 31,410 underwent first revisions in that time[4].

Common risk factors for osteoarthritis are age, sex, obesity, occupation, joint abnormalities, and genetics. With increasing age, the prevalence of osteoarthritis increases to up to 50% in people aged 75 and over[5,6]. Females are more commonly affected than males, with about 60% of hip and knee replacements being accounted for by females[6]. Obesity increases the likelihood of developing osteoarthritis approximately 2.5 to 4.6-fold, with the average body mass index (BMI) of a patient undergoing hip replacement surgery in the UK being 28.8[7]. Occupations requiring prolonged lifting and standing have also been linked to higher incidences of hip osteoarthritis[8]. An abnormal hip shape accounts for a large proportion of hip replacement surgeries, with 1 in 3 surgeries undertaken in over-65s being due to an abnormality in the hip shape[9]. Finally, some genes, such as collagen II, IX, and XI, have been linked to the incidence of osteoarthritis, with 60% of hip and hand osteoarthritis cases presenting with a genetic abnormality[10].

1.1.1 Socioeconomic burden of hip replacements and revision surgery

In their latest analysis, the National Joint Registry reported that in the UK, across all major failure mechanisms, genders, and age groups, uncemented replacements (see section 1.2) have a higher failure rate than cemented replacements[4], suggesting that there is scope for improvement. The economic burden of failure is substantial. In 2000, the total cost to the NHS of hip and knee revision surgeries, where a failed implant is replaced and any damage is repaired, was £60 million[11], with the total cost of non-elective revision of a hip arthroplasty prompted by peri-prosthetic fracture being £5968, whereas the cost of revision for infection can cost up to £12214[12]. At the current rate of population ageing and revision requirements for hip arthroplasties, many projections suggest a steep rise in both primary and revision surgeries, which will increase the burden on health services both domestically and internationally[13–16]. There is therefore a clinical and socioeconomic need to improve the longevity of hip replacement stems.

1.1.2 Treatment

Current treatment options for osteoarthritis are focussed on pain management until the disease has progressed to the point that the patient's mobility is severely impaired. Other treatments exist for early stage intervention; one example is microfracture, where micron-scale fractures are introduced into a small cartilage lesion, with the aim of stimulating underlying bone marrow to repair the cartilage. Restorative therapies such as this have the drawback of being more effective in the knee, where intra-articular manipulation is more readily achievable, and cartilage defects are more easily identified radiographically. Nonetheless, they are a promising intervention for traumatic injuries or early stages of osteoarthritis in younger patients, provided the defect is identified in an early stage[17]. There are also treatments in development where the inflammation associated with osteoarthritic disease is targeted, as a means to control the progression of the disease. These include corticosteroids and anti-cytokine therapies, and show promising results in pre-clinical and clinical studies[18]. Interventions that aim to target early stages of osteoarthritis can help to prevent the utilisation of total arthroplasty, which has limited lifespan and progressively worsens with subsequent revisions.

For late stage hip osteoarthritis, where the patient's mobility is severely impaired or the pain becomes intolerable, total hip arthroplasty is considered a gold standard treatment[19]. A primary total hip arthroplasty involves the removal of both the femoral

head and the acetabular cup. A metal stem in inserted into the femur with a modular femoral head attached, which articulates with an artificial acetabular cup.

A large array of hip replacement types exist, broadly characterised into cemented and non-cemented with reference to the stem. These are then further characterised by the interface between acetabular cup and the ball joint on the stem, defined by the material of each. There are four main combinations of bearing surface materials for the femoral head and acetabular cup: metal-on-metal, metal-on-polyethylene, ceramic-on-ceramic, and ceramic-on-polyethylene[20–23]. For the purposes of this introduction, the focus will be on hip stem fixation differences.

1.2 Cemented versus non-cemented hip stems: overview and major causes of failure.

Hip stems are broadly characterised into cemented and non-cemented hip stems. Cemented hip stems use polymethylmethacrylate (PMMA) as a grout, interlocking with the trabecular bone and hip stem surface. This means that no true adhesive bond is achieved, but that the prosthesis is mechanically bonded with the surrounding bone tissue. A potential issue with cementing is that there are two interfacial regions of potential failure: the bone-cement interface and the cement-prosthesis interface. PMMA is an inert, non-porous material that does not allow for any remodelling of the bone, such that any failure has a reduced potential for remodelling, increasing risk of loosening[24]. Furthermore, PMMA polymerisation is an exothermic process, where the temperature it reaches is entirely dependent on the specific batches, manufacturers, and techniques used[25], resulting in inconsistencies. Peak temperatures of up to 74°C have been reported, in some cases resulting in thermal necrosis of the surrounding bone tissue, and a drop in *in situ* osteocyte viability[26]. This could explain aseptic loosening in cemented hip stems, which is a major reason for revision surgeries[27].

Cemented hip stem failure is most commonly associated with peri-implant osteolysis. There is evidence to suggest that this is caused by particulate cement wear debris generated near articular interfaces, where macrophages phagocytose these particles. These macrophages then secrete inflammatory cytokines leading to the development of inflamed, granulomatous tissue in the cement-bone interfacial area. A subsequent osteoclast recruitment leads to osteolysis by their resorption of the surrounding bone tissue, culminating in eventual aseptic prosthetic loosening[28–30].

Non-cemented hip stems are typically porous or hydroxyapatite (HA) coated, and rely on “press-fitting”, where a bone-bed is prepared which is slightly smaller in diameter than the prosthesis, causing compressive hoop stresses which help keep the prosthesis in place. In the case of HA coated stems, the ceramic material is often considered to have favourable characteristics for bony ingrowth and anchorage[31–35]. Some studies also show that HA has osteoinductive properties, with the likely mechanism of recruiting osteoprogenitor cells, including mesenchymal stem/stromal cells (MSCs), from surrounding tissue and causing them to proliferate as well as possibly differentiate into bone-forming cells[36,37]. The main advantage of HA over cemented stems is the absence of an inflammatory response in the surrounding tissues, which can be attributed to the fact that HA is not a foreign material, occurring in normal human bone naturally in the form of nano-scale apatite platelets[38,39]. The main disadvantage of an uncemented hip stem is that the bond is very strong and irreversible, making it critical that the insertion is executed as precisely as possible in order to optimise loading, avoiding micromovement of the implant and consequent aseptic loosening[40]. Another major disadvantage is that in the event of deep infection in the bone, removal of a well-fixed uncemented hip stem can be very challenging, risking healthy bone loss and the potential need for larger bone reconstruction[41,42].

Uncemented hips most often fail due to peri-implant fracture caused by stress shielding. Stress shielding is the process by which bone density is reduced due to a change in bone loading caused by the change in weight bearing after the hip stem is implanted[41,43]. The extent to which stress shielding occurs and affects healthy bone is largely dependent on prosthesis design and insertion angle, as weight bearing will vary quite widely depending on the angle between the artificial hip stem and acetabular cup[44–46].

1.3 Plasma sprayed ceramic coatings for orthopaedic applications

1.3.1 Plasma spray process

The process of plasma spraying is a thermal spray technique used to coat surfaces in a material of choice evenly and quickly. It is highly complex and multifactorial, and requires precise optimisation in order to yield results which are both desirable and reproducible. Historically, the plasma spraying torch technology was initially described

by Gerdien and Lotz in 1922[47], which was later adapted into a spraying apparatus and patented as a collimated electric arc powder deposition process in 1962[48].

The features of the plasma spray technique that make it attractive to large manufacturing processes are that resulting coatings can be very closely controlled and varied according to the desired properties. This is due to the fact that the plasma spraying process is violent in terms of the chemistry involved, with the plasma flame reaching temperatures in excess of 14,000K[49], and the molten droplets impacting surfaces with very high kinetic energies at velocities at the exit nozzle of up to 2900 m/s in high-power plasmas settings[49–51], resulting in chemical changes in the sprayed material. With decades of careful study, it has been possible to predict how materials respond to these extreme conditions and how to control them in order to direct changes reliably and reproducibly.

In principle, a plasma sprayer consists of a plasma generator and a robotic arm. A circular anode surrounds a cathode, where an electric arc discharge is generated, which heats up plasma gases to the point at which they ionise into plasma. Gases used for this process usually have properties favouring the plasma state. Typically, argon, hydrogen, helium, nitrogen, or mixtures thereof are used for this[52,53]. Argon is usually used as the axial flow by argon in the nozzle aids in retaining a stable arc[54,55], whereas other gases such as helium, nitrogen, and hydrogen have been shown to improve thermal conductivity of the gas, enhancing melting behaviour of material particles[54,56–59] (Figure 1.1).

The material to be deposited onto a substrate surface is suspended in an inert carrier gas and introduced into the plasma flame. The powder properties are extremely important, especially when it comes to HA coatings for orthopaedic implants, as particle size, for example, can drastically change the properties of the quenched material. Similarly, the rate at which the powder is fed and the carrier gas flows changes properties of the final product such that each parameter requires detailed optimisation.[60–66]

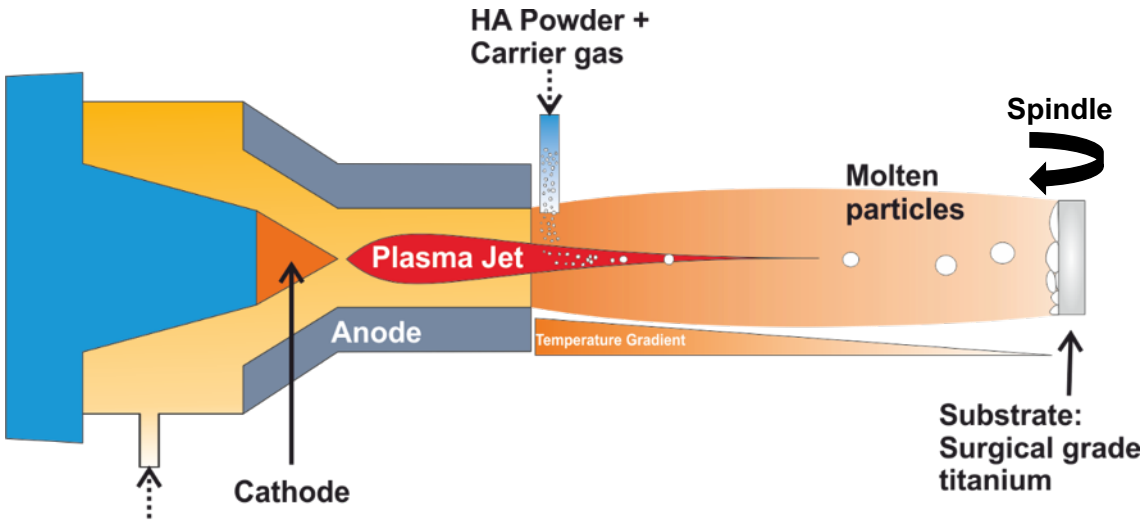

Figure 1.1: Overview of the plasma spraying process

1.3.2 Hydroxyapatite

Hydroxyapatite (HA) is a calcium phosphate ceramic that has gained a lot of attention in orthopaedic research in recent years. Its popularity as a subject of research in skeletal regeneration is due to the fact that HA shares chemical similarities with the natural biological apatite found in human bone and teeth[67]. Human bone comprises collagen I fibrils, water and HA ($Ca_{10}(PO_4)_6(OH)_2$) at a ratio of 7:1:2[67] – however, natural apatites do not conform to the canonical synthetic HA stoichiometry of 1.67, as some phosphate groups are replaced by carbonate groups, hydroxyl groups, and other impurities[68].

HA bioceramics have been used extensively in orthopaedic applications due to reports of its osteoconductive[69,70] and osteoinductive[37,71] properties. The gradual and controlled dissolution of bioceramics, such as HA, provides a microenvironment that is favourable for the attachment, proliferation, and differentiation of MSCs, and therefore regeneration of bone[72,73].

A plasma sprayed bioceramic is typically considered to have both amorphous and crystalline phases in their bulk, as the very nature of the coating technique readily yields different calcium phosphate phases from the HA feedstock powder, which has a calcium/phosphate ratio (Ca/P) of 1.67. These may include α-tricalcium-phosphate (Ca/P = 1.5) or β-tricalcium-phosphate (Ca/P = 1.5), which have different resorptive and dissolution properties[74,75].

1.4 Biological response to HA surfaces

1.4.1 Peri-implant cellular response to biomaterials

The fixation mechanisms in cemented and non-cemented hip stems differ in the sense that a PMMA grout is used to hold the hip stem in place in a cemented setting[76], whereas non-cemented hip are press-fit[77–79]. The microenvironment surrounding the implant is therefore directly exposed to the surface of the non-cemented hip stem. When a biomaterial is implanted, a foreign-body response may occur, which has similarities to a fracture response in that an inflammatory cascade can culminate in fibrotic tissue, but may have detrimental effects on implant longevity[80].

During the initial foreign body response, blood-material interactions occur following the 'injury' caused by surgical intervention and insertion of the hip stem into the prepared cavity in the femur. Blood proteins adsorb to the surface, and an inflammatory response results in a transient, provisional matrix surrounding the stem, which is a large thrombus at the bone/implant interface[81]. It is this layer of proteins that inflammatory cells initially respond to, which initiate tissue repair[82]. The nature of these adsorbed proteins have been shown to differ with different biomaterials, with factors such as surface charge, chemistry, and topography playing a substantial role in protein adsorption behaviour[83–85]. Bioactive agents present in the thrombus surrounding the implant mediate cell activity in the peri-implant space, instigating a healing response.

Pro-inflammatory cytokines, chemokines, and growth factors recruit immune cells to the site of the provisional matrix surrounding the implant[86–88], followed by acute and chronic inflammatory responses. The severity of the responses depend on the size and severity of the damage caused by surgery, as well as the biomaterial itself[89,90]. Integrin signalling mediates the bulk of cellular adhesion and activation to the protein-coated implant surface, which has been implicated specifically in dendritic cell adhesion to biomaterials and maturation[91,92].

β2 integrins are also involved in neutrophil adhesion to the implantation site. Neutrophils are typically involved in the early response to injury and inflammation, where they are responsible for pathogen phagocytosis and secretion of pro-inflammatory factors. At early stages of implantation, neutrophils degranulate and secrete proteolytic enzymes in an attempt to mediate the inflammatory response[93,94]. In some cases, neutrophils release an excess of neutrophil extracellular traps (NETs), which usually trap pathogens to prevent spreading infection, preventing proper

osteointegration and the impairment of tissue regeneration. This contributes to excess collagen I deposition by MSCs recruited to the site by pro-fibrogenic factors during chronic inflammation, resulting in the implant being encapsulated in fibrotic tissue, which does not allow for osteointegration and is often a risk factor for implant failure by aseptic loosening[95,96].

When neutrophil function progresses with appropriate NET release, CX chemokine ligand 8 (CXCL8), C chemokine ligand 2 (CCL2), and CCL4 are also released, which trigger infiltration of monocytes, which progress into activation into M1 macrophages[97,98]. Adherent macrophages secrete further chemokines, including CCL2, CCL4, and CXCL8, and release degrading enzymes with the aim of breaking down the biomaterial. These adherent macrophages eventually shift to the M2 phenotype, where anti-inflammatory cytokines are released, and tissue remodelling activity is increased[99,100].

In some cases, the mechanisms underlying the unsuccessful phagocytosis of the implant biomaterial (due to it being too large to be phagocytosed by macrophages), result in macrophages fusing to create foreign body giant cells (FBGCs). This, similar to fibrotic encapsulation of the implant by excess collagen I deposition of MSCs, is indicative of chronic inflammation, and can impair regenerative potential[101,102]. One study shows that FBGCs are able to resorb HA in a manner similar to osteoclasts, implying that there is a possibility that calcium phosphate ceramics used in orthopaedic applications may be susceptible to similar resorption by FBGCs[103].

M2 macrophages with an anti-inflammatory phenotype engage in T-regulatory cell (T-reg) crosstalk, prompting interleukin-10 (IL10) secretion, which aids in the maintenance of an anti-inflammatory environment. Amphiregulin is upregulated, and has been implicated in macrophage proliferation and differentiation, and was found to be crucial in tissue regeneration[104]. Interestingly, amphiregulin has also been implicated in bone marrow mesenchymal stromal cell migration via epidermal growth factor receptor (EGFR)[105].

In the absence of fibrotic tissue formation and FBGCs, angiogenesis follows this initial inflammatory response. Matrix metalloproteinases (MMPs), in concert with pro-angiogenic factors, allow for the formation of new vessels. Vascular endothelial growth factor (VEGF) is the main driver in new vessel formation, and is released from matrix by MMPs[106–108]. The peri-implant microenvironment, as well as the high signalling

activity at the healing site, induce the recruitment of MSCs, which will facilitate the formation of new bone tissue[109].

MSCs migrate toward the implant in order to attach and differentiate, for which the pathway is not fully understood, although micro- and nanotextured surfaces have been shown to influence MSC migration and adhesion to some surfaces[110]. It is also likely that there is involvement of the stromal cell-derived factor 1 (SDF1)/CXCR4 signalling axis, which is a commonly cited pathway for MSC recruitment to fracture sites[111–113]. MSCs adhere to the implant surface and secrete matrix, creating an afibrillar, interfacial zone, which is reported to be 200 nm – 500 nm thick, consisting of osteopontin, bone sialoprotein, and proteoglycans[114]. This matrix is mineralised by seeding of nanocrystalline calcium phosphate, followed by laying down of a layer of collagenous matrix by mature osteoblasts[115]. These layers are continually produced and mineralised, until an osteoblast is trapped within these layers, resulting in differentiation into an osteocyte and the formation of immature woven bone[116].

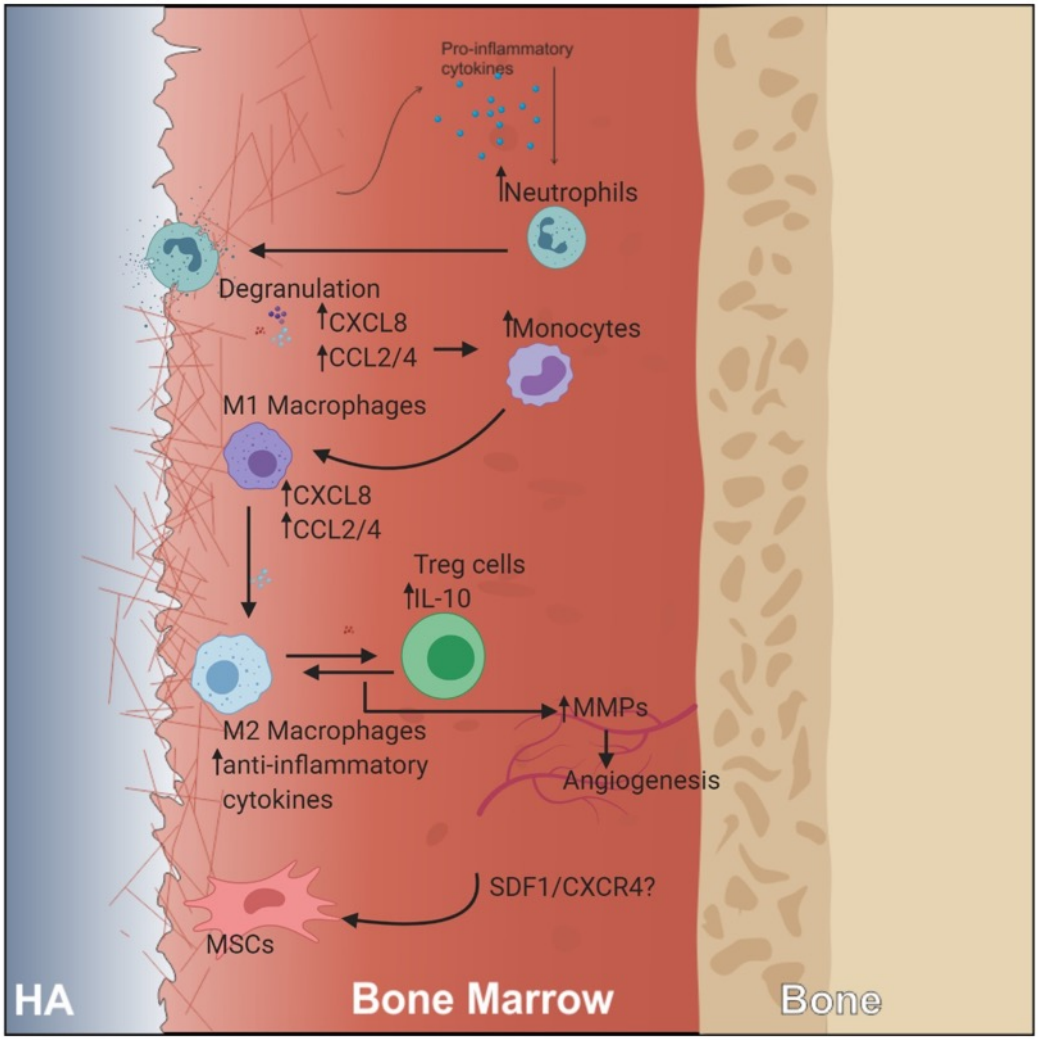

Figure 1.2: Response to implanted material in bone. Adsorbed proteins on the implant surface promote neutrophil recruitment to the implant site. Degranulation recruits monocytes to the site, which eventually mature into M1, then M2 macrophages. T-regulatory cell (Treg) crosstalk prompts MMP secretion, triggering angiogenesis. MSCs are recruited and adhere to the implant, possibly by SDF1/CXCR4 signalling.

1.5 Mesenchymal stromal cells

1.5.1 Overview

The first report of a subpopulation of cells in bone marrow with the capability to form bone was made by Friedenstein et al in 1966, where it was found that in mice, diffusion chambers filled with bone marrow would promote ectopic bone formation[117]. In a follow-up publication, Friedenstein et al showed that it was possible to isolate fibroblastic cells from guinea pig bone marrow based on their adhesive properties to glass. These cells were then developed into colonies and seeded into diffusion chambers, which were implanted intraperitoneally. This triggered "spontaneous bone formation", which was not possible from fibroblastic cells from guinea pig spleen.

The term "mesenchymal stem cell" was initially proposed by Arnold Caplan in 1991 to describe a population of cells resident in many tissue types with the potential to form skeletal tissues[118]. Today, a multitude of terms are used. Here, the term mesenchymal stromal cell (MSC) will be used in order to recognise the heterogeneity of cells isolated from bone marrow and the notion that not all plastic adherent cells isolated from bone marrow have multipotent differentiation capability[119].

MSCs are classically considered to have trilineage potential, where differentiation into osteoblastic, adipocytic, and chondrogenic lineages is possible *in vitro* with the addition of the appropriate factors. This was first reported by Pittenger et al in 1999, where bone marrow cells isolated from aspirates from the iliac crest were cultured and differentiated into all three lineages[120].

In order to identify MSCs, Dominici et al proposed a set of surface markers to discriminate between MSCs and other cell populations isolated from tissues: $CD105^+$, $CD73^+$, $CD90^+$, $CD45^-$, $CD34^-$, $CD14^-$, $CD19^-$, $CD79^-$. Moreover, the statement suggested that in order to qualify as an MSC, the cells would have to be plastic-adherent and have osteogenic, adipocytic, and chondrogenic differentiation potential[121]. While published as a position statement intended only as a guide, these markers are now widely used to demonstrate the identity of cells.

1.5.2 MSC differentiation

Bone marrow derived MSCs are the most widely studied MSC for application in bone regenerative medicine, as they have been implicated in bone homeostasis and

remodelling[122,123] via differentiation into osteoblasts and modulation of osteoclast behaviour[124].

MSC osteogenic differentiation can broadly be characterised by the differential temporal expression of osteogenic markers. Differentiating MSCs committed into osteogenic lineage pass through the stages of osteoprogenitors, preosteoblasts, and osteoblasts, with the potential to terminally differentiate into osteocytes[125].

1.5.2.1 *Molecular pathway regulation of MSC osteogenic differentiation*

Runt-related transcription factor 2 (RUNX2) is considered the master regulator of osteogenic differentiation. RUNX2 is a marker of early differentiation, with its expression reducing as MSCs mature into osteoblasts[126]. RUNX2 is target to many different pathways, including bone morphogenetic protein (BMP) and wingless-related integration site (Wnt) signalling[123,127–129].

BMP signalling is initiated by binding to transmembrane serine-threonine receptors (BMP type I; BMP type 2), triggering phosphorylation of mothers against decapentaplegic (Smad) proteins 1, 5, and 8. A complex is formed with Smad4, which translocates to the nucleus and activates transcription of RUNX2, osteopontin (OPTN), osteocalcin (OCN) and osterix (Osx)[127]. Osx is a transcription factor involved in osteoblast maturation, and has been shown to play a key role in bone homeostasis by conditional deletion in postnatal mice[130]. Independently of Smad, other signalling events involving mitogen-activated protein kinase (MAPK) are activated, which was also shown to be essential for BMP-induced osteoblastic maturation by aiding in ascorbic acid-dependent assembly of collagenous extracellular matrix and integrin-collagen interactions, which in turn reinforces activation of RUNX2[131].

Wnt signalling functions in ‘canonical’ and ‘non-canonical’ ways, each dependent on different ligands and co-receptors. Canonical Wnt signalling is characterised by the stabilisation and translocation of β-catenin into the nucleus to activate downstream genes, whereas non-canonical Wnt signalling is independent of β-catenin stabilisation and functions via an intracellular Ca^{2+} flux, resulting in nuclear translocation of nuclear factor of activated T-cells (NFAT) and activation of downstream genes. There are 19 members in the Wnt family of glycoproteins, and their function in activating either pathway is highly context-specific, depending on the availability of co-receptors on Wnt-responding cells.

Wnt proteins are palmitoylated by acyltransferase porcupine and N-glycosylated in the endoplasmic reticulum and are then secreted. Palmitoylation is thought to assist in receptor binding, thereby possibly influencing pathway activation fate[132]. The main receptor for Wnt proteins is Frizzled (Fzd), which is a seven-pass transmembrane receptor with a large cysteine-rich domain comprising 10 cysteine residues in a conserved motif[133]. A co-receptor is often required for Wnt-binding to Fzd, and depending on the co-receptor, the canonical or non-canonical pathway is activated. The most commonly cited co-receptors are low-density lipoprotein receptor related proteins 5 or 6 (LRP5/6) and Ror, responsible for canonical and non-canonical activation respectively[134–136].

At least 7 of the 19 Wnt proteins (Wnts 1, 2, 3a, 3b, 4, 8, and 10b) have been reported to date to be able to activate the canonical Wnt pathway[137]. Upon Wnt binding to Fzd co-receptor LRP5/6, Dishevelled (Dvl) is activated, which prevents glycogen synthase kinase 3β (GSK3β) incorporation into a β-catenin destruction complex by recruitment to the intracellular domain of LRP5/6[138]. This prevents phosphorylation of β-catenin, stabilising it and allowing its translocation into the nucleus, activating downstream genes (Figure 1.3).

Aberrations in canonical Wnt signalling have been shown to be correlated to either excess bone growth or resorption. For example, a loss of function mutation in LRP5 was found to result in low bone mass and propensity for bone fractures[139,140]. Conversely, a gain of function in LRP5 leads to higher bone mass, suggesting a pivotal role for canonical Wnt signalling in bone mineralisation[141–143].

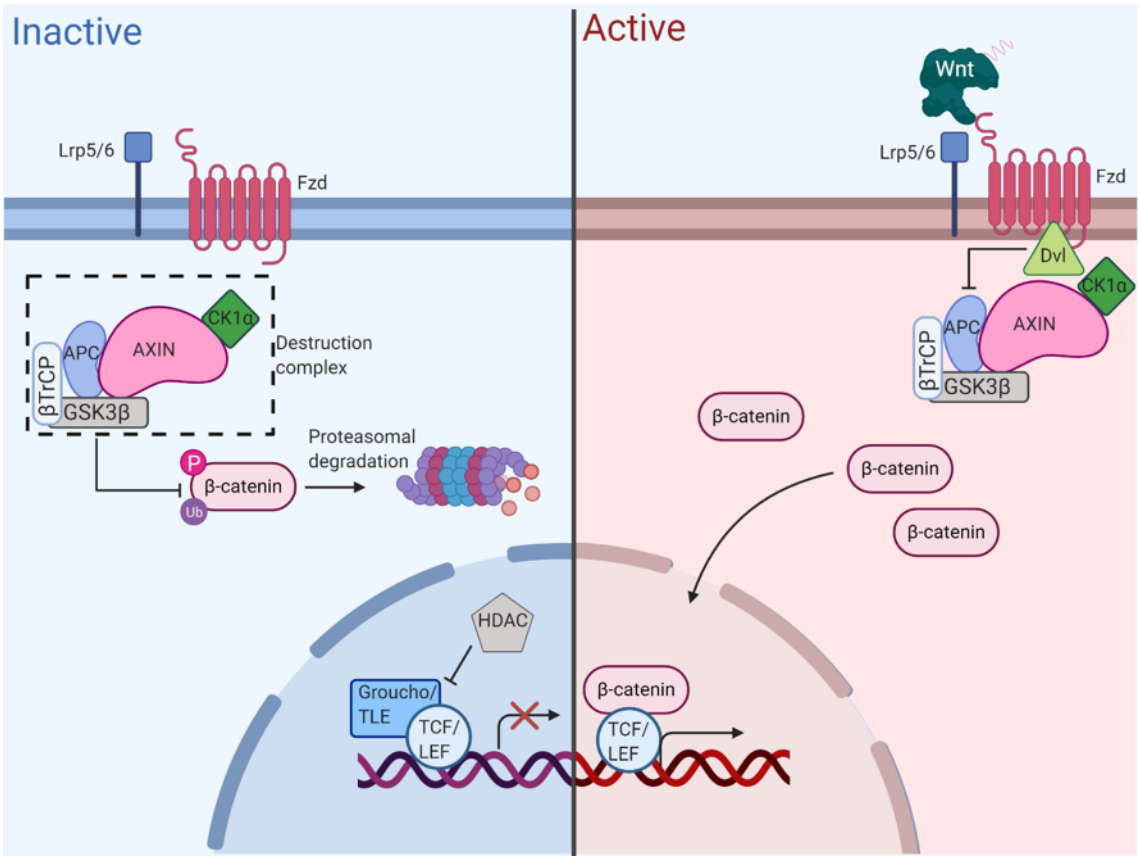

Figure 1.3: Overview of canonical Wnt signalling. Without activation, β-catenin is phosphorylated by GSK3β and ubiquitinated by βTrCP of the destruction complex, comprising Axin, casein kinase 1α (CK1α), adenomatous polyposis coli (APC), glycogen synthase kinase 3β (GSK3β) and β-transducin repeats containing protein (βTrCP), causing proteasomal degradation and T-cell factor/lymphoid enhancer-binding factor (TCF/LEF) inhibition by Groucho/transducing-like enhancer of split (TLE) and histone deacetylase (HDAC). Upon Wnt activation, the destruction complex is recruited to the plasma membrane by Dishevelled (Dvl), allowing for β-catenin accumulation in the cytoplasm and nuclear translocation. TCF/LEF is activated, allowing for transcription of downstream genes.

1.6 Media in *in vitro* experimentation

In order to experiment with cells *in vitro*, the most common approach to culturing cells is to supplement a basal medium with antibiotics and serum. The function of cell culture medium is to provide adequate nutrition to the cultured cell type to support cell survival, proliferation, and any required cell functions, while maintaining phenotype[144]. In MSC culture, it is particularly important for the medium to support a constant phenotype to maintain MSCs in an undifferentiated state.

1.6.1 Basal medium

The first solution developed for *in vitro* cultivation of animal tissue is reported to be Ringer's solution, developed by Sydney Ringer and published in 1882. It was a balanced salt solution, capable of keeping a frog heart beating after dissection and removal from the body[145]. This breakthrough prompted the scientific community to focus on cell culture technologies, and with the establishment of cell lines in the early 1950s, the development of cell culture medium began to move toward synthetic solutions, rather than using natural sources of nutrients, which was the norm at the time[146]. Today, a multitude of basal cell culture media exist, each tailored to specific applications and cell types.

Modern basal media are generally composed of a buffering system, inorganic salts, amino acids, carbohydrates, and in some cases proteins. Phenol red is a common additive which acts as a pH indicator, which is useful for monitoring of cell growth. These basal media are typically supplemented with antibiotic and serum at concentrations tailored to individual applications. Due to the large range of different media commercially available, it is important to choose a suitable medium for chemically defined medium development. The following have been chosen as basal medium in the development of a chemically defined medium.

Dulbecco's modified Eagle medium (DMEM) is a modification of Eagle's medium (EM). EM is a very minimal medium, originally used for mouse L cell and HeLa cell culture, and is very rarely used today[147]. DMEM is composed of similar ingredients as EM, only with increased concentrations of amino acids and vitamins, as well as addition of non-essential amino acids, glycine, serine, iron, and pyruvate[148].

DMEM/F12 is a further development of DMEM, which is a 1:1 mixture of DMEM and Ham's F-12 medium. Ham's F-12 contains linoleic acid and putrecine, which was originally included as it was shown to support colony formation of Chinese Hamster

ovary (CHO) cells in the absence of protein[149]. This is sometimes cited as being the first published chemically defined medium, as CHO cells can be cultured in Ham's F-12, but proliferation is markedly enhanced with the addition of serum and is often supplemented with it[150].

Another modification of DMEM is Iscove's modified DMEM (IMDM), which has several more non-essential amino acids and vitamins added, including biotin and cyanocobalamin. NaSe, pyruvate, and 4-(2-hydroxyethyl)-1-piperazineethanesulfonic acid (HEPES) are also present in IMDM, making it a very rich basal culture medium. This makes it most suitable for high density or quickly proliferating cultures[151].

Roswell Park Memorial Institute (RPMI 1640) is based on a previous medium called McCoy's 5a medium, originally used for *in vitro* cultivation of hepatoma cells. Its name is 1640 because it was the 1640th medium to be developed during the process of optimising a basal medium for the culture of peripheral blood lymphocytes. RPMI 1640 is richer in vitamins and contains glutathione, which contributes to a favourable redox environment in the culture, and therefore protects from oxidative stress[152,153]. While developed for peripheral blood lymphocytes, it is commonly used for a wide variety of cell types.

1.6.2 Serum

1.6.2.1 *Ethics of serum production*

Serum for cell culture purposes is commonly extracted from bovine foetuses, which has been criticised for its ethics due the nature of extraction. Foetuses are usually attained from pregnant cattle slaughtered in commercial abattoirs. These cattle need to be free-roaming in herds in order to enable impregnation of cows, which is why most FBS comes from countries such as New Zealand, where this is the farming practice utilised in raising cattle[154].

To obtain foetal blood, the foetus is removed, and blood drained by cardiac puncture from its still beating heart. This is a point of contention in the ethics of serum collection, as the optimal point at which blood is harvested is at 6 months of gestation, where it has been found that there may be an awareness of pain and distress[155].

The European Food Standards Agency (EFSA) has recently taken these findings into account when considering the slaughter of pregnant livestock[156], which highlights an acceptance of the notion of foetal welfare at the regulatory level, which may impact the

supply of FBS in future. The demand for FBS has been rising, with a global market value of $695 million in 2017, which has been forecast to rise to $1037 million in 2025 at a compound annual growth rate of 5.1%[157]. More research and development is moving away from animal models to *in vitro* approaches in accordance with the 3 Rs objectives – reduce, replace, and refine – which is increasing FBS demand[158,159].

The blood is pooled and allowed to clot, after which serum is collected. Each foetus contains between 250 ml – 500 ml of blood, around half of which is serum[154]. The estimations for annual FBS consumptions vary, but range from 500,000 litres to 1,000,000 litres a year, which translates to between 2 – 4 million foetuses a year[160]. With demand rising, shortages will become more commonplace, as supply will not be able to satisfy rising demand, making the need for a chemically defined alternative clear.

1.6.2.2 *Scientific issues with the use of serum*

Being a natural animal product, the composition of serum is undefined and will invariably differ from batch to batch. It is a rich mixture of proteins, fats, vitamins, and trace elements that can support cell growth and differentiation, but the nature of it being natural presents a scientific problem when it comes to experimental reproducibility. Growth factors present in serum may affect cell behaviour, which may differ from lot to lot. One example of this is basic fibroblastic growth factor (bFGF or FGF-2), which was shown to be present in some serum lots, but not in others[161]. FGF-2 has been shown to have profound effects on MSC growth, and it would therefore be unsurprising if the presence or absence of it would make a significant difference to experimental outcomes, especially if the pathway tested is involved in crosstalk with this particular growth factor[162].

One major downside of using serum in biomaterials studies is that it is a biomaterial surface in particular that is being studied, which will be modified by the presence of xenoproteins in the serum. Due to the topography and surface energy of differing materials, protein adsorption to the surface will necessarily differ, which likely skews the results of any cell-surface interaction study[163]. It has been shown that macrophage-surface interactions in particular differ when serum was used on different materials, which may have a significant impact on our understanding of macrophage activity on implant materials, as macrophages are understood to be the driving force behind host responses to implanted material[164].

1.6.2.3 *Need for chemically defined medium*

The ethical and scientific problems with the use of serum necessitate the development of a chemically defined medium, suitable for use with MSC culture. It is of particular importance for the study of biomaterial-MSC interactions due to the protein adsorption properties of biomaterials and the potential for differential adhesive and proliferative properties on surfaces with differing proteins adsorbed to them. Moreover, the presence of growth factors known to be of importance in MSC function presents a particular challenge in *in vitro* experimentation due to the potential of aberrant behaviour.

1.7 Mechanical cues and MSC behaviour

Mechanical cues have widely been reported to influence MSC behaviour in terms of proliferation and differentiation behaviour. Mechanical cues can be categorised into substrate stiffness and surface topography. Substrate stiffness is an ongoing field of study, with many promising insights, particularly in relation to the use of hydrogels. Yang et al. show that MSCs have the ability to sense and 'remember' past physical signals – a phototunable polyethylene glycol hydrogel was used to study MSC response to differently stiff surfaces, and it was found that the degree of Yes-associated protein (YAP) and transcriptional coactivator with PDZ-binding domain (TAZ), as well as RUNX2 activation depended on time cultured on stiff tissue culture polystyrene previously. It was also found that YAP/TAZ and RUNX2 could be irreversibly activated above a mechanical dose threshold, suggesting that material stiffness can reprogram MSC behaviour[165].

The topography of a surface has also been widely reported to be tuneable in order to achieve a desired MSC response. The topography effects of a substrate on MSCs is of particular importance in this study, as the topography of plasma sprayed HA is optimisable. The topography of a surface can be interpreted as altering cytoskeletal tension by causing parts of the cell to be stretched or compressed, thereby modulating related mechanosensory signalling pathways, YAP/TAZ being a widely reported one, where MSC geometry was found in to influence YAP/TAZ localisation; a mostly nuclear localisation was observed in spread out MSCs, whereas cells smaller islands exhibited a more cytoplasmic YAP/TAZ distribution[166].

Indeed, Wnt signalling has been shown to activate YAP/TAZ signalling via binding behaviour not considered canonical or non-canonical. Park et al report an alternative Wnt-YAP/TAZ axis, dependant on FZD/Ror binding of Wnt3a or Wnt5a/b ligands, which promotes YAP/TAZ activation via heteromultimeric G-protein $G\alpha_{12/13}$ and Rho guanidine triphosphate-ases (GTPases). They also show that Wnt4 enhanced osteogenic differentiation of MSCs *in vitro*, which was negated upon YAP/TAZ depletion[167].

Wnt involvement in cellular response to topographical changes has been reported widely and shown to influence osteogenic potential of MSCs. One example is a recent publication, where Jieni et al showed how both ordered and random microstructured on titanium surfaces were able to modulate MSC fate. More specifically, a random micro-

nano-patterned structure enhanced expression of osteogenic markers such as RUNX2, osteoprotegerin, and osteocalcin via canonical Wnt activation via integrins[168].

1.8 Strategies for surface optimisation

A biomaterial surface can be tuned in terms of surface chemistry and topography, as was discussed previously (1.3.1). There are several ways in which this could impact implant success. It could either modulate the host immune response to the biomaterial, averting the possibility of fibrous encapsulation and therefore enabling osseointegration, or the approach could assume the avoidance of fibrous encapsulation and enhance osteoblastic response to the surface and therefore enhance differentiation.

Surface chemistries are often changed as part of biomaterial development in an effort to avoid adhesion of certain cell types and enhance adhesion of others. Other outcomes are enhanced osteoblastic differentiation and macrophage response (whether they are phenotypically anti- or pro-inflammatory). One example of this is a study where titanium surfaces where chemically altered to have low hydrophilicity, which induced increased secretion of pro-inflammatory cytokines, including tumour necrosis factor alpha (TNF-α), interleukin 1α (IL-1α), and CCL2, compared to heparin/fibronectin immobilised titanium surfaces[169]. Another study showed that wet chemical treatment of titanium prosthetics with magnesium ions promoted early osteogenic differentiation over untreated controls by enhancing focal adhesion development and stabilization of intracellular β-catenin[170]. It is interesting to note that this particular study found that β-catenin stabilisation was a part of the mechanism of action of enhanced osteogenic response, which is the key outcome of active canonical Wnt signalling, and has been shown to be tuneable by material properties as well[171]. These findings show that surface chemistry is an important factor in implant success. In the case of HA, the reported mechanisms of action to have an effect on MSC behaviour are intrinsically coupled with material crystallinity, as changes in HA crystallinity will invariably affect surface chemistry and ionic release.

Surface topography is another factor that is often experimented with in biomaterial development and has been extensively studied in relation to its effect on MSC fate with promising results. One example of enhanced proliferation and osteogenic differentiation was shown where zirconia and titanium surfaces were either mirror-polished or roughened by sandblasting. On all roughened surfaces, alkaline phosphatase (ALP) activity and RUNX2 expression was increased, suggesting

increased osteogenic differentiation[172]. Another example described bone metabolism and osteogenic differentiation being heavily impacted by surface topography, mediated by Wnt signalling and MAPK crosstalk[173].

These studies demonstrate that the ability to tightly control surface topography would be of tremendous value, as the possibility of fine-tuning osteogenic response of bone marrow-resident MSCs could have an impact on bone formation, and therefore implant success.

1.9 Design of Experiments

Industrial processes, such as plasma spraying, are highly complex and multifactorial in nature. Due to economic pressures and the constant need to improve and innovate, industry continuously endeavours to create new and pioneering technologies. In order to do so efficiently and cost-effectively, a very common process used for the planning and analysis of experiments for research and development is Design of Experiment (DoE). While DoE is commonly used in industry, it is rarely used in academia, with few researchers ever being exposed to the technique due to its traditional application in process development. More recently, there have been some publications have been made using DoE in biological fields, for example for the development of optimised peptide-plasmid DNA vectors for gene delivery in cancer therapy[174], or reviewed for use in metabolomics-related studies[175].

DoE allows for assessment of the effect of an input variable on a measured output. Depending on the size and resolution of the design chosen, this may also allow for analysis of synergistic effects of more than one input variable. The advantage of using DoE over traditional one-factor-at-a-time (OFAT) approaches is that in DoE, combinations of factor settings are strategically chosen and used in order to model the measured response to changes in each input variable. For example, if one were to investigate the effects of factors A, B, and C on measured output X, it may be logical to choose around 4 settings for each factor, then test every possible combination and measure the output for each. In this hypothetical experiment, a total of $4^3 = 64$ factor combinations would have to be tested, the analysis of which also would not easily allow for factor interaction assessment[176].

Using DoE, a low and a high factor setting is chosen in order to initially screen for effects. In the aforementioned hypothetical experiment, at would mean that factors A, B, and C would then be set at low (-1) and high (1) settings, with strategic combinations chosen based on the type of design. 8 different runs would be run in this case, and the main effect of each input factor could be calculated by modelling the response. This type of experimentation is hugely advantageous to traditional approaches, saving time and funds while reducing experimental human error by making experimentation easier to do[176].

DoE was therefore used in order to model material properties to plasma spray inputs and cellular responses, as HA-coated samples were produced on an active production line and the process is highly complex and multifactorial.

1.10 Aims

The aims of the studies presented in this thesis were to conduct an in-depth analysis of plasma sprayed HA coatings, and to model plasma sprayer input settings to material properties deemed relevant to biological response (crystallinity, roughness), and to model input on biological response. Furthermore, a chemically defined medium was to be developed for use with MSCs on biomaterials.

Specific aims of “Chapter 2: Development of a chemically defined medium for the culture of mesenchymal stromal cells” are to:

- Formulate a chemically defined medium which supports viability, growth, and osteogenic differentiation of MSCs
- Test the chemically defined medium in a clinical-grade continuous perfusion bioreactor (Quantum) for the expansion of MSCs
- To produce extracellular vesicles in the Quantum bioreactor using chemically defined medium and to isolate and characterise them

Specific aims of “Chapter 3: Optimisation of plasma sprayed hydroxyapatite coatings for MSC response” are to:

- Fully characterise plasma sprayer input effect on material properties including roughness and crystallinity
- Fully characterise plasma sprayer input effect on biological response using MSCs in terms of proliferation, osteogenic response, and Wnt signalling.
- Use the chemically defined medium presented in Chapter 2 to seed MSCs onto hydroxyapatite surfaces and to assess whether growth is supported by the medium on biomaterial surfaces.

2 Chapter 2: Development of a chemically defined medium for the culture of mesenchymal stromal cells

2.1 Chemically defined medium design

A chemically defined medium (CDM) needs to be able to fulfil the main functions of a foetal bovine serum (FBS)-supplemented MSC line culture medium: maintaining MSCs in an undifferentiated state, promoting cell number expansion, and giving the ability to repeatedly detach and seed cells. The simplest approach to this is to supplement a basal medium of choice, such as Dulbecco's minimal essential medium (DMEM), with the main components known to be in FBS, and to provide additives which enhance these functions. Using a Design of Experiments (DoE) approach in order to develop a chemically defined medium ensures efficient experimentation and close modelling of each additive's effect on measured outcome.

The main FBS components which were considered for the CDM formulation, and their primary functions in serum-supplemented cell growth are introduced below.

2.1.1 Bovine serum albumin

Bovine serum albumin (BSA) was used in the CDM development as albumin comprises up to 60% of protein in FBS, and has historically been a major component of serum development[177–179]. The actions of albumin in the human body are not well understood, but have been summarised to include maintenance of blood oncotic pressure and pH, binding and transport of physiologically important ligands, and antioxidant functions[180,181]. These roles clearly are transferable to a cell culture system, where binding and transport of ligands and antioxidant functions are highly desirable. Albumin is able to bind a large range of both endogenous and exogenous ligands, covalently and non-covalently, making it a vital component of serum[182]. Albumin is able to enter the cells through various mechanisms, and its ability to bind compounds such as fatty acids, steroids, and amino acids therefore made it an important consideration for the CDM[183–189]. Albumin also plays a role as an antioxidant. Reactive oxygen species (ROS), which are generated by medium components and cell metabolism, pose a risk of damage to the cell, both intra- and extracellularly[190]. This becomes particularly important in the extracellular environment, which lacks any mechanisms inherent to the intracellular space which mitigate ROS damage[191].

2.1.2 Trace Elements

Trace elements were added in the form of two commercially available mixes: trace elements B and trace elements C (Corning, 25-022-CI; 25-023-CI respectively – formulations in Appendix 1). Trace elements encompass micronutrients which provide metal ions to the cell culture environment and have been used in cell culture medium development extensively[192]. Most commonly, these are required for the proper functioning of enzymes[147,193–196]. Copper is one such ion that is important in lactate metabolism, for which it was found to be vital at very low levels[196].

2.1.3 Lipids and fatty acids

Lipids and fatty acids were delivered to the cell culture medium in the form of a commercially available, chemically defined lipid mix (Sigma Aldrich, L5146 – formulation in Appendix 2). Lipids are required for cell health and growth, playing an essential role in membrane biosynthesis and metabolism [177,186,197,198]. Lipids and fatty acids were of particular interest in this CDM as the model cell line used in studies, Y201 MSCs, have exhibited a tendency to alter their metabolism to be more fatty acid-based upon serum weaning to 0.5% (data not shown).

2.1.4 Selenium

Selenium is an important cofactor in antioxidant enzymes and redox regulators in mammalian cells[199]. In some cells lines, such as WI-38 diploid human fibroblasts, it has been shown that sodium selenite at 50 nmol/L concentrations, but not >1 µmol/L, is necessary for growth[200], with similar effects seen in haematopoietic cell cultures[151]. It has also been shown to have iron-carrying properties in Chinese hamster ovary cells, being essential for their growth[201]. Selenium was initially introduced into the CDM as part of the insulin-transferrin-selenium (ITS) supplement (Sigma Aldrich; I3146), but was added separately in the form of NaSe.

2.1.5 Insulin

Insulin is a commonly added growth factor in serum-free and serum-reduced culture, and is present in FBS[202]. Due to its broad binding affinity, insulin is able to bind noncognate receptors at supraphysiological concentrations. In mammalian cell culture, it has a strong mitogenic effect via insulin-like growth factor receptor 1 (IGF-1R) and metabolic effects via insulin receptor (IR)[203]. In reduced-serum cultures, insulin has also been shown to prevent apoptosis in several cell lines, making it a potentially vital component of CDM[204–206].

2.1.6 Transferrin

Transferrin is an iron chelator that has widely been described in literature as being essential for cell health[151,207–210]. Its function is to bind iron and regulate iron bioavailability to facilitate metabolic reactions involved in oxygen transport, DNA synthesis, and electron transport[211]. Transferrin's role in iron transport for DNA synthesis is of particular interest, as it has been linked with being essential for proliferation[212].

2.1.7 Other tested additives

Other tested additives included Rho kinase (ROCK) activity inhibitor Y-27632 (ROCKi), heparin, ethanolamine, hydrocortisone, ascorbic acid, and linoleic/oleic acid mix, due to each having been reported to enhance cell growth and proliferation. ROCKi is commonly used in embryonic stem cell (ESC) culture for maintaining stemness and increasing cell viability after cryopreservation[213,214], with similar effects having been reported for MSC post-thaw viability and proliferation[215,216]. Heparin is a vital co-factor in fibroblast growth factor (FGF) signalling and has also been reported to have been used successfully in ESC culture[162], with some studies reporting efficacy in MSC culture[217]. Ethanolamine is a medium supplement often used for cell culture as a precursor for phospholipid biosynthesis and is essential in glycosylphosphatidylinositol-anchored protein (GPI-AP) synthesis. GPI-APs are cytoskeleton regulators, instrumental in cell health and proliferation[218]. Studies have shown ethanolamine to protect from serum-starvation induced apoptosis[219] and aid in proliferation[220,221]. Hydrocortisone is a glucocorticosteroid used in some cell culture systems to promote cell growth via EGF signal modulation[222,223]. Ascorbic acid is commonly used for its antioxidant properties and was shown to have a pro-proliferative effect in MSCs by promoting extracellular matrix secretion[224,225]. Linoleic and oleic acid were introduced into the CDM using a commercially available mixture (linoleic/oleic acid mix; Sigma Aldrich, L9655). These fatty acids were shown to induce proliferation in mouse MSCs[226], but were also added due to data collected previously from serum-starved Y201 MSCs, which suggested that cells were shifting toward fatty acid metabolism.

2.1.8 Quantum bioreactor

Part of this work tested the ability of the CDM to support the scaled-up production of cell-derived products (extracellular vesicles (EVs)) for clinical use. CDM is applied for this work in order to improve yield and remove EV contamination from FBS

supplementation, which has been reported to persist even in vesicle-depleted medium[227].

For this, the Quantum bioreactor (TerumoBCT) was selected, which is a hollow-fibre, automated, continuous perfusion bioreactor working on the principle of continuous replenishment of culture medium to a large surface area (up to 2.1 m^2) upon which cells are cultured. It has been shown to be very effective in large scale manufacturing of clinically usable MSCs from bone marrow aspirates with comparable surface marker expression and differentiation capacity[228,229]. It was also shown to be more cost- and time-effective than manual passaging of primary bone marrow-derived MSCs, due to lower reagent and staff costs[230]. The Quantum system therefore presents a unique opportunity to trial a chemically defined, xeno-free medium in a clinical setting with which expansion of MSCs and EV production and collection on clinically relevant scales is possible.

2.2 Methods

2.2.1 Design of Experiments

The DoE designs used were general full factorials, with three levels (low, medium, high) unless otherwise stated. This was used in order to strike a balance between the size of the experiments and their resolution. For a 5-factor experiment, 17 runs with one medium point achieve a resolution of V, meaning that main factors are confounded with 4-factor combinations and higher and 2-factor combinations are confounded with 3-factor combinations and higher.

Once data were collected, the DoE was analysed using a stepwise backward elimination technique. This means that the model begins with all factors included up to a 2-factor interaction, with factors removed based on their p-values. Any factors not included in the initial design have been removed due to confounding, which can therefore not be estimated. If the p-value is higher than 0.15, the factor with the highest p-value is removed in a stepwise fashion, starting with the interactions. This is done until the model is left only with factors that contribute to the model with a p-value less than 0.15, although the model is forced to keep single factors in. This results in a model that can predict meaningful interactions between factors that otherwise would not have been identified. The p-value of 0.15 was chosen due to the nature of the modelling technique being highly efficient but prone to less significant results than one would achieve with traditional experimentation methods where the size of the experiments is usually much smaller and more repeats are achievable.

DoE results are presented in 6 parts: a table representing each step of the stepwise backward elimination of terms analysis, a pareto chart of effects, a main effect chart, an interaction matrix, contour plots (where available), and the calculated regression equation.

The table depicting the stepwise analysis details the p-values of each included factor and their coefficients in the proposed model. Factors are then removed in a stepwise fashion, starting with the highest p-value until all factors included are either included in interactions or have a p-value that falls below the specified alpha, which in this case is 0.15. Each eliminated factor is highlighted in a colour-coded fashion with legends available for each table. The results are depicted using different formats as explained below.

The pareto chart shows the magnitude a single or combined factors have on the measured output, expressed in standardised effect. The standardised effects are t-statistics that test the null hypothesis that the effect is 0. This aids in assessing what the most important factors are during initial analysis.

The main effects chart depicts the direction an effect has and is useful for assessing whether significant factors have a positive or negative effect on measured output. In cases where a centre point is included in the model, a red point is pictured on the graph, showing where the effect falls when all factors are at their medium setting. This is useful for identifying whether the main effects each factor is having is either affected by interactions or the response is non-linear. In both cases, the point would fall further away from the line than if a single factor were responsible for a linear response, in which case the point would fall exactly on the line.

The interaction matrix, or interaction plot, is used to show whether there are any combinations of factors that act synergistically in a positive or negative fashion. Usually, two lines are plotted onto a space depicting low and high settings of a factor. The direction of each line indicates what the response of the measured output is when the factor depicted using the lines remains at that level and another factor is increased. This is shown in a matrix depicting all 2-factor combinations and how they interact. Grey boxes indicate a non-significant interaction.

If available, contour plots are included in order to graphically represent the design space of two interacting factors and how to fully optimise the factor settings for the desired response. These are available when there are statistically significant interactions present in the model.

The regression equation that has been generated from the analysis is used to determine what the measured output would be if factor settings changed. For example, one could calculate how an output would respond to doubling one of the factor settings, even if that experiment wasn't carried out, based on the model created from the DoE.

2.2.2 Medium preparation

Media were prepared under sterile conditions in basal medium. Reagents used were: Bovine serum albumin (BSA; fatty acid free) (Fisher Scientific, cat. 11433164); Insulin-transferrin-selenium supplement (ITS) (Sigma Aldrich, cat. I3146); Chemically defined lipid concentrate (Lipid Mix) (Gibco, cat. 11548846); Trace Elements mixes B and C (Corning, cat. 25-022-CI/25-023-CI); hydrocortisone (Sigma Aldrich, cat. H6909);

ethanolamine (Sigma Aldrich, cat. E0135); L-ascorbic acid 2-phosphate sesquimagnesium salt hydrate (Sigma Aldrich, A8960); ROCK inhibitor Y-27632 (ROCKi; Cambridge Bioscience, cat. SM02-1), Insulin (Sigma Aldrich, cat. I9278); hTransferrin (Sigma Aldrich, T8158); sodium selenite (Sigma Aldrich, cat. 214485); heparin solution (Stemcell Technologies, cat. 07980).

2.2.3 Viability assay

Y201 viability was tested using resazurin-based Alamar blue (ThermoFisher, cat. DAL1025) over 10 days in different CDM compositions. Cells were seeded at 3 x 10^4 cell/cm^2 in high glucose, high pyruvate Dulbecco's minimal essential medium (DMEM) with 10% foetal bovine serum, 100 Units/mL Penicillin and 100 µg/mL Streptomycin and allowed to settle for 24 hours. Cells were then washed 3 times with phosphate buffered saline (PBS), and CDM formulae were added to the cells. 10 days after media change, cells were washed and Alamar blue reagent was added with DMEM at a 1:1 ratio and incubated at 37°C for 1 hour. Absorbance was measured using a plate spectrophotometer (Multiskan GO, ThermoFisher) at 570 nm.

2.2.4 Proliferation assay

Proliferation was tested by measuring increases in cell number over 3 days using Quant-iT PicoGreen dsDNA quantification kit (ThermoFisher, cat. P7589). Cells were seeded at 30% confluence and left to adhere for 24 hours in DMEM containing 10% FBS. Cells were washed 3 times using PBS, after which CDM formulations were added. At days 0 and 3, cells were washed 3 times in 0.2 M carbonate buffer, then lysed using 0.1% triton-X100 followed by repeated freeze-thawing to ensure complete lysis. 50 µl cell lysate was added to a black microplate alongside a series of standards of salmon sperm dsDNA (0-4 µg/ml), prepared in 0.1% triton X-100. PicoGreen reagent was prepared using TE buffer (10 mM Trizma base, 1.25 mM EDTA in dH_2O, pH 7.5) and added in equal amounts to samples and the standards. Fluorescence was measured using a fluorescent microplate reader (Clariostar Plus, BMG Labtech) at 485 nm excitation and 538 nm emission.

2.2.5 Crystal Violet staining

Cells were fixed and stained in crystal violet solution (in phosphate buffered saline (PBS): 0.05% w/v crystal violet; 1% formaldehyde; 1% methanol). Media was removed from cells and washed gently with PBS. Crystal violet solution was added and

incubated at room temperature for 20 minutes. Fixed and stained cells were then washed using tap water and cells visualised using light microscopy.

2.2.6 Osteogenic differentiation

MSCs were culture expanded in DMEM + 10 % FBS and incubated (37 °C, 5 % CO_2) for 24 hours prior to the addition of osteogenic supplements in FBS-supplemented medium or CDM (DMEM + 10 % FBS/CDM, 100 units/mL Penicillin, 100 µg/mL Streptomycin, 50 µg/mL L-Ascorbic acid 2-phosphate sesquimagnesium salt hydrate (Sigma, Cat: A8960), 10^{-8} M Dexamethasone (Sigma, Cat: D2915), 5 mM β-glycerophosphate (Sigma, Cat: G9422). Media was changed every 3 days for 9 days.

Osteogenic differentiation was assessed by alkaline phosphatase (ALP) activity. This was determined through the colourimetric change that occurs upon dephosphorylation of p-nitrophenyl-phosphate (pNPP) by ALP. At days 3, 6, and 9, cells were washed 3 times in 0.2 M carbonate buffer, then lysed using 0.1% triton-X100 followed by repeated freeze-thawing to ensure complete lysis. A p-nitrophenyl standard with increasing concentration (0-250 nmol/L) was added to a 96 well plate, alongside 50 µl of each sample. 50 µl of pNPP substrate (5mM pNPP, 3.3 mM $MgCl_2$ in 0.2 M carbonate buffer) were added to each sample and incubated for 1 hour at 37°C. Colourimetric change was measured using a spectrophotometer (Multiskan GO, Thermo Fisher) by measuring absorbance at 405 nm.

ALP activity was normalised to double stranded deoxyribonucleic acid (dsDNA) content in each well. dsDNA content was measured using fluorescent PicoGreen reagent (Thermo Fisher, Cat: P7581) as outlined in section 2.4.3.

Osteogenesis assays were carried out on differently treated 6-well tissue culture plates using CDM and osteogenic supplements. Tested culture surfaces were collagen I, vitronectin, amine, gelatin, and standard tissue culture treated polystyrene.

2.2.7 Adipogenic differentiation

MSCs were culture expanded, seeded into 6-well plates and allowed to adhere overnight (37°C, 5% CO_2). Cells were then washed and medium changed to DMEM + 10% FBS or CDM with and without adipogenic supplementation (10^{-6}M Dexamethasone (Sigma, Cat: D2915), 500µM 3-Isobutyl-1-methylxanthine (Acros, Cat: 228420010), 1µg/mL Insulin from bovine pancreas (Sigma, Cat: I5500), 100µM

Indomethacin (Sigma, Cat: I7378)). Medium was changed every 3 days, with time points at day 0, 7, 14, and 21.

Adipogenesis was assessed using Oil Red O (Sigma Aldrich, cat. O0625) staining of lipid droplets. Medium was removed and cells washed gently with PBS. Cells were then fixed in 10% formaldehyde (Polysciences, cat. 04018-1) for 10 minutes, followed by a wash in dH_2O. Oil Red O working solution (0.18g Oil Red O, 60ml 99% isopropanol, 40ml dH_2O) was filtered prior to use using filter paper (Whatman No. 1), and cells stained for 5 minutes at room temperature. The stain was removed, and cells washed using 60% ispropanol, followed by a wash in tap water. Stain was imaged using light microscopy.

2.2.8 Quantum bioreactor

Quantum Bioreactor (Terumo BCT Europe, Zaventem, Belgium) expansion and EV isolation tests were performed using research use only disposables, Y201 cells and the latest iteration of the CDM. Setup of the system, cell expansion monitoring, and harvest of cells was carried out as per manufacturer instructions and personal advice. In brief, the system was primed with PBS for 2 hours to wet the tubing and hollow-fibre interior of the growth chamber in order to prevent air bubbles. This was followed by coating of the growth chamber fibres using 500µg vitronectin initially, which was increased to 10mg in subsequent runs, for 24 hours. The system was washed with PBS, followed by a wash in the culture medium.

Cell growth and metabolism were monitored by daily sampling of waste medium using glucose and lactate dipsticks. As glucose is turned over by metabolising cells, glucose concentration is expected to decrease over time, while lactate concentration is expected to increase.

Baseline glucose and lactate readings were taken on the day of seeding, with subsequent readings taken every 24 hours. Medium was changed every 72 hours. In order to supply sufficient medium for growing cell numbers, flow rate was increased in a stepwise manner in accordance with the manufacturer's advice.

2.2.8.1 *Extracellular vesicle isolation*

N.B. All EV isolation and characterisation work was carried out by Savvas Ioannou.

EVs were collected for 24 hours when lactate levels reached a plateau. These were then isolated and characterised in order to confirm marker profiles and functionality. EV

isolation was performed in a number of centrifugation steps. First, conditioned medium was centrifuged at 300xg for 5 minutes to remove large cells and debris. The supernatant is removed and centrifuged at 2000xg for 20 minutes at 4°C. This supernatant is transferred to Ty45i ultracentrifuge tubes, and ultracentrifuged at 10000xg for 45 minutes at 4°C. The resulting supernatant was transferred into a fresh Ty45i ultracentrifuge tube and the pellet was re-suspended in 600µl cold PBS. This is re-centrifuged at 10000xg for 45 minutes at 4°C. This pellet is the 10000xg fraction (10k fraction). The supernatant reserved from the first 10000xg centrifugation is centrifuged at 100000xg for 90 minutes at 4°C. The pellet is re-suspended in 600µl cold PBS and re-centrifuged at 100000xg for 90 minutes at 4°C. This pellet is the 100000xg fraction (100k fraction).

2.2.8.2 *Transmission electron microscopy*

EVs were suspended in PBS. 10µl of the suspension was deposited on a 200-mesh copper grid with a formvar/carbon support film, left for three minutes to air dry. The grids were washed with three drops of dH_2O to remove the salts from the PBS. Negative staining was then attained by adding 10µl of 1% uranyl-acetate solution and drawing off excess stain. The grids were left in a dry environment for 30mins. The grids were stored in grid storage boxes and imaged the same day. Morphology was observed using the Transmission ThermoFisher Tecnai 12 at 120kV at X18.5K and X49K magnification.

2.2.8.3 *Micro-BCA Protein Assay*

The concentration of the EV lysate protein was determined using a micro-BCA protein assay (Pierce, Cat: 23235). Known standards and EVs were diluted with 0.2M NaOH and the micro-BCA working reaction was added in equal volume as the diluted samples and all samples were incubated at 37°C for 2 hours. The optical density of the samples was measured at 562nm and the concentration of the unknown samples was determined by a standard curve.

2.2.8.4 *Western blot analysis*

A 12% acrylamide gel with a 4% stacking gel was used to for gel electrophoresis of EV lysates. Extracellular vesicles do not require lysis with a lysis buffer, as boiling with loading buffer for 10 minutes is sufficient for lysis. Loading buffer (Laemmli buffer) comprised (in dH_2O) 20% Tris (1M, pH 6.8), 8% SDS, 40% glycerol, 0.13% bromophenol blue, and 20% β-mercaptoethanol. 15µg protein from extracellular vesicle

lysate was loaded onto the gel and run for 90 minutes at 90V. The SDS gel was then transferred using iBlot2 dry transfer system.

Membranes were rinsed in PBS with 0.1% Tween-20 (PBS-T) and blocked in 5% BSA in PBS-T for 1 hour. Primary antibodies were diluted in 5% BSA for 1 hour at room temperature and rinsed 4 times for 5 minutes in PBS-T. Secondary antibodies were labelled with horseradish peroxidase (HRP) and diluted into PBS-T. Membranes were incubated in secondary antibody for 1 hour at room temperature, then washed 4 times for 5 minutes in PBS-T.

Blots were drained and incubated in enhanced chemiluminescence (ECL) solution for up to 5 minutes. ECL was drained off and blots were visualised using iBright.

2.2.8.5 *Nanoparticle tracking analysis*

The concentration and size of extracellular vesicles was determined using the Nanosight LM14, a green laser (532nm) and NTA3.2 software. The extracellular vesicle samples were diluted in PBS until a concentration of 150 particles per frame was achieved. The Nanosight focuses a laser beam through the sample of interest in a chamber. The vesicles are then visualised by light scattering using a conventional light microscope with a 20X lens that is aligned perpendicularly to the beam axis, collecting the light scattered from each particle in the field of view. A script was set up on NTA3.2 software with five 60 second video recordings of all events for further analysis. NTA3.2 tracks the Brownian motion of each particle between frames allowing the calculation of size by applying the Stoke-Einstein equation. The experimental conditions were as follows: i) Measuring time: 5X 60 seconds, ii) Blur: Auto, iii) Detection Threshold: 2, iv) Blur size: Auto, v) Number of frames per run: 1499. The data represents the mean ± standard deviation.

2.3 Results

2.3.1 DoE I: Initial DoE design and screen for main effects of CDM components

An initial screening DoE was designed to screen out ineffective or unnecessary CDM components using a fractional factorial design method. In the first instances, viability was tested in order to assess how well Y201 cells would survive in different CDM compositions. Components tested were trace element mixes B and C, lipid mix, BSA, and ITS at low, medium, and high concentrations (Table 2.1).

Table 2.1: Concentrations used for low, medium, and high factor settings for initial DoE design

	Trace Elements B	**Trace Elements C**	**Lipid Mix**	**BSA**	**ITS**
Low	0.1%	0.1%	0.1%	5 mg/L	1%
Medium	0.55%	0.55%	0.55%	7.5 mg/L	5.5%
High	1%	1%	1%	10 mg/L	10%

CDM outperformed basal DMEM in terms of viability over 10 days in all but one case (CDM 14), but did not perform comparably to FBS containing DMEM (Figure 2.1).

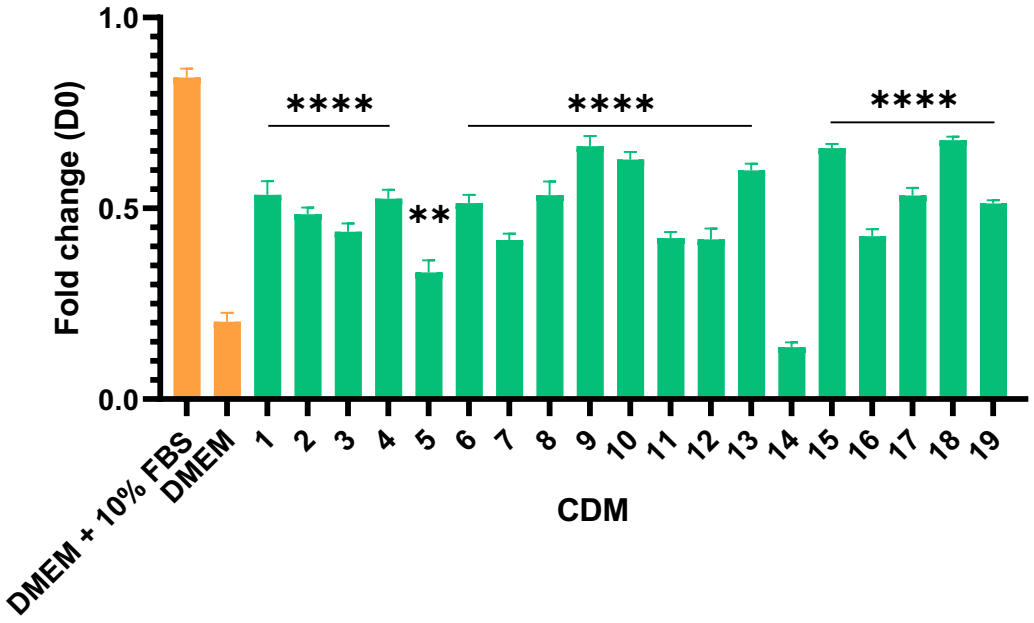

*Figure 2.1: Y201 viability fold change 10 days after media change as assessed by Alamar Blue. Significance is compared to DMEM. ****: p<0.0001; **: p<0.005; ±SEM; ANOVA.*

Stepwise backward elimination of terms analysis identified every added component as having a statistically significant effect on cell viability, including some interactions (Table 2.2; Figure 2.2).

Table 2.2: Stepwise backward elimination of terms analysis of CDMI. Highlighted rows identify eliminated terms. 6 steps of elimination were carried out to obtain a sufficiently powerful model. The main effector was identified to be BSA (p = 0.004). R^2 = 93.69%.

	------Step 1------		------Step 2------		------Step 3------		------Step 4------		------Step 5------		------Step 6------	
	Coef	**P**	**Coef**	**P**	**Coef**	**P**	**Coef**	**P**	**Coef**	**P**	**Coef**	**P**
Constant	0.5103		0.5103		0.5103		0.5103		0.5103		0.5103	
Trace Elements B %	0.0176	0.512	0.0176	0.412	0.0176	0.344	0.0176	0.296	0.0176	0.265	0.0176	0.247
Trace Elements C %	-0.0829	0.065	-0.0829	0.021	-0.0829	0.007	-0.0829	0.003	-0.0829	0.001	-0.0829	0.001
Lipid Mix %	0.0022	0.93	0.0022	0.913	0.0022	0.899	0.0022	0.889	0.0022	0.883	0.0022	0.879
BSA (mg/L)	-0.0596	0.116	-0.0596	0.049	-0.0596	0.022	-0.0596	0.011	-0.0596	0.006	-0.0596	0.004
ITS %	-0.0432	0.192	-0.0432	0.102	-0.0432	0.058	-0.0432	0.035	-0.0432	0.024	-0.0432	0.017
Trace Elements B %*Trace Elements C %	0.0079	0.757	0.0079	0.698	0.0079	0.655						
Trace Elements B %*Lipid Mix %	0.0069	0.786	0.0069	0.734								
Trace Elements B %*BSA (mg/L)	0.0287	0.327	0.0287	0.22	0.0287	0.156	0.0287	0.116	0.0287	0.092	0.0287	0.079
Trace Elements B %*ITS %	0.0096	0.709	0.0096	0.64	0.0096	0.59	0.0096	0.553				
Trace Elements C %*Lipid Mix %	0.0112	0.664	0.0112	0.587	0.0112	0.531	0.0112	0.49	0.0112	0.463		
Trace Elements C %*BSA (mg/L)	-0.0229	0.413	-0.0229	0.305	-0.0229	0.236	-0.0229	0.19	-0.0229	0.162	-0.0229	0.145
Trace Elements C %*ITS %	-0.0412	0.206	-0.0412	0.113	-0.0412	0.066	-0.0412	0.041	-0.0412	0.028	-0.0412	0.021
Lipid Mix %*BSA (mg/L)	0.0269	0.351	0.0269	0.242	0.0269	0.177	0.0269	0.135	0.0269	0.11	0.0269	0.095
Lipid Mix %*ITS %	0.045	0.181	0.045	0.094	0.045	0.052	0.045	0.031	0.045	0.02	0.045	0.015
BSA (mg/L)*ITS %	-0.006	0.813										
Ct Pt	-0.1071	0.197	-0.1071	0.105	-0.1071	0.061	-0.1071	0.037	-0.1071	0.025	-0.1071	0.018

R^2
93.69%

Eliminations: 1st 2nd 3rd 4th 5th

Trace elements B, BSA, and ITS were the most impactful main effectors, with the most impactful interactions being between lipid mix and ITS and trace elements C and ITS, with other interactions also being identified as significant but having a less pronounced effect on Y201 viability (Figure 2.2).

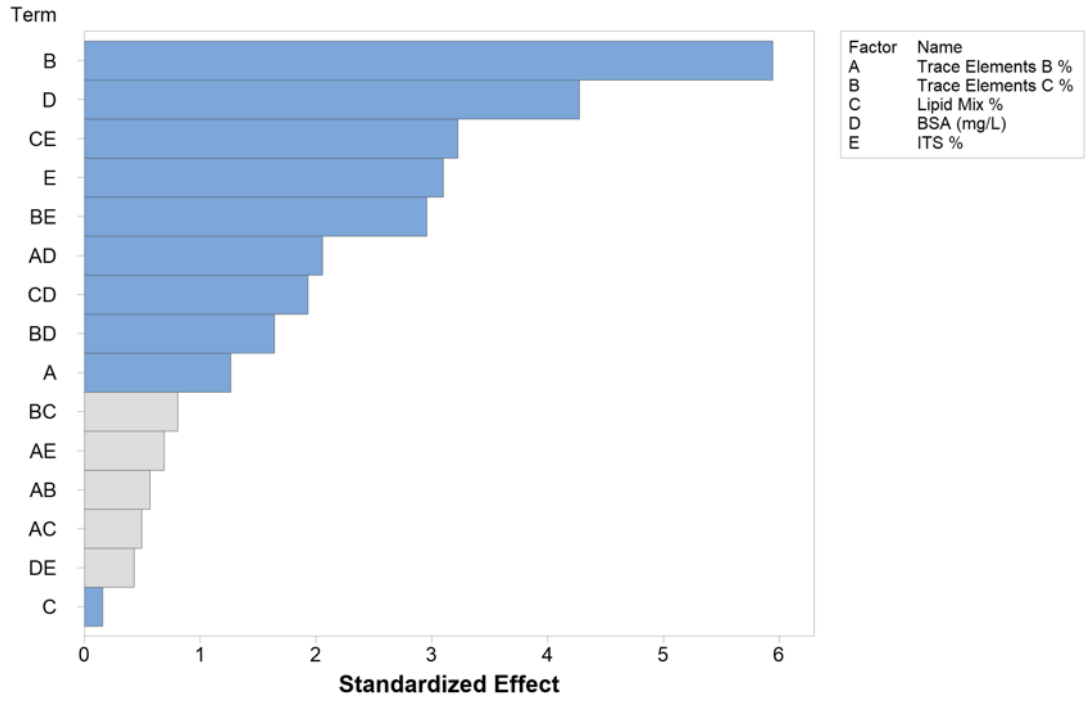

Figure 2.2: Main effects pareto chart depicting magnitude of standardized effect of CDM components (A: trace elements B (%), B: trace elements C (%), C: lipid mix (%), D: BSA (mg/L), E: ITS (%)) on Y201 viability as measured by Alamar blue after 10 days in culture. Blue bars indicate significant effect of the input parameters alone or in combination, while grey bars indicate a non-significant effect and were therefore excluded from the model (n = 3; α = 0.15).

Trace elements C, BSA, and ITS had negative main effects in this DoE, whereas trace elements B and lipid mix caused a marginal increase in viability with increasing concentration. The centre points in the main effects plot suggest that Y201 viability likely cannot be fine-tuned by main effects alone, but that either interactions account for the skewed centre point or curvature is evident in the model (Appendix 3).

Significant interactions have been identified between trace elements B and BSA, trace elements C and BSA, trace elements C and ITS, lipid mix and BSA, and lipid mix and ITS. The interaction plot (Appendix 4) suggests that the centre points in the main effects plot (Appendix 5) can actually be accounted for by these interactions, as they fall very close to some of the response lines.

One good example of this is the interaction between trace elements B and BSA, where at low BSA concentrations, an increase in trace elements B concentration has no

discernible effect on viability, whereas at a high BSA concentration, low amounts of trace elements B result in comparatively low viability, while increasing trace elements B concentration at a high BSA concentration increases viability, though not to the level seen at low BSA concentration. The centre point here falls almost on this response line, suggesting that the interaction is very strong and is skewing the results seen in the main effects plot. This suggests an overall negative effect of increased BSA concentration on Y201 viability, which could to some extent be rescued with increased trace elements B concentration (Appendix 4-3).

Based on the stepwise backward elimination of terms analysis, a regression equation was created for the prediction of CDM components' effect on Y201 viability (Equation 1). Using this model, the optimal CDM formulation was calculated within the bounds of tested component concentrations (Table 2.3). The predicted fold change is 0.6905 after 10 days in culture with the predicted CDM, which is lower than what was achieved by DMEM + 10% FBS, but is higher than DMEM without FBS addition, so an improvement was achieved over basal medium.

Equation 1: Regression equation for Y201 viability based on model created using stepwise backward elimination of terms analysis for the prediction of Y201 fold change in viability from D0 after 10 days in culture.

$$
\begin{aligned}
\text{Y201 viability} = {} & 0.4031 \\
& + 0.0176[\text{Trace Elements B (\%)}] \\
& - 0.0829[\text{Trace Elements C (\%)}] \\
& + 0.0022[\text{Lipid Mix (\%)}] \\
& - 0.0596[\text{BSA (mg/L)}] \\
& - 0.0432[\text{ITS (\%)}] \\
& + 0.0287([\text{Trace Elements B (\%)}] \times [\text{BSA (mg/L)}] \\
& - 0.0229([\text{Trace Elements C (\%)}] \times [\text{BSA (mg/L)}] \\
& - 0.0412([\text{Trace Elements C (\%)} \times [\text{ITS (\%)}]) \\
& + 0.0269([\text{Lipid Mix (\%)}] \times [\text{BSA (mg/L)}]) \\
& + 0.0450([\text{Lipid Mix (\%)} \times [\text{ITS (\%)}] \\
& + 0.1071([\text{Trace Elements B (\%)}] \times [\text{Trace Elements C (\%)}] \times [\text{Lipid Mix (\%)}] \times [\text{BSA (mg/L)}] \times [\text{ITS (\%)}])
\end{aligned}
$$

Table 2.3: Optimal CDM formulation for Y201 viability after 10 days in culture in CDM, as calculated by model created using stepwise backward elimination of terms analysis.

Variable	**Setting**
Trace Elements B	1%
Trace Elements C	0.1%
Lipid Mix	0.1%
BSA (mg/L)	5 mg/ml
ITS %	1%
Response	**Fold change**
Y201 Viability	0.6905

2.3.2 DoE II: Addition of further CDM components and evaluation of main and combined effects

To optimise the performance of the CDM, more components were added, with the aim of promoting viability and cell number increase. Optimal BSA, trace elements B and C, and lipid mix concentrations were carried forward from the previous DoE (Table 2.3), and heparin, a ROCK inhibitor (Y-27632; ROCKi), ascorbic acid, ethanolamine, hydrocortisone, and ITS were tested for their impact on Y201 viability in varying concentrations. The DoE was designed as a screening-type DoE, not including centre points, and only probing for significant main effects of each additive. Factor concentrations are listed in Table 2.4.

Table 2.4: Low and high concentrations for factors input into DoE II.

	Heparin (ng/ml)	**ROCKi (µM)**	**Ascorbic acid (µM)**	**Ethanolamine (µM)**	**Hydrocortisone (µM)**	**ITS (%)**
Low	0	0	0	0	0	0
High	100	10	100	10	20	10

Two CDM formulations statistically significantly outperformed unsupplemented DMEM in terms of viability after 10 days in culture. Other CDM formulations were not significantly different (Figure 2.3).

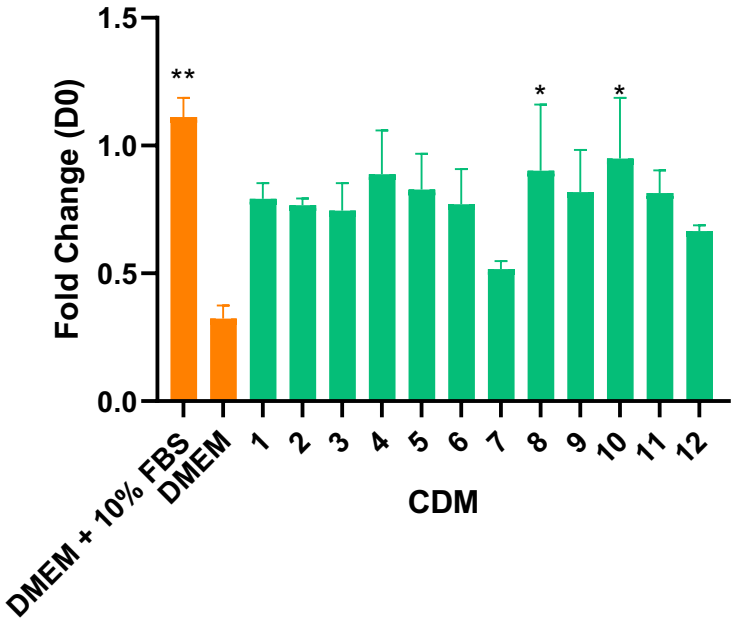

*Figure 2.3: Viability fold change of Y201 MSCs after 10 days in culture in DMEM + 10% FBS, DMEM, and various CDM formulations. Cells were seeded at 3 x 10^4 cell/cm^2 and left to adhere overnight. Cells were then washed and media replaced accordingly. Viability was assessed using Alamar blue viability assay (n = 3; *: p<0.05; **: p<0.005; ±SEM; ANOVA multiple comparisons against DMEM).*

Stepwise backward elimination of terms analysis identified ethanolamine to have no main effect on Y201 viability, with interactions between heparin and ascorbic acid, heparin and hydrocortisone, and ROCKi and ascorbic acid also having a significant effect on viability (Table 2.5; Figure 2.4).

Table 2.5: Stepwise backward elimination of terms analysis for Y201 viability response to addition of various concentrations of heparin, ROCKi, ascorbic acid, hydrocortisone, and ITS (DoE II).

	-----Step 1----	
	Coef	**P**
Constant	130705	
Heparin ng/ml	13743	0.006
ROCKi (µM)	-20008	0.002
Ascorbic Acid (µM)	-4701	0.091
Hydrocortisone (µM)	12219	0.009
ITS %	18790	0.003
Heparin ng/ml*Ascorbic Acid (µM)	-8837	0.026
Heparin ng/ml*Hydrocortisone (µM)	6017	0.078
ROCKi (µM)*Ascorbic Acid (µM)	7456	0.047

R^2
99.27%

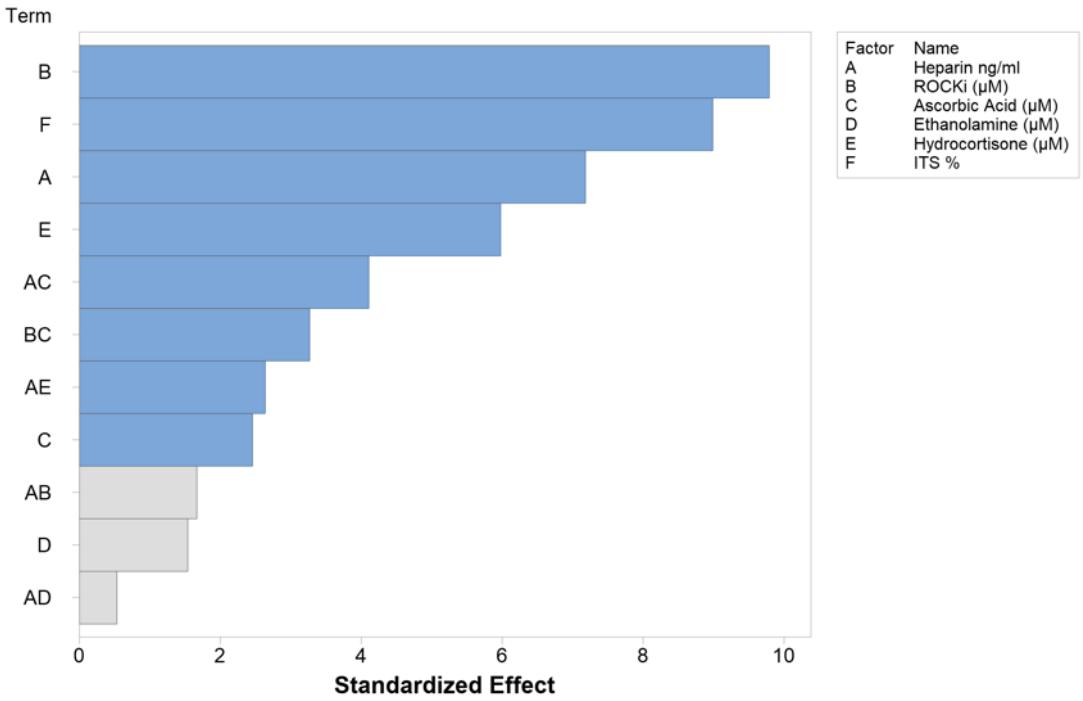

Figure 2.4: Main effects pareto chart depicting magnitude of standardized effect of CDM components (A: Heparin (ng/ml); B: ROCKi (μM); C: Ascorbic acid (μM), D: Ethanolamine (μM), E: Hydrocortisone (μM); F: ITS (%)) on Y201 viability. Blue bars indicate significant effect of the input parameters alone or in combination, while grey bars indicate a non-significant effect and were therefore excluded from the model (n = 3; α = 0.15).

Heparin, hydrocortisone, and ITS had positive effects on Y201 viability, while ROCKi and ascorbic acid had a negative effect on viability. Ethanolamine had a non-significant effect on viability (Appendix 6). Three significant interactions were identified: heparin and ascorbic acid, heparin and hydrocortisone, and ROCKi and ascorbic acid (Appendix 7 and Appendix 8).

This DoE was repeated with changes in cell number over time measured as an output as a proxy for proliferation after 3 days in culture with varying CDM using Quant-iT PicoGreen reagent. CDM formulations 3, 4, 6, 10, and 11 outperformed DMEM to the extent that they were not significantly different from DMEM + 10% FBS (Figure 2.5).

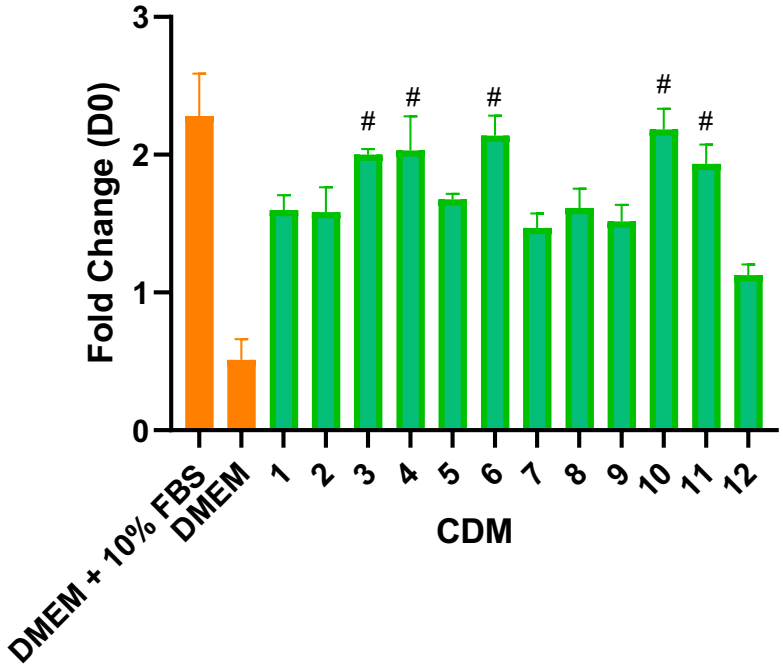

Figure 2.5: Fold change in Y201 cell number as measured by Quant-iT PicoGreen after 3 days in culture with 12 different CDM. Cells were seeded at a density of 1.5 x 10^4 cells/cm^2 and left to adhere for 24 hours. Cells were then washed and media replaced. 3 days after media changes, cells were lysed and DNA quantified. N = 3; #: non-significant difference to DMEM + 10% FBS; ±SEM; ANOVA.

In contrast to viability, all components had a significant main effect on cell number, with significant interactions between heparin and hydrocortisone and heparin and ascorbic acid (Table 2.6; Figure 2.6).

Table 2.6: Stepwise backward elimination of terms analysis of CDM components' effects on Y201 MSC cell number after 3 days in culture. R^2 = 97.76%.

	------Step 1-----	
	Coef	**P**
Constant	5.2168	
Heparin ng/ml	0.5019	0.008
ROCKi (µM)	-0.3101	0.042
Ascorbic Acid (µM)	-0.2357	0.073
Ethanolamine (µM)	0.3673	0.032
Hydrocortisone (µM)	0.3947	0.02
ITS %	0.2569	0.076
Heparin ng/ml*Ascorbic Acid (µM)	0.239	0.114
Heparin ng/ml*Hydrocortisone (µM)	0.244	0.109

R-sq
97.76%

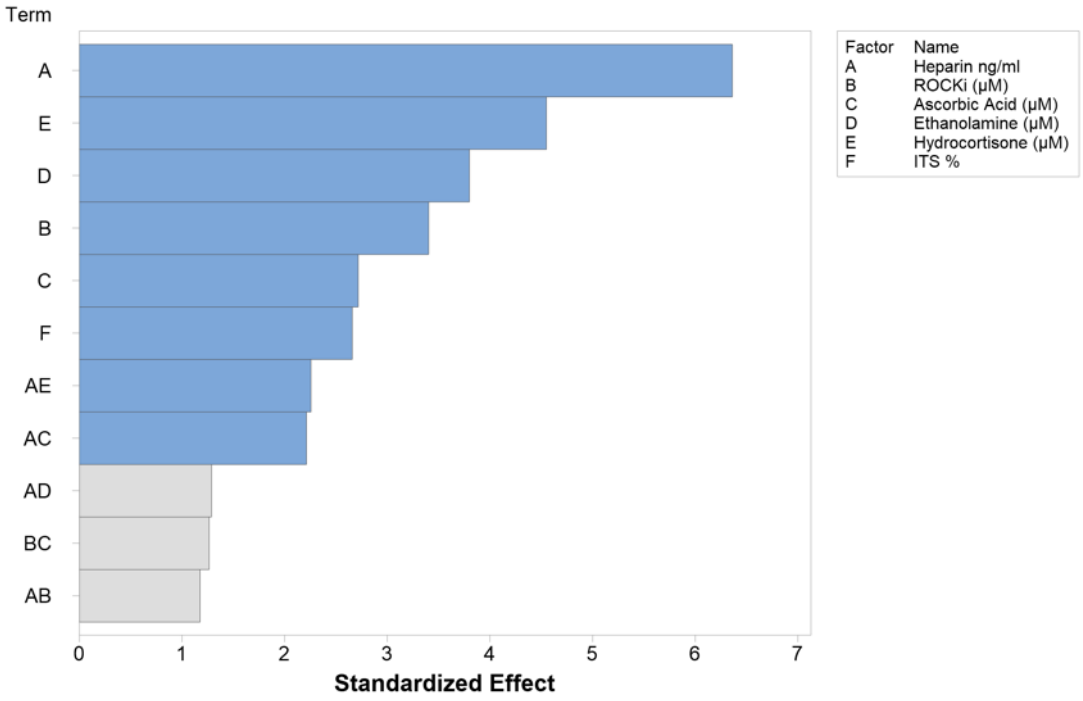

Figure 2.6: Main effects pareto chart depicting magnitude of standardized effect of CDM components (A: Heparin (ng/ml); B: ROCKi (µM); C: Ascorbic acid (µM), D: Ethanolamine (µM), E: Hydrocortisone (µM); F: ITS (%)) on Y201 cell number as assessed by Quant-iT PicoGreen after 3 days in culture (fold change from day 0). Blue bars indicate significant effect of the input parameters alone or in combination, while grey bars indicate a non-significant effect and were therefore excluded from the model (n = 3; α = 0.15).

ROCKi and ascorbic acid had a negative effect on cell numbers, while all other CDM components increased fold change in cell number with increasing concentrations (Appendix 9). Two significant interactions were identified: heparin and ascorbic acid, and heparin and hydrocortisone. For heparin and ascorbic acid, at a high concentration

of ascorbic acid, and low heparin, fold change was significantly lower than at low ascorbic acid and low heparin. At high concentrations of both, the negative effect was negated. In the case of hydrocortisone and heparin, hydrocortisone appeared to have a profound positive effect on fold change (Appendix 10 and Appendix 11).

The optimal medium to take forward into further studies was calculated based on the DoE using cell number change as an output, using the regression equation generated as part of the stepwise backward elimination of terms analysis (Equation 2; Table 2.7: Optimal CDM formulation for Y201 cell number change after 3 days in culture in CDM, as calculated by model created using stepwise backward elimination of terms analysis.).

Equation 2: Regression equation for the prediction of Y201 cell number change after 3 days in culture with CDM.

Y201 cell number change = 4.725
+ 0.00038[Heparin (ng/ml)]
- 0.0620[ROCKi (μM)]
- 0.00949[Ascorbic Acid (μM)]
+ 0.0735[Ethanolamine (μM)]
+ 0.0151 [Hydrocortisone (μM)]
+ 0.0514 [ITS (%)]
+ 0.000096([Heparin (ng/ml)] x [Ascorbic Acid (μM)])
+ 0.000487([Heparin (ng/ml) x [Hydrocortisone (μM)])

Table 2.7: Optimal CDM formulation for Y201 cell number change after 3 days in culture in CDM, as calculated by model created using stepwise backward elimination of terms analysis.

Variable	**Setting**
Heparin	100 ng/ml
ROCKi	0 μM
Ascorbic Acid	100 μM
Ethanolamine	10 μM
Hydrocortisone	20 μM
ITS	10%
Response	**Fold Change**
Y201 cell number change	2.432

Components in Table 2.7 were added to the calculated optimum from the previous DoE (Table 2.3) and taken into further study.

2.3.3 DoE II: Morphology assessment on differently treated culture surfaces

In order to assess MSC morphology in CDM, cells were seeded onto differently treated cell culture surfaces. Surfaces tested were standard tissue culture plastic, amine plates, collagen I coated plates, vitronectin coated plates and gelatin coated plates. Cells were seeded in DMEM + 10% FBS or CDM onto tissue culture surfaces and left to adhere for 24 hours. Medium was then changed and cells were left to culture for 4 days. Cells were fixed and stained with crystal violet.

Cell morphology and density were similar between CDM and DMEM + FBS after 24 hours of seeding. After 4 days in culture in respective media, while density increased in both media, the cells cultured in CDM appeared less dense (Figure 2.7). Otherwise, no visually discernible effect could be seen on differently treated or matrix-coated tissue culture surfaces, and it was decided to test whether differentiation capacity was affected by different surfaces.

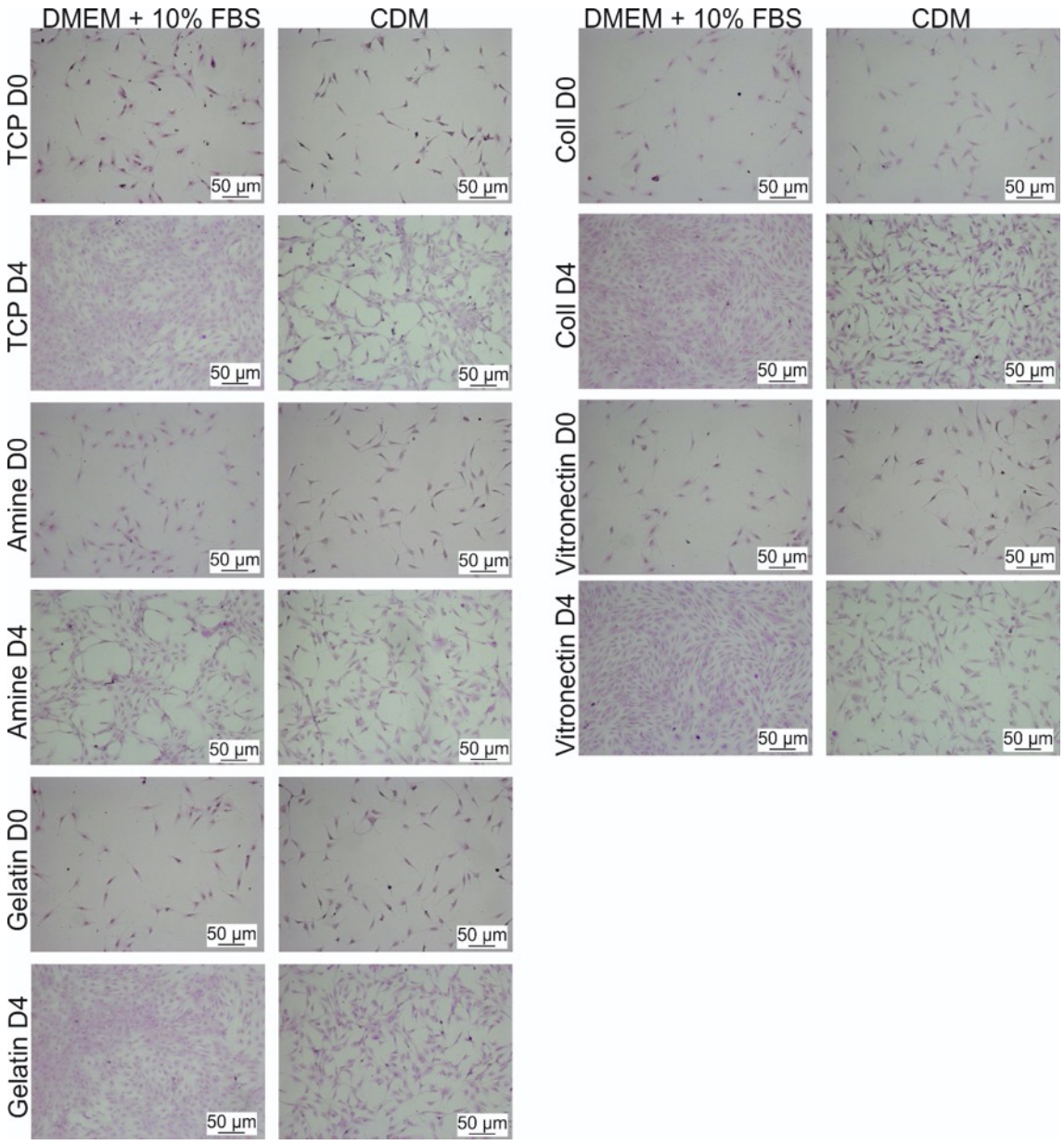

Figure 2.7: Morphological assessment of Y201 MSCs on differently treated tissue culture surfaces. Cells were seeded at a density of 1 x 10^4 cells/cm^2 and left to adhere for 24 hours. Cells were then fixed and stained with crystal violet at days 0 and 4 and imaged using a light microscope. TCP: Tissue culture plastic; ColI: collagen I.

2.3.4 DoE II: Y201 differentiation capacity on differently coated surfaces

Osteogenic differentiation capacity on differently coated surfaces was tested in order to assess whether a coating would improve differentiation of Y201-MSCs. Except for the amine plates, a significant increase in ALP activity was observed in all osteogenic conditions (Figure 2.8). These data suggest that there is no advantage to using a treated tissue culture surface in conjunction with CDM, and that standard tissue culture plastic would yield the desired outcome.

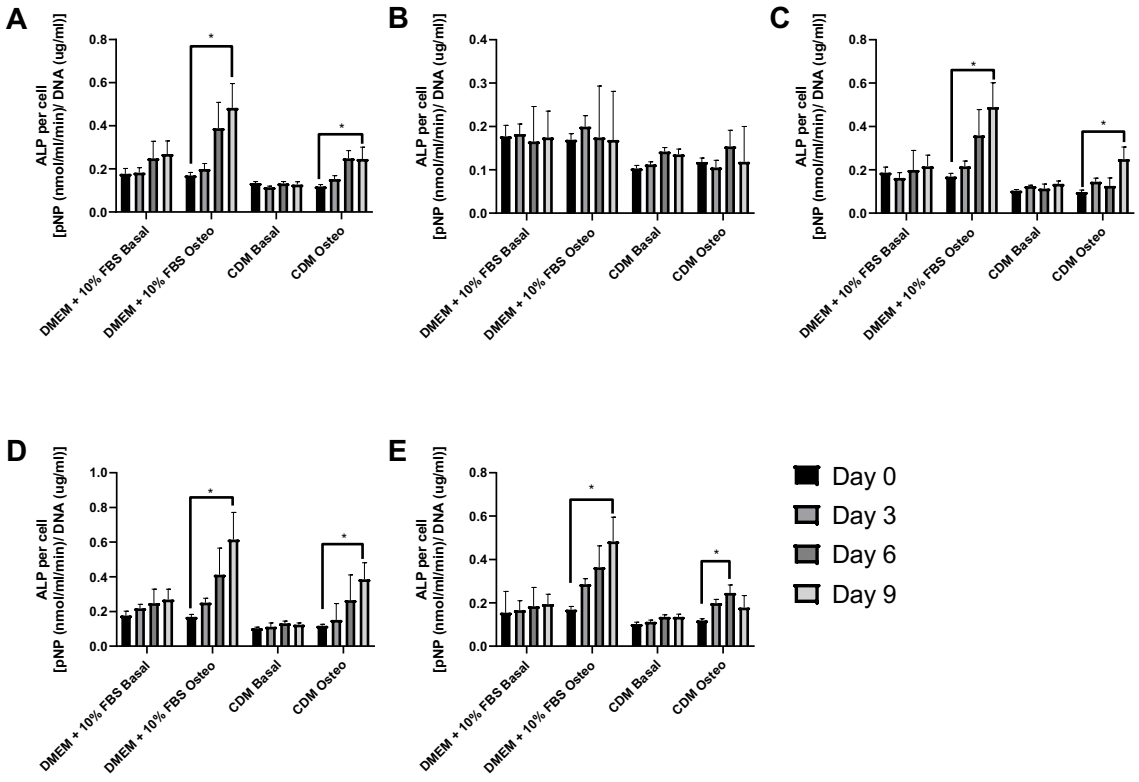

Figure 2.8: Osteogenic differentiation of Y201 MSCs on differently coated tissue culture surfaces. Cells were seeded at a density of 3 x 10^4 cells/cm^2 and left to adhere for 24 hours. Media was then changed to either unsupplemented media (Basal) or osteogenic supplements added (Osteo) in DMEM + 10% FBS or CDM. Tissue culture surface treatments tested were A: Tissue culture plastic control; B: amine treated; C: gelatin coating; D: collagen I coating; E: vitronectin coating (n = 6; p<0.05; ±SEM; ANOVA).

In order to test further Y201 differentiation capacity, adipogenesis was assessed using CDM on standard tissue culture plastic. It was found that while supporting adipogenic differentiation under adipogenic culture conditions, adipogenic differentiation was also spontaneously initiated by the CDM in basal conditions, which rendered it an unsuitable candidate for further study (Figure 2.9).

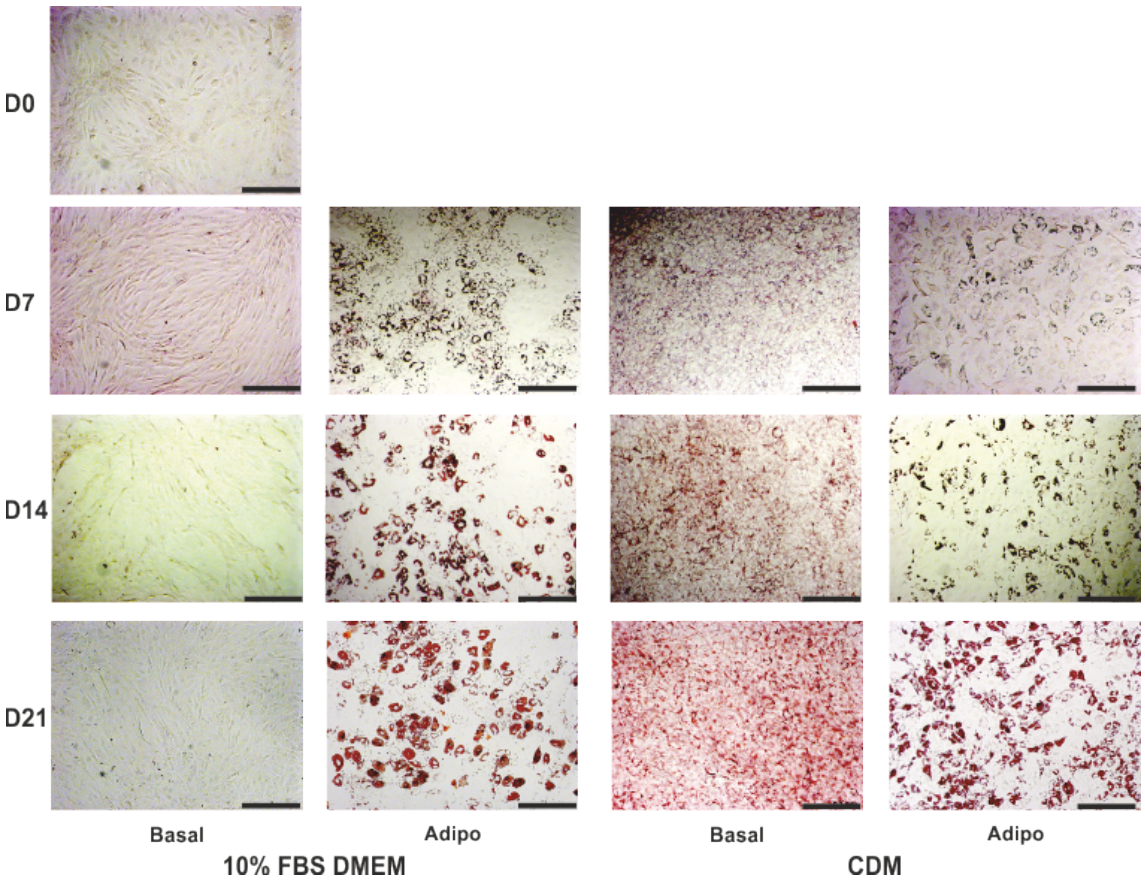

Figure 2.9: Adipogenic differentiation of Y201 MSCs. Cells were seeded onto tissue culture plastic at a density of 3 x 10^4 cells/cm^2 and left to adhere for 24 hours. Media was then changed to either adipogenic medium (Adipo) or non-supplemented medium (basal) in either DMEM + 10% FBS or CDM. Cells were then fixed and lipid droplets were stained with Oil red O stain (red) at days 0, 7, 14, and 21 and imaged using a light microscope. Scale bar: 100µm.

2.3.5 DoE III: Further optimisation of CDM for Y201 cell number change

To design a CDM that would be suitable for Y201 cell number change and survival, a new DoE was set up with different component ranges. A more in-depth, response surface design was used and included ITS, BSA, trace elements B and C, and lipid mix, with 32 different CDM compositions. 21 of the 32 CDM formulae outperformed basal DMEM in terms of Y201 cell number change (Figure 2.10), while others were non-significantly different. Low, medium and high settings are given in Table 2.8.

Table 2.8: Concentrations of low, medium, and high settings for factors input into DoE III.

	BSA (mg/L)	ITS (%)	Trace Elements B (%)	Trace Elements C (%)	Lipid Mix (%)
Low	0	0.1	0.1	0.1	0.1
Medium	50	0.5	0.5	0.5	0.5
High	100	1	1	1	1

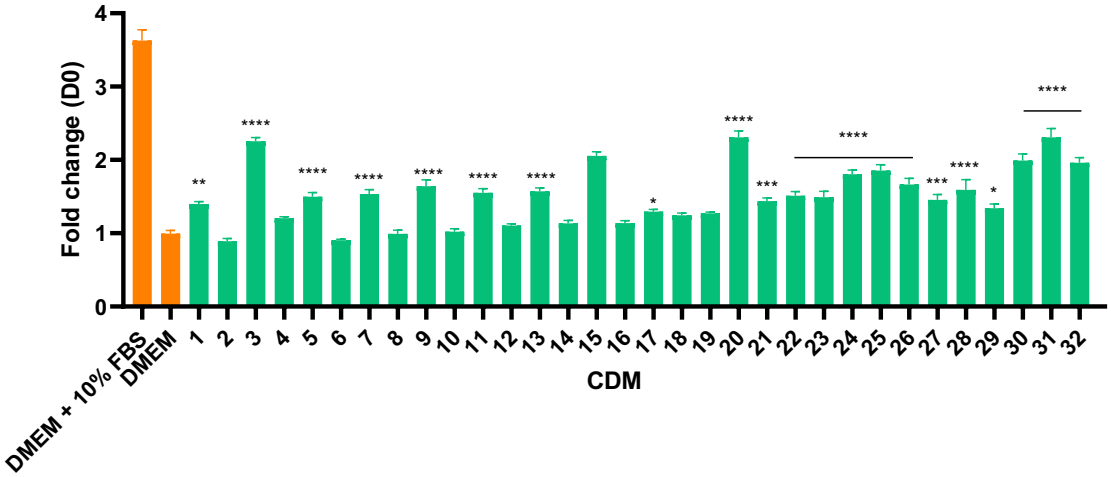

*Figure 2.10: Fold change in cell number as measured by Quant-iT PicoGreen after 3 days in culture with 32 different CDM. N = 3; ****: p<0.0001; ***: p<0.0005; **: p<0.005; *: p<0.05 compared to DMEM; ±SEM; ANOVA.*

Stepwise backward elimination of terms analysis of the response surface DoE identified all components as having a main effect, with several interactions also being identified as significant. BSA was found to be the most significant driver of Y201 proliferative response (p = 0.000) (Table 2.9; Figure 2.11).

Table 2.9: Stepwise backward elimination of terms analysis for modelling of CDM components to Y201 cell number change. R^2 = 91.01%.

	----Step 1----		----Step 2----		----Step 3----		----Step 4----		----Step 5----		----Step 6----		----Step 7----		----Step 8----		----Step 9----	
	Coef	**P**	**Coef**	**P**	**Coef**	**P**	**Coef**	**P**	**Coef**	**P**	**Coef**	**P**	**Coef**	**P**	**Coef**	**P**	**Coef**	**P**
Constant	33000		33006		33006		33006		32964		32964		32883		32989		32989	
Blocks	8770	0.000	8766	0.000	8766	0.000	8766	0.000	8799	0.000	8799	0.000	8863	0.000	8779	0.000	8779	0.000
BSA (mg/L)	-7798	0.000	-7798	0.000	-7798	0.000	-7798	0.000	-7798	0.000	-7798	0.000	-7798	0.000	-7798	0.000	-7798	0.000
ITS %	2629	0.000	2629	0.000	2629	0.000	2629	0.000	2629	0.000	2629	0.000	2629	0.000	2629	0.000	2629	0.000
Trace Elements B %	-368	0.280	-368	0.277	-368	0.274	-368	0.272	-368	0.271	-368	0.270	-368	0.269	-368	0.267	-368	0.269
Trace Elements C %	800	0.020	800	0.020	800	0.019	800	0.019	800	0.018	800	0.018	800	0.018	800	0.017	800	0.018
Lipid %	-1941	0.000	-1941	0.000	-1941	0.000	-1941	0.000	-1941	0.000	-1941	0.000	-1941	0.000	-1941	0.000	-1941	0.000
BSA (mg/L)*BSA (mg/L)	2037	0.298	2085	0.270	2085	0.267	2085	0.265	1729	0.328	1729	0.327	1043	0.503				
ITS %*ITS %	-1174	0.548	-1126	0.550	-1126	0.548	-1126	0.546										
Trace Elements B %*Trace Elements B %	2087	0.286	2135	0.258	2135	0.256	2135	0.254	1779	0.314	1779	0.313	1094	0.483	1992	0.013	1992	0.014
Trace Elements C %*Trace Elements C %	200	0.918																
Lipid %*Lipid %	-1174	0.548	-1126	0.550	-1126	0.548	-1126	0.546	-1482	0.401	-1482	0.400						
BSA (mg/L)*ITS %	-1210	0.001	-1210	0.001	-1210	0.001	-1210	0.001	-1210	0.001	-1210	0.001	-1210	0.001	-1210	0.000	-1210	0.000
BSA (mg/L)*Trace Elements B %	200	0.562	200	0.559	200	0.557												
BSA (mg/L)*Trace Elements C %	410	0.235	410	0.232	410	0.229	410	0.228	410	0.226	410	0.225	410	0.224	410	0.223		
BSA (mg/L)*Lipid %	2331	0.000	2331	0.000	2331	0.000	2331	0.000	2331	0.000	2331	0.000	2331	0.000	2331	0.000	2331	0.000
ITS %*Trace Elements B %	-840	0.016	-840	0.016	-840	0.015	-840	0.015	-840	0.014	-840	0.014	-840	0.014	-840	0.014	-840	0.014
ITS %*Trace Elements C %	-1233	0.001	-1233	0.001	-1233	0.000	-1233	0.000	-1233	0.000	-1233	0.000	-1233	0.000	-1233	0.000	-1233	0.000
ITS %*Lipid %	-1073	0.002	-1073	0.002	-1073	0.002	-1073	0.002	-1073	0.002	-1073	0.002	-1073	0.002	-1073	0.002	-1073	0.002
Trace Elements B %*Trace Elements C %	2121	0.000	2121	0.000	2121	0.000	2121	0.000	2121	0.000	2121	0.000	2121	0.000	2121	0.000	2121	0.000
Trace Elements B %*Lipid %	281	0.414	281	0.411	281	0.408	281	0.406	281	0.405								
Trace Elements C %*Lipid %	-89	0.795	-89	0.794														

R^2
91.01%

Eliminations: 1st 2nd 3rd 4th 5th 6th 7th 8th

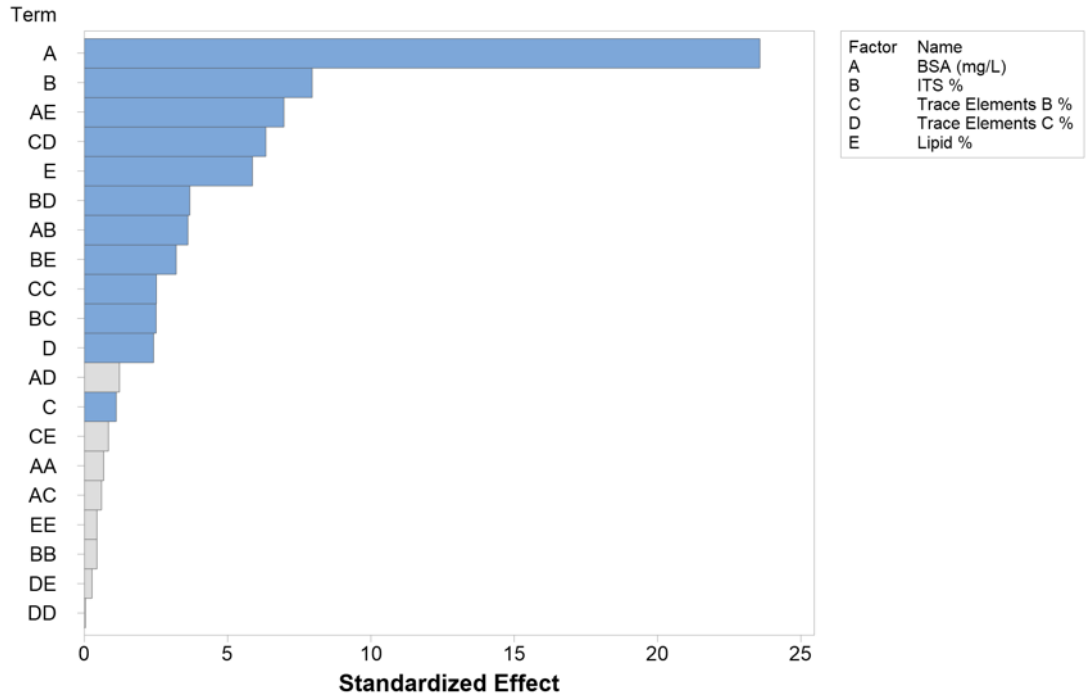

Figure 2.11: Main effects pareto chart depicting magnitude of standardized effect of CDM components (A: BSA (mg/L); B: ITS (%), C: Trace elements B (%), D: Trace elements C (%), E: Lipid Mix (%)) on Y201 cell number change as assessed by Quant-iT PicoGreen after 3 days in culture (fold change from day 0). Blue bars indicate significant effect of the input parameters alone or in combination, while grey bars indicate a non-significant effect and were therefore excluded from the model (n = 5; α = 0.15).

Y201 proliferative response to trace elements B was shown to be non-linear, whereas all other components provoked a linear response with increasing concentration. BSA and lipid mix had negative effects on Y201 cell number change, whereas ITS and trace elements C had a positive effect (Appendix 12).

Significant interactions were identified to be between BSA and ITS, BSA and lipid mix, ITS and trace elements B, ITS and trace elements C, ITS and lipid mix, and trace elements B and C. Y201 proliferative response to these interactions was closely modelled, with curvature detected in the trace elements B and C interaction, whereas other interactions were either additive or subtractive of one another (Appendix 13 - Appendix 14).

The optimum CDM achievable from this DoE was calculated from the regression equation generated as part of the stepwise backward elimination of terms analysis of this response surface DoE (Equation 3). The CDM would achieve a fold change in Y201 cell number of 2.29 after 3 days in culture (

Table 2.10).

Equation 3: Regression equation generated from response surface DoE for the prediction of Y201 proliferative response to changes in CDM component concentrations.

Y201 cell number change = 44270
- 203.7[BSA (mg/L)]
+ 17673[ITS (%)]
- 15117 [Trace Elements B (%)]
- 635[Trace Elements C (%)]
- 7731[Lipid (%)]
+ 9835[Trace Elements B (%)] x [Trace Elements B (%)]
- 59.8[BSA (mg/L)] x [ITS (%)]
+ 115.1[BSA (mg/L) x [Lipid (%)]
- 4146[ITS (%)] x [Trace Elements B (%)]
- 6089[ITS (%)] x [Trace Elements C (%)]
- 5298[ITS (%) x [Lipid (%)]
+ 10475[Trace Elements B (%) x [Trace Elements C (%)]

Table 2.10: Optimum CDM as calculated from the regression equation generated from the stepwise backward elimination of terms analysis of the response surface DoE.

Variable	**Setting**
BSA (mg/L)	10
ITS %	1
Trace Elements B %	0.1
Trace Elements C %	0.1
Lipid %	0.1
Response	
Fold Change (D0)	2.2912

2.3.6 DoE IV: ITS and basal medium optimisation for cell number change

To take the CDM further into scale-up testing, a final DoE was carried out in order to assess whether an improvement could be achieved by using different basal media. Media tested were Advanced Roswell Park Memorial Institute (RPMI)-1640, DMEM, DMEM/F12, and Iscove's modified Dulbecco's medium (IMDM). In addition to this, ITS was split into its component parts – insulin, transferrin, and selenium – in order to model more closely the response to each component. Furthermore, heparin and linoleic acid/oleic acid mix were added with the aim of improving CDM performance (Table 2.11). This DoE was designed to be a short, 12-run screening experiment, as a working formulation was found. This type of design did not allow for modelling of interactions, and it served as a tool to understand whether any major advantages could be found if a different basal medium had been used.

Of all basal media tested, DMEM performed the best, with 3 CDM formulations being non-significantly different from FBS supplemented DMEM. IMDM performed the worst, while DMEM/F12 and Advanced RPMI had fewer working formulations than DMEM (Figure 2.12).

Table 2.11: Concentrations for input factors use in DoE IV

	BSA	Insulin	Transferrin	NaSe	Trace Elements B	Trace Elements C	Lipid Mix	Linoleic/ Oleic Acid mix	Heparin
Low	10	2	1.1	1	0.1	0.1	0.1	0.5	10
High	100	20	11	10	1	1	1	5	100

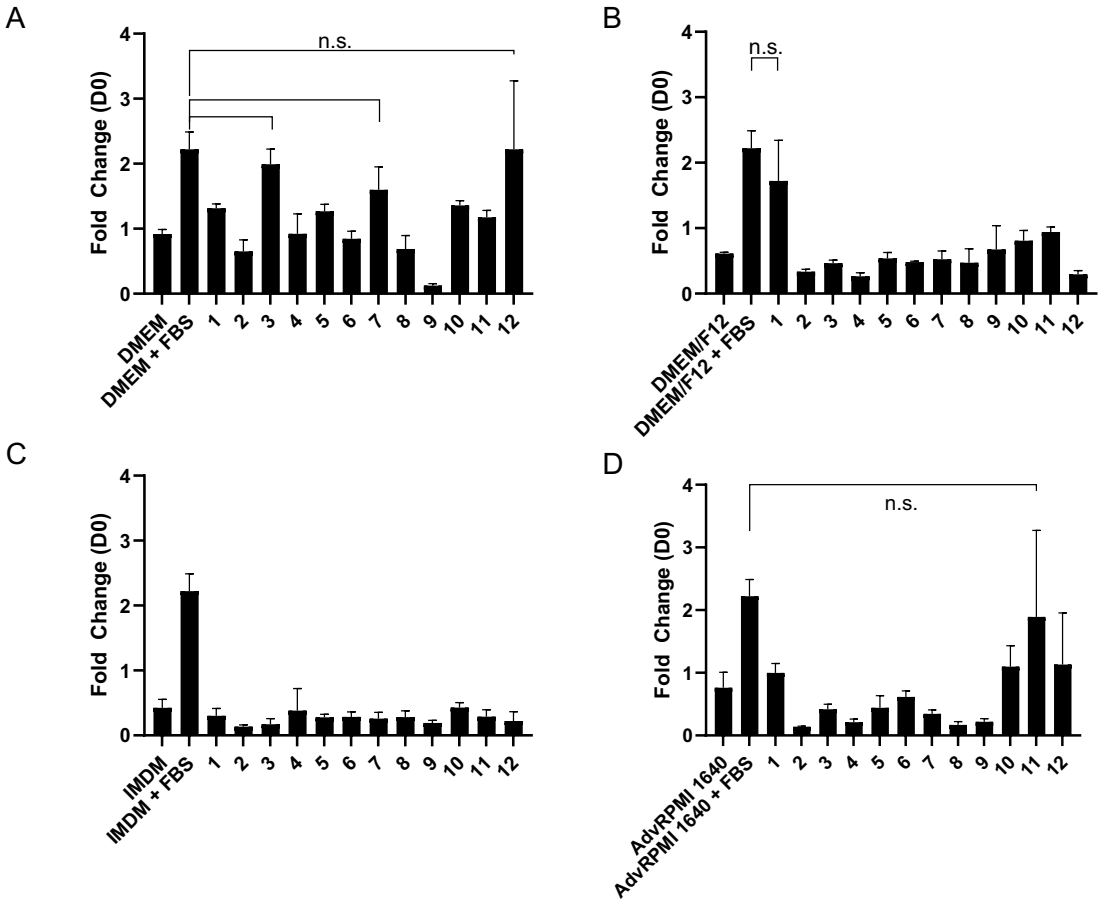

Figure 2.12: Y201 proliferative response as measured by Quant-iT PicoGreen after 3 days in culture in different CDM compositions using varying basal media. A: DMEM; B: DMEM/F12; C: IMDM; D: Advanced RPMI 1640 (AdvRPMI 1640). N = 3, α = 0.05; ±SEM; ANOVA.

Using DMEM basal medium, stepwise backward elimination of terms analysis identified linoleic/oleic acid mix (p = 0.000), NaSe (p = 0.000), trace elements C (p = 0.025), trace elements B (p = 0.048), and BSA (p = 0.090) as having significant effect on Y201 cell number change. The fit was good for a screening DoE, with an R^2 value of 77.24% (Table 2.12; Figure 2.13).

BSA, NaSe, trace elements B and C, and linoleic/oleic acid mix had a negative effect with increasing concentrations, while the reverse was the case for the rest of the additives (Appendix 15).

Table 2.12: Stepwise backward elimination of terms analysis on screening DoE for DMEM basal medium with added components. R^2 = 77.24%

	------Step 1-----	
	Coef	**P**
Constant	1.0316	
BSA (mg/L)	-0.1116	0.090
Insulin (mg/L)	0.0536	0.405
Transferrin (mgL)	0.0379	0.555
NaSe (mg/L)	-0.2684	0.000
Trace Elements B %	-0.1318	0.048
Trace Elements C %	-0.1512	0.025
Lipid Mix %	0.0392	0.541
Linoleic/Oleic Acid %	-0.3504	0.000
Heparin (ng/ml)	-0.0099	0.877
Blocks	-0.351	0.001

R^2
77.24%

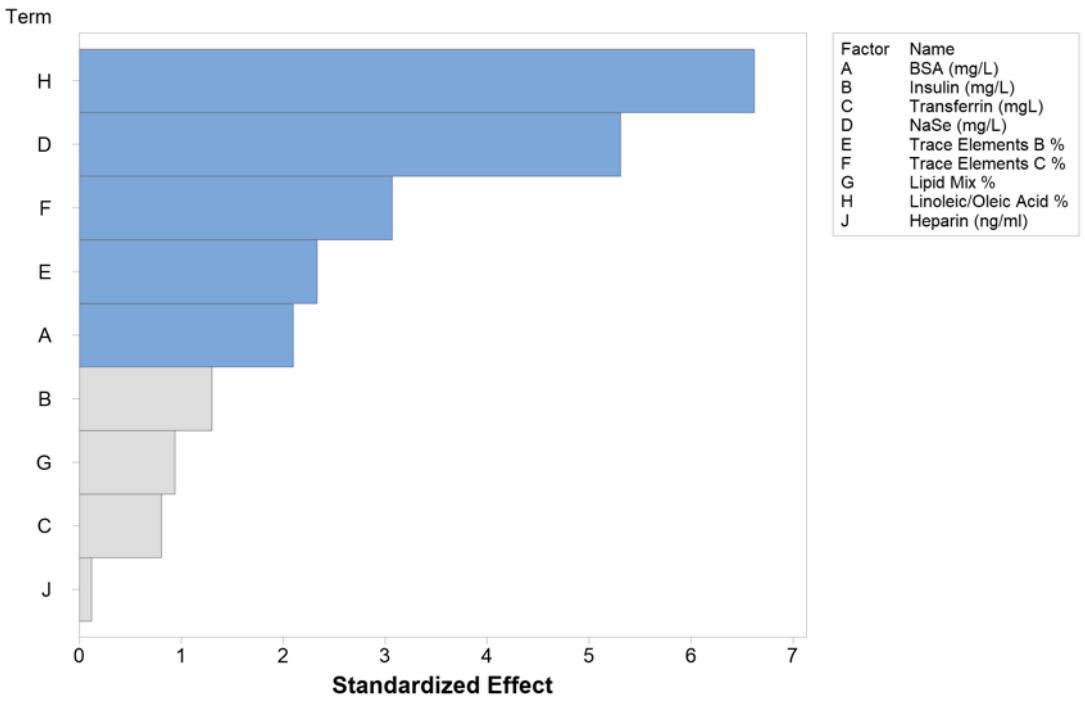

Figure 2.13: Main effects pareto chart depicting magnitude of standardized effect of CDM components (A: BSA (mg/L); B: insulin (mg/L); C: transferrin (mg/L); D: NaSe (mg/L); E: trace elements B (%); F: trace elements C (%); G: lipid mix (%); H: linoleic/oleic acid (%); J: heparin (ng/ml)) on Y201 cell number change as assessed by Quant-iT PicoGreen after 3 days in culture (fold change from day 0) with DMEM as basal medium. Blue bars indicate significant effect of the input parameters alone or in combination, while grey bars indicate a non-significant effect and were therefore excluded from the model. α = 0.15.

Using DMEM/F12 as a basal medium, stepwise backward elimination of terms analysis yielded a model with worse fit than the previous model, with an R^2 value of 61.00% (Table 2.13). In contrast to DMEM, only two main effectors were identified as significant: NaSe ($p = 0.000$) and lipid mix ($p = 0.001$) (Table 2.13; Figure 2.14). Increasing concentrations of NaSe had a negative main effect on cell number change, whereas an increase in lipid mix had a positive effect (Appendix 16).

Table 2.13: Stepwise backward elimination of terms analysis on screening DoE for DMEM/F12 basal medium with added components. R^2 = 61.00%

	------Step 1-----		------Step 2-----		------Step 3-----		------Step 4-----		------Step 5-----		------Step 6-----		------Step 7-----		------Step 8-----	
	Coef	**P**	**Coef**	**P**	**Coef**	**P**	**Coef**	**P**	**Coef**	**P**	**Coef**	**P**	**Coef**	**P**	**Coef**	**P**
Constant	0.5609		0.5609		0.5609		0.5609		0.5609		0.5609		0.5609		0.5609	
Blocks	-0.153	0.076	-0.153	0.071	-0.153	0.070	-0.153	0.069	-0.153	0.069	-0.153	0.071	-0.153	0.075	-0.153	0.081
BSA (mg/L)	0.0657	0.159	0.0657	0.153	0.0657	0.152	0.0657	0.152	0.0657	0.153	0.0657	0.154	0.0657	0.16		
Insulin (mg/L)	-0.0433	0.348	-0.0433	0.341												
Transferrin (mgL)	-0.0614	0.187	-0.0614	0.181	-0.0614	0.180	-0.0614	0.18	-0.0614	0.180	-0.0614	0.182				
NaSe (mg/L)	-0.2563	0.000	-0.2563	0.000	-0.2563	0.000	-0.2563	0.000	-0.2563	0.000	-0.2563	0.000	-0.2563	0.000	-0.2563	0.000
Trace Elements B %	-0.046	0.319	-0.046	0.312	-0.046	0.311	-0.046	0.312								
Trace Elements C %	0.0459	0.320	0.0459	0.313	0.0459	0.312										
Lipid Mix %	0.1632	0.001	0.1632	0.001	0.1632	0.001	0.1632	0.001	0.1632	0.001	0.1632	0.001	0.1632	0.001	0.1632	0.001
Linoleic/Oleic Acid %	0.0515	0.266	0.0515	0.259	0.0515	0.258	0.0515	0.258	0.0515	0.259						
Heparin (ng/ml)	0.0257	0.575														

R^2	**Eliminations:**	1st	2nd	3rd	4th	5th	6th	7th
61.00%								

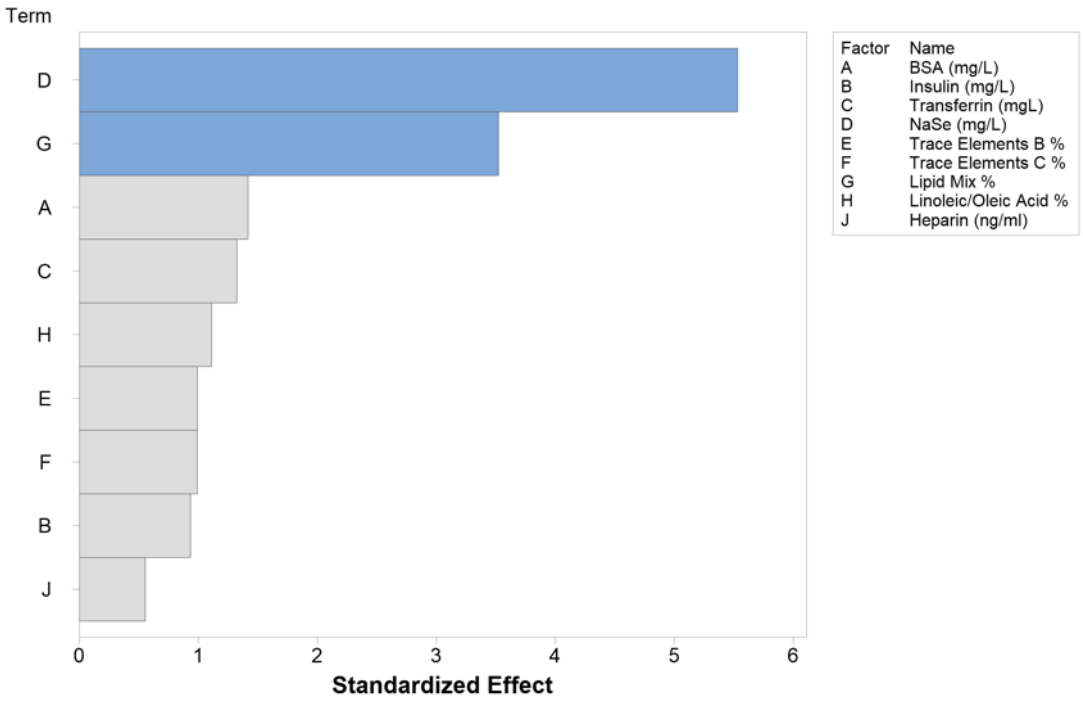

Figure 2.14: Main effects pareto chart depicting magnitude of standardized effect of CDM components (A: BSA (mg/L); B: insulin (mg/L); C: transferrin (mg/L); D: NaSe (mg/L); E: trace elements B (%); F: trace elements C (%); G: lipid mix (%); H: linoleic/oleic acid (%); J: heparin (ng/ml)) on Y201 proliferation as assessed by Quant-iT PicoGreen after 3 days in culture (fold change from day 0) with DMEM/F12 as basal medium. Blue bars indicate significant effect of the input parameters alone or in combination, while grey bars indicate a non-significant effect and were therefore excluded from the model. α = 0.15.

For IMDM as a basal medium, the DoE yielded a relatively poor fitting model, with an R^2 value of 44.78%. The significant effectors were insulin (p = 0.079), BSA (p = 0.095), lipid mix (p = 0.116), and trace elements C (p = 0.121) (Table 2.14; Figure 2.15). BSA, insulin, and lipid mix had a positive effect on cell number, whereas trace elements C decreased cell number with increasing concentration (Appendix 17).

In the case of IMDM, none of the CDM formulae outperformed basal medium, so IMDM was clearly not suited for use with Y201s in a serum free culture setting. It is also clear that the serum-free culture components added to DMEM did not seem to translate to IMDM, as the p-values of the significant terms are relatively high, and therefore have very little effect on Y201.

Table 2.14: Stepwise backward elimination of terms analysis on screening DoE for IMDM basal medium with added components. R^2 = 44.78%

	------Step 1-----		------Step 2-----		------Step 3-----		------Step 4-----		------Step 5-----		------Step 6-----	
	Coef	**P**	**Coef**	**P**	**Coef**	**P**	**Coef**	**P**	**Coef**	**P**	**Coef**	**P**
Constant	0.2368		0.2368		0.2368		0.2368		0.2368		0.2368	
Blocks	-0.0941	0.011	-0.0941	0.009	-0.0941	0.008	-0.0941	0.007	-0.0941	0.006	-0.0941	0.007
BSA (mg/L)	0.0336	0.111	0.0336	0.104	0.0336	0.099	0.0336	0.097	0.0336	0.094	0.0336	0.095
Insulin (mg/L)	-0.0355	0.093	-0.0355	0.086	-0.0355	0.082	-0.0355	0.08	-0.0355	0.078	-0.0355	0.079
Transferrin (mgL)	0.0163	0.43	0.0163	0.42	0.0163	0.413	0.0163	0.41				
NaSe (mg/L)	-0.0105	0.61	-0.0105	0.603								
Trace Elements B %	0.0021	0.918										
Trace Elements C %	0.0312	0.138	0.0312	0.13	0.0312	0.124	0.0312	0.122	0.0312	0.119	0.0312	0.121
Lipid Mix %	0.0316	0.133	0.0316	0.125	0.0316	0.119	0.0316	0.117	0.0316	0.115	0.0316	0.116
Linoleic/Oleic Acid %	-0.0216	0.298	-0.0216	0.288	-0.0216	0.281	-0.0216	0.278	-0.0216	0.275		
Heparin (ng/ml)	-0.0163	0.43	-0.0163	0.42	-0.0163	0.414						

R^2	Eliminations:	1st	2nd	3rd	4th	5th
44.78%						

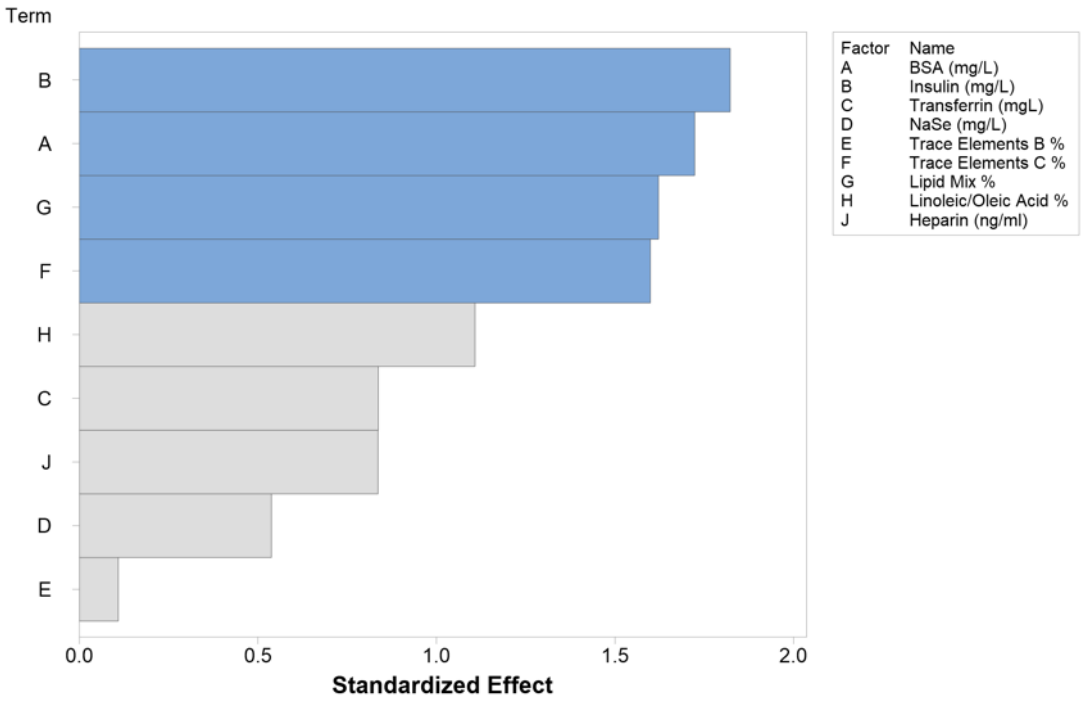

Figure 2.15: Main effects pareto chart depicting magnitude of standardized effect of CDM components (A: BSA (mg/L); B: insulin (mg/L); C: transferrin (mg/L); D: NaSe (mg/L); E: trace elements B (%); F: trace elements C (%); G: lipid mix (%); H: linoleic/oleic acid (%); J: heparin (ng/ml)) on Y201 cell number change as assessed by Quant-iT PicoGreen after 3 days in culture (fold change from day 0) with IMDM as basal medium. Blue bars indicate significant effect of the input parameters alone or in combination, while grey bars indicate a non-significant effect and were therefore excluded from the model. α = 0.15.

Advanced RPMI 1640 was tested as a basal medium for CDM development, and it was found that similar to DMEM/F12 and IMDM, it was less suitable than DMEM for Y201 MSC culture. Stepwise backward elimination of terms analysis yielded a model with an R^2 value of 77.23%, with significant effects from NaSe ($p = 0.000$), lipid mix ($p = 0.001$), transferrin ($p = 0.005$), and trace elements B ($p = 0.051$) (Table 2.15; Figure 2.16). NaSe, transferrin, and lipid mix had negative effects on cell number change, whereas trace elements B had a positive effect with increasing concentrations (Appendix 18).

Table 2.15: Stepwise backward elimination of terms analysis on screening DoE for Advanced RPMI 1640 basal medium with added components. R^2 = 77.23%

	------Step 1------		------Step 2------		------Step 3------		------Step 4------		------Step 5------		------Step 6-----		------Step 7-----	
	Coef	**P**	**Coef**	**P**	**Coef**	**P**	**Coef**	**P**	**Coef**	**P**	**Coef**	**P**	**Coef**	**P**
Constant	0.5942		0.5942		0.5942		0.5942		0.5942		0.5942		0.5942	
Blocks	-0.08658	0.258	-0.08658	0.248	-0.08658	0.238	-0.08658	0.241	-0.08658	0.244				
BSA (mg/L)	0.0193	0.599	0.0193	0.593										
Insulin (mg/L)	-0.0473	0.204	-0.0473	0.197	-0.0473	0.191	-0.0473	0.193	-0.0473	0.195	-0.0473	0.201		
Transferrin (mgL)	-0.112	0.005	-0.112	0.004	-0.112	0.004	-0.112	0.004	-0.112	0.004	-0.112	0.004	-0.112	0.005
NaSe (mg/L)	-0.3227	0.000	-0.3227	0.000	-0.3227	0.000	-0.3227	0.000	-0.3227	0.000	-0.3227	0.000	-0.3227	0.000
Trace Elements B %	-0.0744	0.051	-0.0744	0.048	-0.0744	0.044	-0.0744	0.045	-0.0744	0.046	-0.0744	0.049	-0.0744	0.051
Trace Elements C %	0.0407	0.273	0.0407	0.265	0.0407	0.258	0.0407	0.261						
Lipid Mix %	0.1373	0.001	0.1373	0.001	0.1373	0.001	0.1373	0.001	0.1373	0.001	0.1373	0.001	0.1373	0.001
Linoleic/Oleic Acid %	-0.0184	0.616												
Heparin (ng/ml)	-0.0405	0.275	-0.0405	0.268	-0.0405	0.261								

R-sq	Eliminations:	1st	2nd	3rd	4th	5th	6th
77.23%							

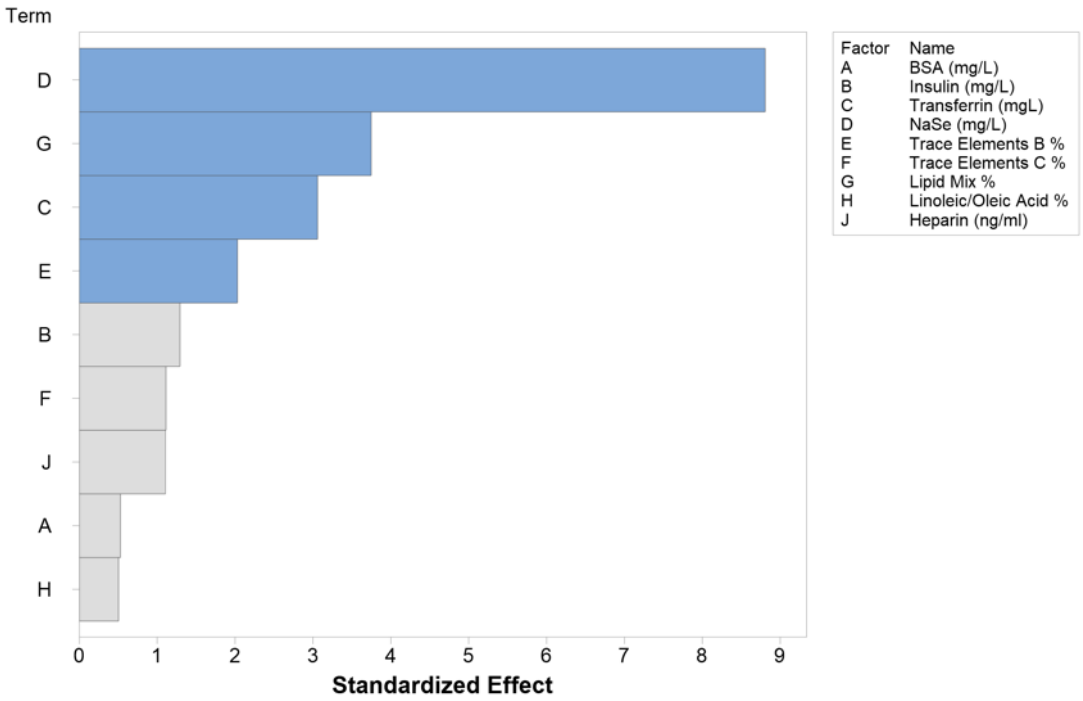

Figure 2.16: Main effects pareto chart depicting magnitude of standardized effect of CDM components (A: BSA (mg/L); B: insulin (mg/L); C: transferrin (mg/L); D: NaSe (mg/L); E: trace elements B (%); F: trace elements C (%); G: lipid mix (%); H: linoleic/oleic acid (%); J: heparin (ng/ml)) on Y201 cell number change as assessed by Quant-iT PicoGreen after 3 days in culture (fold change from day 0) with Advanced RPMI 1640 as basal medium. Blue bars indicate significant effect of the input parameters alone or in combination, while grey bars indicate a non-significant effect and were therefore excluded from the model. α = 0.15.

Table 2.16: Regression equations calculated for final medium formulation for use in Quantum bioreactor.

Basal Medium	Regression Equation
DMEM	2.123 - 0.00248[BSA (mg/L)] + 0.00596[Insulin (mg/L)] + 0.0076[Transferrin (mgL)] - 0.0597[NaSe (mg/L)] - 0.293[Trace Elements B (%)] - 0.336[Trace Elements C (%)] + 0.087[Lipid Mix (%)] - 0.1557[Linoleic/Oleic Acid (%)] - 0.00022([Heparin (ng/ml)])
DMEM/F12	0.6748 - 0.0570[NaSe (mg/L)] + 0.363[Lipid Mix (%)]
IMDM	0.1625 + 0.000746[BSA (mg/L)] - 0.00395[Insulin (mg/L)] + 0.0692[Trace Elements C (%)] + 0.0702([Lipid Mix (%)])
AdvRPMI	1.0486 - 0.02263[Transferrin (mgL)] - 0.07171[NaSe (mg/L)] - 0.1654[Trace Elements B (%)] + 0.3052[Lipid Mix (%)]

Due to DMEM's superior performance, it was decided to use DMEM as a basal medium for CDM development going forward. Using the regression equation generated for DMEM (Table 2.16), an optimal medium was formulated (Table 2.17) and compared to two CDM formulations (Figure 2.17) which were non-significantly different from FBS-supplemented medium in the initial DoE study (Figure 2.12).

Table 2.17: Optimal CDM formulation as calculated from the regression equation generated from the screening DoE using DMEM as a basal medium.

Variable	**Setting**
BSA (mg/L)	10
Insulin (mg/L)	20
Transferrin (mgL)	11
NaSe (mg/L)	1
Trace Elements B %	0.1
Trace Elements C %	0.1
Lipid Mix %	1
Linoleic/Oleic Acid %	0.5
Heparin (ng/ml)	10
Response	**Fold Change**
Y201 cell number change	2.186

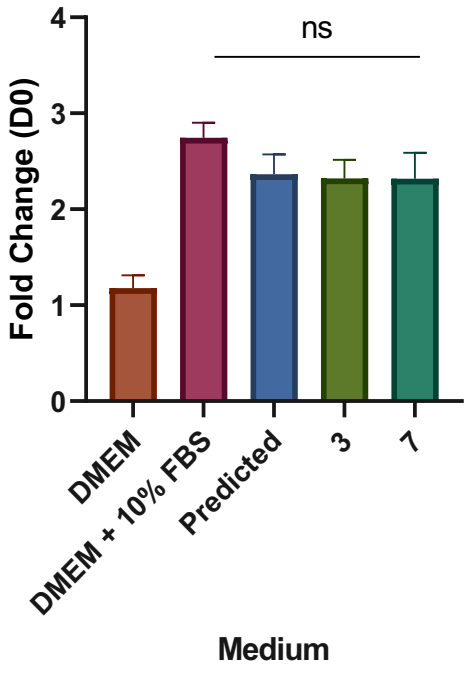

Figure 2.17: Y201 cell number change as assessed by fold change in Quant-iT PicoGreen fluorescence after 3 days in culture with CDM 3, CDM 7, and predicted CDM. Cells were seeded in corresponding media at a density of 1.5 x 10^4 cells/cm^2 and left to adhere for 24 hours. Cells were then washed and media changed. Fluorescence was assessed in a fluorescence spectrophotometer. ns: non-significant; n=3; α = 0.05; ±SEM; ANOVA.

Using DoE, a chemically defined medium was developed, supporting Y201 viability and growth. In order to test the CDM for use in a clinically relevant setting, it was tested for

the scaled up bulk production of EVs in a continuous perfusion bioreactor system (Quantum, TerumoBCT).

2.3.7 Quantum bioreactor studies

The CDM was tested for scaled up applications using the Quantum bioreactor to determine if it could support the bulk production of cell-based products, in this case EVs released by the Y201 MSCs. The Quantum bioreactor is a clinical grade, continuous perfusion bioreactor with 1.6 m^2 growth surface area, which allows for rapid, large scale expansion of cells. It was hypothesised that the continuous perfusion would be of benefit to cellular expansion and EV production due to the nature of the medium being relatively minimal and the principle of the Quantum bioreactor being the continuous replenishment of fresh medium. Two successful cell expansions and EV collections were completed in CDM.

2.3.7.1 *Y201 proliferation in Quantum bioreactor using CDM*

2 x 10^6 cells were seeded into the bioreactor and left to adhere for 24 hours. Cell growth was monitored using lactate readings. There was a decrease in lactate levels over time in both runs, as is expected when cells expand in the bioreactor as glucose from the medium is turned over by expanding cells.

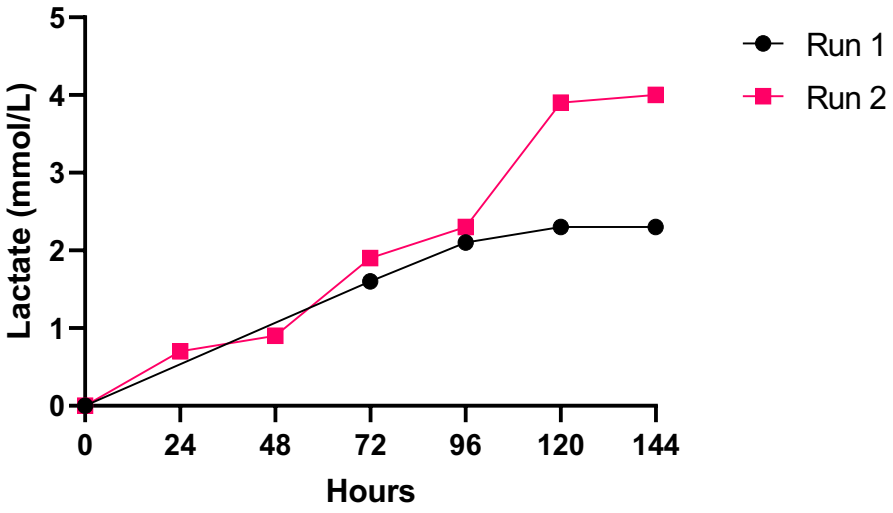

Figure 2.18: Lactate readings of Quantum bioreactor test runs. 2 x 10^6 cells were seeded into the bioreactor and left to adhere for 24 hours. CDM was perfused continually and flow increased as per manufacturer's advice with every stepwise increase in lactate concentration. Lactate concentration was measured by dipstick.

2.3.7.2 *Extracellular vesicle collection in Quantum bioreactor using CDM*

N.B. Experiments and data collection in this section (2.3.7.2) were carried by Savvas Ioannou.

EVs were collected and isolated over 24 hours at the point at which lactate levels in the bioreactor reached a plateau. Extracellular vesicles were then characterised in terms of their size and marker profile and compared to extracellular vesicles collected from tissue culture flasks.

Extracellular vesicle characterisation confirmed that the vesicles collected were indeed extracellular vesicles by transmission electron micrograph (Figure 2.19) and detection of HSP70 and flotillin by western blot analysis from extracellular vesicle lysates (Figure 2.20). Using nanoparticle tracking analysis, an approximately 3-fold increase in vesicles isolated at 100,000 x g (100k fraction) per million cells (1.32×10^{10} versus 4.52×10^{9} particles/million cells), while the 10,000 x g fraction (10k fraction) was broadly unchanged in Quantum-cultured Y201 MSCs as compared to standard tissue culture conditions. A broader distribution of sizes was observed in the 10k fraction, with major size peaks at 27nm, 65nm, 104nm, and 139nm versus 115nm and 151nm in EVs collected from standard tissue culture conditions (Figure 2.21 and Figure 2.22; Table 2.18).

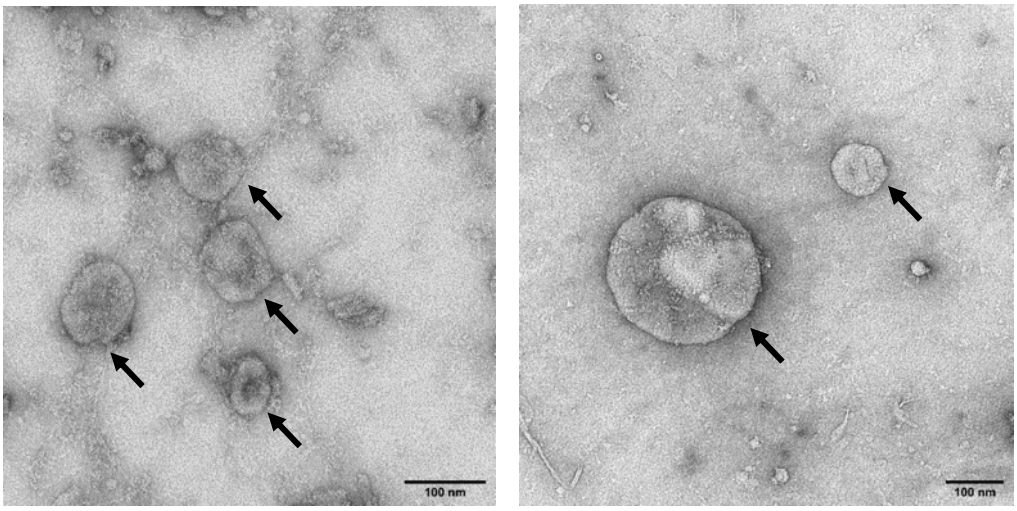

Figure 2.19: Transmission electron micrograph (TEM) of extracellular vesicles (arrows) from 10k fraction (left) and 100k fraction (right). (Savvas Ioannou)

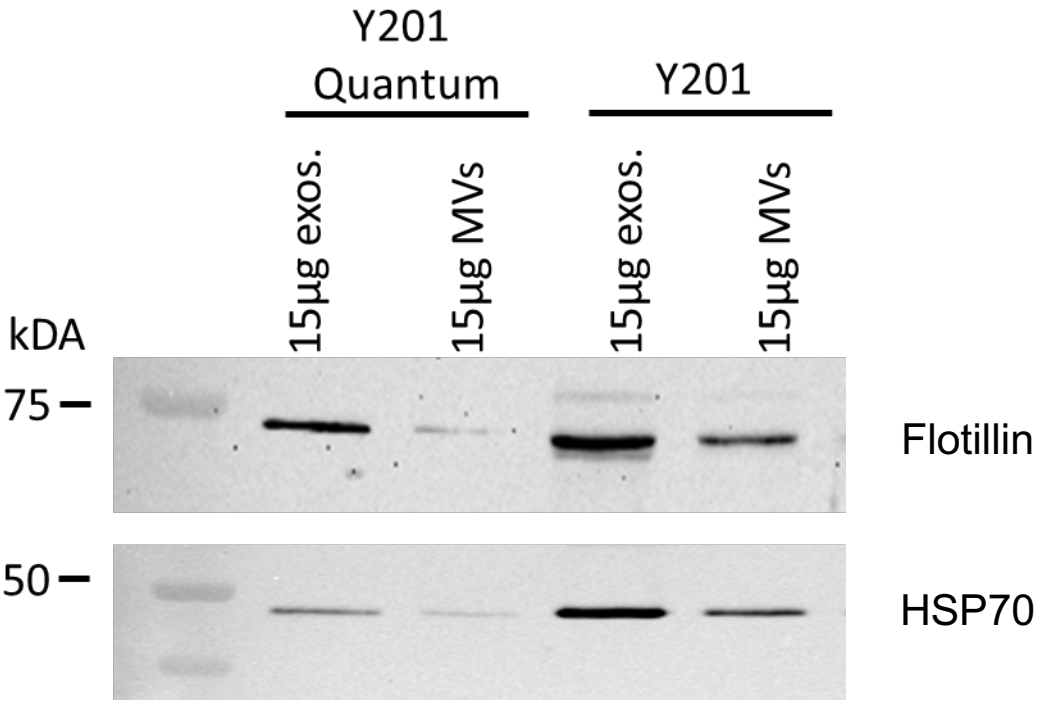

Figure 2.20: Western blot analysis of extracellular vesicle lysates from 100k fractions (exos.) and 10k fractions (MVs) (Savvas Ioannou).

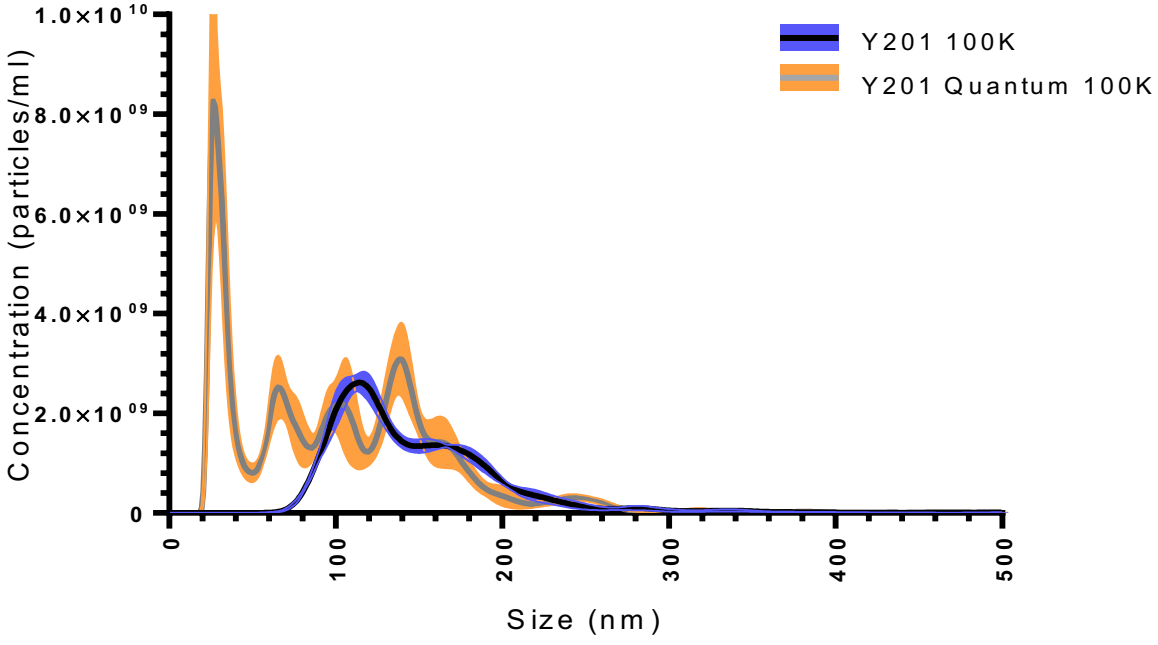

Figure 2.21: Nanoparticle tracking analysis of 100k fraction of extracellular vesicles collected from Quantum bioreactor run 1 (orange) and tissue culture flasks (blue) (Savvas Ioannou).

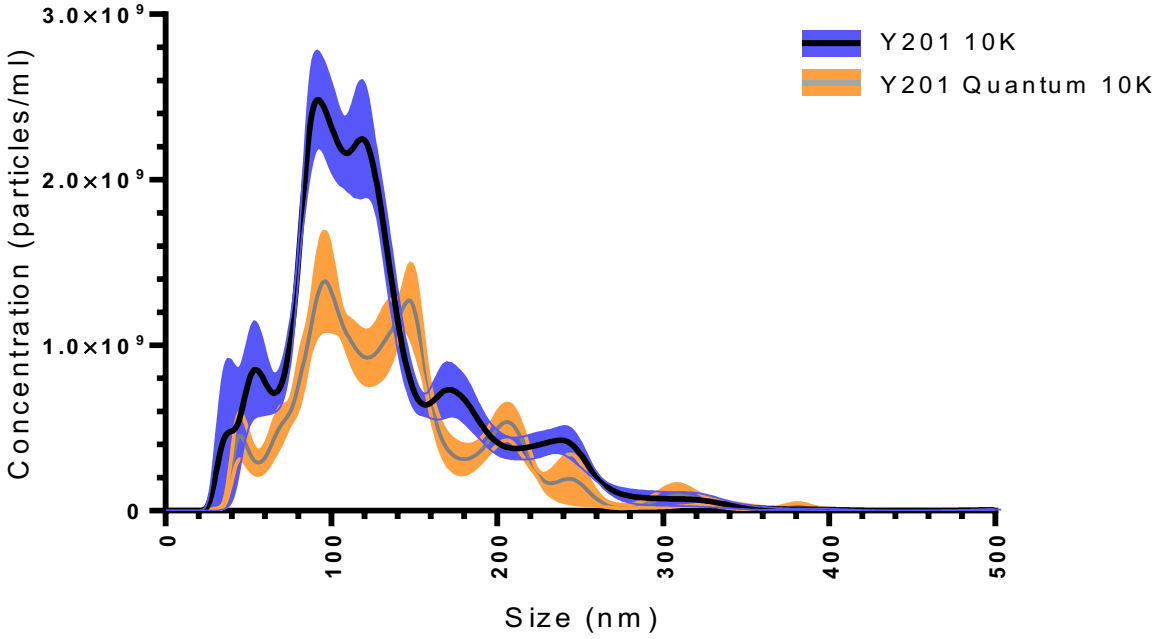

Figure 2.22: Nanoparticle tracking analysis of 10k fraction of extracellular vesicles collected from Quantum bioreactor run 1 (orange) and tissue culture flasks (blue) (Savvas Ioannou).

Table 2.18: Summary of extracellular vesicle characterisations from 100k and 10k fractions (Savvas Ioannou).

Growth condition	Concentration (particles/ml)	Yield (per million cells)	Mean size (nm)	Median size (nm)
100k fraction				
Y201 Standard	2.10×10^{11}	4.52×10^{9}	149	113
Y201 Quantum	3.72×10^{11}	1.32×10^{10}	106	49
10k fraction				
Y201 Standard	2.32×10^{11}	4.99×10^{9}	129	106
Y201 Quantum	1.43×10^{11}	5.11×10^{9}	139	110

2.4 Discussion

This study presented that there is an application for DoE approaches in biological research, enabling the development of a chemically defined medium for use with MSCs in a relatively short period of time, supporting viability and expansion of MSCs to a level equivalent to FBS-containing medium, and statistically significantly higher than unsupplemented basal medium. This was particularly aided by the use of the regression equation in the final DoE (DoE IV, section 0), where an optimal medium was predicted from the model created for Y201 growth, using DMEM as a basal medium. The predicted medium outperformed basal medium significantly and performed to a level equivalent to FBS-containing medium (Figure 2.17). This study was a valuable proof of concept for the use of DoE in biological systems and has implications on experimental design and analysis.

The use of CDM in a clinically relevant, continuous perfusion bioreactor was also shown to be successful. Using CDM, Y201 MSCs expanded over time and produced EVs in a manner comparable to standard tissue culture conditions (cells expanded on tissue culture plastic). The use of a bioreactor with continuous perfusion was hypothesised to be of benefit to the growth of the MSCs, as the medium was very minimal relative to FBS-supplemented medium, meaning that constant replenishment of nutrients from the CDM may have been of benefit. Due to the cost and time implications of using the bioreactor, it was not possible to prove or disprove this particular notion, as no FBS-containing runs were done with the cell line used for these studies. It can be said, though, that growth was indeed supported by the CDM, and that the continuous perfusion did not have a deleterious effect.

EV production was enhanced using the continuous perfusion bioreactor, with a 3-fold increase in EV particles per million cells observed in Quantum-grown cells compared to standard culture conditions (Table 2.18).

3 Chapter 3: Optimisation of plasma sprayed hydroxyapatite coatings for MSC response

3.1 Plasma Spraying Process

A multitude of orthopaedic implant devices are plasma sprayed with hydroxyapatite in order to improve patient outcomes. In principle, plasma spraying is a type of thermal spraying process which is used to deposit one or multiple layers of molten or partially molten material onto a surface, creating a coating several microns thick. Hydroxyapatite-sprayed devices have been reported to improve osteointegration[231] and osteoinduction[71], which in turn shortens patient recovery times and allows for patients to be mobile sooner after arthroplasty than they would with a non-coated, cemented orthopaedic implant.

To prepare a surface for plasma spraying, the surface is grit-blasted, which involves spraying it with grit of a given average size to roughen it. This dramatically increases the surface area of the material, which helps with the adhesion of the coating to the surface. To create the plasma flame, also known as a plasma plume or plasma jet, a high frequency arc is ignited between an anode and a tungsten cathode. An inert gas or a mixture of gases, in this case a mixture of factor A and factor B, passes through the electrodes and is ionised. This results in a jet several centimetres in length which can reach temperatures of up to 16,000 K. Hydroxyapatite powder is then introduced into the jet, which will melt and form agglomerates as it is propelled toward a surface. The partially melted globules of hydroxyapatite impact onto the relatively cool titanium surface, which quickly quenches the material, hardening almost instantly upon impact[232].

3.1.1 Plasma spray settings and their effect on surface properties

The resulting coating will have different properties depending on the plasma sprayer settings, which will determine how fully the hydroxyapatite particles melt, how they agglomerate into larger globules in flight, how thick the deposited layer is, and how much force they contact the substrate with. The energy that is exerted upon the material and the rate at which it quenches on impact have the most substantial effect on the calcium phosphate phases created on the surface. This determines the crystallinity of the surface and thereby the rate and composition of any resorbed material and ions released from the material[70].

Plasma spraying is a highly complex process and can be fine-tuned by changing a number of things about how the powder is introduced, how the plasma flame is created, and how the spray is applied to the surface. The plasma sprayer used in these studies can be adjusted in ways that can influence measured material properties such as crystallinity and roughness (Figure 3.1).

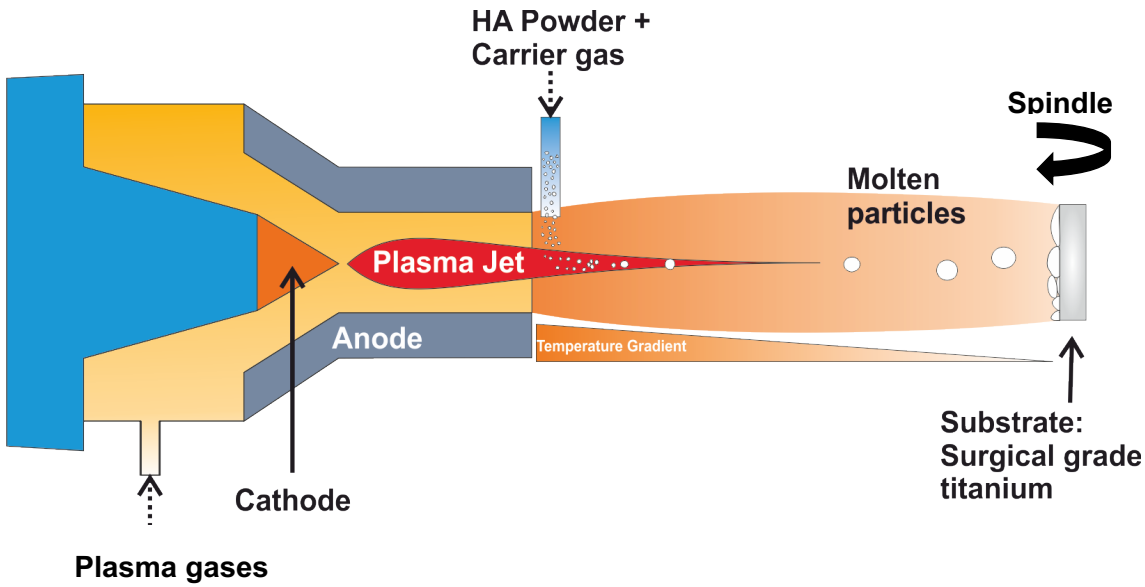

Figure 3.1: Plasma spraying process. An anode and a cathode are used to create a plasma flame from an A and B mixture. HA powder is introduced at a specific C using a D gas. The substrate is mounted on a spindle, allowing for rotation at specific speeds, aiding in even coating of the substrate.

3.1.1.1 *Gases*

In order for the plasma jet to be created, an inert gas is passed through an anode and a cathode such that it can be ionised to the plasma state, with the resulting jet accomplishing a temperature high enough to melt ceramic. Plasma sprayers typically use a mixture of primary and secondary gases which help to create the plasma flame. Factor A is most commonly used as a primary gas, as it strikes a balance between its relatively low ionisation energy and low reactivity with the sprayed substrates. A secondary gas, such as factor B, is often included in order to optimise the temperature achieved by the plasma jet[53].

In addition to the gases used to create the plasma, a carrier gas is used to propel ceramic powder into the hottest part of the plasma jet. This is usually an inert gas and needs to be carefully optimised in order to balance with powder feed rate so that there is as little ceramic waste as possible. If powder feed rate is increased, the carrier gas rate needs to also be increased so that the pressure of the gas flow can efficiently propel the ceramic particles into the appropriate part of the plasma jet.

3.1.1.2 *Ceramic feedstocks*

Both the properties of the powders used in the thermal spray process as well as the handling of these powders can affect the resulting coating. The hydroxyapatite powder used, also known as the feedstock, can have a significant impact on the resulting coating. Fundamentally, feedstocks can differ in architecture, particle size distribution, and density. These differences in feedstock properties affect the flowability, melting, and propulsion of the powder, which in turn affect coating properties such as crystallinity, phase composition, thickness and adhesion strength[65,233,234].

The flowability of a feedstock is mainly dictated by the particle architecture. A particle can range from being spherical to being angular, which is a direct result of how it was manufactured. Agglomerated and sintered powders tend to be spherical, whereas crushed powders have a more angular, fragmented architecture. Other factors, such as apparent and true densities and particle size distribution affect flowability, which in turn affects the reproducibility and performance of the plasma sprayer[60–62].

How a feedstock is handled will depend on the properties of the feedstock; if the powder does not flow well, for example, the powder feed rate, which is the amount of powder fed into the plasma spray per minute, may be increased so as to introduce the appropriate amount of powder into the plasma jet. As mentioned above, the carrier gas plays a crucial role in ensuring that the powder is propelled to the correct point in the plasma jet to ensure proper melting and deposition onto the substrate to be coated, and needs to be adapted to the powder feed rate[232,235,236].

3.1.1.3 *Part rotation*

The part rotation refers to the speed at which the part to be sprayed revolves, measured in revolutions per minute (RPM). The main outcome of changing the part rotation is changing the angle at which partially molten droplets will impact the material. The angle of the droplet impact has a significant effect on the quenching behaviour of the material, and therefore the presence of other calcium phosphate species, such as tetracalcium phosphate in the material, affecting the crystallinity as well as its resorption properties. It is widely reported that the quenched material droplet exhibits a so-called crystallinity gradient, with varying abundances of differently crystalline calcium phosphates throughout the thickness and radius of the droplet[237].

3.1.2 Properties of Hydroxyapatite: Crystallinity and roughness

The crystallinity of a solid can be described as the degree of structural order – the more crystalline a solid is the more ordered its molecular structure. In its purest form, hydroxyapatite is a crystalline solid. Solids with no long term order are described as being amorphous[238]. The crystallinity of a calcium phosphates such as hydroxyapatite can substantially affect its material properties, which in turn may affect the behaviour of cells that adhere to it. Properties that may be affected include its hardness, its rate of resorption, and how proteins adhere to it. These are crucial properties of an implanted prosthesis, as they can have a profound impact on implant performance.

The roughness of the surface is defined by several metrics, taking into account an area of the surface and how peaks and valleys across that surface are distributed, what their sizes are, and how frequent they are. A mean line is created around which heights are measured for surface measurements by a high-pass filtration of a primary profile. Surface roughness is calculated from readings then taken about the mean line.

It is challenging to condense the roughness of a surface down to one metric, as there are very different types of roughness, and each measured metric is informative in a different way. For example, a surface with few, large peaks may be described to have the same average roughness as an area with many smaller peaks, but that average roughness coupled with information about the distribution and size of the features on the surface gives a better quantification of the overall surface topography.

Roughness parameters measured were Sa (arithmetic mean height), Sp (maximum peak height), Sv (maximum valley depth), Sz (maximum height), Sq (root mean square height), Ssk (skewness) and Sku (kurtosis). Sa describes the average overall height of features, not measured from the mean line but from pit and peak maxima. Sp and Sv describe the surface's maximal peak height and valley depth respectively, as measured from the mean line. Sz is described as the absolute value of the height from the maximal valley depth and peak heights, usually not separately measured but calculated as Sp + Sv. Sq described the standard deviation of heights and is calculated from absolute values of raw height data. Ssk describes the general distribution of topographical features about the mean line and is between -1 and 1. An Ssk of 0 suggests a normal distribution of peaks and valleys, whereas a positive Ssk suggests a tendency for peaks, and a negative value a tendency for valleys. The Sku, or kurtosis, relates to the tip geometry of peaks and valleys, and is an indication for contact surface

area. An Sku below 3 suggests a flatter peak or valley, while an Sku over 3 suggests a sharper point. A summary of Sp, Sv, Sz, Sku, and Ssk is given in Figure 3.2 below.

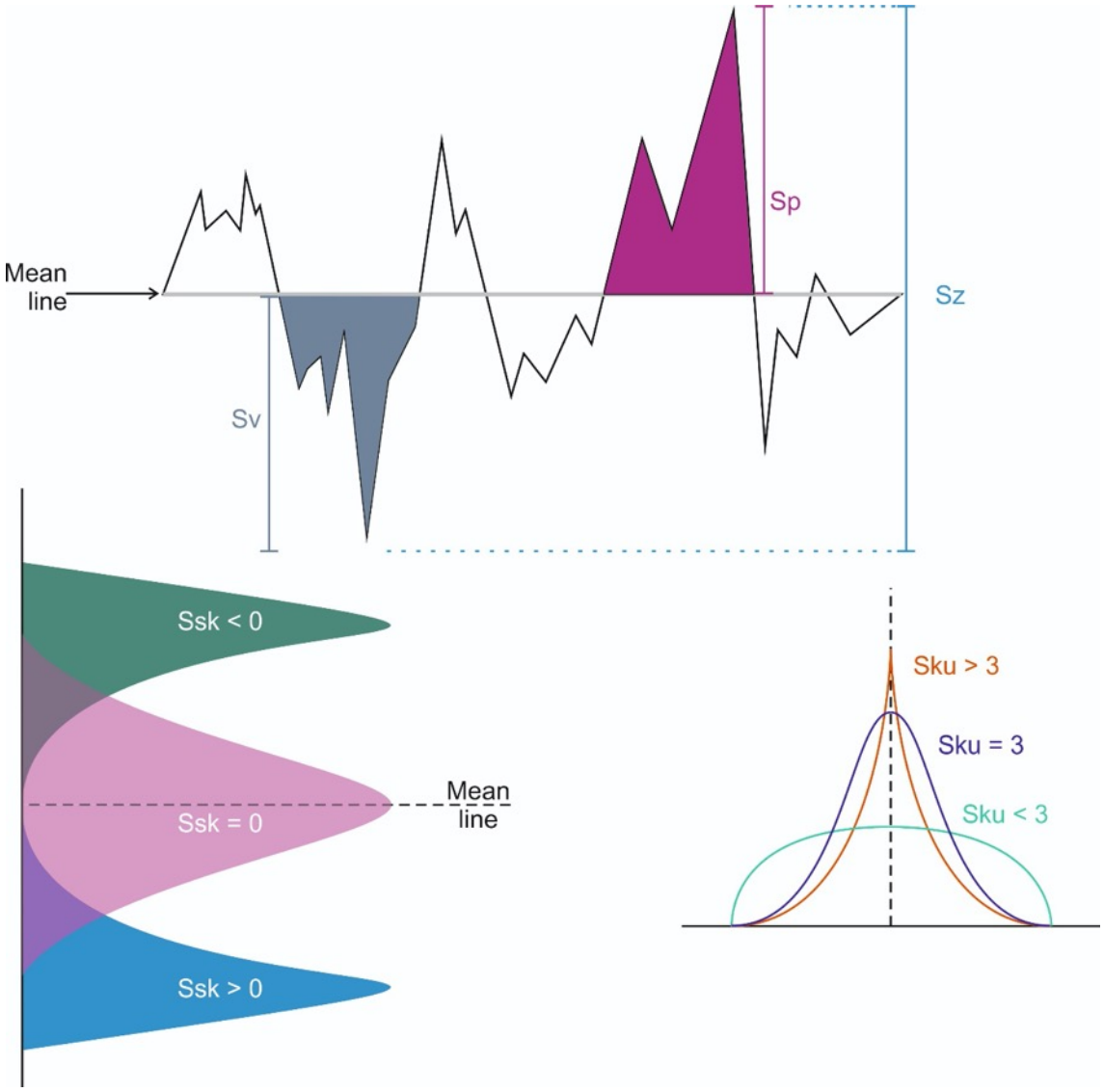

Figure 3.2: Summary of Sp, Sv, Sz, Ssk, and Sku roughness parameters. Sp, Sv, and Sz measure maximal peak height, maximal valley depth, and the absolute value of the largest valley depth to peak height distance respectively. Ssk measures the distribution of peaks and valleys, i.e. if Ssk = 0, peaks and valleys are normally distributed. An Ssk>0 suggests mostly valleys in an area, whereas an Ssk<0 suggests an area of mostly peaks. Sku is an index for how sharp features are. An Sku>3 is a sharp point, while an Sku<3 is a flat surface.

3.1.2.1 *Effect of crystallinity and roughness on cell behaviour*

Surface characteristics have been shown in many studies to have a significant impact on MSC behaviour. Calcium phosphate crystallinity has been shown to affect bone marrow MSC adhesion, proliferation, and differentiation. In one study, more crystalline calcium phosphate allowed for slightly better MSC adhesion, proliferation, and differentiation[69]. Another study showed that implanted calcium phosphate at a fibular fracture site induced expression of BMP-2 and differentiation of MSCs recruited to the implant site[71].

Surface roughness has been more widely studied as a factor in MSC behaviour. TGFbeta, Wnt, and Notch signalling have been implicated in enhanced osteoprogenitor differentiation on modified titanium surfaces, where 7 and 14 days post-seeding on these surfaces, an upregulation in bone markers bone sialoprotein and osteocalcin was observed, as well as increased alkaline phosphatase activity[239].

3.2 Methods

3.2.1 Manufacture of HA-coated titanium coupons

In order to closely mimic the HA-coated implant coating procedure used in the DePuy production line, clinical grade titanium rods (Ti6Al4V alloy) were cut into coupons of several mm thickness and either 5 mm or 10 mm diameter, depending on the application. Plasma coating of titanium coupons was undertaken at DePuy Synthes, Cork, Ireland, based on a DoE taking into account their previous work. Due to the commercially sensitive nature of this study, the factors and factor settings were codified. Factors A-E were varied in a DoE setting according to low (-1), medium (0), and high (1) settings previously determined internally using a factorial design method within Minitab software (Table 3.1). In brief, surgical grade titanium coupons were grit-blasted, then sprayed using the parameter settings set out in the DoE to produce a panel of 17 HA-coated titanium surfaces. Plasma sprayed coupons were stored at ambient conditions and sterilised by autoclaving.

Overall, 24 coupons were manufactured per condition, per batch, allowing for experiments to be run with three internal repeats, 3 times. For non-destructive material studies, the same coupons were used throughout, whereas coupons were not reused when brought into contact with biological material.

Table 3.1: Factorial design of experiments table describing combinations of plasma sprayer parameter settings in standard order.

Coupon	A	B	C	D	E
1	-1	-1	-1	-1	1
2	1	-1	-1	-1	-1
3	-1	1	-1	-1	-1
4	1	1	-1	-1	1
5	-1	-1	1	-1	-1
6	1	-1	1	-1	1
7	-1	1	1	-1	1
8	1	1	1	-1	-1
9	-1	-1	-1	1	-1
10	1	-1	-1	1	1
11	-1	1	-1	1	1
12	1	1	-1	1	-1
13	-1	-1	1	1	1
14	1	-1	1	1	-1
15	-1	1	1	1	-1
16	1	1	1	1	1
17	0	0	0	0	0

3.2.2 X-ray diffraction

X-ray diffraction (XRD) was carried out at DePuy Synthes according to ISO standard 13779-3, where the HA coating is scraped off of the titanium coupon and ground into a uniform powder. XRD spectra were then collected between 20° and 60°. The crystallinity is determined by calculating the area under certain peaks in the spectrum and comparing to a reference standard, which in this case was the stock HA powder. A relative crystallinity percentage was then expressed related to the reference standard.

3.2.3 Roughness measurements

Roughness measurements were carried out using a stylus profilometer (Bruker DekTakXT). Five areas of 0.36 mm^2 were measured with a stylus pressure of 10 mg at 0.3 mm/min. Roughness parameter outputs were arithmetic mean roughness (Sa), kurtosis (Sku), maximum peak height (Sp), maximum pit depth (Sv), maximum height (Sz), root mean square height (Sq), and skewness (Ssk). A 3D map of the surfaces was rendered and a heat map created using DekTak software.

3.2.4 Cell culture

Clonal MSCs, termed Y201, generated from primary bone marrow derived MSCs engineered to overexpress human telomerase reverse transcriptase (hTERT)[119], were used as a model cell system in some assays and has been stated where appropriate. Y201 MSCs were expanded in high glucose Dulbecco's minimal essential medium (DMEM) supplemented with 10 % Foetal Bovine Serum (FBS), 100 Units/mL Penicillin and 100 µg/mL Streptomycin and passaged using 0.05% trypsin-EDTA once 80-90 % confluency was achieved. Cells were incubated at 37°C and 5% CO_2 Cultures were regularly tested for mycoplasma contamination during expansion and prior to experimentation. Cells were seeded in to 4-well plates for a minimum of 24 hours, rinsed with PBS, fixed with methanol, washed with deionised water and stained with 2 µg/mL 4', 6-diamidino-2-phenylindole (DAPI). Cultures were inspected using the Leica IRB inverted microscope for the punctate fluorescent staining within the cytoplasm that is indicative of contamination.

3.2.5 Scanning electron microscopy/Energy dispersive X-ray analysis

Cells were fixed in 4% paraformaldehyde and 2.5% glutaraldehyde, prepared in phosphate buffered saline (PBS) pH7.0, for 2 hours at room temperature. Fixative was removed and samples were rinsed in PBS (2 x 10 minutes). This was followed by a secondary fixation in 1% osmium tetroxide for 1 hour on ice, followed by two more 10-

minute washes in PBS. Samples were then dehydrated in increasing percentages of ethanol (25%, 50%, 70%, 90%, 100%) for 15 minutes at each stage, with 3 incubations at 100%. Final dehydration in hexamethyldisilazane was performed for 15 minutes. Excess was removed and samples were allowed to air dry. Samples were then coated in gold and imaged using SEM/Energy dispersive X-ray analysis.

3.2.6 Wnt reporting

An immortalised, fluorescent Wnt reporter MSC line was developed for the detection of canonical Wnt signalling in response to various stimuli using the Y201 cell line, expressing enhanced green fluorescent protein (EGFP) upon canonical Wnt activation[240]. To assess Wnt activation quantitatively, cells were lysed in 0.1% triton-X100 in 0.2M carbonate buffer and freeze-thawed 3 times to ensure complete lysis. EGFP was detected using a fluorescent microplate reader (Clariostar Plus, BMG Labtech) with excitation at 485 nm and emission at 530 nm. EGFP signal was normalised to cell number by protein quantitation using a bicinchoninic (BCA) assay.

BCA assay was carried out using Pierce BCA assay kit (ThermoFisher, cat. 23225) according to manufacturer's instructions. In brief, a standard curve was created using bovine serum albumin (BSA) with concentration ranging from 25 – 2000 µg/ml. The supplied working reagent was prepared and added to the standards and unknown samples and incubated at 60°C for 30 min. Absorbance was then read using a spectrophotometer (Clariostar, BMG Labtech) at 562 nm. Sample protein concentrations were calculated using the standard curve.

3.2.7 Proliferation assays

Proliferation was assessed using fluorescent PicoGreen reagent (Thermo Fisher, Cat: P7581) over 72 hours and expressed as a change in cell number over time as a proxy for proliferation. HA-coated coupons were seeded with Y201-MSCs to a density of 1 x 10^4 cells/cm^2 and allowed to settle and attach for 24 hours. Cells were cultured at 37°C, 5% CO_2 for 72 hours. Cells were lysed as previously described in section 3.2.6. Fluorescence was measured in a microplate reader with excitation at 485 nm and emission at 530 nm (Clariostar Plus, BMG Labtech).

To test chemically defined medium performance on the plasma sprayed coupons, a continuous-read assay was used to enable monitoring of cell growth over time (RealTime Glo MT Cell Viability Assay; Promega, Cat: G9711). Cells were seeded onto plasma sprayed coupons, placed inside white microtitre plates, at a density of 1 x 10^4

cells/cm^2 and allowed to settle and attach for 24 hours. These were then washed in phosphate buffered saline and medium replaced with optimum CDM (see 2.4). Plates were placed in a microplate reader (Clariostar Plus, BMG Labtech) for continuous monitoring of luminescence over 4 days, at 12 hour intervals. Conditions within the plate reader were kept at 5% CO_2 and 37°C.

3.2.8 Osteogenic differentiation

MSCs were culture expanded, seeded onto coupons at a density of 3 x 10^4 cells/cm^2 in DMEM + 10 % FBS and incubated (37 °C, 5 % CO_2) for 24 hours prior to the addition of osteogenic media (DMEM, 10 % FBS, 100 units/mL Penicillin, 100 µg/mL Streptomycin, 50 µg/mL L-Ascorbic acid 2-phosphate sesquimagnesium salt hydrate (Sigma, Cat: A8960), 10^{-8} M Dexamethasone (Sigma, Cat: D2915), 5 mM β-glycerophosphate (Sigma, Cat: G9422)). Medium was changed every 3 days for 9 days.

Osteogenic differentiation was assessed by alkaline phosphatase (ALP) activity. This was determined through the colourimetric change that occurs upon dephosphorylation of p-nitrophenyl-phosphate (pNPP) by ALP. At day 9, cells were washed 3 times in 0.2 M carbonate buffer, then lysed using 0.1% triton-X100 followed by repeated freeze-thawing to ensure complete lysis. A p-nitrophenyl standard with increasing concentration (0-250 nmol/L) was added to a 96 well plate, alongside 50 µl of each sample. 50 µl of pNPP substrate (5mM pNPP, 3.3 mM $MgCl_2$ in 0.2 M carbonate buffer) were added to each sample and incubated for 1 hour at 37°C. Colourimetric change was measured using a spectrophotometer (Multiskan GO, Thermo Fisher) by measuring absorbance at 405 nm.

ALP activity was normalised to double stranded deoxyribonucleic acid (dsDNA) content in each well. dsDNA content was measured using fluorescent PicoGreen reagent (Thermo Fisher, Cat: P7581). 50 µl cell lysate was added to a black microplate alongside a series of standards of salmon sperm dsDNA (0-4 µg/ml), prepared in 0.1% triton X-100. PicoGreen reagent was prepared using TE buffer (10 mM Trizma base, 1.25 mM EDTA in dH_2O, pH 7.5) and added in equal amounts to samples and the standards. Fluorescence was measured using a fluorescent microplate reader (Clariostar Plus, BMG Labtech) at 485 nm excitation and 538 nm emission.

3.3 Results

3.3.1 Relative crystallinity assessment of HA coatings

A range of crystallinities was achieved by altering the spray parameters according to the DoE created. Crystallinities ranged between 48% and 108%, relative to the starting feedstock material (Table 3.2). Measurements were taken in triplicate.

Table 3.2: Relative crystallinity measurements obtained by XRD for each plasma spray parameter setting combination.

Coupon	Factor A	Factor B	Factor C	Factor D	Factor E	Relative crystallinity (%)
1	-1	-1	-1	-1	1	87.78
2	1	-1	-1	-1	-1	108.4
3	-1	1	-1	-1	-1	62.28
4	1	1	-1	-1	1	104.67
5	-1	-1	1	-1	-1	67.97
6	1	-1	1	-1	1	85.03
7	-1	1	1	-1	1	63.14
8	1	1	1	-1	-1	61.11
9	-1	-1	-1	1	-1	48.34
10	1	-1	-1	1	1	92.53
11	-1	1	-1	1	1	58.98
12	1	1	-1	1	-1	86.28
13	-1	-1	1	1	1	58.05
14	1	-1	1	1	-1	74.54
15	-1	1	1	1	-1	60.52
16	1	1	1	1	1	76.7
17	0	0	0	0	0	59.23

3.3.1.1 *Backward Elimination of Terms – Relative crystallinity*

The relative crystallinity response was successfully modelled to each sprayer input, enabling the fine-tuning of relative crystallinity by changing spray parameters accordingly using stepwise backward elimination of terms analysis. Every factor included in the analysis (excluding ones with evidence of confounding) fell below the stipulated α-value of 0.15. The R^2 achieved was 99.63%, suggesting the relative crystallinity was closely modelled to the candidate terms (Table 3.3). A regression equation was generated, allowing for accurate prediction of relative crystallinity resulting from changes in the plasma sprayer input parameter settings (Equation 4).

Table 3.3: Stepwise backward elimination of terms analysis on general factorial DoE for plasma sprayer input effects on measure Sa of HA coatings. R^2 = 99.63.

	-----Step 1----	
	Coef	**P**
Constant	74.770	
A	11.387	0.000
B	-3.060	0.005
C	-6.388	0.000
D	-5.277	0.001
E	3.590	0.003
A*C	-5.425	0.001
A*D	1.633	0.038
B*D	4.188	0.001
C*D	4.347	0.001
C*E	-1.242	0.082
D*E	-1.518	0.048
Ct Pt	-15.54	0.002

R^2
99.63%

Equation 4: Regression equation for the prediction of HA coating relative crystallinity based on plasma sprayer input settings.

$$\text{Relative crystallinity} = 74.770 + 11.387\,A - 3.060\,B - 6.388\,C - 5.277\,D + 3.590\,E - 5.425\,A{*}C + 1.633\,A{*}D + 4.188\,B{*}D + 4.348\,C{*}D - 1.242\,C{*}E - 1.518\,D{*}E - 15.54\,Ct\,Pt$$

3.3.1.2 *Main effects and interactions – Relative crystallinity*

The analysis that A had the most significant effect on relative crystallinity, followed by the factor C and the combination of factor C and factor A (Figure 3.3; Appendix 19). This combined effect between factor C and factor A presented itself as a diminished effect by factor A at a higher factor C, where at a low factor C, increasing factor A increased the relative crystallinity of the resulting surface (*Appendix* 20; Appendix 21).

Another notable combined effect was observed with factor D. At low factor D, there appeared to be an insignificant change in relative crystallinity in response to increasing factor B and factor C, but at a high factor D setting, low levels of factor C and factor B resulted in a higher relative crystallinity.

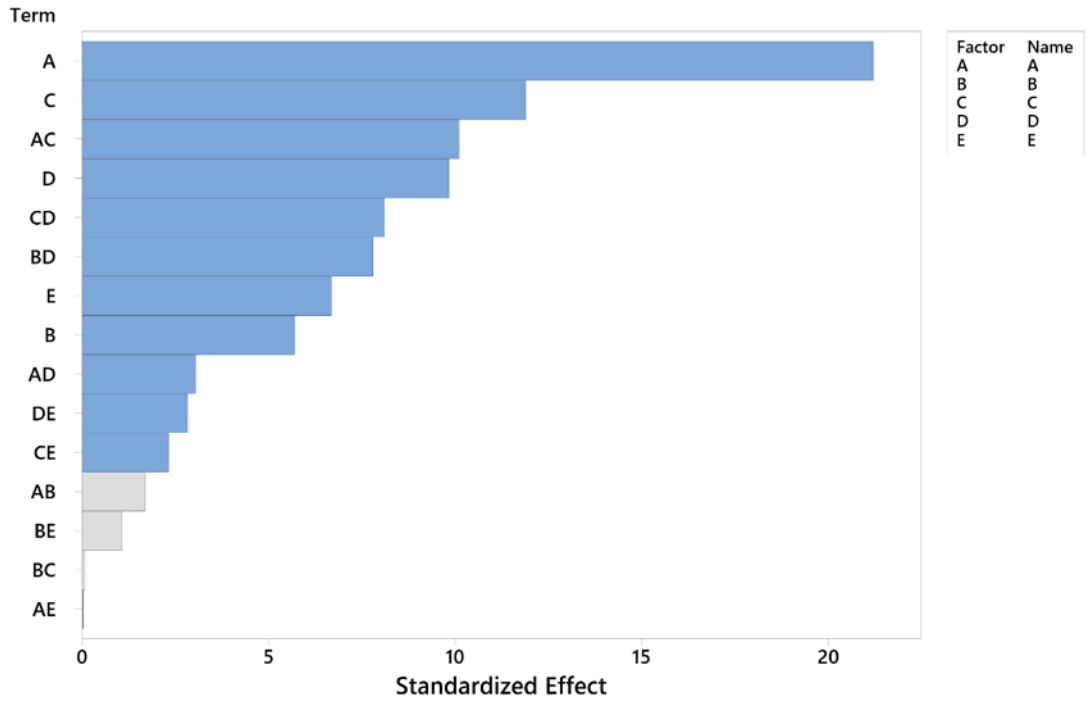

Figure 3.3: Main effects pareto chart depicting magnitude of standardized effect of plasma sprayer input parameters on relative crystallinity measurements. Blue bars indicate significant effect of the input parameters alone or in combination, while grey bars indicate a non-significant effect and were therefore excluded from the model. P<0.15.

3.3.2 Roughness assessment of HA coatings

In order to further model material properties to plasma spray parameters, roughness of the 17 differently sprayed HA coatings was determined by stylus profilometry. Roughness parameters assessed were arithmetic mean roughness (Sa), maximum peak height (Sp), maximum pit depth (Sv), maximum height (Sz), root mean square height (Sq), skewness (Ssk) and kurtosis (Sku) (Figure 3.2). As roughness was not factored into routine production specifications and plasma spray optimisation at DePuy Synthes, it was unclear whether a significant change in roughness would be observed between differently sprayed coupons. For each measurement, 3 coupons were measured in 5 different regions of each coupon, and the result averaged. Roughness measurements varied broadly between discs, with Sa ranging between 8324.63 nm and 17275.97 nm, Sp between 29471.71 nm and 73326.20 nm, Sv between -33017.42 nm and -65053.32 nm, Sz between 62489.13 nm and 138379.52 nm, Sq between 10387.46 nm and 20565.87 nm, Ssk between -0.40 and 0.22, and Sku of 2.38 to 3.40 (Table 3.4). 2D and 3D heat maps were rendered from measured surfaces on each coupon (Figure 3.4 - Figure 3.5).

Table 3.4: Summary of roughness measurements as measured by stylus profilometry.

Coupon	Factor A	Factor B	Factor C	Factor D	Factor E	Sa (nm)	Sp (nm)	Sv (nm)	Sz (nm)	Sq (nm)	Ssk	Sku
1	-1	-1	-1	-1	1	16247.53	73326.2	-65053.32	138379.52	20565.87	0.22	3.4
2	1	-1	-1	-1	-1	8836.62	35517.46	-39997.47	75514.93	11077.39	-0.24	3.19
3	-1	1	-1	-1	-1	14585.38	47367.18	-61062.66	108429.85	18291.71	-0.2	2.95
4	1	1	-1	-1	1	8767.01	29471.71	-33017.42	62489.13	10627.89	-0.1	2.38
5	-1	-1	1	-1	-1	17275.97	65307.12	-57954.19	123261.31	21797.34	0.19	2.83
6	1	-1	1	-1	1	9827.77	32083.19	-43249.2	75332.39	12296.63	-0.4	3.01
7	-1	1	1	-1	1	15680.02	60429.73	-59604.2	120033.93	19473.52	-0.04	2.68
8	1	1	1	-1	-1	10371.91	37425.71	-33028.11	70453.82	12748.42	0.15	2.51
9	-1	-1	-1	1	-1	14646.2	52482.18	-47564.01	100046.2	17837.92	0.14	2.51
10	1	-1	-1	1	1	8324.63	29583.78	-36139.76	65723.54	10387.46	-0.26	2.86
11	-1	1	-1	1	1	15047.31	62620.86	-57833.77	120454.62	18364.72	-0.07	2.58
12	1	1	-1	1	-1	10447.79	35805.67	-40501.15	76306.82	12801.08	-0.06	2.55
13	-1	-1	1	1	1	14329.62	55043.98	-48602.45	103646.43	17655.56	0.33	2.78
14	1	-1	1	1	-1	11035.1	37427.73	-47193.54	84621.27	14118.69	-0.4	3.09
15	-1	1	1	1	-1	15606.29	52866	-61357.46	114223.46	19205.93	0.16	2.64
16	1	1	1	1	1	9903.02	36743.98	-41108.42	77852.4	12440.58	-0.27	2.99
17	0	0	0	0	0	12270.36	43815.54	-43863.97	87679.51	15238.71	0.09	2.66

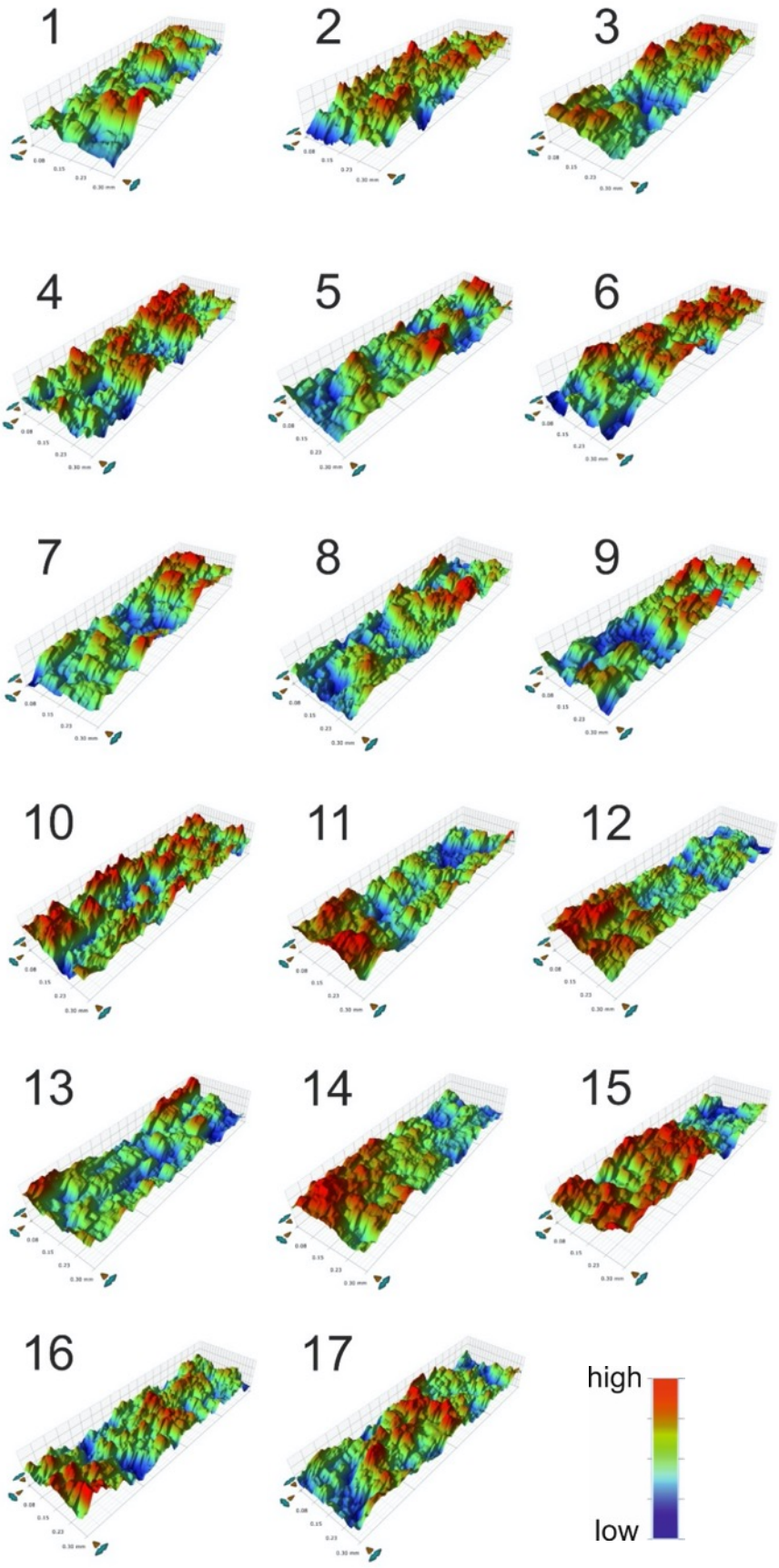

Figure 3.4: Representative overview of 3D topography heatmaps of plasma sprayed HA surfaces 1-17 as measured by stylus profilometry. Clear differences can be seen in peak and valley distribution across each sample.

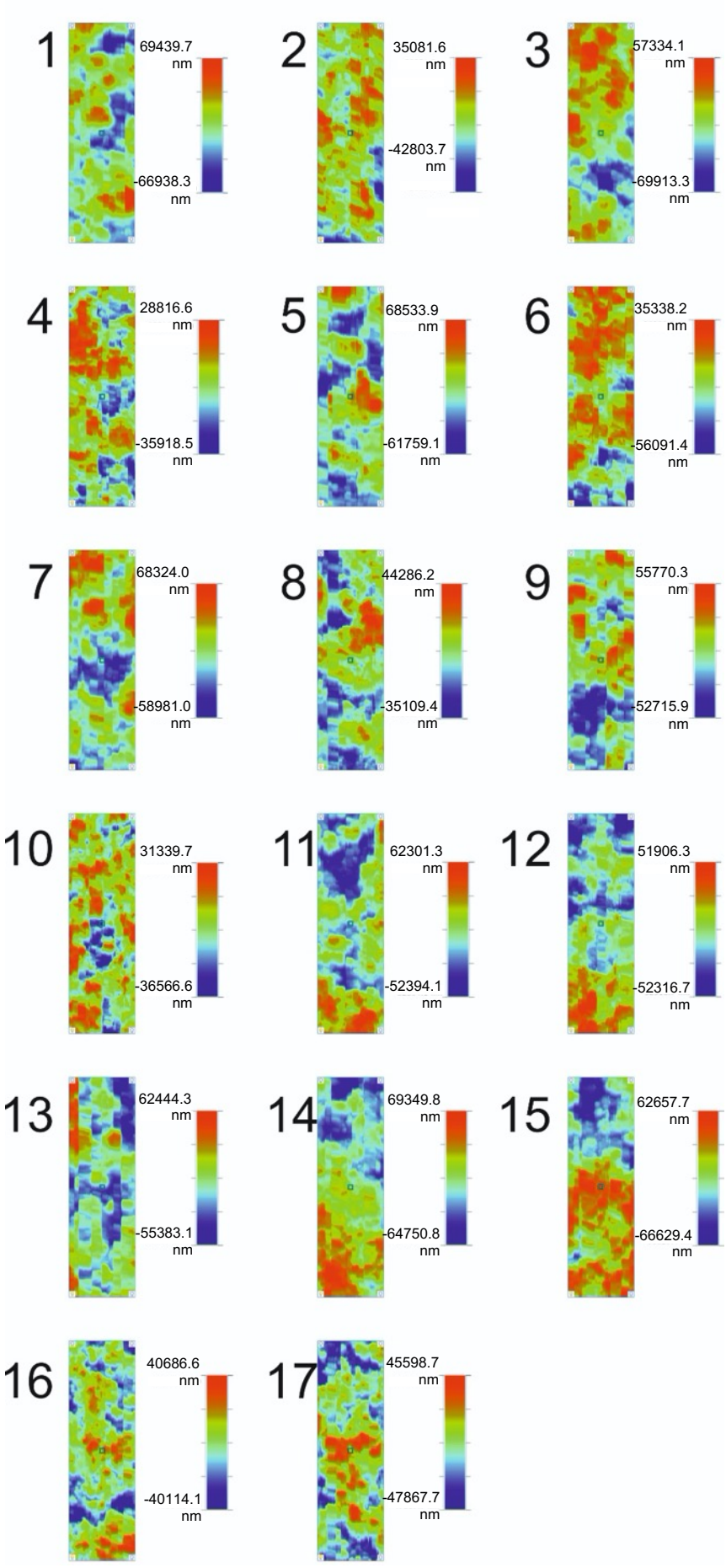

Figure 3.5: 2D view of surface topography heatmaps for plasma sprayed HA surfaces 1-17 as measured by stylus profilometry.

3.3.2.1 *Backward elimination of terms – Sa*

The previous section demonstrated that plasma spray parameters could reliably be related to relative crystallinity. In the following sections, each roughness parameter (Sa (3.3.2.1 - 0); Sp (3.3.2.3 - 3.3.2.4); Sv (3.3.2.5 - 3.3.2.6); Sz (3.3.2.7 - 3.3.2.8); Sq (3.3.2.9 - 3.3.2.10); Ssk (3.3.2.11 - 3.3.2.13); Sku (3.3.2.15 - 3.3.2.17)) will be correlated to plasma spray parameter inputs by way of backward elimination of terms analyses of the measured data. Data will be presented as raw data for each coupon (1 – 17), followed by backward elimination of terms analysis, regression equation, pareto chart of main effects, main effects chart, interaction matrix, and contour plots.

Average roughness (Sa) measurements varied between samples cyclically, which is indicative of factor A being responsible for these changes, as factor A alternated in the same pattern (Figure 3.6).

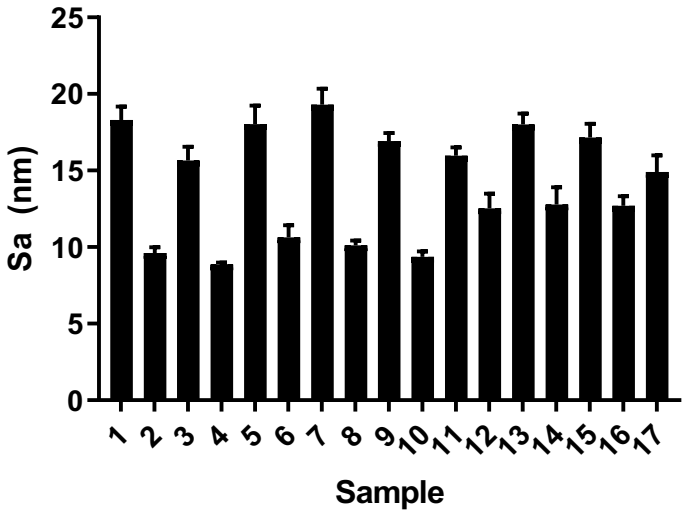

Figure 3.6: Sa measurements as assessed by stylus profilometry. The 17 HA-coated coupon samples were measured in 5 distinct areas of 0.3 mm x 1.0 mm for each sample, in triplicate. Means ± SEM.

Factor A involvement was confirmed by stepwise backward elimination analysis of the general factorial DoE, where changes were mainly driven by factor A (p = 0.000). 5 steps were required to create a model with appropriate terms included (Table 3.5). A regression equation was generated to allow for prediction of Sa values based on changes in plasma spray parameter input settings (Equation 5).

Table 3.5: Stepwise backward elimination of terms analysis on general factorial DoE for plasma sprayer input effects on measure Sa of HA coatings. Coloured cells indicate eliminated terms at each step of the analysis. R^2 is given for the final model.

	----Step 1----		----Step 2----		----Step 3----		----Step 4----	
	Coef	**P**	**Coef**	**P**	**Coef**	**P**	**Coef**	**P**
Constant	12541		12541		12541		12541	
A	-2869	0.000	-2869	0.000	-2869	0.000	-2869	0.000
B	-7	0.949	-7	0.953	-7	0.958	-7	0.961
C	445	0.014	445	0.012	445	0.015	445	0.016
D	-141	0.256	-141	0.280	-141	0.326	-141	0.353
E	-292	0.051	-292	0.054	-292	0.068	-292	0.078
A*B	190	0.148	190	0.163				
A*C	150	0.232						
A*D	379	0.023	379	0.022	379	0.028	379	0.032
A*E	-191	0.147	-191	0.161	-191	0.196		
B*D	341	0.033	341	0.033	341	0.041	341	0.047
C*E	-276	0.060	-276	0.064	-276	0.081	-276	0.092
D*E	-224	0.103	-224	0.112	-224	0.140	-224	0.158

	----Step 5----	
	Coef	**P**
Constant	12541	
A	-2869	0.000
B	-7	0.964
C	445	0.020
D	-141	0.388
E	-292	0.095
A*B		
A*C		
A*D	379	0.040
A*E		
B*D	341	0.058
C*E	-276	0.111
D*E		

R^2	**Eliminations:**	**1st**	**2nd**	**3rd**	**4th**
97.90%					

Equation 5: Regression equation for the prediction of Sa of HA coatings based on changes in plasma sprayer input parameter settings.

Sa = 12541 - 2869 A - 7 B + 445 C - 141 D - 292 E + 379 A*D + 341 B*D - 276 C*E

3.3.2.2 *Main effects and interactions – Sa*

The Sa response to changing plasma spray input parameter settings was a linear one, with the centre point not included in the model (Table 3.5; Figure 3.7). The most pronounced main effect on Sa was achieved by factor A (p = 0.000), which was followed by factor C (p = 0.020), and factor E (p = 0.095). An increase in factor A caused a significant drop in Sa, while an increase in factor C would cause a significant but less pronounced decrease in Sa (Appendix 22).

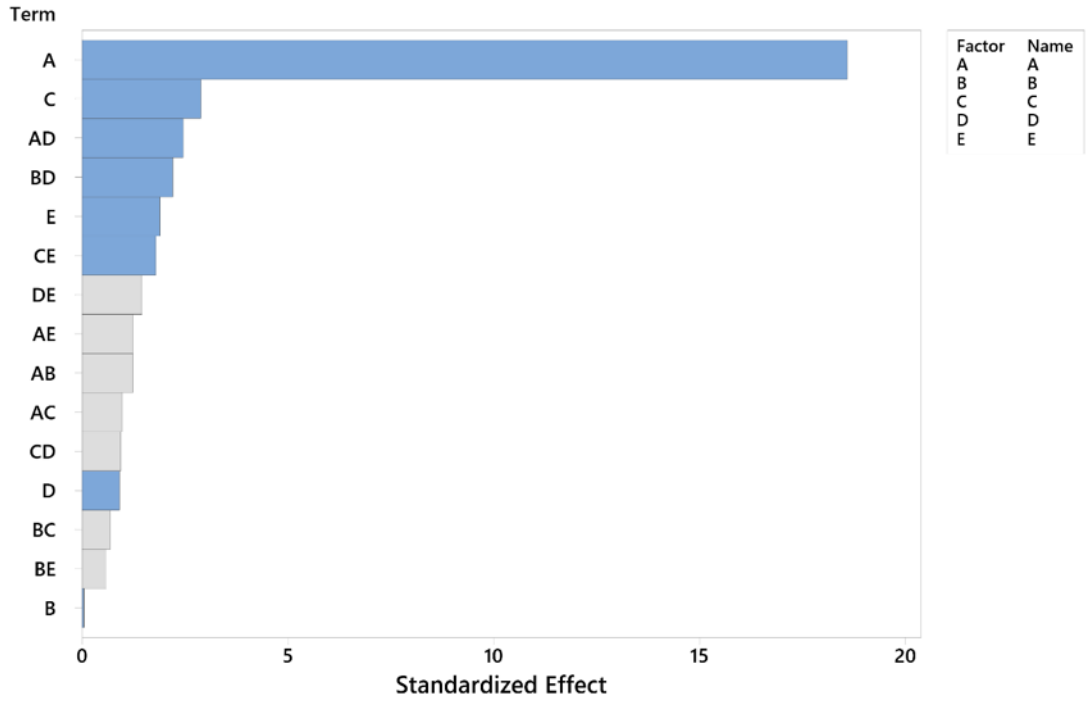

Figure 3.7: Main effects pareto chart depicting magnitude of standardized effect of plasma sprayer input parameters on Sa measurements. A was identified to have the most significant effect on Sa. Blue bars indicate significant effect, while grey bars indicate an insignificant effect and were therefore excluded from the model. p<0.15.

Significant interactions were observed between factor A and factor D (p = 0.040), factor B and factor D (p = 0.058), and factor C and factor E (p = 0.111), while other interactions observed were insignificant (Appendix 23). An increased factor D appeared to slightly diminish factor A's effect on Sa, whilst an increased factor D appeared to reverse the effect of factor B (from decreasing Sa to increasing Sa). A low factor E also appeared to cause an increase in Sa in response to increasing factor C, whilst a higher factor E negated this effect, resulting in no differences in Sa in response to increasing factor C (Appendix 23; Appendix 24).

3.3.2.3 *Backward Elimination of terms – Sp*

Using backward elimination of terms analysis, maximal peak height (Sp) was modelled to plasma sprayer input changes. Measured values across the 17 HA-sprayed coupons ranged between 29471.71 nm and 73326.20 nm, with a similar pattern coinciding with factor A alternating seen as was previously observed for Sa (Figure 3.8).

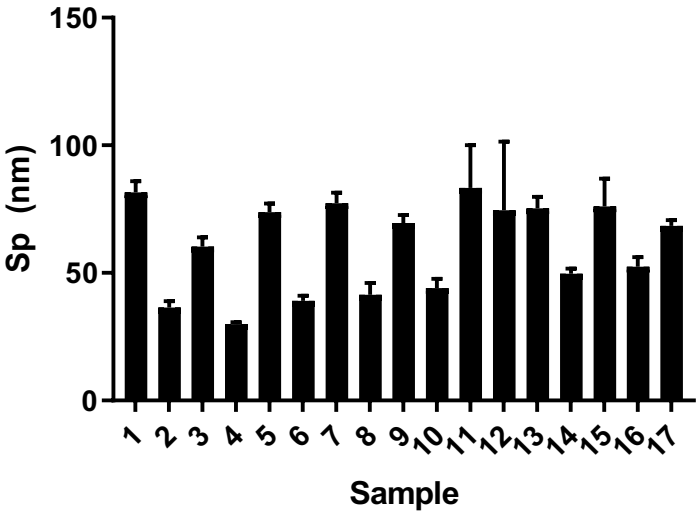

Figure 3.8: Sp measurements as assessed by stylus profilometry. Samples were measured in 5 distinct areas of 0.3 mm x 1.0 mm for each sample, in triplicate. Means ± SEM.

Stepwise backward elimination analysis of the general factorial DoE confirmed factor A involvement as being the most profound (p = 0.000), with several interactions being significant in Sp response to changing plasma spray input parameters as well (Table 3.6). Three steps were required to form a model for the Sp response. A regression equation was generated to allow for prediction of Sp values based on changes in plasma spray parameter input settings (Equation 6).

Table 3.6: Stepwise backward elimination of terms analysis on general factorial DoE for plasma sprayer input effects on measured Sp of HA coatings. Coloured cells indicated eliminated terms at each step of the analysis. R^2 is given for the final model.

	-----Step 1----		-----Step 2----		-----Step 3----	
	Coef	**P**	**Coef**	**P**	**Coef**	**P**
Constant	46313		46313		46313	
A	-12212	0.000	-12212	0.000	-12212	0.000
B	-1128	0.131	-1128	0.161	-1128	0.186
C	697	0.307	697	0.356	697	0.391
D	-1147	0.126	-1147	0.155	-1147	0.179
E	944	0.188	944	0.227	944	0.257
A*B	1732	0.044	1732	0.053	1732	0.061
A*C	966	0.180				
A*D	1780	0.040	1780	0.049	1780	0.056
A*E	-3231	0.006	-3231	0.005	-3231	0.005
B*D	2815	0.009	2815	0.009	2815	0.010
B*E	1031	0.159	1031	0.193		
C*E	-2035	0.027	-2035	0.031	-2035	0.036

R^2	**Eliminations:**	**1st**	**2nd**
98.16%			

Equation 6: Regression equation for the prediction of Sp of HA coatings based on changes in plasma sprayer input parameter settings.

$$Sp = 46313 - 12212\,A - 1128\,B + 697\,C - 1147\,D + 944\,E + 1732\,A*B + 1780\,A*D - 3231\,A*E + 2815\,B*D - 2035\,C*E$$

3.3.2.4 *Main effects and interactions – Sp*

Factor A had the most profound effect on Sp (p = 0.000) (Figure *3.9*; Appendix 25). Significant interactions were observed between factor A and factor B (p = 0.061), factor A and factor D (p = 0.056), A and factor E (p = 0.005), factor B and factor D (p = 0.010), and factor C and factor E (p = 0.036) (Appendix 26; Appendix 27).

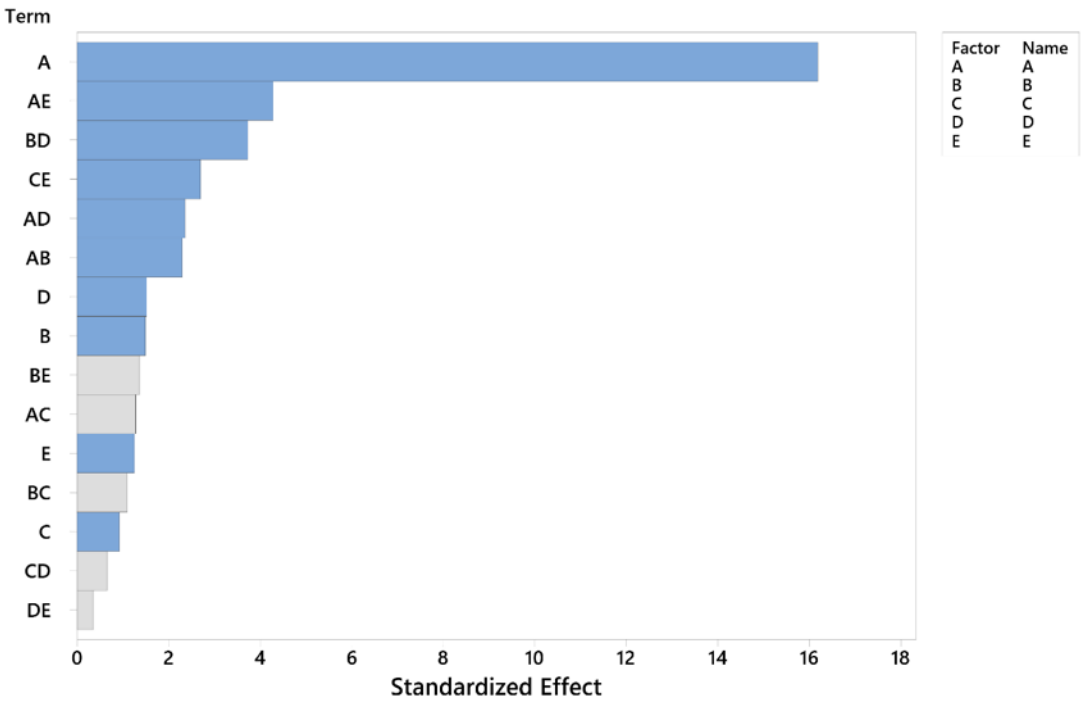

Figure 3.9*: Main effects pareto chart depicting magnitude of standardized effect of plasma sprayer input parameters on Sp measurements. A was identified to have the largest main effect. Blue bars indicate significant effect, while grey bars indicate an insignificant effect and were therefore excluded from the model. P<0.15.*

Similarly to Sa, an increase in factor A resulted in a decrease in Sp (Appendix 25). These responses were linear, with the resulting model not including the centre point.

Higher factor B and factor D diminished the effect of increasing factor A on Sp, while a higher factor E increased factor A's effect on Sp. A high factor D, in turn, caused a decrease in Sp in response to increasing factor B, whereas the opposite effect is seen at low factor D. Finally, a low factor E had a negative effect of Sp with increasing factor C, whereas the opposite effect is seen at high factor E (Appendix 26; Appendix 27).

3.3.2.5 *Backward Elimination of terms – Sv*

Plasma spray input parameter settings were modelled to maximal valley depth (Sv). Measurements varied similarly to Sa and Sv, with a correlation being observed between factor A alternating similarly to Sv values in the raw measured data. Sv values ranged between -33017.42 nm and -65053.32 nm across the 17 different HA-coated coupons (Figure 3.10).

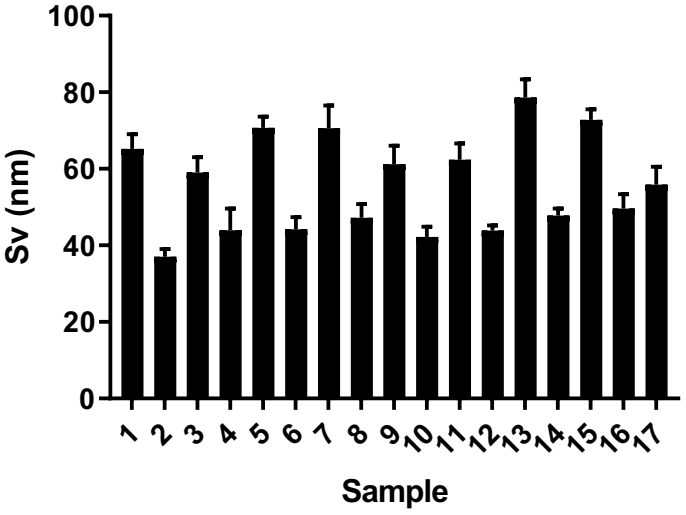

Figure 3.10: Sv measurements as assessed by stylus profilometry. Samples were measured in 5 distinct areas of 0.3 mm x 1.0 mm for each sample, in triplicate. Means ± SEM.

Stepwise backward elimination analysis identified factor A as being a significant factor in Sp response to changing plasma sprayer input parameter settings. Only one step was required in the analysis, as all input parameters were involved to some extent in significant interactions (Table 3.7).

Table 3.7: Stepwise backward elimination of terms analysis on general factorial DoE for plasma sprayer input effects on measured Sp of HA coatings. No eliminations were made in the backward elimination procedure. R^2 is given for the final model.

	-----Step 1----	
	Coef	**P**
Constant	-48329	
A	9050	0.000
B	-110	0.837
C	-683	0.245
D	792	0.190
E	253	0.641
A*B	2476	0.008
A*C	-1182	0.078
A*D	-2748	0.005
B*D	-2553	0.007
C*D	-1345	0.055
D*E	1363	0.053
Ct Pt	4465	0.097

R^2
99.09%

A regression equation was generated for the prediction of Sv of plasma sprayed HA surfaces in response to changing plasma sprayer input settings (Equation 7).

Equation 7: Regression equation for the prediction of Sv of HA coatings based on changes in plasma sprayer input parameter settings.

$$Sv = -48329 + 9050\,A - 110\,B - 683\,C + 792\,D + 253\,E + 2476\,A*B - 1182\,A*C - 2748\,A*D - 2553\,B*D - 1345\,C*D + 1363\,D*E + 4465\,Ct\,Pt$$

3.3.2.6 *Main effects and interactions – Sv*

As was suggested by the raw data, factor A was identified as the most driving factor Behind Sv response (p = 0.000) (Figure 3.11), with interactions between factor A and factor D (p = 0.005), factor B and factor D (p = 0.007), factor A and factor Bs (p = 0.008), factor D and factor E (p = 0.053), factor C and factor D (p = 0.055), and factor A and factor C (p = 0.078) having been determined to participate in the Sv response (Table 3.5; Figure 3.11 -).

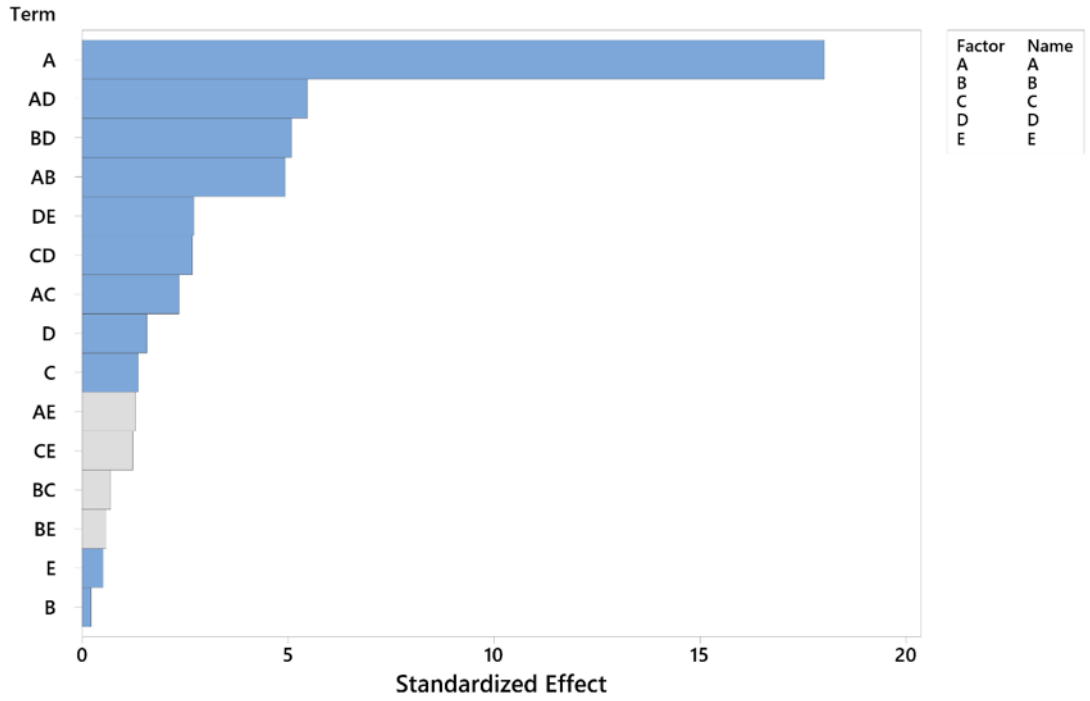

Figure 3.11: Main effects pareto chart depicting magnitude of standardized effect of plasma sprayer input parameters on Sv measurements. The most pronounced effect is conveyed by A (A), with several interactions causing significant change to Sv. Blue bars indicate significant effect, while grey bars indicate an insignificant effect and were therefore excluded from the model. p<0.15.

An increase in factor A caused an increase in Sv, whilst other main effects were significantly less pronounced (Appendix 28). Interactions occurred between factor A and factor D, factor B and factor D, factor A and factor B, factor D and factor E, factor C and factor D, and factor A and factor C, where factor A interactions with low factor D and factor C increased the effect factor A had on Sv, whilst factor A interaction with factor B was the opposite, where an increase factor B increased factor A's effect on Sv. Factor D interactions with factor B and factor C were such that at a high factor B and factor C settings, increasing factor D would decrease Sv, while the reverse was true at

low factor B and factor C. At low factor Es, an increase in factor D would decrease Sv, while a high factor E would have the opposite effect (Appendix 29 - Appendix 30).

3.3.2.7 *Backward Elimination of terms – Sz*

Maximum height (Sz) was modelled to plasma sprayer input parameter setting changed by way of backward elimination of terms analysis. A similar alternating pattern of values was observed for Sz as was observed for Sa, Sp, and Sv, coinciding with factor A fluctuations in the raw data. Values ranged between 62489.13 nm and 138379.52 nm (Figure 3.12).

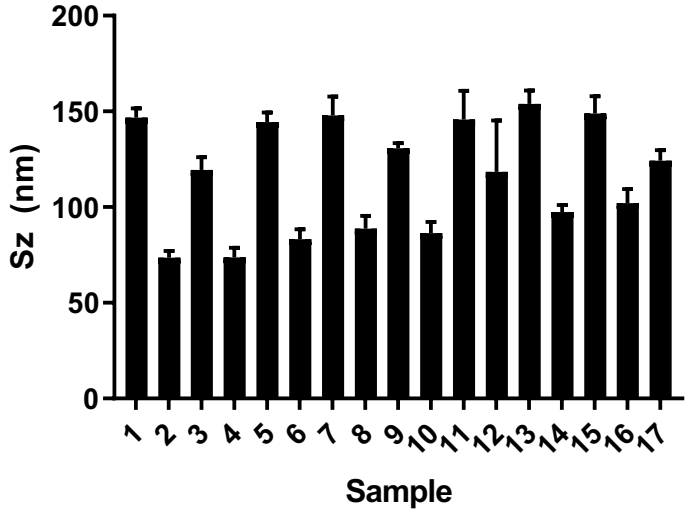

Figure 3.12: Sz measurements as assessed by stylus profilometry. Samples were measured in 5 distinct areas of 0.3 mm x 1.0 mm for each sample, in triplicate. Means ± SEM.

Stepwise backward elimination of terms analysis confirmed the most significant factor in determining Sz was factor A (p = 0.000), followed by factor D (p = 0.053) and factor C (p = 0.126). Several interactions were found to be significant and were therefore included in the model, with only one step required for successful modelling of Sz response (Table 3.8). A regression equation was generated to allow for prediction of Sz of plasma sprayed HA coatings in response to changed plasma sprayer input parameter settings (Equation 8).

Table 3.8: Stepwise backward elimination of terms analysis on general factorial DoE for plasma sprayer input effects on measure Sz of HA coatings. R^2 is given for the final model.

	-----Step 1----	
	Coef	**P**
Constant	94798	
A	-21261	0.000
B	-1018	0.228
C	1380	0.126
D	-1939	0.053
E	691	0.388
A*C	2148	0.040
A*D	4528	0.003
A*E	-3878	0.006
B*D	5368	0.002
C*E	-2653	0.021
D*E	-1631	0.085
Ct Pt	-7119	0.073

R^2
99.62%

Equation 8: Regression equation for the prediction of Sz of HA coatings based on changes in plasma sprayer input parameter settings.

$$Sz = 94798 - 21261\,A - 1018\,B + 1380\,C - 1939\,D + 691\,E + 2148\,A*C + 4528\,A*D - 3878\,A*E + 5368\,B*D - 2653\,C*E - 1631\,D*E - 7119\,Ct\,Pt$$

3.3.2.8 *Main effects and interactions – Sz*

Factor A was shown to have the most pronounced effect on Sz (p = 0.000), with interactions between factor B and factor D (p = 0.002), factor A and factor D (p = 0.003), factor A and factor E (p = 0.006), factor C and factor E (p = 0.021), factor A and factor C (p = 0.040), and factor D and factor E (p = 0.085) also being significant (Figure 3.13).

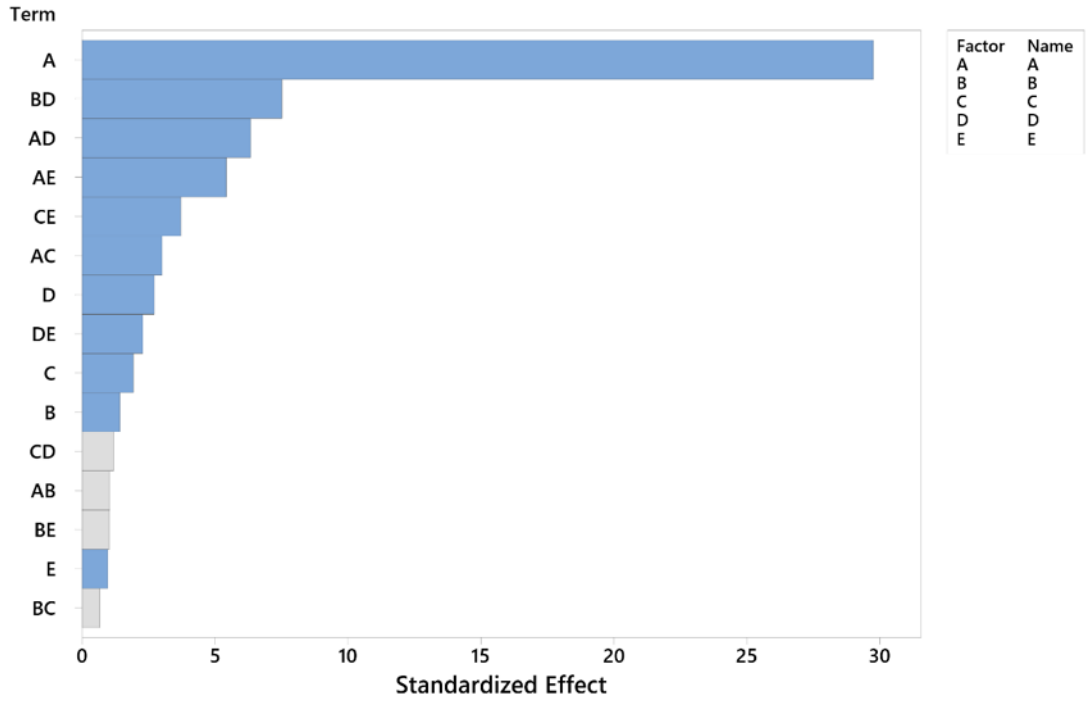

Figure 3.13: Main effects pareto chart depicting magnitude of standardized effect of plasma sprayer input parameters on Sz measurements. The main effect was shown to come from A (A) changes. Blue bars indicate significant effect, while grey bars indicate an insignificant effect and were therefore excluded from the model. p<0.15.

The most significant main effect was from factor A (p = 0.000), where an increase in factor A would decrease Sz (Appendix 31). Interactions between factor A and factor C, factor D and factor E were such that with increased factor A at high factor C and factor D, increased factor A would maintain a higher Sz, while at low factor C and factor D, Sz decline was more steep (Appendix 32- Appendix 33).

3.3.2.9 *Backward Elimination of terms – Sq*

Root mean square height (Sq) was modelled in the same fashion as described previously. A similar pattern of alternating values is again observed for Sq, suggesting heavy factor A involvement. Sq measurements ranged between 10387.46 nm and 20565.87 nm (Figure 3.14).

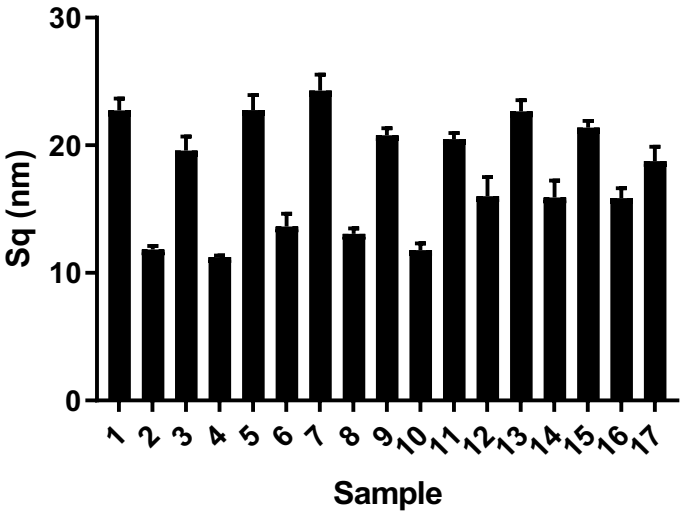

Figure 3.14: Sq measurements as assessed by stylus profilometry. Samples were measured in 5 distinct areas of 0.3 mm x 1.0 mm for each sample, in triplicate. Means ± SEM.

Stepwise backward elimination of terms confirmed factor A to be the most significant factor in Sq response ($p = 0.000$), with factor C ($p = 0.006$), factor D ($p = 0.088$), and factor E ($p = 0.029$) also having a significant effect on Sq. Several interactions were also identified. Analysis was completed in one step (Table 3.9). A regression equation was generated for the prediction of Sq of plasma sprayed HA surfaces in response to changes in parameter input settings (Equation 9).

Table 3.9: Stepwise backward elimination of terms analysis on general factorial DoE for plasma sprayer input effects on measure Sq of HA coatings. R^2 is given for the final model.

	----Step 1----	
	Coef	**P**
Constant	15584	
A	-3543	0.000
B	-111	0.380
C	611	0.006
D	-254	0.088
E	-379	0.029
A*B	204	0.146
A*C	227	0.115
A*D	629	0.005
A*E	-245	0.096
B*D	463	0.015
C*E	-371	0.030
D*E	-260	0.083

R^2
99.64%

Equation 9: Regression equation for the prediction of Sq of HA coatings based on changes in plasma sprayer input parameter settings.

$$Sq = 15584 - 3543\,A - 111\,B + 611\,C - 254\,D - 379\,E + 204\,A*B + 227\,A*C + 629\,A*D - 245\,A*E + 463\,B*D - 371\,C*E - 260\,D*E$$

3.3.2.10 *Main effects and interactions – Sq*

The most significant effect was produced by factor A, with other significant effects being much less pronounced (Figure 3.15). An increase in factor A resulted in a decrease in coating Sq (Appendix 34), with several interactions also playing a role in Sq response to changing plasma sprayer parameter input settings (Appendix 35).

The most significant interaction was observed between factor A and factor D (p = 0.005), where an increase in factor A would cause a less pronounced decrease in Sq at high factor D than at low factor D (Appendix 35 - Appendix 36).

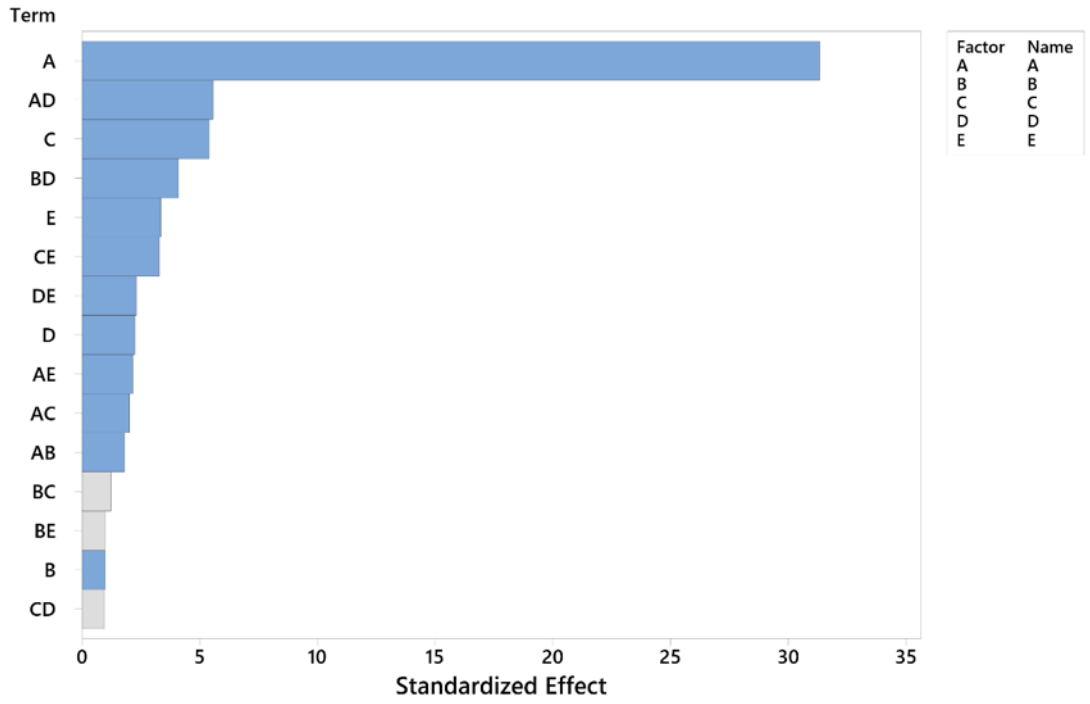

Figure 3.15: Main effects pareto chart depicting magnitude of standardized effect of plasma sprayer input parameters on Sq measurements. The most significant and pronounced effect comes from A (A). Blue bars indicate significant effect, while grey bars indicate an insignificant effect and were therefore excluded from the model. p<0.15.

3.3.2.11 *Backward Elimination of terms – Ssk*

Skewness (Ssk) was also evaluated in terms of how changing plasma spray parameter settings would impact it. Measured values varied more broadly with no discernible pattern, ranging between -0.40 and 0.22 (Figure 3.16). This does not suggest strong involvement of a single input parameter, but that interactions are taking place which would offset the pattern that might be expected if only one factor played the most significant role.

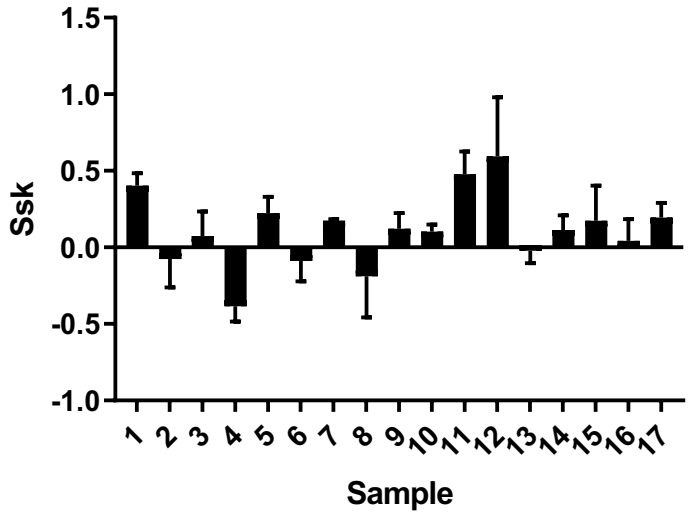

Figure 3.16: Ssk measurements as assessed by stylus profilometry. Samples were measured in 5 distinct areas of 0.3 mm x 1.0 mm for each sample, in triplicate. Means ± SEM.

Stepwise backward elimination of terms analysis showed that factor A was the most significant factor ($p = 0.002$), but that the factor A and factor B have a very strong interaction ($p = 0.002$) (Table 3.10). Other interactions, such as factor A and factor C ($p = 0.054$) and factor A and factor D ($p = 0.61$) also were significant. Analysis was completed in one step.

Table 3.10: Stepwise backward elimination of terms analysis on general factorial DoE for plasma sprayer input effects on measure Ssk of HA coatings. R^2 is given for the final model.

	------Step 1------	
	Coef	**P**
Constant	-0.0450	
A	-0.1438	0.002
B	0.0004	0.983
C	0.0197	0.358
D	-0.0001	0.998
E	-0.0202	0.347
A*B	0.1283	0.002
A*C	-0.0512	0.054
A*D	-0.0489	0.061
A*E	-0.0386	0.112
B*C	0.0363	0.128
B*E	-0.0448	0.077
C*E	-0.0393	0.107

R^2
97.17%

Equation 10: Regression equation for the prediction of Ssk of HA coatings based on changes in plasma sprayer input parameter settings.

$$\begin{aligned} Ssk = {} & -0.0450 - 0.1438\,A + 0.0004\,B + 0.0197\,C - 0.0001\,D - 0.0202\,E \\ & + 0.1283\,A*B \\ & - 0.0512\,A*C - 0.0489\,A*D - 0.0386\,A*E + 0.0363\,B*C - 0.0448\,B*E \\ & - 0.0393\,C*E \end{aligned}$$

3.3.2.13 *Main effects and interactions – Ssk*

The most pronounced effects were caused by factor A interactions with factor B, factor C, and factor D (Figure 3.17).

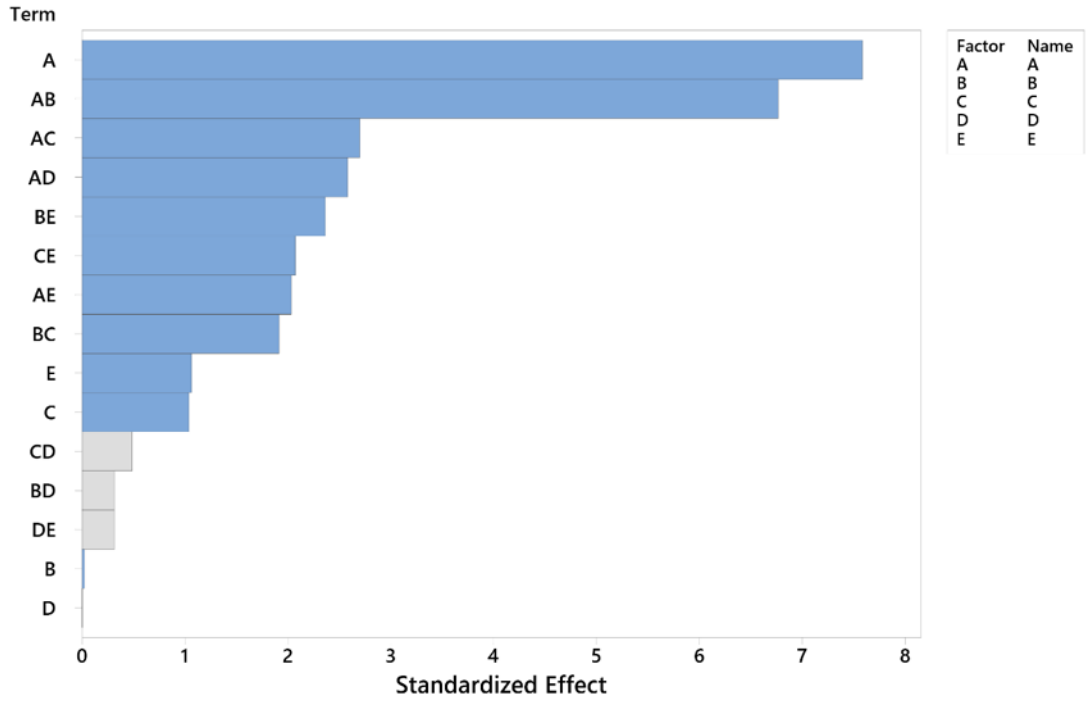

Figure 3.17: Main effects pareto chart depicting magnitude of standardized effect of plasma sprayer input parameters on Ssk measurements. Both A (A) and the A and B interaction (AB) have a very pronounced effect on Ssk. Blue bars indicate significant effect, while grey bars indicate an insignificant effect and were therefore excluded from the model. P<0.15.

The main effect observed by factor A alone was a decrease in Ssk with increasing factor A (Appendix 37). The factor A and factor B interaction is highly significant, where a high factor B completely negates the effect of factor A on Ssk. Increased factor C and factor D both increased the effect factor A had on Ssk (Appendix 38 - Appendix 39).

3.3.2.15 *Backward Eliminations of terms – Sku*

Kurtosis (Sku) varied across a less broad range than other measured roughness properties, between 2.38 and 3.40 (Figure 3.18). This suggests that Sku may be a parameter that cannot greatly be altered by manipulation of plasma spray input parameter settings.

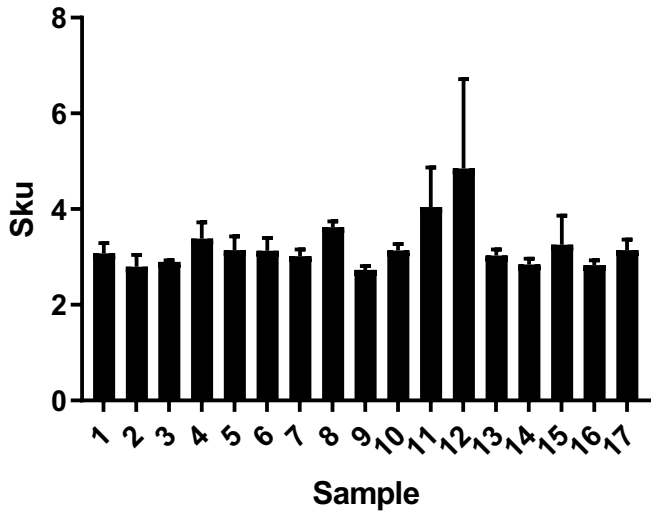

Figure 3.18: Sku measurements as assessed by stylus profilometry. Samples were measure in 5 distinct areas of 0.3 mm x 1.0 mm for each sample, in triplicate. Means ± SEM.

Stepwise backward elimination of terms analysis identified factor B to be the most significant factor in affecting Sku ($p = 0.002$), with factor C and factor D interaction being the strongest interaction ($p = 0.010$), though other interactions were also significant. 4 steps were required to create a model with sufficient fit (Table 3.11). A regression equation was generated in order to predict Sku changes in response to changing plasma sprayer input parameter settings (Equation 11).

Table 3.11: Stepwise backward elimination of terms analysis on general factorial DoE for plasma sprayer input effects on measure Sku of HA coatings. Coloured cells indicate eliminated terms at each step of the analysis. R^2 is given for the final model.

	------Step 1-----		------Step 2-----		------Step 3-----	
	Coef	**P**	**Coef**	**P**	**Coef**	**P**
Constant	2.8009		2.8009		2.8009	
A	0.0133	0.669	0.0133	0.684	0.0133	0.672
B	-0.1499	0.007	-0.1499	0.005	-0.1499	0.002
C	0.0068	0.825	0.0068	0.834	0.0068	0.827
D	-0.0589	0.111	-0.0589	0.115	-0.0589	0.096
E	0.0244	0.446	0.0244	0.465		
A*B	-0.0651	0.088	-0.0651	0.089	-0.0651	0.073
A*C	0.0712	0.070	0.0712	0.069	0.0712	0.055
A*D	0.1112	0.018	0.1112	0.016	0.1112	0.010
A*E	-0.0377	0.263				
B*C	0.0394	0.245	0.0394	0.258	0.0394	0.235
B*D	0.0894	0.037	0.0894	0.034	0.0894	0.024
C*D	0.1172	0.015	0.1172	0.013	0.1172	0.008

	------Step 4-----	
	Coef	**P**
Constant	2.8009	
A	0.0133	0.685
B	-0.1499	0.002
C	0.0068	0.835
D	-0.0589	0.103
E		
A*B	-0.0651	0.077
A*C	0.0712	0.058
A*D	0.1112	0.010
A*E		
B*C		
B*D	0.0894	0.025
C*D	0.1172	0.007

R^2	**Eliminations:**	**1st**	**2nd**	**3rd**
90.95%				

Equation 11: Regression equation for the prediction of Sku of HA coatings based on changes in plasma sprayer input parameter settings.

$$\text{Sku} = 2.8009 + 0.0133\,A - 0.1499\,B + 0.0068\,C - 0.0589\,D - 0.0651\,A*B + 0.0712\,A*C + 0.1112\,A*D + 0.0894\,B*D + 0.1172\,C*D$$

3.3.2.17 *Main effects and interactions – Sku*

Factor B had the most pronounced effect on Sku (p = 0.002), with several interactions being identified as being significant. Factor E on its own as well as in combination with any other factor was determined to have no effect on Sku and was therefore excluded from the model (Figure 3.19).

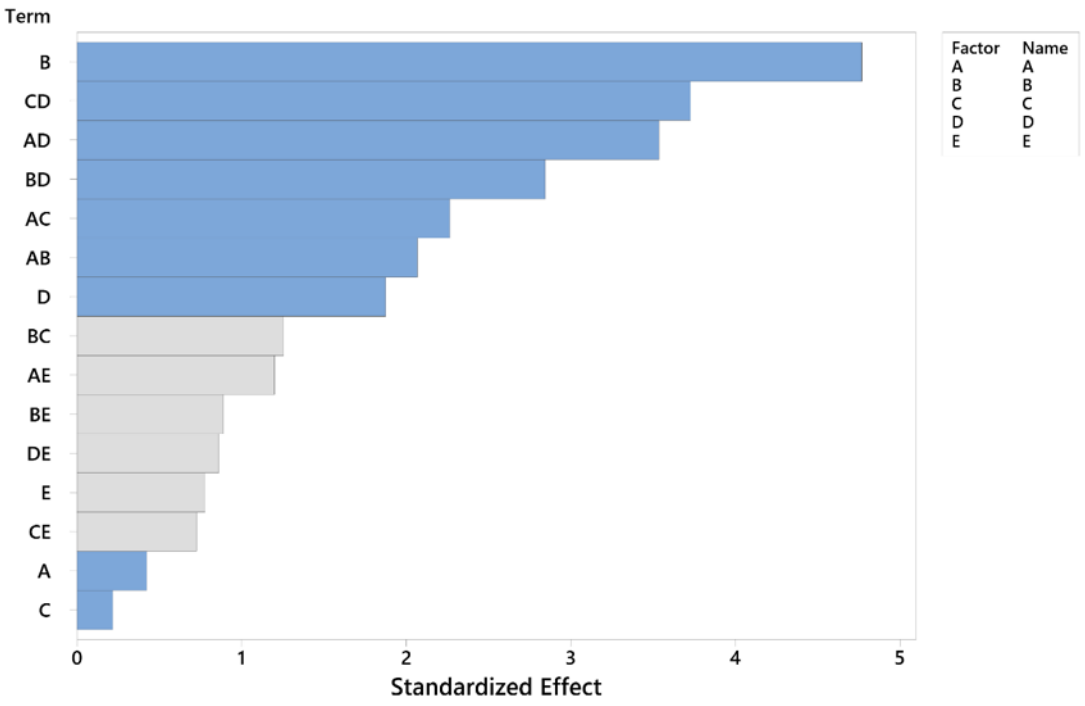

Figure 3.19: Main effects pareto chart depicting magnitude of standardized effect of plasma sprayer input parameters on Sku measurements. The strongest effect was conveyed by B, with the C and D interaction being the strongest interaction. Blue bars indicate significant effect, while grey bars indicate an insignificant effect and were therefore excluded from the model. p<0.15.

An increase in factor B and factor D decreased Sku, with very small effects from factor A and factor C by themselves (Appendix 40). Interactions between factor C and factor D (p = 0.007), factor A and factor D (p = 0.010), factor B and factor D (p = 0.025), factor A and factor C (p = 0.058), and factor A and factor Bs (p = 0.077) were determined to be significant (Table 3.11; Appendix 41 - Appendix 42). The strongest interaction between factor C and factor D was similar to the interactions between factor A and factor D, factor A and factor C, factor B and factor D, and factor A and factor Bs, where a high level of the latter would result in the opposite effect than at a low level.

To summarise, these analyses enabled modelling of HA relative crystallinity, Sa, Sp, Sv, Sz, Sq, Ssk, and Sku to changing plasma spray parameter input settings. This allows for reproducible and predictable production of surfaces with desired relative crystallinity and roughnesses.

Next, to determine the biological implications of variations in plasma sprayer parameter settings, and therefore variations in material properties, osteogenic MSCs were grown on the 17 HA-coated surfaces and effects on Wnt signalling, proliferation, and osteogenic differentiation were assessed. These effects were also then modelled on plasma spray parameter settings with the aim of cross-referencing significant plasma spray parameters on biological outcomes with those impacting material properties in order to understand whether any of the measured properties were implicated in biological effect.

3.3.3 MSC spreading on HA coated discs

Soaking scaffolds or biomaterials in medium before seeding is a common practice. Due to the variety of crystallinities observed and the potential implications this may have on dissolution and redeposition behaviour, the effect of soaking the surfaces was tested on a selection of 7 differently crystalline discs. SEM showed a significant change in surface morphology after incubation in cell culture medium for 6 hours at 37°C (Figure 3.20). It was observed that on 48.34% and 67.34% crystalline coatings, a crystal-like structure had formed across the entire surface (Figure 3.20Figure 3.21). EDS analysis showed that in these coatings, the calcium/phosphate ratio had decreased due to an increase in the atomic percentage of phosphorus on the surface, implying that the crystalline structures were forming due to the presence of phosphates in the cell culture medium (Table 3.12). Due to the changes caused by incubation in culture medium and to ensure a consistent experimental approach, it was decided not to soak the coupons in medium prior to seeding.

It was first investigated whether MSCs could successfully be seeded onto HA-coated titanium discs with a range of differently crystalline surfaces in order to optimise cell culture technique on them. It was observed that cells seeded and spread as expected onto HA-coated discs (Figure 3.22).

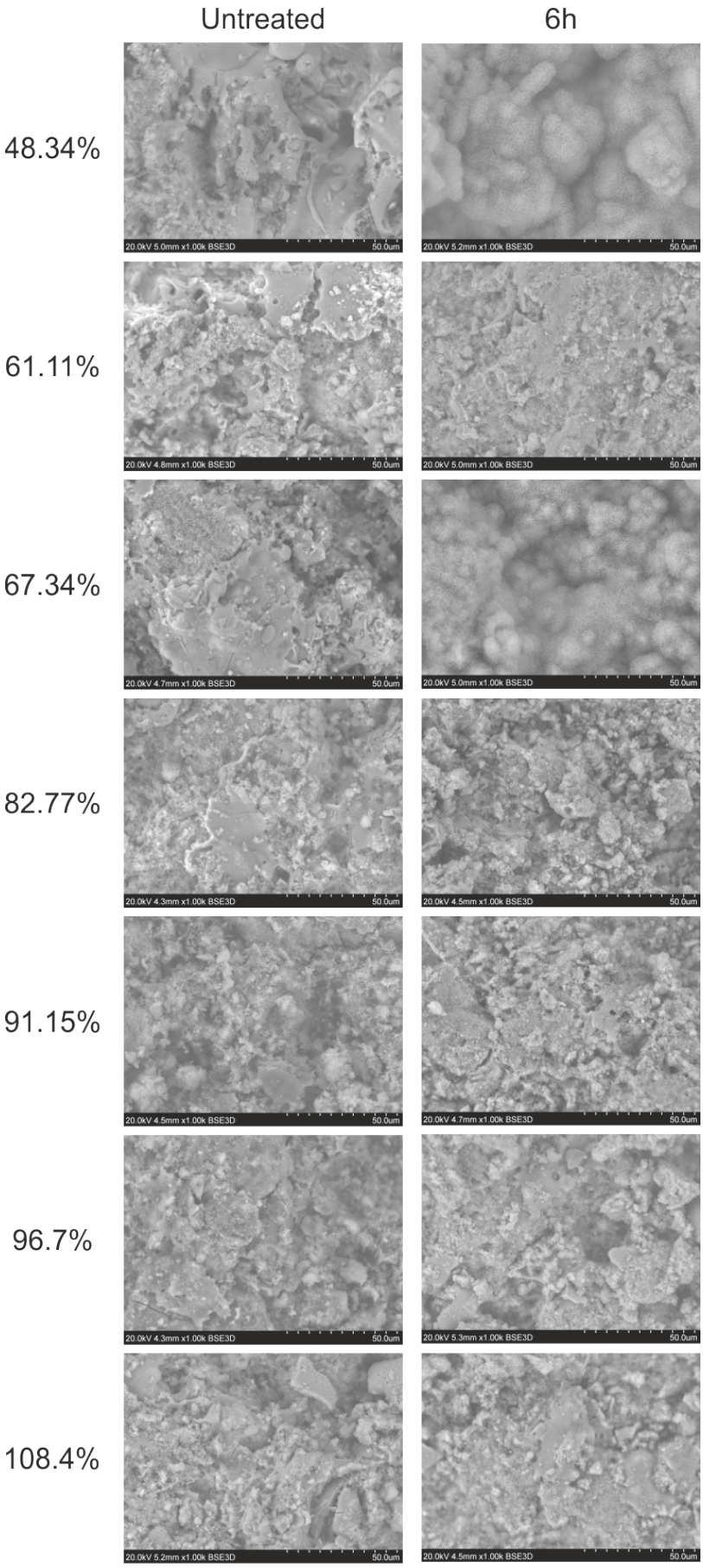

Figure 3.20: SEM analysis of HA coating-titanium coupons with 48.34%, 61.11%, 67.34%, 82.77%, 91.15%, 96.7%, and 108.4% relative crystallinity. Analyses were performed on untreated surfaces or following incubation DMEM + 10% FBS at 37°C for 6h to determine effects on surface features.

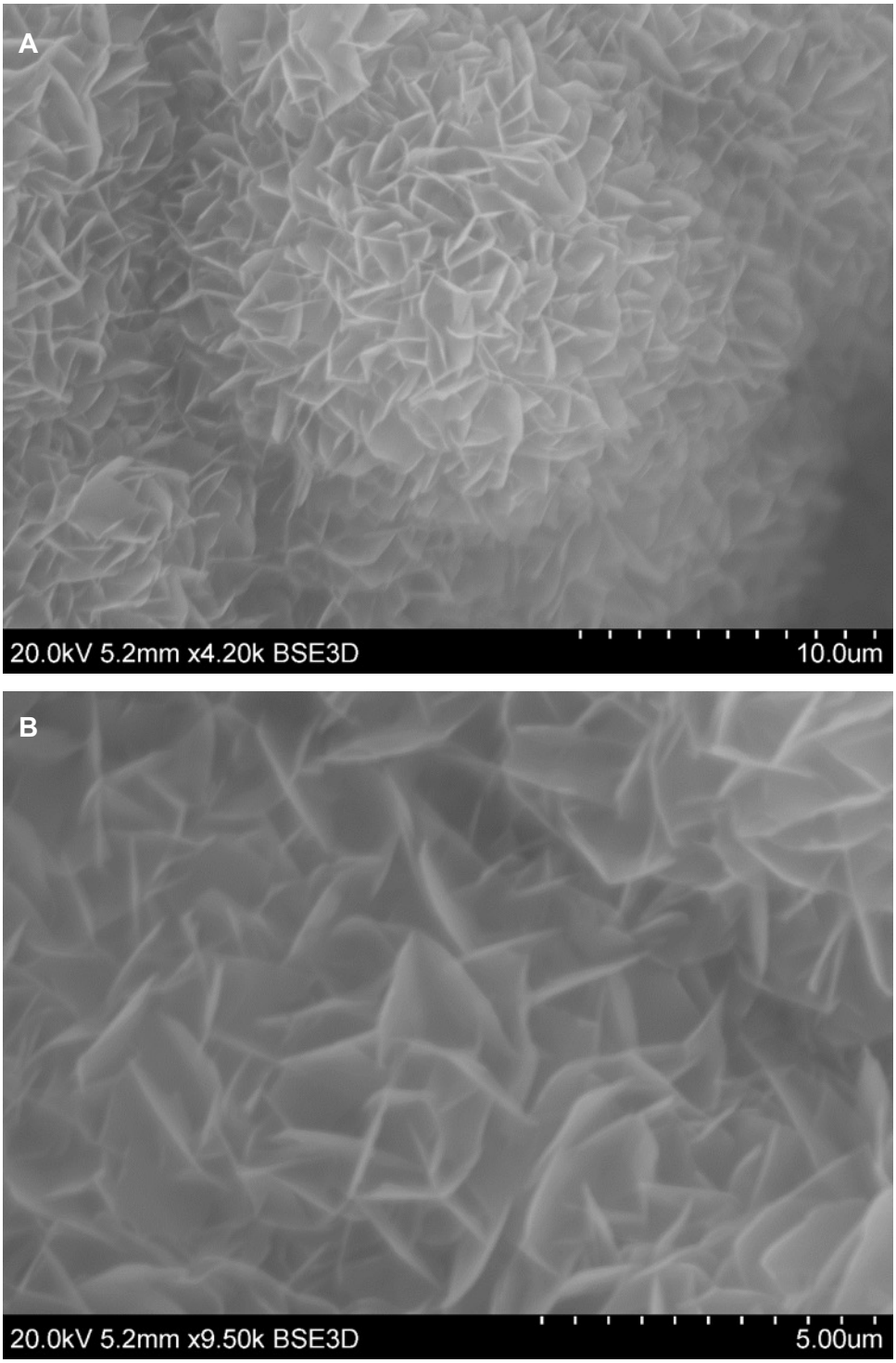

Figure 3.21: A: Higher magnification SEM image (4200x) of crystalline structure on 48.34% crystalline HA surface after 6h incubation in DMEM + 10% FBS at 37°C. B: Higher magnification image (9500x) of 48.34% crystalline HA surface after 6h incubation in DMEM + 10% FBS at 37°C.

Table 3.12: Atomic percentages of calcium and phosphorus before and after 6h incubation in DMEM + 10% FBS at 37°C.

	Untreated			**6h**		
Relative crystallinity	Ca (at%)	P (at%)	Ca/P (at%)	Ca (at%)	P (at%)	Ca/P (at%)
48.34%	19.85	10.94	1.81	18.87	12.01	1.57
61.11%	22.53	11.97	1.88	22.7	12.33	1.84
67.34%	20.29	10.99	1.85	19.95	12.47	1.60
82.77%	22.81	12.12	1.88	23.26	12.62	1.84
91.15%	22.69	12.44	1.82	22.85	12.78	1.79
96.7%	21.55	11.51	1.87	23.68	13.17	1.80
108.4%	21.69	12.07	1.80	23.13	12.79	1.81

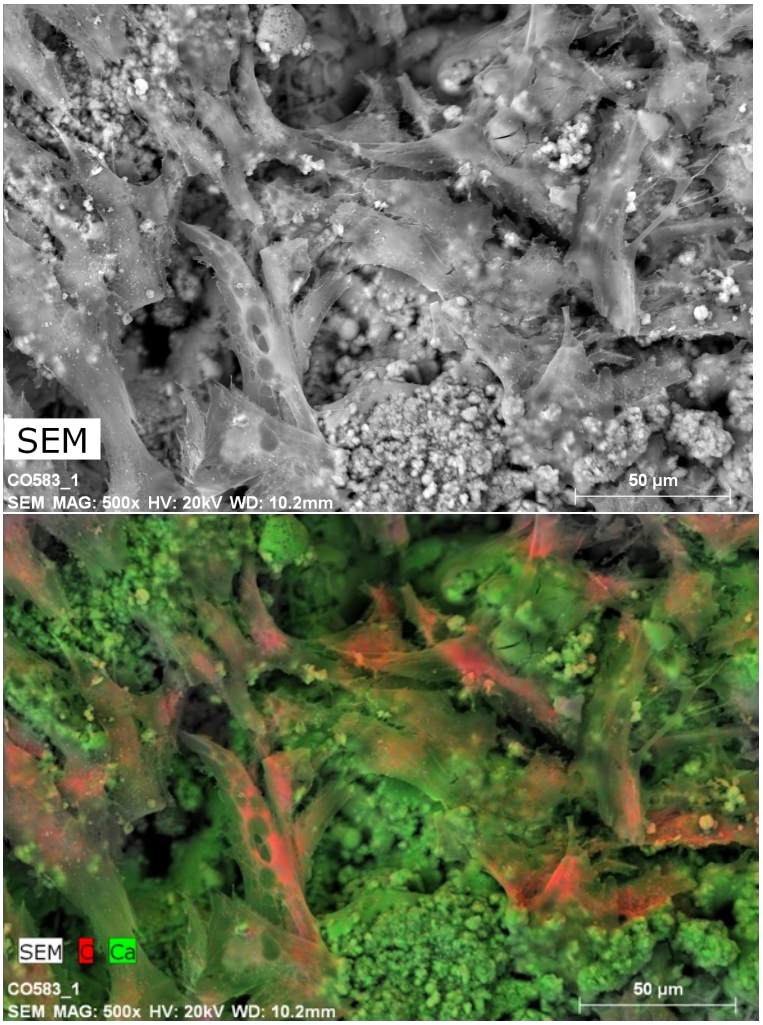

Figure 3.22: Analysis of interaction of MSCs with HA-coated titanium surfaces. SEM (above) and EDS-SEM (below) for Y201 MSCs seeded onto a representative HA-sprayed coupon (82.77% relative crystallinity). Using EDS, green labelling identifies the calcium component of the HA and red labels cellular carbon.

With coupon sample preparation and handling, as well as MSC culture on the discs optimised, Y201 MSCs were used to study the effects of varying HA surfaces on Wnt signalling.

3.3.4 Wnt response to differently crystalline and rough HA coatings

Wnt signalling is a significant pathway in MSC proliferation and osteogenic response[241–244], and has been implicated in MSC response to topographical cues in relation to osteogenic response[239,245–248]. MSC response to Wnt3a, a canonical Wnt ligand, was tested on coupons 1-17. Wnt response was measured using an in-house MSC Wnt-reporter line. There was a fold-increased response in treated MSCs seeded onto HA-coated coupons as compared to tissue culture plastic on surfaces 1-3 and 9-13. In the absence of ligand, baseline Wnt activity was dampened on surfaces 5, 6, 8, and 14, whereas surfaces 9 and 11 exhibited an increase in Wnt activity. All other surfaces were not significantly different (Figure 3.23).

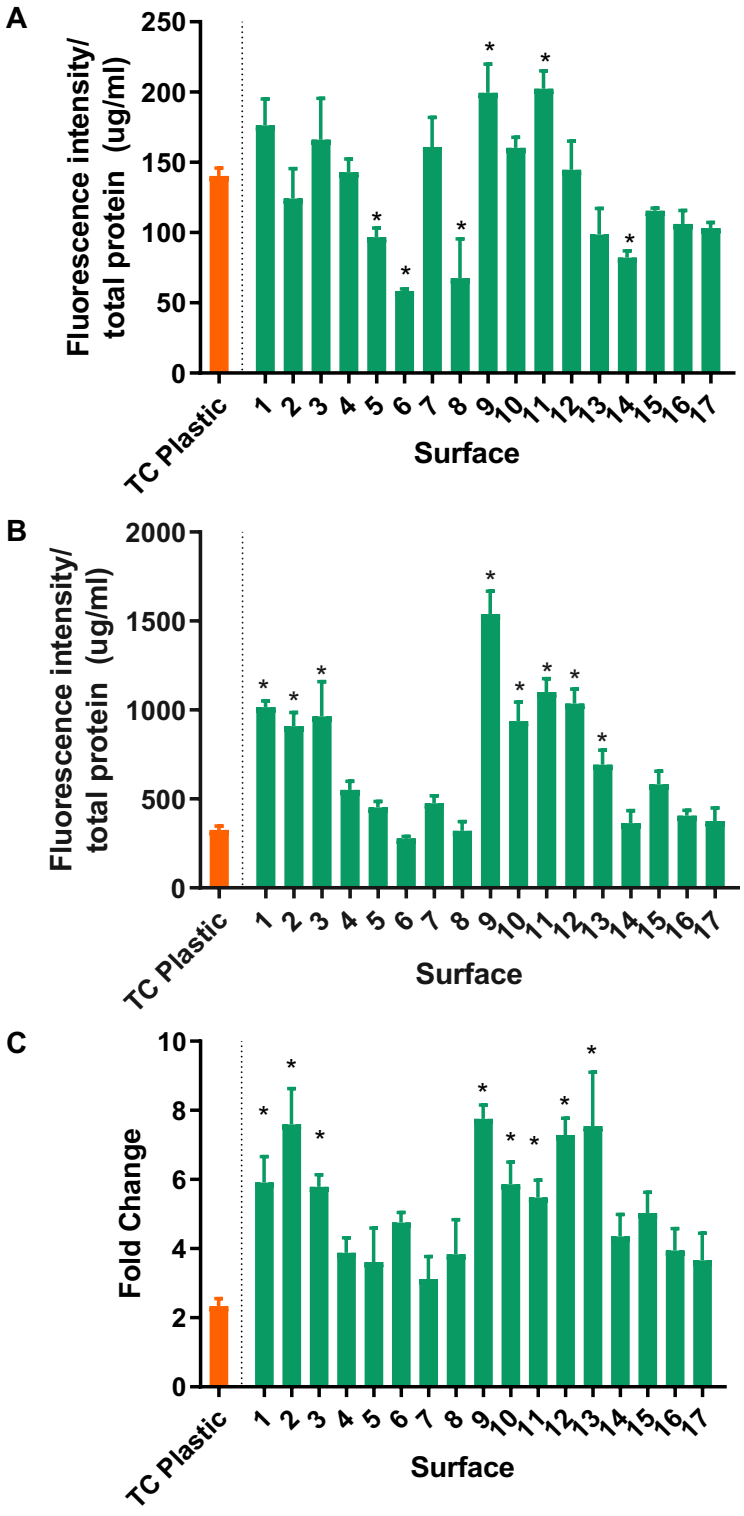

.

Figure 3.23: A: Wnt activity as measured by EGFP fluorescence normalised to total protein in the absence of Wnt3a. B: Wnt activity in response to exogenous Wnt3a (300ng/ml). C: Fold change in EGFP fluorescence in response to Wnt3a. Surfaces 1-3 and 9-13 showed statistically significant increases in Wnt-mediated fluorescence fold change as compared to tissue culture plastic. Experiment was carried out 3 times, each with n = 3, ±SEM; ANOVA.

Stepwise backward elimination of terms analysis was used to determine which factors in the plasma spraying process made a significant difference to both endogenous Wnt signalling in untreated Y201 MSCs and Y201 MSC response to exogenous Wnt3a in order to cross-reference the factors that influence Wnt signalling with those that influence material properties.

3.3.4.1 *Backward elimination of terms – endogenous Wnt signalling on HA surfaces*

Stepwise backward elimination of terms analysis identified the strongest factor in endogenous Wnt signalling to be the interaction between factor B and factor E ($p = 0.020$), with all other main effects being identified as significant as the centre point was determined to have a significant impact on the model, suggesting very strong curvature (centre point $p = 0.003$). Due to the non-linear nature of the response and the strong impact of the centre point, the model has a relatively poor fit ($R^2 = 33.37\%$) The analysis required 10 steps to complete the model with sufficient significance (Table 3.13).

A regression equation was generated for the prediction of endogenous Wnt response to changes in plasma spray parameter input settings (Equation 12).

Equation 12: Regression equation for the prediction of endogenous Y201 Wnt response to changes in plasma spray parameter input settings.

$$\text{Endogenous Y201 Wnt response} = 30853 - 1952\,A + 1421\,B + 222\,C + 1812\,D - 1166\,E + 3745\,B{*}E + 20138\,Ct\,Pt$$

Table 3.13: Stepwise backward elimination of terms analysis of general factorial DoE for endogenous Y201 MSC Wnt response to differently coated HA surfaces. 10 steps of elimination were carried out to obtain a sufficiently powerful model. The main effector was identified to be the interaction between B and E. R^2 = 31.93%

	----Step 1----		----Step 2----		----Step 3----		----Step 4----		----Step 5----		----Step 6----		----Step 7----		----Step 8----		----Step 9----		----Step 10---	
	Coef	**P**	**Coef**	**P**	**Coef**	**P**	**Coef**	**P**	**Coef**	**P**	**Coef**	**P**	**Coef**	**P**	**Coef**	**P**	**Coef**	**P**	**Coef**	**P**
Constant	30853		30853		30853		30853		30853		30853		30853		30853		30853		30853	
A	-1952	0.246	-1952	0.239	-1952	0.233	-1952	0.227	-1952	0.223	-1952	0.22	-1952	0.218	-1952	0.216	-1952	0.215	-1952	0.214
B	1421	0.397	1421	0.39	1421	0.383	1421	0.377	1421	0.373	1421	0.37	1421	0.367	1421	0.366	1421	0.365	1421	0.364
C	222	0.894	222	0.892	222	0.891	222	0.889	222	0.889	222	0.888	222	0.887	222	0.887	222	0.887	222	0.887
D	1812	0.281	1812	0.274	1812	0.267	1812	0.261	1812	0.257	1812	0.254	1812	0.252	1812	0.25	1812	0.249	1812	0.248
E	-1166	0.486	-1166	0.479	-1166	0.473	-1166	0.467	-1166	0.464	-1166	0.461	-1166	0.459	-1166	0.457	-1166	0.456	-1166	0.456
A*B	1264	0.45	1264	0.443	1264	0.437	1264	0.431	1264	0.427	1264	0.424								
A*C	-147	0.93																		
A*D	224	0.893	224	0.891																
A*E	1474	0.379	1474	0.372	1474	0.366	1474	0.359	1474	0.355	1474	0.352	1474	0.35	1474	0.348	1474	0.347		
B*C	1430	0.394	1430	0.387	1430	0.38	1430	0.374	1430	0.37	1430	0.367	1430	0.364	1430	0.363				
B*D	314	0.851	314	0.848	314	0.846														
B*E	3745	0.03	3745	0.028	3745	0.026	3745	0.024	3745	0.023	3745	0.022	3745	0.021	3745	0.02	3745	0.02	3745	0.02
C*D	-1338	0.424	-1338	0.418	-1338	0.411	-1338	0.405	-1338	0.401	-1338	0.398	-1338	0.396						
C*E	1031	0.537	1031	0.531	1031	0.526	1031	0.52												
D*E	-1111	0.506	-1111	0.5	-1111	0.494	-1111	0.488	-1111	0.485										
Ct Pt	20138	0.006	20138	0.005	20138	0.004	20138	0.004	20138	0.004	20138	0.003	20138	0.003	20138	0.003	20138	0.003	20138	0.003

R^2	Eliminations:	1st	2nd	3rd	4th	5th	6th	7th	8th	9th
31.93%										

3.3.4.2 *Main effects and interactions – endogenous Wnt signalling on HA surfaces*

Endogenous Wnt signalling was determined to be mostly affected by factor B and factor E, with some main effects determined to have significant effect (Figure 3.24). The fit of the model is relatively low (R^2 = 31.93%), meaning that while main effectors may be accurate, prediction will be inaccurate.

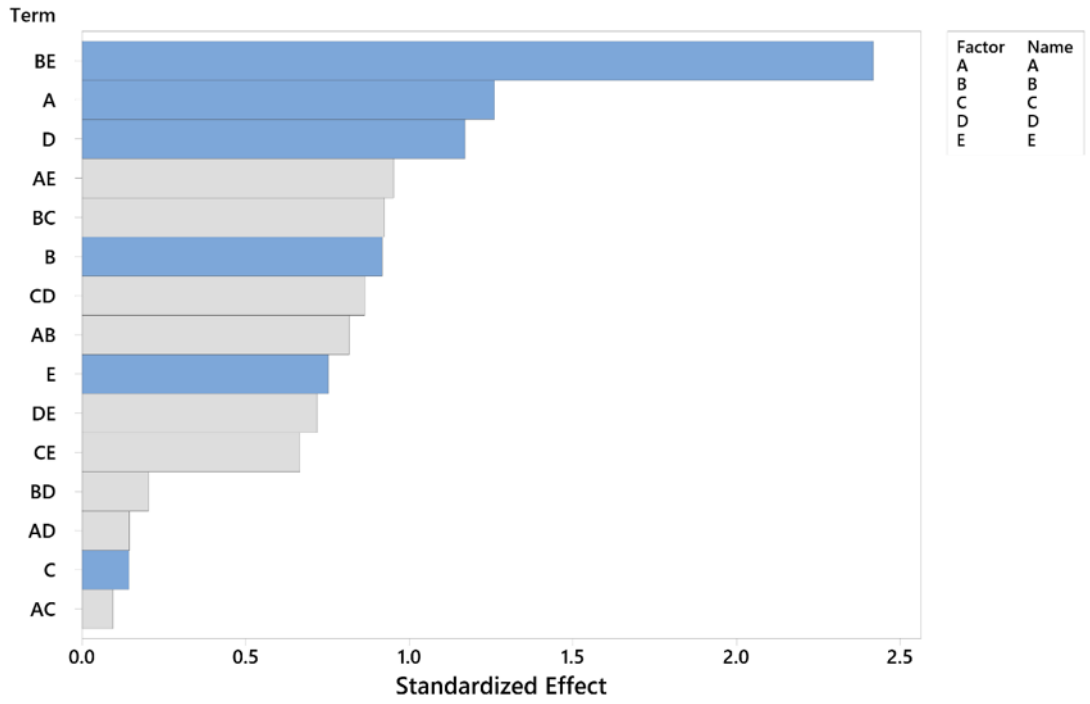

Figure 3.24: Main effects pareto chart depicting magnitude of standardized effect of plasma sprayer input parameters on endogenous Wnt signalling in Y201 MSCs as measured by EGFP activity. The main effect was shown to come from an interaction between B and E. Blue bars indicate significant effect, while grey bars indicate an insignificant effect and were therefore excluded from the model. p<0.15.

The most significant main effect determined to have significant impact on endogenous Wnt signalling was factor A, where an increase in factor A decreased EGFP signal. The centre point was very far away from any main effect, which can be interpreted as either the low and high levels of the DoE being too far apart, or higher level interactions having a significant effect (Appendix 43). One significant interaction was identified (factor B and factor E), where at a low factor E, increasing factor B would decrease EGFP signal, whilst at a high factor E the EGFP signal increased (Appendix 44 - Appendix 45). Again, due to the lack of fit in the model, the magnitude of this effect is difficult to determine from these data.

The same analysis was run on Wnt-mediated EGFP signal in Wnt3a-treated cells in response to varying plasma sprayer input parameter settings.

3.3.4.4 *Backward elimination of terms – response to Wnt3a on HA surfaces*

Stepwise backward elimination of terms analysis identified the main effectors as being factor C ($p = 0.001$), and factor D ($p = 0.010$), with interactions also statistically significantly involved ($p = 0.061$). 9 steps of elimination were required to achieve the significance required. The fit in this case was relatively low ($R^2 = 41.81\%$) (Table 3.14). A regression equation was generated for the prediction of Y201 response to Wnt3a on HA surfaces (Equation 13).

Equation 13: Regression equation for the prediction of changes in Y201 reporter activity response to Wnt3a in response to changing plasma sprayer input parameter settings.

$$\begin{aligned}\text{Exogenous Y201 Wnt response} = {} & 145443 - 3233\,A + 5418\,B - 22437\,C + 16333\,D + 1078\,E - 8905\,A{*}E \\ & + 10402\,B{*}C + 10149\,C{*}E\end{aligned}$$

Table 3.14: Stepwise backward elimination of terms analysis of general factorial DoE for exogenous Y201 MSC Wnt response to differently coated HA surfaces in the presence of 300 ng/ml Wnt3a. 9 steps of elimination were carried out to obtain a sufficiently powerful model. The main effector was identified to be the interaction between B and E. R^2 = 41.81%.

	-----Step 1----		-----Step 2----		-----Step 3----		-----Step 4----		-----Step 5----		-----Step 6----		-----Step 7----		-----Step 8----		-----Step 9----	
	Coef	**P**	**Coef**	**P**	**Coef**	**P**	**Coef**	**P**	**Coef**	**P**	**Coef**	**P**	**Coef**	**P**	**Coef**	**P**	**Coef**	**P**
Constant	147231		147231		147231		147231		147231		147231		147231		145443		145443	
A	-3233	0.603	-3233	0.598	-3233	0.593	-3233	0.589	-3233	0.586	-3233	0.587	-3233	0.589	-3233	0.591	-3233	0.595
B	5418	0.385	5418	0.378	5418	0.372	5418	0.366	5418	0.363	5418	0.365	5418	0.367	5418	0.37	5418	0.375
C	-22437	0.001	-22437	0.001	-22437	0.001	-22437	0.001	-22437	0	-22437	0	-22437	0.001	-22437	0.001	-22437	0.001
D	16333	0.012	16333	0.011	16333	0.01	16333	0.009	16333	0.009	16333	0.009	16333	0.009	16333	0.009	16333	0.01
E	1078	0.862	1078	0.86	1078	0.858	1078	0.857	1078	0.856	1078	0.856	1078	0.857	1078	0.858	1078	0.859
A*B	1181	0.849	1181	0.847														
A*C	2781	0.655	2781	0.65	2781	0.645												
A*D	-6543	0.296	-6543	0.289	-6543	0.282	-6543	0.277	-6543	0.274								
A*E	-8905	0.157	-8905	0.151	-8905	0.146	-8905	0.141	-8905	0.139	-8905	0.14	-8905	0.141	-8905	0.144	-8905	0.148
B*C	10402	0.1	10402	0.096	10402	0.091	10402	0.087	10402	0.085	10402	0.086	10402	0.087	10402	0.089	10402	0.093
B*D	4335	0.486	4335	0.48	4335	0.474	4335	0.469										
B*E	-8416	0.181	-8416	0.174	-8416	0.169	-8416	0.164	-8416	0.161	-8416	0.162	-8416	0.164	-8416	0.166		
C*D	-106	0.986																
C*E	10149	0.109	10149	0.104	10149	0.099	10149	0.095	10149	0.093	10149	0.094	10149	0.095	10149	0.097	10149	0.1
D*E	6894	0.271	6894	0.264	6894	0.257	6894	0.252	6894	0.249	6894	0.25						
Ct Pt	-30396	0.24	-30396	0.233	-30396	0.226	-30396	0.221	-30396	0.218	-30396	0.219	-30396	0.221				

R^2									
41.81%	Eliminations:	1st	2nd	3rd	4th	5th	6th	7th	8th

3.3.4.5 *Main effects and interactions – response to Wnt3a on HA surfaces*

Wnt signalling in response to 300 ng/ml Wnt3a was tested on each surface in order to determine whether Y201 MSCs seeded onto plasma sprayed surfaces were sensitised to the presence of Wnt ligand, and what plasma spray parameter could affect Wnt responsiveness.

The main effect was determined to be from factor C, with factor D also appearing to have an effect (Figure 3.25). The fit of this model is similarly low to that of the endogenous signalling model (R^2 = 41.81%), which also means that these data will not allow for accurate prediction of Wnt signalling in response to canonical Wnt ligand Wnt3a.

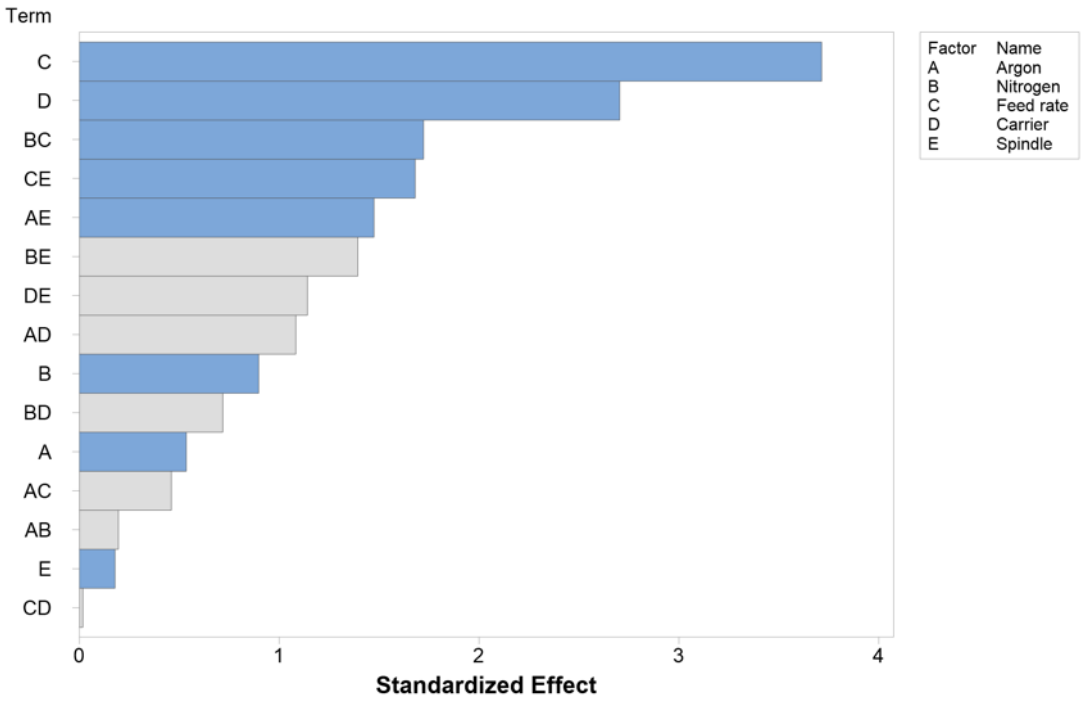

Figure 3.25: Main effects pareto chart depicting magnitude of standardized effect of plasma sprayer input parameters on Wnt signalling response to 300 ng/ml Wnt3a in Y201 MSCs as measured by EGFP activity. The main effect was shown to come from C. Blue bars indicate significant effect, while grey bars indicate an insignificant effect and were therefore excluded from the model. p<0.15.

The effect of factor C was determined to be negative, where an increasing factor C decreased EGFP activity (Appendix 46). 3 interactions were determined to be significant: Factor A*Factor E, Factor B*Factor C, and Factor C*Factor E (Appendix 47 - Appendix 48). The most significant of these, Factor B*Factor C, was such that at a low factor C, the signal marginally decreased with factor B increase, whereas at a high factor C, an increase in factor B would increase signal, although the starting point at low factor B was significantly lower than low factor B and low factor C. This suggests

higher level interactions for which this DoE design was not sufficient and would have required a larger set of combinations.

3.3.6 Proliferation on differently plasma sprayed HA coatings

It was hypothesised that changes in Wnt signalling in MSCs grown on different surfaces was mediating MSC proliferation, as is suggested in the literature[242,243,247,249]. Therefore, a canonical Wnt pathway inhibitor, XAV939, was used to inhibit Wnt signalling in order to elucidate whether there was Wnt involvement in MSC proliferative behaviour in response to different HA surfaces. Proliferation was quantified using change in DNA concentration over time as a proxy for cell number change over time by Quant-iT PicoGreen dsDNA quantitation kit.

It was observed that MSC proliferation was indeed affected by different surfaces, but it was not consistently affected across different surfaces. In control conditions, without XAV939 treatment, surfaces 8 (p=0.0437) and 9 (p = 0.0469) appeared to enhance fluorescent fold change compared to tissue culture plastic, whereas no significant effect was observed on other surfaces. Of the surfaces enhancing proliferation XAV939 treatment significantly decreased fluorescent fold change. Surfaces 6, 7, 13, and 16 appeared to affect Y201 MSC response to XAV939 treatment, where a decrease in fluorescent fold change was observed in surfaces 7 and 16, whereas an increase in fold change was seen in surfaces 6 and 13 (Figure 3.26).

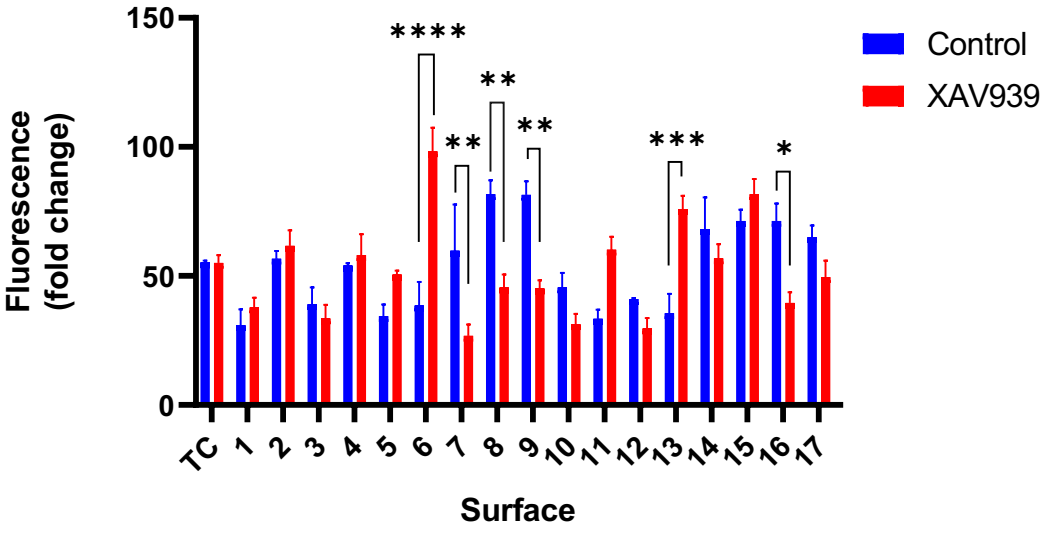

*Figure 3.26: Fold change in fluorescent signal 3 days post-treatment in Y201 MSCs as measured by Quant-iT PicoGreen assay. Y201 MSCs were seeded onto surfaces 1-17 and tissue culture plastic (TC) and allowed to settle for 24 hours. Cells were lysed at days 0 and 3 and fold change in fluorescence was calculated. *: p<0.05; **: p<0.01; ***: p<0.005; ****: p<0.0001. Experiment was carried out 3 times, each with n = 3; ±SEM; ANOVA.*

Backward elimination of terms analysis was performed on the data acquired from both the control conditions and XAV939 treated Y201 MSCs in order to determine the effect of plasma sprayer effects on Y201 MSC proliferation.

3.3.6.1 *Backward elimination of terms – Proliferation of Y201 MSCs*

A stepwise backward elimination of terms analysis was performed on the DoE in order to determine the main and combined effects of plasma spray input parameter settings on proliferation of Y201 MSCs under control conditions.

Table 3.15: Stepwise backward elimination of terms analysis of general factorial DoE for Y201 MSC proliferation response to differently coated HA surfaces. 1 step was required to obtain a sufficiently powerful model. The main effector was identified to be the interaction between B and C. R^2 = 98.35%.

	----Step 1----	
	Coef	**P**
Constant	52.70	
A	4.45	0.016
B	3.78	0.028
C	4.91	0.012
D	3.30	0.042
E	-6.53	0.004
A*C	2.88	0.062
A*D	-3.91	0.025
B*C	9.66	0.001
B*D	-5.47	0.008
B*E	4.72	0.013
D*E	-2.98	0.056
Ct Pt	12.32	0.056

R^2
98.35%

A regression equation was generated for the prediction of Y201 MSC proliferative behaviour on differently coated surfaces in response to changes in plasma sprayer parameter settings (Equation 14).

Equation 14: Regression equation for the prediction of Y201 MSC proliferation response to changes in plasma sprayer parameter settings.

$$\text{Y201 proliferation} = 52.70 + 4.45\,A + 3.78\,B + 4.91\,C + 3.30\,D - 6.53\,E + 2.88\,A{*}C - 3.91\,A{*}D + 9.66\,B{*}C - 5.47\,B{*}D + 4.72\,B{*}E - 2.98\,D{*}E + 12.32\,Ct\,Pt$$

3.3.6.2 *Main effects and interactions – Proliferation of Y201 MSCs*

The most pronounced effect was determined to be conveyed by a factor B and factor C interaction (p = 0.001), with the largest main effect being from factor E (p = 0.004) (Figure 3.27).

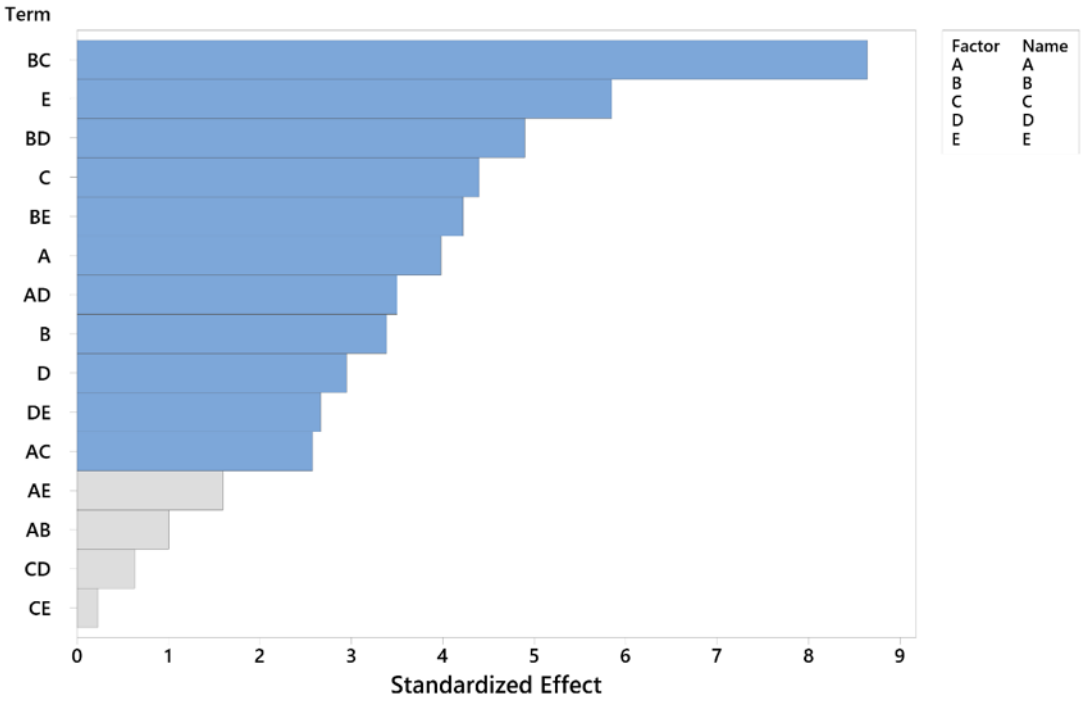

Figure 3.27: Main effects pareto chart depicting magnitude of standardized effect of plasma sprayer input parameters on Y201 proliferation measured using PicoGreen 3 days post-seeding. The main effect was shown to come from an interaction between B and C. Blue bars indicate significant effect, while grey bars indicate an insignificant effect and were therefore excluded from the model. p<0.15.

The main effect from factor E was such that an increase in factor E caused a decrease in proliferation of Y201 MSCs. The position of the centre point suggested curvature in the response (Appendix 49).

Significant interactions were determined to be Factor A*Factor C ($p = 0.062$), Factor A*Factor D ($p = 0.025$), Factor B*Factor C ($p = 0.001$), Factor B*Factor D ($p = 0.008$), Factor B*Factor E ($p = 0.013$), Factor D*Factor E ($p = 0.056$). The most significant of these, Factor B*Factor C, showed that a high factor D resulted in higher proliferation at low levels of factor B, similar to levels at high factor B and factor D (Appendix 50 - Appendix 51).

3.3.6.3 *Backward elimination of terms – Proliferation of XAV939 treated Y201 MSCs*

Stepwise backward elimination of terms analysis was carried out in order to determine the main effectors in Y201 MSC response to differently sprayed surfaces with XAV939 treatment, and a regression equation generated for the prediction of Y201 MSC proliferative behaviour on differently sprayed surfaces in the presence of XAV939 (Table 3.16; Equation 15)

Table 3.16: Stepwise backward elimination of terms analysis of general factorial DoE for Y201 MSC proliferation response to differently coated HA surfaces with XAV939 treatment. 1 step was required to obtain a sufficiently powerful model. The main effector was identified to be the interaction between A and Ds. R^2 = 98.54%.

	-----Step 1----	
	Coef	**P**
Constant	51.92	
A	0.59	0.646
B	-5.15	0.012
C	7.36	0.003
D	0.50	0.697
E	1.46	0.286
A*B	-4.27	0.023
A*D	-13.79	0.000
A*E	2.74	0.082
B*C	-5.83	0.008
B*D	5.39	0.010
C*D	3.60	0.038
D*E	-2.26	0.129

R^2
98.54%

Equation 15: Regression equation for the prediction of Y201 proliferation response to changing HA plasma sprayer input parameter settings in the presence of XAV939.

Y201 Proliferation with XAV939 = 51.92 + 0.59 A - 5.15 B + 7.36 C + 0.50 D + 1.46 E - 4.27 A*B - 13.79 A*D + 2.74 A*E - 5.83 B*C + 5.39 B*D + 3.60 C*D - 2.26 D*E

3.3.6.4 *Main effects and interactions – Proliferation of XAV939 treated Y201 MSCs*

A factor A and factor D interaction was identified and determined to be the most impactful (p = 0.000). The most pronounced main effect was from factor C (p = 0.003) (Figure 3.28).

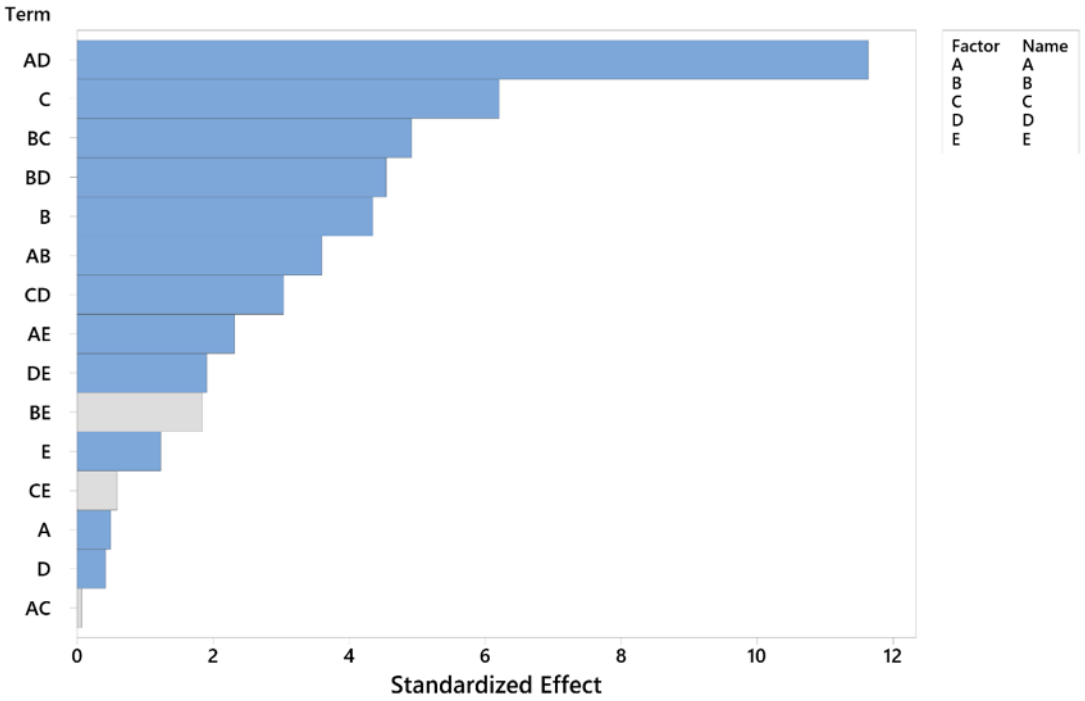

Figure 3.28: Main effects pareto chart depicting magnitude of standardized effect of plasma sprayer input parameters on Y201 MSC proliferation with XAV939 treatment 3 days post seeding, measured using PicoGreen 3 days post-seeding. The main effect was shown to come from an interaction between B and E. Blue bars indicate significant effect, while grey bars indicate an insignificant effect and were therefore excluded from the model. p<0.15.

The main effect from factor C was an increase in fold change in fluorescence with increasing factor C. Factor B also had a significant main effect ($p = 0.012$), where an increase in factor B resulted in a decrease in proliferation (Appendix 52).

Significant interactions were identified as being the Factor A*Factor B ($p = 0.023$), Factor A*Factor D ($p =0.000$), Factor A*Factor E ($p = 0.082$), Factor B*Factor C ($p = 0.008$), Factor B*Factor D ($p = 0.010$), Factor C*Factor D ($p = 0.038$), and Factor D*Factor E ($p = 0.129$) interactions. The most significant interaction was between factor A and factor D, where a low factor D resulted in a 1.5-fold increase in fluorescent signal with increasing factor A, whereas a 1.5-fold decrease was observed at a high factor D with increasing factor A. At low factor D and low factor A, the level of fluorescent signal fold change was similar to the level at high factor D and high factor A (Appendix 53 - Appendix 54).

3.3.7 Osteogenic differentiation on differently sprayed HA surfaces

Osteogenic differentiation was measured by alkaline phosphatase (ALP) activity in order to assess the effect of changing plasma sprayer input parameter settings on Y201 MSC differentiation. The fold change in ALP activity from day 0 to day 9 was used in all DoE analyses as a measure of osteogenic differentiation capacity.

With basal medium, no ALP activity was observed on tissue culture plastic, while there was significant increase in ALP activity over 9 days on several HA surfaces. The most significant ALP increases in basal conditions occurred on surfaces 6, 7, 8, 14 and 16, while no significant increase was seen in tissue culture plastic and surfaces 4, 9, 10, 12, 15 and 17. With the addition of osteogenic supplements, every surface exhibited significantly increased ALP activity at day 9 (Figure 3.29).

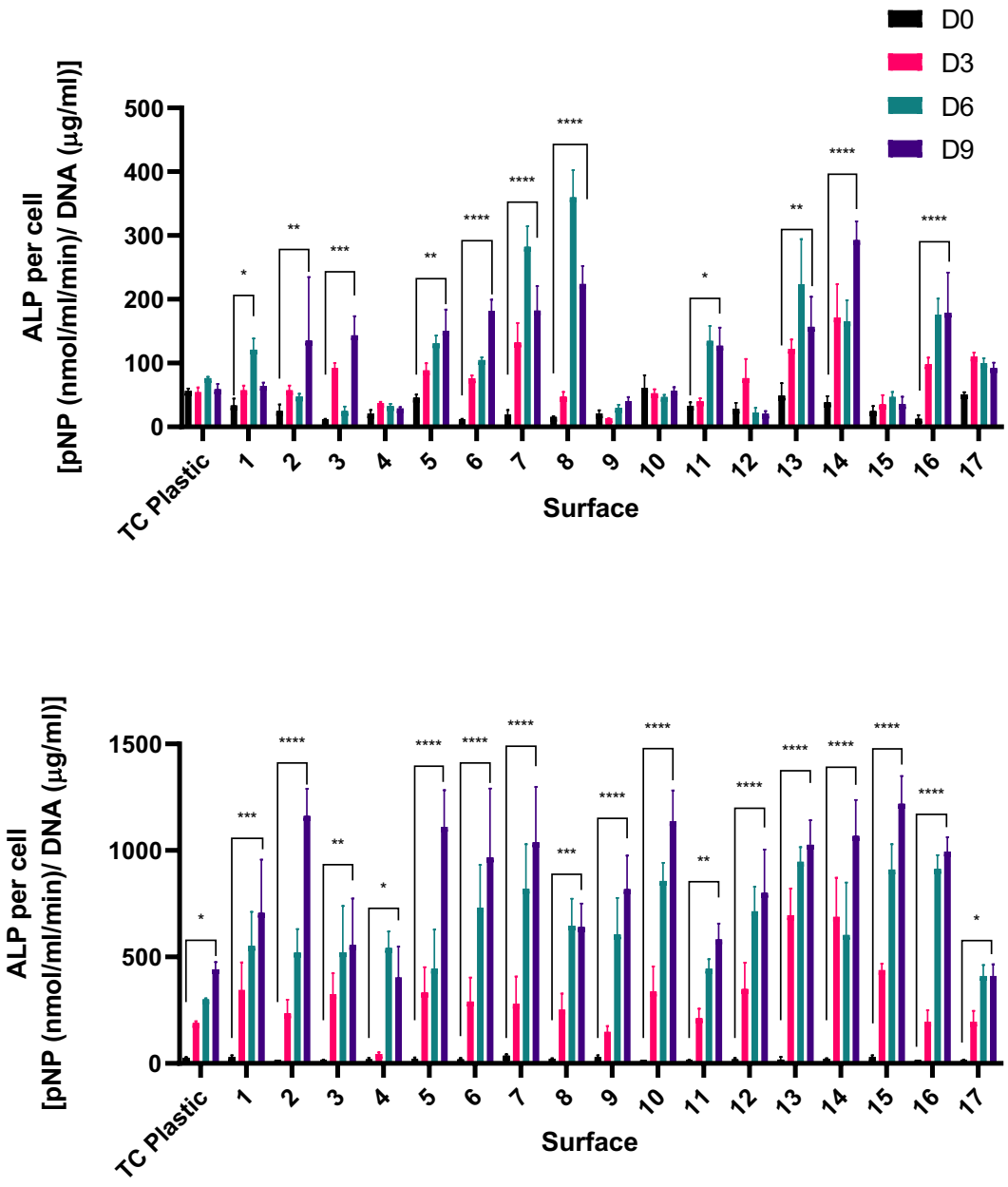

*Figure 3.29: ALP activity in basal (above) and osteogenic (below) conditions on differently sprayed HA surfaces. ALP activity was normalised to cell number and measured at 0, 3, 6, and 9 days. Experiment was carried out 3 times, each with n = 6. *: p<0.05; **: p<0.005; ***: p<0.0005; ****: p<0.0001; ±SEM; ANOVA.*

3.3.7.2 *Backward elimination of terms – osteogenesis under basal conditions*

These data were analysed in order to define the effect of each plasma sprayer input parameter on Y201 MSC osteogenic differentiation. Stepwise backward elimination of terms analysis determined the most significant factor in osteogenic response under basal culture conditions to be an interaction between factor A and factor C ($p = 0.008$), with the strongest main effect being from factor C ($p = 0.009$) (Table 3.17). 5 steps were required to complete the analysis. A regression equation was generated for the prediction of osteogenic activity under basal culture conditions in response to changes in plasma spray parameter settings (Equation 16).

Table 3.17: Stepwise backward elimination of terms analysis of general factorial DoE for Y201 MSC osteogenic response to differently coated HA surfaces under basal culture conditions. 5 steps were required to obtain a sufficiently powerful model. The main effector was identified to be the interaction between A and C. R^2 = 86.19%.

	-----Step 1----		-----Step 2----		-----Step 3----		-----Step 4----		----Step 5----	
	Coef	**P**	**Coef**	**P**	**Coef**	**P**	**Coef**	**P**	**Coef**	**P**
Constant	8.051		8.051		8.051		8.051		7.69	
A	2.569	0.03	2.569	0.033	2.569	0.035	2.569	0.036	2.57	0.043
B	1.885	0.073	1.885	0.085	1.885	0.093	1.885	0.099	1.89	0.116
C	3.667	0.009	3.667	0.009	3.667	0.008	3.667	0.008	3.67	0.009
D	-1.023	0.261	-1.023	0.298	-1.023	0.321	-1.023	0.337	-1.02	0.367
E	1.275	0.178	1.275	0.208	1.275	0.227	1.275	0.24	1.27	0.267
A*C	3.783	0.008	3.783	0.008	3.783	0.007	3.783	0.007	3.78	0.008
A*D	1.199	0.2								
B*C	1.232	0.19	1.232	0.221	1.232	0.24				
C*D	1.22	0.194	1.22	0.225						
C*E	3.326	0.013	3.326	0.013	3.326	0.013	3.326	0.012	3.33	0.014
D*E	2.33	0.041	2.33	0.046	2.33	0.049	2.33	0.051	2.33	0.061
Ct Pt	-6.2	0.127	-6.2	0.149	-6.2	0.163	-6.2	0.174		

R^2					
86.19%	Eliminations:	1st	2nd	3rd	4th

Equation 16: Regression equation for the prediction of osteogenic activity in Y201 MSCs under basal culture conditions in response to changes in plasma sprayer parameter settings.

ALP Activity under basal conditions = 7.69 + 2.57 A + 1.89 B + 3.67 C - 1.02 D + 1.27 E + 3.78 A*C + 3.33 C*E + 2.33 D*E

3.3.7.3 *Main effects and interactions – osteogenesis under basal conditions*

The most pronounced effects on ALP activity under basal culture conditions were due to the factor A*factor C interaction (p = 0.008), factor C (p = 0.009), and a factor C*factor E interaction (p = 0.014). Factor C (p = 0.009) and factor A (p = 0.03) were the most significant main effects (Table 3.17; Figure 3.30). For the main effects, an increase in factor C or factor A increased osteogenic response from Y201 MSCs (Appendix 55).

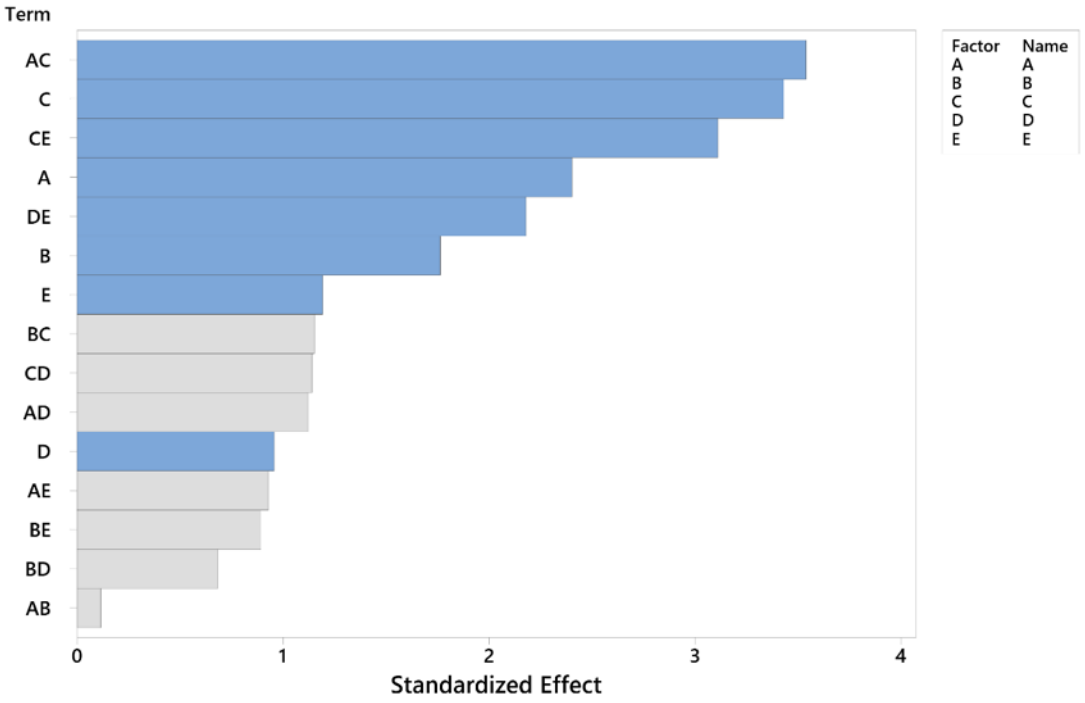

Figure 3.30: Main effects pareto chart depicting magnitude of standardized effect of plasma sprayer input parameters on osteogenic response in Y201 MSCs under basal culture conditions as measured by ALP activity. The main effect was shown to come from an interaction between A and C. Blue bars indicate significant effect, while grey bars indicate an insignificant effect and were therefore excluded from the model. p<0.15.

The factor A*factor C interaction was such that at a low factor C, a marginal decrease in ALP activity was observed with increasing factor A, whereas at a high factor C, a substantial increase in ALP activity was observed with increasing factor A. The factor C*factor E interaction showed a similar trend, while the factor D*factor E interaction is characterised by decreasing ALP activity with increasing factor D at low factor E, and a marginal increase in ALP activity at high factor Es (Appendix 56 - Appendix 57).

3.3.7.5 *Backward elimination of terms – osteogenesis with the addition of osteogenic supplements*

In order to understand how plasma sprayer input parameter settings influence Y201 MSC response to addition of osteogenic supplements to culture medium, stepwise backward elimination of terms analysis was carried out. It was determined that the most significant factors in osteogenic response to plasma spray parameter setting changes under osteogenic conditions are interactions between factor A and factor C ($p = 0.002$) and factor D and factor E ($p = 0.002$). The most significant main effects were from factor B ($p = 0.005$) and factor D ($p = 0.007$) (Table 3.18). A regression equation for the prediction of osteogenic response to plasma spray parameter setting changes with osteogenic supplements was generated (Equation 17).

Table 3.18: Stepwise backward elimination of terms analysis of general factorial DoE for Y201 MSC osteogenic response to differently coated HA surfaces under osteogenic culture conditions. 1 step was required to obtain a sufficiently powerful model. The main effector was identified to be the interaction between A and C. R^2 = 96.33%.

	-----Step 1----	
	Coef	**P**
Constant	50.72	
A	2.12	0.300
B	-10.07	0.005
C	6.89	0.018
D	8.91	0.007
E	2.88	0.181
A*C	-12.12	0.002
B*C	-5.31	0.041
B*E	-3.47	0.123
C*D	3.68	0.108
C*E	7.77	0.012
D*E	12.11	0.002
Ct Pt	-23.28	0.034

R^2
96.33

Equation 17: Regression equation for the prediction of Y201 MSC osteogenic response to changing HA plasma sprayer parameter settings under osteogenic culture conditions.

ALP Activity with osteogenic supplements = 50.72 + 2.12 A - 10.07 B + 6.89 C + 8.91 D + 2.88 E - 12.12 A*C - 5.31 B*C - 3.47 B*E + 3.68 C*D + 7.77 C*E + 12.11 D*E - 23.28 Ct Pt

3.3.7.7 *Main effects and interactions – osteogenesis with the addition of osteogenic supplements*

The factors with the most pronounced effect on osteogenic response with osteogenic supplements were found to be interactions between factor A and factor C (p = 0.002) and factor D and factor E (p = 0.002). The most pronounced main effects were factor B (p = 0.005) and factor D (p = 0.007).

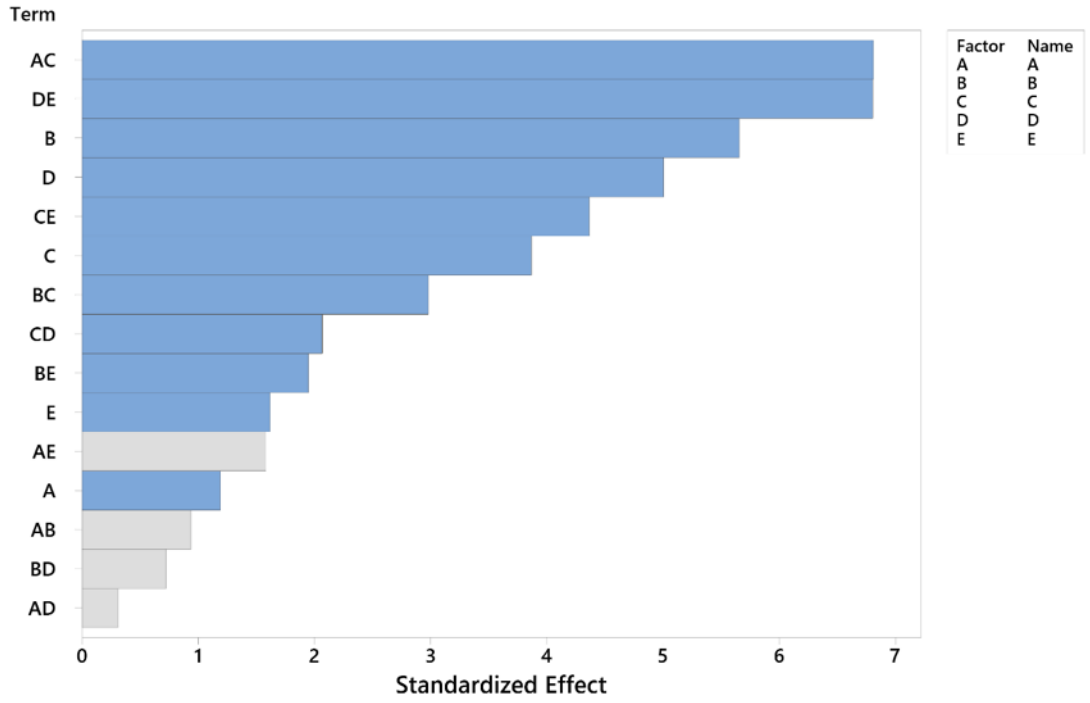

Figure 3.31: Main effects pareto chart depicting magnitude of standardized effect of plasma sprayer input parameters on osteogenic response in Y201 MSCs under osteogenic culture conditions as measured by ALP activity. The main effect was shown to come from an interaction between A and C. Blue bars indicate significant effect, while grey bars indicate an insignificant effect and were therefore excluded from the model. p<0.15.

Increasing factor B resulted in decreased ALP activity, whereas increasing factor D resulted in increased ALP activity. The centre point suggests a non-linear response in ALP activity (Appendix 58).

Several significant interactions were identified. The factor A*factor C, factor B*factor C, and factor B*factor E interactions all showed that at high levels of the latter, an increase in the former resulted in a marked decrease in ALP activity, whereas at low levels, the effect was either dampened or reversed. The factor C*factor D, factor C*factor E, and factor D*factor E interactions were such that at high levels of the latter, an increase in the former resulted in increased ALP activity, whereas at lower levels the effect was significantly diminished (Appendix 59 - Appendix 60).

3.3.8 Proliferation of Y201 MSCs on HA coated coupons

In order to test the CDM in an application where the omission of FBS would be advantageous, Y201 MSCs were seeded onto and cultured on the 17 HA coated coupons using CDM. Y201 MSC proliferation was assessed using RealTime Glo assay over 4 days, with readings taken every 12 hours.

There was a statistically significant increase in luminescent signal from Realtime Glo assay from day 0 to day 4 on all HA surfaces and tissue culture plastic (Figure 3.32), with fold change from day 0 to day 4 non-significantly different between all HA surfaces and tissue culture plastic control (Figure 3.33).

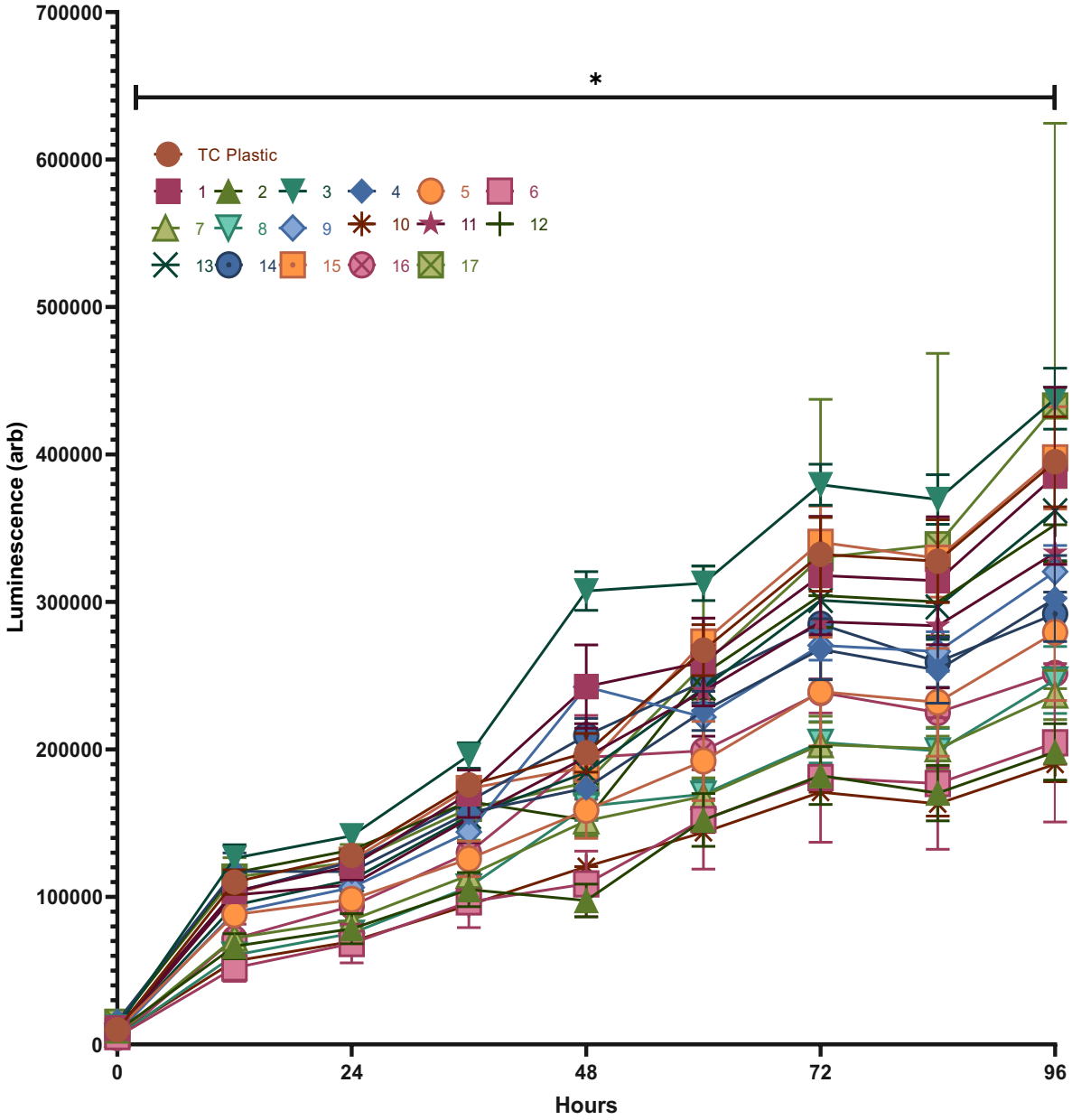

Figure 3.32: Y201 MSC luminescence signal on HA-coated coupons as assessed by Realtime Glo. Cells were seeded at a density of 1.5 x 10^4 cells/cm^2 in CDM and allowed to adhere for 24 hours. Cells were then washed and CDM replenished. Luminescence was measured continually over 96 hours every 12 hours using a spectrophotometer (n = 3, $p<0.05$; ANOVA).

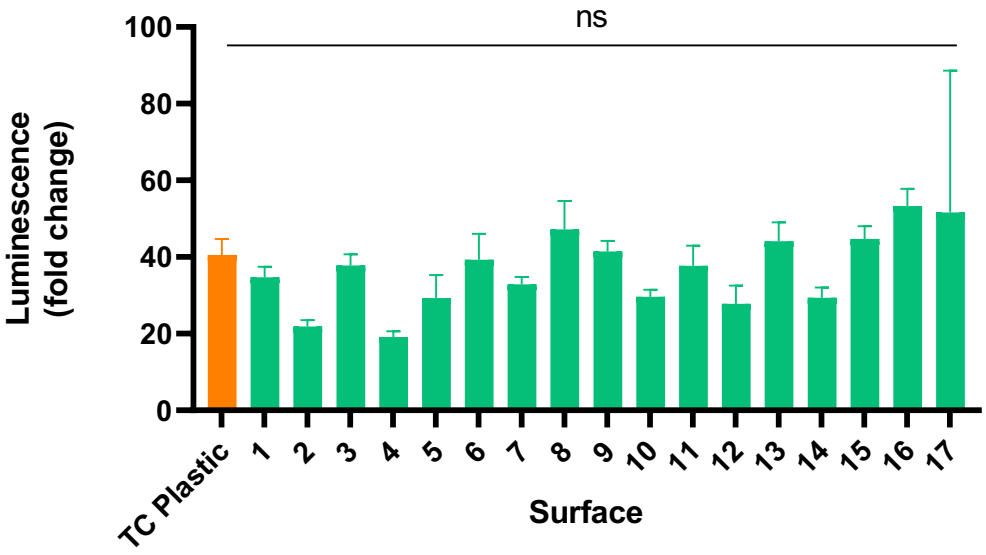

Figure 3.33: Luminescence fold change over 4 days from Y201 MSCs seeded onto differently HA sprayed titanium coupons as measured by Realtime Glo. Cells were seeded at a density of 1.5 x 10^4 cells/cm^2 in CDM and allowed to adhere for 24 hours. Cells were then washed and CDM replenished. Luminescence was measured over 4 days (n = 3, $p<0.05$; ANOVA).

3.4 Discussion

3.4.1 Controlling roughness and crystallinity of plasma sprayed HA coatings by plasma spray parameter optimisation

Using a DoE approach, 17 differently coated HA surfaces were manufactured on clinical grade Ti6Al4V titanium alloy coupons at the DePuy Synthes production line in Cork, Ireland, for the study of crystallinity and roughness response to changing plasma spray parameters, as well as the study of biological response of an immortalised human MSC line (Y201) to differently sprayed surfaces. This multidisciplinary study took a novel approach, with the aim of improving joint replacement prostheses at the manufacturing level, where changes can be readily implemented, with samples carefully selected to be in line with current production specifications.

Crystallinity and roughness responses to changes in plasma spray parameter changes have been successfully modelled, giving the ability to predict how relative crystallinity and roughness change when factors A - E are changed. This can be done either by using the factorial plots and contour plots created for each surface property in order to narrow down a region within which the desired response is achieved, or by using the factorial regression equation to calculate the response when settings are changed. This sets a new precedent for future production of plasma-coated HA surfaces, as it enables fine-tuning of two significant properties of the coating which can have an effect on material performance as well as MSC behaviour, and therefore on implant success.

It is important to note the small size of the DoE (17 runs, 1 centre point), which was chosen due to the manageability of experimentation and the feasibility of producing samples for this work at DePuy Synthes in Cork, Ireland. Due to the number of runs and points chosen, this DoE is classified as a resolution V DoE, which has several advantages and disadvantages. A significant advantage of this is that it is considered one of the least risky types of fractional factorials, meaning that for its size, it exhibits the least chance of confounding. Confounding occurs when parameter effects cannot be distinguished from one another, and is a feature of lower resolution DoE designs. A resolution V design can in theory discriminate between single factor effects and two-way interactions with no confounding, though higher order interactions are likely confounded with two-factor effects or higher. This is not usually a problem, as most processes a DoE is applied for do not consider higher order interactions, as they would be too complex to handle and it would be unfeasible to address these. In the case of plasma spraying, it is conceivable that higher order interactions would have a profound

effect on coating properties, as the process itself is extremely complex and very sensitive to minor changes.

Confounding became evident in several cases, where the centre point in the runs did not come close to any individual effects, or were far away from the effect due to a strong interaction. A good example of this was the analysis of relative crystallinity. In the main effects plot for relative crystallinity (Appendix 1) it was clear that the centre point (red) was very far away from any main effect, which usually means either that there is curvature in the response, or that confounding has taken place. In the interaction and contour plots (Appendix 3), it becomes evident that the centre point is still not falling on any lines, but is very close to some, such as the relative crystallinity response to increasing factor A at high factor D. The fact that it comes close to them but does not fall on a line suggests a level of curvature in the response, requiring further experimentation, known as folding, to examine fully. This skewed the model slightly, meaning that while prediction is possible and likely accurate due to the centre point being included in the model, a more detailed relative crystallinity response model can still be achieved with further experimentation. To model fully the response of each surface property to plasma sprayer settings, a further 17 runs would be designed in a manner which would combine medium settings for some plasma spray parameters with high and low settings of others.

3.4.2 MSC response to plasma sprayed HA surfaces

MSCs were successfully seeded onto HA surfaces, and it was determined that the common practice of soaking the HA coated coupons in cell culture medium should be avoided, as it created a crystalline coating on the surface and decreased the Ca/P ratio due to an increase in atomic percentage of phosphorus in the deposited material (Figure 3.20 - Figure 3.22). There is evidence to suggest that HA reactivity in cell culture medium can affect its morphology and properties. Gustavsson et al describe an ionic exchange that occurs when hydroxyapatite is exposed to FBS-containing cell culture media, which not only alters the composition of the HA material, but also drastically affects the composition of the culture medium[250]. This ionic exchange will differ depending on the relative crystallinity and available surface area of the material[33,251,252], and has been shown to have an effect *in vivo* in a rabbit model[253]. While not directly applicable to implant manufacture and success, this is an important finding for future study of HA biomaterials and must be taken into consideration for *in vitro* experimentation.

Wnt is a key pathway in MSC proliferation and differentiation[135,243,246,254–257] and has been shown to be affected by topographical cues *in vitro*[245–248]. It was therefore chosen as a candidate pathway for study in relation to HA material properties. It was shown that Wnt response differs on differently plasma sprayed surfaces, though no clear connection was found between any roughness parameters or relative crystallinity and Wnt signalling. Inferences about the topographical features that may affect Wnt signalling can be made from cross-referencing of plasma sprayer inputs that commonly affect Wnt and surface roughness, though the model has a relatively poor fit, meaning that prediction and cross references are likely to be inaccurate.

In the untreated cells, the most significant effector is the combination of factor B and factor E (B*E) (Figure 3.24). No material property has this interaction involved, though factor A, which is the next most significant factor in endogenous Wnt signalling, is involved in all material properties. This does not give enough information to accurately draw conclusions about which material property might be driving any effect. There is also a very strong suggestion of curvature in the model (Appendix 43), probably caused by higher order interactions. This is likely the case as measuring cellular signalling is highly sensitive, and the resolution used in the DoE was not refined enough for determining small details of the effect of plasma spray parameter setting changes on Wnt signalling.

In Wnt3a-treated cells, the most significant effector was factor C (Figure 3.25), which was identified as the parameter with the second largest effect on relative crystallinity (Figure 3.3). With increasing factor C, Wnt3a treated cells exhibited significantly less Wnt activity. Increasing factor C decreased relative crystallinity, and it can therefore be inferred that a high relative crystallinity may enhance Wnt signalling. This assessment, though, does not agree with the results of the assay, where coatings with the most significantly increased fold changes as compared to tissue culture plastic represent the entire range of crystallinities measured (48.43%-108.4%). It can therefore be concluded that the effect of surface properties on Wnt cannot be deduced from these models, merely that plasma sprayer parameters can be related to Wnt activity. It is likely that a combination of relative crystallinity, roughness, and possibly other factors such as porosity and foreign calcium phosphate phases have an effect on Wnt activity, which is beyond the scope of this model.

Y201 MSC proliferative behaviour also appears affected by different plasma sprayer settings, and Wnt involvement is evident, though inconsistent, pointing again toward

higher order interactions beyond the capabilities of this size and resolution of DoE. Nonetheless, some notable insights were made. In non-Wnt-treated cells, the largest contribution was made by a combined effect between factor B and factor C (Figure 3.28), which was that at a low factor C, a slight decline in proliferation was observed with increasing factor B, whilst at a high factor C a significant increase in proliferation was observed with increasing factor B (Appendix 50). No similar effect was observed in any of the surface properties, which points again toward either a higher order interaction being responsible or a different property entirely. There may be an indication of Wnt involvement, as a similar trend is seen in Wnt response to Wnt3a, suggesting a sensitisation of Y201s to Wnt at these settings. As Wnt ligands are known to enhance proliferation[241,244,254,258], it is possible that these settings sensitise MSCs to Wnt stimuli, and therefore proliferate accordingly.

Y201 MSCs were used for all studies as a model MSC line which exhibits classically tripotent MSC differentiation behaviour and cell surface marker expression[119]. While just a model, this cell line represents a stem-like subpopulation of MSCs resident in bone marrow, within the environment a prosthesis would be inserted into. These studies provide a proof of concept, showing that a tripotent cell type responds differently to differently coated HA surfaces, highlighting the notion that within the manufacturing stipulations of plasma sprayed, HA-coated titanium joint replacement devices, a range of MSC responses are evident. This suggests scope for improvement and refinement of the plasma spraying technique for optimised implant success, but still requires validation with primary donor MSCs. A cell line was used for these experiment as a DoE approach is very sensitive to variation in repeated experiments, which is inherent in biological studies, but would be exacerbated with the use of primary donor cells as donor to donor variation is orders of magnitude higher than the variation observed between experiments making use of a reproducible cell line.

3.4.3 Prediction of optimal plasma spray parameters for enhanced Y201 MSC proliferation

The model created for the proliferative response of the Y201 MSCs to changing plasma spray parameter settings had a very good fit (R^2 = 98.35%). This allows for an accurate prediction of plasma spray settings required for optimal cell behaviour in terms of proliferation, which translates to enhanced osteointegration and therefore implant success. For this, the regression equation is used (Equation 14), within the bounds of plasma spray settings used in the DoE, as extrapolation would be inaccurate due to the

cellular response inevitably reaching a plateau, which was not identified in this study. The highest fold change in PicoGreen signal 3 days post-seeding was observed to be 81.6937-fold (Figure 3.26), which was on surface 8, with the following parameter settings (Table 3.19):

Table 3.19: Parameter settings for coating with highest observed fold change in fluorescence by PicoGreen 3 days post-seeding.

	Factor A	**Factor B**	**Factor C**	**Factor D**	**Factor E**
Setting	1	1	1	-1	-1

Within the parameter settings used, it was predicted that a fold change of 110.2761 in PicoGreen signal from day 0 to day 3 could be achieved with parameter settings not tested in this DoE listed below (Table 3.20):

Table 3.20: Optimal plasma spray parameter settings for Y201 proliferation.

	Factor A	**Factor B**	**Factor C**	**Factor D**	**Factor E**
Setting	1	1	1	-1	1

Higher fold changes are theoretically possible, where a minor increase in factor B could yield a fold change of 132.403. This needs to be further tested in order to find the limits of the system, where cell response reaches a plateau.

3.4.3.1 *Prediction of material properties of plasma coated surface optimised for Y201 MSC proliferation*

In order to predict the surface properties of a plasma sprayed surface yielding maximum proliferative response as calculate in Table 3.20, regression equations for relative crystallinity (Equation 4), Sa (Equation 5), Sp (Equation 6), Sv (Equation 7), Sz (Equation 8), Sq (Equation 9), Ssk (Equation 10), and Sku (Equation 11) are used with the parameter settings for this surface (Table 3.20). Predicted values are shown in

Table 3.21.

Table 3.21: Optimal surface properties achievable by plasma spray within the tested parameter settings.

	Relative crystallinity	Sa (nm)	Sp (nm)	Sv (nm)	Sz (nm)	Sq (nm)	Ssk	Sku
Predicted Value	38.88%	8905.64	26073.7	-23196.8	49270.5	10767.2	0.15	2.12

The relative crystallinity of the theoretical surface is outside of the production specifications for ISO 13779 compliant HA coatings (>45%), so this particular surface would be unviable unless it could be proven to be substantially equivalent to a hip stem within target specifications.

3.4.4 Prediction of optimal plasma spray parameter for enhanced Y201 MSC osteogenesis

The model created for osteogenic response to changing plasma spray parameter settings was good for both basal conditions (86.19%; Table 3.17) and osteogenic conditions (96.33%; Table 3.18), allowing for prediction of optimal plasma sprayer settings for enhanced osteogenesis.

Osteogenic response under basal conditions gives the most physiologically relevant data for osteoinductive potential of the HA-coated surfaces. Therefore, Equation 16 is used in order to predict maximal ALP activity 9 days post-seeding. Within the calculated model, a 25.5-fold increase in ALP activity from day 0 to day 9 is predicted to be achievable, whereas tissue culture plastic did now show a significant fold change in ALP activity from day 0 to day 9 (Figure 3.29).

Table 3.22: Optimal plasma spray parameter settings for osteogenic response under basal culture conditions.

	Factor A	Factor B	Factor C	Factor D	Factor E
Setting	1	1	1	1	1

Outside of the constraints of the tested values, it was possible to extrapolate that a minor increase in factor C could yield an ALP activity fold change of 32.68. This can theoretically go much higher, though more experimentation is required to find the limits of cellular response to changing plasma spray parameters. This information could be used to improve implant performance without making dramatic changes to the implant

production process. These insights may be transferable to implant performance *in situ*, as basal culture conditions, while not an emulation of the conditions an implant would be exposed to, are much more minimal than the standard model of adding osteogenic supplements to culture, and therefore do resemble the bone environment more closely.

3.4.4.1 *Prediction of material properties of plasma coated surface for optimal Y201 osteogenic response*

In order to predict the surface properties of a plasma sprayed surface, regression equations for relative crystallinity (Equation 4), Sa (Equation 5), Sp (Equation 6), Sv (Equation 7), Sz (Equation 8), Sq (Equation 9), Ssk (Equation 10), and Sku (Equation 11) are used with the parameter settings for the optimal surface (Table 3.20). Predicted values are shown in

Table 3.23.

Table 3.23: Predicted material properties of plasma sprayed HA surface for optimal osteogenic response under basal culture conditions.

	Relative crystallinity	**Sa (nm)**	**Sp (nm)**	**Sv (nm)**	**Sz (nm)**	**Sq (nm)**	**Ssk**	**Sku**
Predicted Value	77.005%	10121.2	34529.0	-42476.8	76859.7	12553.7	-0.25	3.0

The relative crystallinity of this surface lies within product specification and is therefore suitable for use in patients already. This information may be used to improve implant performance.

With the addition of osteogenic supplements in culture, ALP activity increases markedly on all HA surfaces, and a strong model was created to predict changes in osteogenic behaviour. Optimal plasma spray parameter settings were calculated from the model and are given in Table 3.24.

Table 3.24: Predicted optimal plasma spray parameter settings for osteogenic response under osteogenic culture conditions.

	Factor A	**Factor B**	**Factor C**	**Factor D**	**Factor E**
Setting	-1	-1	1	1	1

The values above yield a 121.81-fold change in ALP activity based on the model created, compared to a 16.961-fold increase in ALP activity from day 0 to day 9 on

tissue culture plastic (Figure 3.29). This could theoretically reach 145.66-fold increase with slight increase to factor C. Similarly to the other predictions, in order to verify that this increase is indeed possible, a more in-depth study would be required.

3.4.4.2 *Prediction of material properties of plasma coated surface for optimal Y201 osteogenic response under osteogenic culture conditions*

In order to predict the surface properties of a plasma sprayed surface, regression equations for relative crystallinity (Equation 4), Sa (Equation 5), Sp (Equation 6), Sv (Equation 7), Sz (Equation 8), Sq (Equation 9), Ssk (Equation 10), and Sku (Equation 11) are used with the parameter settings for the optimal surface (Table 3.20). Predicted values are shown in

Table 3.25.

Table 3.25: Predicted material properties for surface created using optimal plasma spray parameter settings for osteogenic differentiation of Y201 cells under osteogenic culture conditions.

	Relative crystallinity	**Sa (nm)**	**Sp (nm)**	**Sv (nm)**	**Sz (nm)**	**Sq (nm)**	**Ssk**	**Sku**
Predicted Value	59.56 %	14433.7	58478.8	-47610.3	103052.0	17714.7	0.334	2.7

This surface, too, falls within production specifications, and could therefore be used. However, this does not reflect the environment a hip stem would be exposed to, and would therefore be better suited for applications such as HA scaffolds that are pre-seeded with cells.

In summary, a novel, multidisciplinary approach was taken to characterise and understand the relationships between process parameter settings and a resulting HA coating, and its effect on MSC behaviour. This information enables the prediction of not only HA surface material properties based on the model created, but also MSC response. Using these data, plasma spray settings were predicted for optimal MSC differentiation and proliferation, which are both essential to implant success. These settings were used to predict the material properties of the resulting surface, and it was found that surfaces can be produced that fall within production specifications that are more beneficial to MSC response than others. Future work should focus on expanding the DoE to incorporate broader plasma spray settings, as well as a higher resolution

design which would allow for closer modelling of sensitive responses, such as Wnt pathway response.

3.4.5 Use of CDM on biomaterial surfaces

CDM was also used to successfully seed and culture cells on HA-coated titanium surfaces, which would allow for more physiologically relevant, minimal conditions to be maintained in experimentation with these surfaces, as protein adsorption to biomaterials is a commonly described factor in biomaterials studies which may interfere with or skew findings to a significant extent[83,259–262]. The lack of FBS and a therefore more chemically defined cell culture environment is an equally useful tool for cell biology research, as the undefined nature of FBS and batch-to-batch variability is a source of uncertainty, where very sensitive systems, such as undifferentiated cells, may be affected by growth factors or other peptides present in FBS. FBS is also a source of contention due to its possibly unreliable future supply and rising cost, making it essential to replace with synthetic, xeno-free alternatives[154,160,178,263,264].

4 Chapter 4: General Discussion

Orthopaedic device failure has a profound impact on both the patient and health services. Patients can suffer severe pain and psychological effect upon hip arthroplasty complications, often causing intense personal distress[265,266]. Moreover, the strain on health services is profound, both with the high costs of revision surgery and the general strain on health services resulting from funding cuts causing staff and infrastructure shortages in the UK[267]. The burden on both the individual and healthcare providers could be alleviated by an improvement to hip stem performance and therefore longevity, preventing further hospitalisations after primary hip replacement surgery and increasing quality of life.

When an HA-coated implant is manufactured, there is a requirement to adhere to ISO 13779, which is a standard imposed on manufacturers which ensures the general safety of an implanted device. Unfortunately, these standards are not based on extensive trials and experimentation, but are historical in origin, and are merely in place for safety, not for optimal performance[268]. There is therefore a requirement to investigate whether there are differences in implant performance within the specified ranges, which can be very broad. Furthermore, while ample evidence exists in the literature implying that surface roughness has an effect on osteogenic potential[110,255,269], and the ISO guidelines do stipulate that roughness is retained after implantation, there no guidelines for what that roughness should be[270]. This creates further precedent to investigate the effect of plasma sprayed HA roughness on MSCs.

The use of serum has ethical, technical, and financial implications. With rising serum costs and waning supply, the ethical implications of the foetal origin of serum, and the multitude of scientific issues associated with its ill-defined nature, the move toward synthetic, chemically defined media is inevitable. While commercial options exist, their formulations, without exception, are proprietary, which may alleviate the batch-to-batch variability problem inherent in serum, but has no other utility to the researcher as they are still working with an undefined medium. The use of DoE allows researchers to develop a medium suitable for their biological system in a relatively short space of time and within reasonable cost.

The development of chemically defined medium has further applications than basic research, with the cell therapy industry still relying heavily on bovine serum for production of novel MSC therapies. The U.S. Food and Drug Administration (FDA) has

recently published that more than 80% of 66 investigational new drug applications for MSC products described a reliance on FBS for manufacturing[271]. This is troubling, as serum carries with it issues such as batch-to-batch variability, making quality assurance challenging, and opens up the potential for pathogen transmission and other contamination[272].

4.1 Chemically defined medium development

A chemically defined medium for use in MSC culture and EV production has been developed using DoE methodology. The media supplements used in the final chemically defined medium formula included BSA, trace elements mixes, lipid mix, linoleic/oleic acid mix, insulin, transferrin, selenium, and heparin. Each of these fulfil a function in the CDM, and have been optimised to the extent to which they could be optimised within the scope of the project to produce a medium fulfilling the requirement of growth on tissue culture plastic, a biomaterial (HA), and a bioreactor (Quantum). MSC differentiation was supported to an extent using the CDM, though it was not comparable to FBS-supplemented medium.

A limitation of this CDM was that primary cells from human donors could not be cultured in it (data not shown). Whilst cells attached to tissue culture plastic and spread as expected, there was no discernible proliferative activity observed across several donors. This aspect was not further examined, and is a potential avenue for further research, as a serum-free method for primary MSC isolation and expansion could reveal a very interesting aspect of MSC biology that might previously have been masked with the use of serum. In the context of the DoE methodology, the use of primary cells in the DoE would not have been possible, as the variation inherent between donors would not have allowed for DoE-led optimisation in the iterative manner required for this. There are some publications claiming serum-free isolation and expansion of MSCs, for example from bone marrow aspirate[273] or canine adipose-derived MSCs[274], but both of these rely heavily on hormones and growth factors, which was intentionally avoided for the purposes of this project, with the final formulation containing only insulin as a growth factor and relying on supporting the cells' own secreted factors for growth.

To enhance this CDM performance, a possible solution for the lack of satisfactory osteogenic differentiation potential may be to wean the cells off of FBS in a stepwise manner, which has been shown to improve low-serum and serum-free medium performance in other cell lines[275,276]. Another solution would be to employ the DoE methodology on optimising the osteogenic media supplement mixture, as these supplement concentrations have been optimised for FBS-containing medium, and invariably relies on FBS components for proper functioning. Other possible solutions could be to add further differentiation-enhancing growth factors, such as BMP-2, or to add a low amount of serum for differentiation studies[277].

Using the CDM, this work has also demonstrated that MSC expansion and EV production could be achieved in a serum-free environment at clinically relevant numbers. The EVs were characterised and confirmed to express all the relevant surface markers as outlined by the International Society for Extracellular Vesicles statement[278]. A more diverse population of EVs was observed, which has been reported from hollow fibre bioreactor EV production previously[279].

While this is promising, this study can be taken further by performing functional studies of these EVs to determine their efficacy *in vitro*, as has been reviewed in the literature[280]. Furthermore, it was hypothesised that the growth achieved in the two runs completed could be exceeded by optimising perfusion rates of the bioreactor to allow for medium enrichment with secreted factors, based on previous work relating to conditioned medium experiments.

A further aim of CDM development was to produce a medium devoid of undefined proteins that could adsorb onto biomaterial surfaces and cloud interpretation of cellular interactions events. This was achieved, with adhesion and growth being supported on every tested HA surface.

4.2 Plasma sprayed HA coatings: Material properties

The effects of plasma sprayer settings on HA material properties has been extensively modelled in this thesis, with the effects of each factor (A-E) having been modelled to roughness properties (Sa, Sp, Sv, Sz, Sq, Ssk, Sku) and relative crystallinity with a good fit (R^2>90% for each). This allows for fine control over surface properties which can now be reliably reproduced using the same machinery. This is of particular interest, as the machinery used for the coating of the samples studied was the plasma sprayer on the hip stem production line at DePuy Synthes, Cork, who have kindly provided these samples. This made available surface coatings on clinical grade titanium as they would be received by a patient, thereby simulating 'real world' conditions very closely.

It was found that it was the same factor that had the largest effect on changes in the majority of cases (Factor A; Relative crystallinity, Sa, Sp, Sv, Sz, Sq, Ssk), while factor B had the most significant effect on Sku (see section 3.3). This could be interpreted as being a challenge for changing individual effects, but it is important to note that most roughness parameters are a function of the other (for example, Sz = Sp + Sv), which is an inherent confounding factor in the interpretation of the data. Nevertheless, the plasma spraying process is a high throughput technique that cannot be expected to enable extremely fine control over material properties, and given the constraints of the technique, a high level of control was determined. A more finely controlled surface can be achieved using etching or lithography techniques, which have been shown in numerous cases to reproducibly create regular, structured surfaces with the ability to influence cell behaviour and fate[172,247,281,282].

A limitation of this study was that other material factors, such as porosity, were not considered. Porous HA scaffolds have been shown to accelerate healing in critically-sized bone defects, which has been attributed to increasing available surface area for MSC adhesion[283], and has also been implicated in enhanced vascularisation when combined with bioactive coatings containing VEGF and heparin[284]. Further study could include porosity and study the effect of porosity of plasma sprayed coatings on MSC behaviour.

4.3 Plasma sprayed HA coatings: MSC response

MSC response to changing plasma sprayer settings was assessed in terms of proliferation, osteogenesis, and Wnt signalling. It was found that while some insights could be made in relation to plasma spray parameter setting effects on biological response, with good model fits for proliferation and osteogenesis, Wnt signalling modelling was less successful. Also, it was not possible to correlate plasma sprayer settings for biological response to material properties directly, although the material properties for optimal surfaces for each measured response were calculated. The fact that no definite correlation between plasma sprayer settings and biological response and plasma sprayer settings and material properties was found suggests that higher order interactions between roughness, relative crystallinity, and other material properties not measured here are likely to be responsible for the biological response, which was outside of the scope of this project.

However, the model fits for proliferation and osteogenesis were successful, and optimal surfaces were predicted. This showed that for optimised MSC proliferative behaviour, a relatively low relative crystallinity would be required (38.88%; Table 3.21), rendering the coating non-compliant with ISO standards necessary for manufacture and marketing, therefore making it unviable for process optimisation. Taking osteogenesis as an optimised output, it was found that a higher relative crystallinity, falling within specification, would yield optimised osteogenic response (77.005%; Table 3.23). An overall rougher surface was found to enhance optimal osteogenic response (Sa = 10121.2 nm; Table 3.23). This suggests that within current production specifications, there exists a plasma sprayer input setting that promotes osteogenic response, which would suggest that an improvement may be achieved without a drastic change to production parameters.

These findings are caveated by the use of the Y201 cell line in all of these studies. Y201 MSCs are a clonally expanded, hTERT immortalised cell line produced in the Genever laboratory which exhibit markers typical of MSCs and have trilineage potential[119], making them a suitable model representing what is considered a subpopulation of multipotent cells resident in the bone marrow. In order to fully confirm these findings, primary cells from human donors would need to be used. Furthermore, *in vivo* experiments with differently sprayed HA coatings would confirm whether enhanced proliferation or osteogenesis would indeed lead to enhanced osteointegration and implant success.

4.4 Proposed mode of action

As it was shown that Wnt signalling is altered on differently sprayed surfaces in different ways, and proliferation and osteogenesis are altered in response to these surfaces, the following hypothesis was formulated describing how an optimal surface may enhance implant success.

HA surfaces readily allow for protein adsorption from the peri-implant environment, which initiates the cascade of cellular responses as described in section 1.4. An optimised surface will adsorb proteins for cell optimal cell recruitment at the stage of MSC involvement, after the initial immune response. MSCs adhering to this surface will be prompted to undergo osteogenic differentiation, stimulated by a combination of the roughness of the surface, Wnt signalling modulation, and enhanced proliferative behaviour, as has been shown in these studies and numerous publications previously[34,85,168,239,245,247,269]. This combinatorial effect of an optimal surface may enhance the osteointegration of the implant and therefore longevity (Figure 4.1).

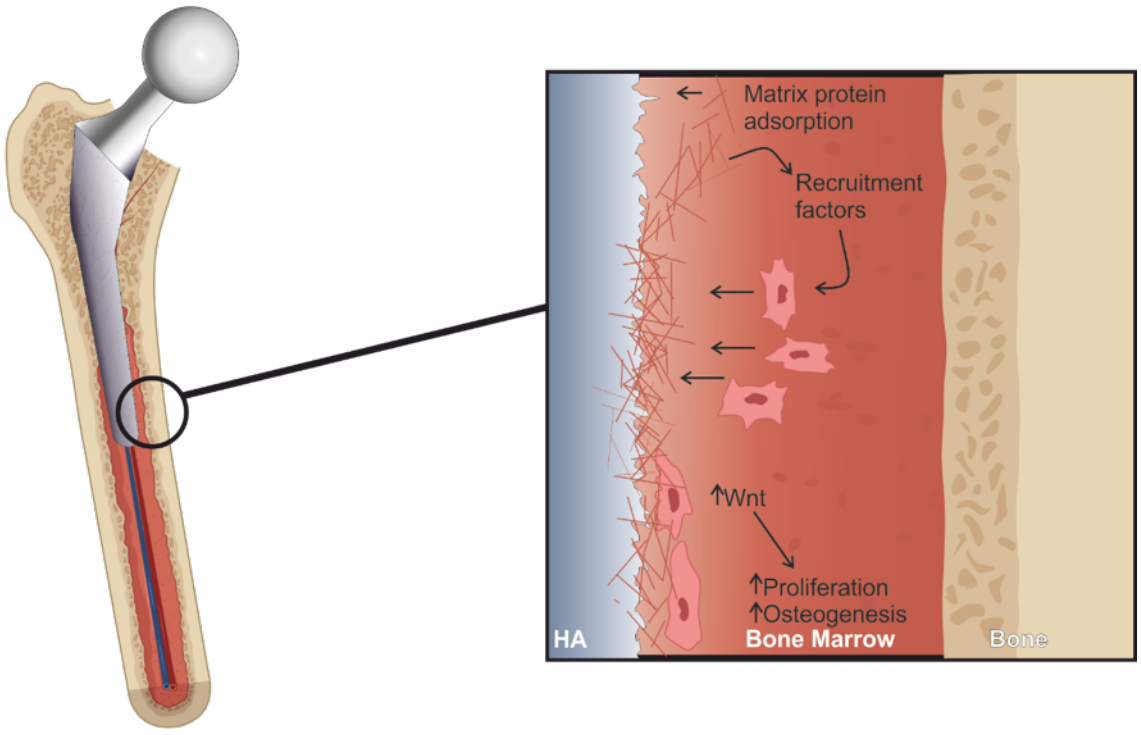

Figure 4.1: Proposed hypothesis for mechanism of action of HA surfaces' effect on resident MSCs in the peri-implant space. Matrix proteins adsorb to the HA surface, with differences depending on the surface properties. Fibrogenic recruitment factors initiate MSC recruitment to the surface, where upon binding, Wnt signalling is modulated, enhancing proliferation and osteogenesis of MSCs in situ.

4.5 Final remarks

The work presented here has focussed on the fine control of plasma sprayed HA surfaces with the aim of providing tools for the enhancement of cellular responses predictably. The data provide an indication of the plasma sprayer settings that influence MSC behaviours relevant to the healing process following implantation of an artificial hip, with suggested plasma sprayer settings that would modulate MSC response favourably. For example, to maximise osteogenic response under basal conditions, factors A-E can be set to their high settings in order to achieve a 25.5-fold increase in ALP activity over 9 days, where the same conditions result in no ALP activity increase on tissue culture plastic. Moreover, the material properties of the resulting surfaces were predicted in terms of roughness and relative crystallinity, which may provide information for researchers working with plasma sprayed hydroxyapatite to further add to the growing body of knowledge describing MSC response to these surfaces.

Should more information become available about specific protein adsorption *in situ*, immune response, and other MSC behaviours not studied here in response to roughness or crystallinity, a detailed model has been created for a number of roughness parameters and crystallinity. This will allow for the creation of material properties in line with any new findings relating to the influence of roughness or crystallinity on implant success.

The findings presented here will inform future work. In order to validate fully the MSC responses to differently sprayed surfaces, a large-scale study will need to be done using primary donor cells, followed by *in vivo* investigation of osteointegration. Also, these studies could be done in the absence of FBS, which may provide a better indication of MSC responses in the bone marrow environment.

The notion of varying calcium phosphate stoichiometry with varying plasma sprayer settings is highly significant, as this could affect biocompatibility and resorption behaviour of the material, thereby potentially affecting implant performance. A better understanding of these effects in an *in vivo* environment could inform critical quality attributes of the production process, leading to a higher quality implant product. The calcium phosphate phase composition could be further characterised using Raman spectroscopy or magnetic resonance (NMR) spectroscopy. Conclusions could be made based on material composition, when put into the context of further *in vivo* studies, to optimise plasma spray technique to achieve optimal material performance.

Finally, regarding EV production, initial steps have been taken for scaled up applications, where Y201 MSCs were grown in serum-free conditions and EVs collected and characterised in the same CDM. This showed enhanced production of some EV fractions with the CDM, opening up the possibility of further in-depth research into its application for EV therapeutics. The immortalised Y201 MSCs may be used to produce a consistent source of therapeutic EVs under defined, xeno-free conditions. Further studies needed to validate this will be to study EV functionality *in vitro* and *in vivo*, as well as the possibility of loading specific cargo into EVs for engineered approaches to cell product therapy. This particular line of research has been recently reviewed[285], and is a novel and potentially ground-breaking approach to therapeutics.

List of Abbreviations

ALP	alkaline phosphatase
APC	adenomatous polyposis coli
bFGF/FGF-2	fibroblastic growth factor 2
BMI	Body mass index
BMP	Bone morphogenetic protein
BSA	bovine serum albumin
CCL2	C chemokine ligand 2
CCL4	C chemokine ligand 4
CD	cluster of differentiation
CDM	chemically defined medium
CHO	Chinese Hamster Ovary
CK1α	casein kinase 1α
CXCL8	CX chemokine ligand 8
DMEM	Dulbecco's modified Eagle medium
DoE	Design of Experiments
dsDNA	double stranded deoxyribonucleic acid
Dvl	Dishevelled
ECL	enhanced chemiluminescence
EFSA	European Food Standards Agency
EGFR	epidermal growth factor receptor
EM	Eagle's medium
ESC	embryonic stem cell
EV	extracellular vesicle
FBGC	foreign body giant cells
FBS	Foetal Bovine Serum
FDA	Food and drug administration
Fzd	Frizzled
GPI-AP	glycosylphosphatidylinositol-anchored protein
GSK3β	glycogen synthase kinase 3β
GTPases	guanidine triphosphate-ases
HA	hydroxyapatite
HDAC	histone deacetylase
HEPES	4-(2-hydroxyethyl)-1-piperazineethanesulfonic acid
IGF-1R	insulin-like growth factor receptor 1
IL10	Interleukin 10
IL-1α	interleukin 1α
IMDM	Iscove's modified DMEM
IR	insulin receptor

ITS	insulin-transferrin-selenium
Lrp5/6	lipoprotein receptor related proteins 5 or 6
MAPK	mitogen-activated protein kinase
MMP	matrix metalloproteinases
MSC	mesenchymal stromal cell
NET	Neutrophil extracellular trap
NFAT	nuclear factor of activated T-cells
OCN	osteocalcin
OFAT	one-factor-at-a-time
OPTN	osteopontin
Osx	osterix
PBS	phosphate buffered saline
PBS-T	phosphate buffered saline/0.1% Tween-20
PMMA	polymethyl methacrylate
pNPP	p-nitrophenyl-phosphate
ROCK	Rho kinase
ROCKi	Y-27632
ROS	reactive oxygen species
RPMI	Roswell Park Memorial Institute
RUNX2	Runt-related transcription factor 2
Sa	Mean roughness
SDF1	Stromal cell-derived factor 1
Sku	Kurtosis
Sp	Maximal peak height
Sq	Root mean square height
Ssk	Skewness
Sv	Maximal valley depth
Sz	Maximal Height
TAZ	transcriptional coactivator with PDZ-binding domain
TCF/LEF	T-cell factor/lymphoid enhancer-binding factor
TLE	transducing-like enhancer of split
TNF-α	tumour necrosis factor α
T-reg	T-regulatory cells
VEGF	vascular endothelial growth factor
Wnt	wingless-related integration site
YAP	Yes-associated protein
βTrCP	β-transducin repeats containing protein

References

1. Arthritis, V. *The State of Musculoskeletal health 2019*. https://www.versusarthritis.org/media/14594/state-of-musculoskeletal-health-2019.pdf (2019).

2. Overview of the UK population - Office for National Statistics. https://www.ons.gov.uk/peoplepopulationandcommunity/populationandmigration/populationestimates/articles/overviewoftheukpopulation/august2019.

3. Abramoff, B. & Caldera, F. E. Osteoarthritis: Pathology, Diagnosis, and Treatment Options. *Medical Clinics of North America* vol. 104 293–311 (2020).

4. (No Title). https://reports.njrcentre.org.uk/Portals/0/PDFdownloads/NJR 16th Annual Report 2019.pdf.

5. Prieto-Alhambra, D. *et al.* Incidence and risk factors for clinically diagnosed knee, hip and hand osteoarthritis: influences of age, gender and osteoarthritis affecting other joints. *Ann. Rheum. Dis.* **73**, 1659–64 (2014).

6. Oliveria, S. A., Felson, D. T., Reed, J. I., Cirillo, P. A. & Walker, A. M. Incidence of symptomatic hand, hip, and knee osteoarthritis among patients in a health maintenance organization. *Arthritis Rheum.* **38**, 1134–1141 (1995).

7. Wluka, A. E., Lombard, C. B. & Cicuttini, F. M. Tackling obesity in knee osteoarthritis. *Nature Reviews Rheumatology* vol. 9 225–235 (2013).

8. Palazzo, C., Nguyen, C., Lefevre-Colau, M. M., Rannou, F. & Poiraudeau, S. Risk factors and burden of osteoarthritis. *Annals of Physical and Rehabilitation Medicine* vol. 59 134–138 (2016).

9. Furnes, O. *et al.* Hip disease and the prognosis of total hip replacements. A review of 53,698 primary total hip replacements reported to the Norwegian Arthroplasty Register 1987-99. *J. Bone Joint Surg. Br.* **83**, 579–86 (2001).

10. Spector, T. D. & MacGregor, A. J. Risk factors for osteoarthritis: Genetics. *Osteoarthr. Cartil.* **12**, 39–44 (2004).

11. Dixon, T., Shaw, M., Ebrahim, S. & Dieppe, P. Trends in hip and knee joint replacement: Socioeconomic inequalities and projections of need. *Ann. Rheum. Dis.* **63**, 825–830 (2004).

12. [ARCHIVED CONTENT] Payment by Results in the NHS: tariff for 2013 to 2014 - GOV.UK. https://webarchive.nationalarchives.gov.uk/20180718030527/https://www.gov.uk/government/publications/payment-by-results-pbr-operational-guidance-and-tariffs.

13. Birrell, F., Johnell, O. & Silman, A. Projecting the need for hip replacement over the next three decades: Influence of changing demography and threshold for surgery. *Ann. Rheum. Dis.* **58**, 569–572 (1999).

14. Culliford Y X, D. *et al.* Future projections of total hip and knee arthroplasty in the UK: results from the UK Clinical Practice Research Datalink. *Osteoarthr. Cartil.* **23**, 594–600 (2015).

15. Kurtz, S., Ong, K., Lau, E., Mowat, F. & Halpern, M. Projections of primary and

revision hip and knee arthroplasty in the United States from 2005 to 2030. *J. Bone Jt. Surg. - Ser. A* **89**, 780–785 (2007).

16. Patel, A., Pavlou, G., Mújica-Mota, R. E. & Toms, A. D. The epidemiology of revision total knee and hip arthroplasty in England and Wales: A comparative analysis with projections for the United States. a study using the national joint registry dataset. *Bone Jt. J.* **97**-**B**, 1076–1081 (2015).

17. Mcgill, K. C., Bush-Joseph, C. A. & Nho, S. J. Hip microfracture: Indications, technique, and outcomes. *Cartilage* **1**, 127–136 (2010).

18. Vincent, T. L. Of mice and men: converging on a common molecular understanding of osteoarthritis. *The Lancet Rheumatology* vol. 2 e633–e645 (2020).

19. Osteoarthritis - NICE CKS. https://cks.nice.org.uk/osteoarthritis#!scenario.

20. Jeffers, J. R. T. & Walter, W. L. Ceramic-on-ceramic bearings in hip arthroplasty: State of the art and the future. *Journal of Bone and Joint Surgery - Series B* vol. 94 B 735–745 (2012).

21. Al-Hajjar, M. *et al.* Wear of novel ceramic-on-ceramic bearings under adverse and clinically relevant hip simulator conditions. *J. Biomed. Mater. Res. - Part B Appl. Biomater.* **101**, 1456–1462 (2013).

22. Kumar, N., Arora, N. C. & Datta, B. Bearing surfaces in hip replacement - Evolution and likely future. *Medical Journal Armed Forces India* vol. 70 371–376 (2014).

23. Zagra, L. & Gallazzi, E. Bearing surfaces in primary total hip arthroplasty. *EFORT Open Rev.* **3**, 217–224 (2018).

24. Mirza, S. B. *et al.* Basic Science Considerations in Primary Total Hip Replacement Arthroplasty. *Open Orthop. J.* **4**, 169–180 (2010).

25. Gergely, R. C. R., Toohey, K. S., Jones, M. E., Small, S. R. & Berend, M. E. Towards the optimization of the preparation procedures of PMMA bone cement. *J. Orthop. Res.* **34**, 915–923 (2016).

26. Whitehouse, M. R. . A. N. S. . P. M. . B. A. W. . B. G. C. OSTEONECROSIS WITH THE USE OF POLYMETHYLMETHACRYLATE CEMENT FOR HIP REPLACEMENT: THERMAL-INDUCED DAMAGE EVIDENCED IN VIVO BY DECREASED OSTEOCYTE VIABILITY. 50–63 (2014) doi:10.22203/eCM.v027a05.

27. Maggs, J. & Wilson, M. The relative merits of cemented and uncemented prostheses in total hip arthroplasty. in *Indian Journal of Orthopaedics* vol. 51 377–385 (Medknow Publications, 2017).

28. Gilbert, T. J. *et al.* Osteolysis complicating total knee arthroplasty. *JBJS Reviews* vol. 4 (2016).

29. Ingham, E. & Fisher, J. The role of macrophages in osteolysis of total joint replacement. *Biomaterials* vol. 26 1271–1286 (2005).

30. Goodman, S. B., Gibon, E. & Yao, Z. The basic science of periprosthetic osteolysis. *Instr. Course Lect.* **62**, 201–206 (2013).

31. Bauer, T. W., Geesink, R. C. T., Zimmerman, R. & McMahon, J. T. Hydroxyapatite-coated femoral stems. Histological analysis of components retrieved at autopsy. *J. Bone Jt. Surg. - Ser. A* (1991) doi:10.2106/00004623-199173100-00001.

32. Sun, L., Berndt, C. C., Gross, K. A. & Kucuk, A. Material fundamentals and clinical performance of plasma-sprayed hydroxyapatite coatings: A review. *Journal of Biomedical Materials Research* (2001) doi:10.1002/jbm.1056.

33. Roy, M., Bandyopadhyay, A. & Bose, S. Induction plasma sprayed nano hydroxyapatite coatings on titanium for orthopaedic and dental implants. *Surf. Coatings Technol.* (2011) doi:10.1016/j.surfcoat.2010.10.042.

34. Lin, L. *et al.* Enhanced osteointegration of medical titanium implant with surface modifications in micro/nanoscale structures. *J. Orthop. Transl.* (2014) doi:10.1016/j.jot.2013.08.001.

35. De Groot, K., Geesink, R., Klein, C. P. A. T. & Serekian, P. Plasma sprayed coatings of hydroxylapatite. *J. Biomed. Mater. Res.* (1987) doi:10.1002/jbm.820211203.

36. Chapman, M. W., Bucholz, R. & Cornell, C. Treatment of acute fractures with a collagen-calcium phosphate graft material: A randomized clinical trial. *J. Bone Jt. Surg. - Ser. A* **79**, 495–502 (1997).

37. Bhalla, A., Tsiridis, E., Goodship, A. E. & di Silvio, L. Enhancing the osseoinductive properties of hydroxyapatite by the addition of human mesenchymal stem cells, and recombinant human osteogenic protein 1 (BMP-7). in *European Cells and Materials* vol. 4 129 (2002).

38. Fratzl, P., Gupta, H. S., Paschalis, E. P. & Roschger, P. Structure and mechanical quality of the collagen-mineral nano-composite in bone. *Journal of Materials Chemistry* vol. 14 2115–2123 (2004).

39. Rubin, M. A. *et al.* TEM analysis of the nanostructure of normal and osteoporotic human trabecular bone. *Bone* **33**, 270–282 (2003).

40. Aspenberg, P. & Herbertsson, P. Periprosthetic bone resorption. Particles versus movement. *J. Bone Jt. Surg. - Ser. B* **78**, 641–646 (1996).

41. Gorab, R. S., Covino, B. M. & Borden, L. S. The rationale for cementless revision total hip replacement with contemporary technology. *Orthop. Clin. North Am.* **24**, 627–33 (1993).

42. Cherubino, P., Puricelli, M. & D'Angelo, F. Revision in Cemented and Cementless Infected Hip Arthroplasty. *Open Orthop. J.* **7**, 190–196 (2013).

43. Hu, C. Y. & Yoon, T. R. Recent updates for biomaterials used in total hip arthroplasty. *Biomaterials Research* vol. 22 (2018).

44. Rivière, C. *et al.* Long-term bone remodelling around 'legendary' cementless femoral stems. *EFORT Open Rev.* **3**, 45–57 (2018).

45. Piao, C., Wu, D., Luo, M. & Ma, H. Stress shielding effects of two prosthetic groups after total hip joint simulation replacement. *J. Orthop. Surg. Res.* **9**, 71 (2014).

46. Kawaji, H. *et al.* Influence of femoral implant alignment in uncemented total hip

replacement arthroplasty: Varus insertion and stress shielding. *J. Nippon Med. Sch.* **83**, 223–227 (2016).

47. Gerdien, H. & Lotz, A. Über eine Lichtquelle von sehr hoher Flächenhelligkeit. (1922).

48. Gage, R. M., Nestor, D. M. & Yenni, Y. M. Collimated electric arc powder deposition process. (1962).

49. Witherspoon, F. D., Massey, D. W., Kincaid, R. W., Whichard, G. C. & Mozhi, T. A. High velocity pulsed plasma thermal spray. *J. Therm. Spray Technol.* **11**, 119–128 (2002).

50. Steffens, H. D., Nassenstein, K., Keller, S. & Barbezat, G. The 'sonarc' process: Combining the advantages of arc and HVOF spraying. *Journal of Thermal Spray Technology* vol. 3 398–403 (1994).

51. Pawlowski, L. *The Science and Engineering of Thermal Spray Coatings: Second Edition*. *The Science and Engineering of Thermal Spray Coatings: Second Edition* (John Wiley and Sons, 2008). doi:10.1002/9780470754085.

52. Janisson, S. *et al.* Plasma spraying using Ar-He-H2 gas mixtures. *J. Therm. Spray Technol.* **8**, 545–552 (1999).

53. Leylavergne, M., Dussoubs, B., Vardelle, A. & Goubot, N. Comparison of Plasma-Sprayed Coatings Produced in Argon or Nitrogen Atmosphere. *Journal of Thermal Spray Technology* (1998) doi:10.1361/105996398770350756.

54. Djebali, R., Pateyron, B. & Elganaoui, M. Scrutiny of plasma spraying complexities with case study on the optimized conditions toward coating process control. *Case Stud. Therm. Eng.* **6**, 171–181 (2015).

55. Jeništa, J. *et al.* Modeling of inhomogeneous mixing of plasma species in argon-steam arc discharge. *J. Phys. D. Appl. Phys.* **51**, (2018).

56. Murphy, A. B. & Arundelli, C. J. Transport coefficients of argon, nitrogen, oxygen, argon-nitrogen, and argon-oxygen plasmas. *Plasma Chem. Plasma Process.* **14**, 451–490 (1994).

57. Shanmugavelayutham, G. & Selvarajan, V. *Electrothermal efficiency, temperature and thermal conductivity of plasma jet in a DC plasma spray torch*. *PRAMANA c - Indian Academy of Sciences* vol. 61 (2003).

58. Bisson, J. F., Moreau, C., Dorfman, M., Dambra, C. & Mallon, J. Influence of hydrogen on the microstructure of plasma-sprayed yttria-stabilized zirconia coatings. *J. Therm. Spray Technol.* **14**, 85–90 (2005).

59. Bisson, J. F., Gauthier, B. & Moreau, C. Effect of plasma fluctuations on in-flight particle parameters. *Journal of Thermal Spray Technology* vol. 12 38–43 (2003).

60. Kweh, S. W. K., Khor, K. A. & Cheang, P. Production and characterization of hydroxyapatite (HA) powders. *J. Mater. Process. Technol.* **89**–**90**, 373–377 (1999).

61. Kweh, S. W. K., Khor, K. A. & Cheang, P. Plasma-sprayed hydroxyapatite (HA) coatings with flame-spheroidized feedstock: Microstructure and mechanical properties. *Biomaterials* **21**, 1223–1234 (2000).

62. Cheang, P. & Khor, K. A. Thermal spraying of hydroxyapatite (HA) coatings: Effects of powder feedstock. *J. Mater. Process. Tech.* **48**, 429–436 (1995).

63. Cheang, P. & Khor, K. A. Influence of powder characteristics on plasma sprayed hydroxyapatite coatings. *J. Therm. Spray Technol.* **5**, 310–316 (1996).

64. Khor, K. A. & Cheang, P. Characterization of thermal sprayed hydroxyapatite powders and coatings. *Journal of Thermal Spray Technology* vol. 3 45–50 (1994).

65. Levingstone, T. J., Ardhaoui, M., Benyounis, K., Looney, L. & Stokes, J. T. Plasma sprayed hydroxyapatite coatings: Understanding process relationships using design of experiment analysis. *Surf. Coatings Technol.* **283**, 29–36 (2015).

66. Zhang, W., Zheng, L., Zhang, H. & Sampath, S. Study of Injection Angle and Carrier Gas Flow Rate Effects on Particles In-Flight Characteristics in Plasma Spray Process: Modeling and Experiments. *Plasma Chem. Plasma Process.* **27**, 701–716 (2007).

67. Dorozhkin, S. V. *Calcium Orthophosphates: Applications in Nature, Biology, and Medicine - Sergey V. Dorozhkin - Google Books*. (2012).

68. Liu, Q., Huang, S., Matinlinna, J. P., Chen, Z. & Pan, H. Insight into biological apatite: Physiochemical properties and preparation approaches. *BioMed Research International* vol. 2013 (2013).

69. Hu, Q. *et al.* Effect of crystallinity of calcium phosphate nanoparticles on adhesion, proliferation, and differentiation of bone marrow mesenchymal stem cells. *J. Mater. Chem.* **17**, 4690–4698 (2007).

70. Tsui, Y. C., Doyle, C. & Clyne, T. W. *Plasma sprayed hydroxyapatite coatings on titanium substrates Part 1: Mechanical properties and residual stress levels*. *Biomaterials* vol. 19 (1998).

71. Cheng, L. *et al.* Osteoinduction of hydroxyapatite/β-tricalcium phosphate bioceramics in mice with a fractured fibula. *Acta Biomater.* **6**, 1569–1574 (2010).

72. Sumer, M. *et al.* Autogenous cortical bone and bioactive glass grafting for treatment of intraosseous periodontal defects. *Eur. J. Dent.* **7**, 6–14 (2013).

73. Sasaki, G. *et al.* Induced membrane technique using beta-tricalcium phosphate for reconstruction of femoral and tibial segmental bone loss due to infection: technical tips and preliminary clinical results. *Int. Orthop.* **42**, 17–24 (2018).

74. Vahabzadeh, S., Roy, M., Bandyopadhyay, A. & Bose, S. Phase stability and biological property evaluation of plasma sprayed hydroxyapatite coatings for orthopedic and dental applications. *Acta Biomater.* **17**, 47–55 (2015).

75. Heimann, R. B. Plasma-Sprayed Hydroxylapatite-Based Coatings: Chemical, Mechanical, Microstructural, and Biomedical Properties. *Journal of Thermal Spray Technology* **25** 827–850 (2016).

76. Burnett, R. S. J. Total hip arthroplasty: Techniques and results. *BCMJ* **52**, 455–464 (2010).

77. Yamada, H. *et al.* Cementless total hip replacement: Past, present, and future. *J. Orthop. Sci.* **14**, 228–241 (2009).

78. Manley, M. T., Dumbleton, J. H. & Sutton, K. Fixation Choices for Primary Hip and Knee Applications. *Semin. Arthroplasty* **17**, 56–60 (2006).

79. Reigstad, O., Siewers, P., Røkkum, M. & Espehaug, B. Excellent long-term survival of an uncemented press-fit stem and screw cup in young patients: Follow-up of 75 hips for 15-18 years. *Acta Orthop.* **79**, 194–202 (2008).

80. Bertrand, J. *et al.* Ceramic prosthesis surfaces induce an inflammatory cell response and fibrotic tissue changes. *Bone Joint J.* **100-B**, 882–890 (2018).

81. Anderson, J. M., Rodriguez, A. & Chang, D. T. Foreign body reaction to biomaterials. *Seminars in Immunology* vol. 20 86–100 (2008).

82. Wilson, C. J., Clegg, R. E., Leavesley, D. I. & Pearcy, M. J. Mediation of biomaterial-cell interactions by adsorbed proteins: A review. *Tissue Engineering* vol. 11 1–18 (2005).

83. Tagaya, M., Ikoma, T., Hanagata, N., Yoshioka, T. & Tanaka, J. Competitive adsorption of fibronectin and albumin on hydroxyapatite nanocrystals. *Sci. Technol. Adv. Mater.* **12**, (2011).

84. Yang, N. *et al.* Immobilised Macrophage Colony-Stimulating Factor (M-CSF) regulates the foreign body response to implanted materials. *ACS Biomater. Sci. Eng.* (2020) doi:10.1021/acsbiomaterials.9b01887.

85. Steeves, A. J. & Variola, F. Elucidating structure-function relationships governing the interfacial response of human mesenchymal stem cells to polydopamine coatings. *J. Mater. Chem. B* **8**, 199–215 (2020).

86. Esche, C., Stellato, C. & Beck, L. A. Chemokines: Key players in innate and adaptive immunity. *J. Invest. Dermatol.* **125**, 615–628 (2005).

87. Szaba, F. M. & Smiley, S. T. Roles for thrombin and fibrin(ogen) in cytokine/chemokine production and macrophage adhesion in vivo. *Blood* **99**, 1053–1059 (2002).

88. Flick, M. J. *et al.* Leukocyte engagement of fibrin(ogen) via the integrin receptor αMβ2/Mac-1 is critical for host inflammatory response in vivo. *J. Clin. Invest.* **113**, 1596–1606 (2004).

89. Ort, M. J., Geissler, S., Rakow, A. & Schoon, J. The Allergic Bone Marrow? The Immuno-Capacity of the Human Bone Marrow in Context of Metal-Associated Hypersensitivity Reactions. *Frontiers in Immunology* vol. 10 (2019).

90. Chen, X., Bai, C., Xie, L., Zhang, Y. & Wang, K. Inflammatory response to orthopedic biomaterials after total hip replacement. *J. Orthop. Sci.* **17**, 407–412 (2012).

91. Kinashi, T. Overview of integrin signaling in the immune system. *Methods Mol. Biol.* **757**, 261–278 (2011).

92. Rogers, T. H. & Babensee, J. E. The role of integrins in the recognition and response of dendritic cells to biomaterials. *Biomaterials* **32**, 1270–1279 (2011).

93. Selders, G. S., Fetz, A. E., Radic, M. Z. & Bowlin, G. L. An overview of the role of neutrophils in innate immunity, inflammation and host-biomaterial integration. *Regen. Biomater.* **4**, 55–68 (2017).

94. Jhunjhunwala, S. *et al.* Neutrophil Responses to Sterile Implant Materials. *PLoS One* **10**, e0137550 (2015).

95. Tang, L. & Eaton, J. W. Natural responses to unnatural materials: A molecular mechanism for foreign body reactions. *Molecular Medicine* vol. 5 351–358 (1999).

96. Vasconcelos, D. M. *et al.* Immune response and innervation signatures in aseptic hip implant loosening. *J. Transl. Med.* **14**, (2016).

97. Badylak, S. F. & Gilbert, T. W. Immune response to biologic scaffold materials. *Seminars in Immunology* vol. 20 109–116 (2008).

98. Soltan, M., Rohrer, M. D. & Prasad, H. S. Monocytes: Super cells for bone regeneration. *Implant Dent.* **21**, 13–20 (2012).

99. Fernandes, K. R., Zhang, Y., Magri, A. M. P., Renno, A. C. M. & Van Den Beucken, J. J. J. P. Biomaterial Property Effects on Platelets and Macrophages: An in Vitro Study. *ACS Biomater. Sci. Eng.* **3**, 3318–3327 (2017).

100. Zheng, Z. wei *et al.* Development of an accurate and proactive immunomodulatory strategy to improve bone substitute material-mediated osteogenesis and angiogenesis. *Theranostics* **8**, 5482–5500 (2018).

101. Williams, D. F. On the nature of biomaterials. *Biomaterials* **30**, 5897–5909 (2009).

102. Sheikh, Z., Brooks, P. J., Barzilay, O., Fine, N. & Glogauer, M. Macrophages, foreign body giant cells and their response to implantable biomaterials. *Materials* vol. 8 5671–5701 (2015).

103. ten Harkel, B. *et al.* The Foreign Body Giant Cell Cannot Resorb Bone, But Dissolves Hydroxyapatite Like Osteoclasts. *PLoS One* **10**, e0139564 (2015).

104. Zaiss, D. M. W., Gause, W. C., Osborne, L. C. & Artis, D. Emerging functions of amphiregulin in orchestrating immunity, inflammation, and tissue repair. *Immunity* vol. 42 216–226 (2015).

105. Zhu, J. *et al.* Amphiregulin-EGFR Signaling Mediates the Migration of Bone Marrow Mesenchymal Progenitors toward PTH-Stimulated Osteoblasts and Osteocytes. *PLoS One* **7**, e50099 (2012).

106. Lu, C., Marcucio, R. & Miclau, T. Assessing angiogenesis during fracture healing. *Iowa Orthop. J.* **26**, 17–26 (2006).

107. Hankenson, K. D., Dishowitz, M., Gray, C. & Schenker, M. Angiogenesis in bone regeneration. *Injury* **42**, 556–561 (2011).

108. Street, J. *et al.* Vascular endothelial growth factor stimulates bone repair by promoting angiogenesis and bone turnover. *Proc. Natl. Acad. Sci. U. S. A.* **99**, 9656–9661 (2002).

109. Oryan, A., Kamali, A., Moshiri, A. & Baghaban Eslaminejad, M. Role of Mesenchymal Stem Cells in Bone Regenerative Medicine: What Is the Evidence? *Cells Tissues Organs* **204**, 59–83 (2017).

110. Long, E. G., Buluk, M., Gallagher, M. B., Schneider, J. M. & Brown, J. L. Human mesenchymal stem cell morphology, migration, and differentiation on micro and

nano-textured titanium. *Bioact. Mater.* **4**, 249–255 (2019).

111. Okada, K. *et al.* Stromal cell-derived factor-1 mediates changes of bone marrow stem cells during the bone repair process. *Am. J. Physiol. Metab.* **310**, E15–E23 (2016).

112. Liu, X. *et al.* SDF-1/CXCR4 axis modulates bone marrow mesenchymal stem cell apoptosis, migration and cytokine secretion. *Protein Cell* **2**, 845–854 (2011).

113. Marquez-Curtis, L. A. & Janowska-Wieczorek, A. Enhancing the migration ability of mesenchymal stromal cells by targeting the SDF-1/CXCR4 axis. *BioMed Research International* vol. 2013 (2013).

114. Puleo, D. A. & Nanci, A. Understanding and controlling the bone-implant interface. *Biomaterials* **20**, 2311–2321 (1999).

115. Davies, J. E. In vitro modeling of the bone/implant interface. *Anat. Rec.* **245**, 426–445 (1996).

116. Davies, J. E. Understanding peri-implant endosseous healing. *J. Dent. Educ.* **67**, 932–949 (2003).

117. Friedenstein, A. J., Piatetzky-Shapiro, I. I. & Petrakova, K. V. Osteogenesis in transplants of bone marrow cells. *J. Embryol. Exp. Morphol.* **16**, 381–390 (1966).

118. Caplan, A. I. Mesenchymal stem cells. *J. Orthop. Res.* **9**, 641–50 (1991).

119. James, S., Fox, J., Afsari, F., Lee, J., Clough, S., Kight, C., Ashmore, J., Ashton, P., Preham, O., Hoogduijn, M., Ponzoni, R., Hancock, Y., Coles, M., Genever, P. Multiparameter Analysis of Human Bone Marrow Stromal Cells Identifies Distinct Immunomodulatory and Differentiation-Competent Subtypes. *Stem Cell Reports* **4**, 1004-1015 (2015).

120. Pittenger, M. F. *et al.* Multilineage potential of adult human mesenchymal stem cells. *Science* **284**, 143–7 (1999).

121. Dominici, M. *et al.* Minimal criteria for defining multipotent mesenchymal stromal cells. The International Society for Cellular Therapy position statement. *Cytotherapy* **8**, 315–7 (2006).

122. Zaidi, M. Skeletal remodeling in health and disease. *Nature Medicine* vol. 13 791–801 (2007).

123. Kang, S. *et al.* Wnt signaling stimulates osteoblastogenesis of mesenchymal precursors by suppressing CCAAT/enhancer-binding protein α and peroxisome proliferator-activated receptor γ. *J. Biol. Chem.* **282**, 14515–14524 (2007).

124. Guo, Y. *et al.* BMP-IHH-mediated interplay between mesenchymal stem cells and osteoclasts supports calvarial bone homeostasis and repair. *Bone Res.* **6**, (2018).

125. Long, M. W. Osteogenesis and bone-marrow-derived cells. in *Blood Cells, Molecules, and Diseases* vol. 27 677–690 (Academic Press Inc., 2001).

126. Lee, M. H. *et al.* Transient upregulation of CBFA1 in response to bone morphogenetic protein-2 and transforming growth factor beta1 in C2C12 myogenic cells coincides with suppression of the myogenic phenotype but is not sufficient for osteoblast differentiation. *J. Cell. Biochem.* **73**, 114–25 (1999).

127. Chen, G., Deng, C. & Li, Y. P. TGF-β and BMP signaling in osteoblast differentiation and bone formation. *International Journal of Biological Sciences* vol. 8 272–288 (2012).

128. Gaur, T. *et al.* Canonical WNT signaling promotes osteogenesis by directly stimulating Runx2 gene expression. *J. Biol. Chem.* **280**, 33132–33140 (2005).

129. McCarthy, T. L. & Centrella, M. Novel links among Wnt and TGF-βsignaling and Runx2. *Mol. Endocrinol.* **24**, 587–597 (2010).

130. Zhou, X. *et al.* Multiple functions of Osterix are required for bone growth and homeostasis in postnatal mice. *Proc. Natl. Acad. Sci. U. S. A.* **107**, 12919–12924 (2010).

131. Xiao, G. *et al.* Bone Morphogenetic Proteins, Extracellular Matrix, and Mitogen-Activated Protein Kinase Signaling Pathways Are Required for Osteoblast-Specific Gene Expression and Differentiation in MC3T3-E1 Cells. *J. Bone Miner. Res.* **17**, 101–110 (2002).

132. Komekado, H., Yamamoto, H., Chiba, T. & Kikuchi, A. Glycosylation and palmitoylation of Wnt-3a are coupled to produce an active form of Wnt-3a. *Genes to Cells* **12**, 521–534 (2007).

133. Huang, H. C. & Klein, P. S. The frizzled family: Receptor for multiple signal transduction pathways. *Genome Biology* vol. 5 (2004).

134. MacDonald, B. T. & He, X. Frizzled and LRp5/6 receptors for wnt/β-catenin signaling. *Cold Spring Harb. Perspect. Biol.* **4**, (2012).

135. De, A. Wnt/Ca2+ signaling pathway: a brief overview. *Acta Biochim. Biophys. Sin. (Shanghai).* **43**, 745–756 (2011).

136. Green, J., Nusse, R. & van Amerongen, R. The role of Ryk and Ror receptor tyrosine kinases in wnt signal transduction. *Cold Spring Harb. Perspect. Biol.* **6**, (2014).

137. Chen, C. *et al.* Aberrant activation of Wnt/β-catenin signaling drives proliferation of bone sarcoma cells. *Oncotarget* **6**, 17570–17583 (2015).

138. Medina, M. & Wandosell, F. Deconstructing GSK-3: The fine regulation of its activity. *International Journal of Alzheimer's Disease* (2011) doi:10.4061/2011/479249.

139. Krishnan, V., Bryant, H. U. & MacDougald, O. A. Regulation of bone mass by Wnt signaling. *Journal of Clinical Investigation* vol. 116 1202–1209 (2006).

140. Bennett, C. N. *et al.* Regulation of osteoblastogenesis and bone mass by Wnt10b. *Proc. Natl. Acad. Sci. U. S. A.* **102**, 3324–3329 (2005).

141. Kim, J. B. *et al.* Bone regeneration is regulated by Wnt signaling. *J. Bone Miner. Res.* **22**, 1913–1923 (2007).

142. Little, R. D. *et al.* A mutation in the LDL receptor-related protein 5 gene results in the autosomal dominant high-bone-mass trait. *Am. J. Hum. Genet.* **70**, 11–19 (2002).

143. Morvan, F. *et al.* Deletion of a single allele of the Dkk1 gene leads to an increase in bone formation and bone mass. *J. Bone Miner. Res.* **21**, 934–945 (2006).

144. Freshney, R. I. *Culture of Animal Cells: A Manual of Basic Technique and Specialized Applications*. (Wiley Blackwell, 2015).

145. Ringer, S. Concerning the Influence exerted by each of the Constituents of the Blood on the Contraction of the Ventricle. *J. Physiol.* **3**, 380–393 (1882).

146. Jedrzejczak-Silicka, M. History of Cell Culture. in *New Insights into Cell Culture Technology* (InTech, 2017). doi:10.5772/66905.

147. Arora, M. Cell Culture Media: A Review. *Mater. Methods* **3**, (2013).

148. Dulbecco, R. & Freeman, G. Plaque production by the polyoma virus. *Virology* vol. 8 396–397 (1959).

149. HAM, R. G. Clonal growth of mammalian cells in a chemically defined, synthetic medium. *Proc. Natl. Acad. Sci. U. S. A.* **53**, 288–293 (1965).

150. Rezaei, M., Zarkesh-Esfahani, S. H. & Gharagozloo, M. The effect of different media composition and temperatures on the production of recombinant human growth hormone by CHO cells. *Res. Pharm. Sci.* **8**, 211–217 (2013).

151. Guilbert, L. J. & Iscove, N. N. Partial replacement of serum by selenite, transferrin, albumin and lecithin in haemopoitec cell cultures. *Nature* **263**, 594–595 (1976).

152. Moore, G. E., Gerner, R. E. & Franklin, H. A. Culture of Normal Human Leukocytes. *JAMA J. Am. Med. Assoc.* **199**, 519–524 (1967).

153. Moore, G. E. . et al. Culture of Human Leukemia Cells. *Cancer* **19**, 713-723 (.

154. Hodgson, J. Checking sources: The serum supply secret. *Bio/Technology* **9**, 1320–1324 (1991).

155. Mellor, D. J., Diesch, T. J., Gunn, A. J. & Bennet, L. The importance of 'awareness' for understanding fetal pain. *Brain Research Reviews* vol. 49 455–471 (2005).

156. More, S. *et al.* Animal welfare aspects in respect of the slaughter or killing of pregnant livestock animals (cattle, pigs, sheep, goats, horses). *EFSA J.* **15**, (2017).

157. Global Fetal Bovine Serum Market | Opportunity Analysis & Industry Forecast to 2025 - ResearchAndMarkets.com | Business Wire. https://www.businesswire.com/news/home/20191022005912/en/Global-Fetal-Bovine-Serum-Market-Opportunity-Analysis.

158. Törnqvist, E. *et al.* Strategic focus on 3R principles reveals major reductions in the use of animals in pharmaceutical toxicity testing. *PLoS One* **9**, (2014).

159. Hendriksen, C. F. M. Refinement Reduction, and Replacement of Animal Use for Regulatory Testing: Current Best Scientific Practices for the Evaluation of Safety and Potency of Biologicals. *ILAR J.* **43**, S43–S48 (2002).

160. Van Der Valk, J. *et al.* The humane collection of fetal bovine serum and possibilities for serum-free cell and tissue culture. in *Toxicology in Vitro* vol. 18 1–12 (Elsevier Ltd, 2004).

161. Zheng, X. *et al.* Proteomic Analysis for the Assessment of Different Lots of Fetal

Bovine Serum as a Raw Material for Cell Culture. Part IV. Application of Proteomics to the Manufacture of Biological Drugs. *Biotechnol. Prog.* **22**, 1294–1300 (2008).

162. Furue, M. K. *et al.* Heparin promotes the growth of human embryonic stem cells in a defined serum-free medium. *Proc. Natl. Acad. Sci. U. S. A.* **105**, 13409–13414 (2008).

163. Olivieri, M. P., Kittle, K. H., Tweden, K. S. & Loomis, R. E. Comparative biophysical study of adsorbed calf serum, fetal bovine serum and mussel adhesive protein films. *Biomaterials* **13**, 201–208 (1992).

164. Schmidt, D., Joyce, E. J. & Kao, W. J. Fetal bovine serum xenoproteins modulate human monocyte adhesion and protein release on biomaterials in vitro. *Acta Biomater.* (2011) doi:10.1016/j.actbio.2010.08.022.

165. Yang, C., Tibbitt, M. W., Basta, L. & Anseth, K. S. Mechanical memory and dosing influence stem cell fate. *Nat. Mater.* **13**, 645–652 (2014).

166. Dupont, S. *et al.* Role of YAP/TAZ in mechanotransduction. *Nature* **474**, 179–184 (2011).

167. Park, H. W. *et al.* Alternative Wnt Signaling Activates YAP/TAZ. *Cell* **162**, 780–794 (2015).

168. Fu, J. *et al.* Modulation of the mechanosensing of mesenchymal stem cells by laser-induced patterning for the acceleration of tissue reconstruction through the Wnt/β-catenin signaling pathway activation. *Acta Biomater.* **101**, 152–167 (2020).

169. Li, G., Yang, P., Guo, X., Huang, N. & Shen, R. An in vitro evaluation of inflammation response of titanium functionalized with heparin/fibronectin complex. *Cytokine* **56**, 208–217 (2011).

170. Park, J. W., Hanawa, T. & Chung, J. H. The relative effects of Ca and Mg ions on MSC osteogenesis in the surface modification of microrough Ti implants. *Int. J. Nanomedicine* **14**, 5697–5711 (2019).

171. Galli, C. *et al.* The importance of WNT pathways for bone metabolism and their regulation by implant topography. *European Cells and Materials* vol. 24 46–59 (2012).

172. Hirano, T. *et al.* Proliferation and osteogenic differentiation of human mesenchymal stem cells on zirconia and titanium with different surface topography. *Dent. Mater. J.* **34**, 872–880 (2015).

173. Niu, H. *et al.* Surface Topography Regulates Osteogenic Differentiation of MSCs via Crosstalk between FAK/MAPK and ILK/β-Catenin Pathways in a Hierarchically Porous Environment. *ACS Biomater. Sci. Eng.* **3**, 3161–3175 (2017).

174. Sousa, Â. *et al.* Optimization of peptide-plasmid DNA vectors formulation for gene delivery in cancer therapy exploring design of experiments. *Colloids Surfaces B Biointerfaces* **183**, (2019).

175. Jacyna, J., Kordalewska, M. & Markuszewski, M. J. Design of Experiments in metabolomics-related studies: An overview. *Journal of Pharmaceutical and Biomedical Analysis* vol. 164 598–606 (2019).

176. Antony, J. *Design of experiments for engineers and scientists*. (Butterworth-Heinemann, 2003).

177. Francis, G. L. Albumin and mammalian cell culture: Implications for biotechnology applications. *Cytotechnology* vol. 62 1–16 (2010).

178. Brunner, D. *et al.* Serum-free cell culture: the serum-free media interactive online database. *ALTEX* **27**, 53–62 (2010).

179. Barnes, D. & Sato, G. Serum-free cell culture: a unifying approach. *Cell* vol. 22 649–655 (1980).

180. Doweiko, J. P. & Nompleggi, D. J. Reviews: The Role of Albumin in Human Physiology and Pathophysiology, Part III: Albumin and Disease States. *J. Parenter. Enter. Nutr.* **15**, 476–483 (1991).

181. Merlot, A. M., Kalinowski, D. S. & Richardson, D. R. Unraveling the mysteries of serum albumin - more than just a serum protein. *Front. Physiol.* **5**, (2014).

182. Carter, D. C. & Ho, J. X. Structure of serum albumin. *Adv. Protein Chem.* **45**, 153–176 (1994).

183. Petitpas, I., Grüne, T., Bhattacharya, A. A. & Curry, S. Crystal structures of human serum albumin complexed with monounsaturated and polyunsaturated fatty acids. *J. Mol. Biol.* **314**, 955–960 (2001).

184. Simard, J. R., Zunszain, P. A., Hamilton, J. A. & Curry, S. Location of High and Low Affinity Fatty Acid Binding Sites on Human Serum Albumin Revealed by NMR Drug-competition Analysis. *J. Mol. Biol.* **361**, 336–351 (2006).

185. Trigatti, B. L. & Gerber, G. E. A direct role for serum albumin in the cellular uptake of long-chain fatty acids. *Biochem. J.* **308**, 155–159 (1995).

186. Abumrad, N. A., Sfeir, Z., Connelly, M. A. & Coburn, C. Lipid transporters: Membrane transport systems for cholesterol and fatty acids. *Current Opinion in Clinical Nutrition and Metabolic Care* vol. 3 255–262 (2000).

187. Stremmel, W., Pohl, J., Ring, A. & Herrmann, T. A new concept of cellular uptake and intracellular trafficking of long-chain fatty acids. *Lipids* **36**, 981–989 (2001).

188. Zhao, Y. & Marcel, Y. L. Serum albumin is a significant intermediate in cholesterol transfer between cells and lipoproteins. *Biochemistry* **35**, 7174–7180 (1996).

189. Ha, J. S. *et al.* Human serum albumin and its structural variants mediate cholesterol efflux from cultured endothelial cells. *Biochim. Biophys. Acta - Mol. Cell Res.* **1640**, 119–128 (2003).

190. Halliwell, B. & Whiteman, M. Measuring reactive species and oxidative damage in vivo and in cell culture: How should you do it and what do the results mean? *British Journal of Pharmacology* vol. 142 231–255 (2004).

191. Roche, M., Rondeau, P., Singh, N. R., Tarnus, E. & Bourdon, E. The antioxidant properties of serum albumin. *FEBS Letters* vol. 582 1783–1787 (2008).

192. Jacobia, S. J. *et al.* Trace element optimization enhances performance and reproducibility of serum-free medium. in *Animal Cell Technology: Basic &*

Applied Aspects 193–199 (Springer Netherlands, 2006). doi:10.1007/1-4020-4457-7_27.

193. Keenan, J. *et al.* Unexpected fluctuations of trace element levels in cell culture medium in vitro: caveat emptor. *Vitr. Cell. Dev. Biol. - Anim.* **54**, 555–558 (2018).

194. Arigony, A. L. V. *et al.* The influence of micronutrients in cell culture: A reflection on viability and genomic stability. *BioMed Research International* vol. 2013 (2013).

195. Esaki, N. & Soda, K. [Trace elements as activation factors of enzymes: characteristic enzymes and their activation mechanisms]. *Nihon Rinsho.* **54**, 17–25 (1996).

196. Yuk, I. H. *et al.* Effects of copper on CHO cells: Cellular requirements and product quality considerations. *Biotechnol. Prog.* **31**, 226–238 (2015).

197. Savonnière, S. *et al.* Effects of lipid supplementation of culture media on cell growth, antibody production, membrane structure and dynamics in hybridomas. *J. Biotechnol.* **48**, 161–173 (1996).

198. Bailey, J. M., Howard, B. V & Tillman, S. F. Lipid metabolism in cultured cells xi. Utilization of serum triglycerides. *The journal of biological chemistry* **24** (1973).

199. Huawei, Z. Selenium as an essential micronutrient: Roles in cell cycle and apoptosis. *Molecules* **14**, 1263–1278 (2009).

200. McKeehan, W. L., Hamilton, W. G. & Ham, R. G. Selenium is an essential trace nutrient for growth of WI-38 diploid human fibroblasts. *Proc. Natl. Acad. Sci. U. S. A.* **73**, 2023–2027 (1976).

201. Zhang, J., Robinson, D. & Salmon, P. A novel function for selenium in biological system: Selenite as a highly effective iron carrier for Chinese hamster ovary cell growth and monoclonal antibody production. *Biotechnol. Bioeng.* **95**, 1188–1197 (2006).

202. Stout, R. W., Bierman, E. L. & Ross, R. *Effect of Insulin on the Proliferation of Cultured Primate Arterial Smooth Muscle Cells*. http://ahajournals.org.

203. Rhee, Y. H. *et al.* Insulin concentration is critical in culturing human neural stem cells and neurons. *Cell Death Dis.* **4**, (2013).

204. Bertrand, F. *et al.* A role for nuclear factor κB in the antiapoptotic function of insulin. *J. Biol. Chem.* **273**, 2931–2938 (1998).

205. Rampalli, A. M. & Zelenka, P. S. Insulin regulates expression of c-fos and c-jun and suppresses apoptosis of lens epithelial cells. *Cell Growth Differ.* **6**, 945–53 (1995).

206. Kang, S. *et al.* Insulin can block apoptosis by decreasing oxidative stress via phosphatidylinositol 3-kinase- and extracellular signal-regulated protein kinase-dependent signaling pathways in HepG2 cells. *Eur. J. Endocrinol.* **148**, 147–155 (2003).

207. Conrad, M. E., Umbreit, J. N., Moore, E. G. Iron Absorption and Transport. *Am. J. Med. Sci.* **318**, 213 (1999).

208. Kan, M. & Yamane, I. Effects of ferrous iron and transferrin on cell proliferation

of human diploid fibroblasts in serum-free culture. *In Vitro* **20**, 89–94 (1984).

209. Kovář, J. & Franěk, F. Growth-stimulating effect of transferrin on a hybridoma cell line: Relation to transferrin iron-transporting function. *Exp. Cell Res.* **182**, 358–369 (1989).

210. Keenan, J., Pearson, D., O'Driscoll, L., Gammell, P. & Clynes, M. Evaluation of recombinant human transferrin (DeltaFerrin™) as an iron chelator in serum-free media for mammalian cell culture. *Cytotechnology* **51**, 29–37 (2006).

211. Richardson, D. R. & Ponka, P. The molecular mechanisms of the metabolism and transport of iron in normal and neoplastic cells. *Biochim. Biophys. Acta - Rev. Biomembr.* **1331**, 1–40 (1997).

212. Laskey, J., Webb, I., Schulman, H. M. & Ponka, P. Evidence that transferrin supports cell proliferation by supplying iron for DNA synthesis. *Exp. Cell Res.* **176**, 87–95 (1988).

213. Claassen, D. A., Desler, M. M. & Rizzino, A. ROCK inhibition enhances the recovery and growth of cryopreserved human embryonic stem cells and human induced pluripotent stem cells. *Mol. Reprod. Dev.* **76**, 722–732 (2009).

214. Vernardis, S. I., Terzoudis, K., Panoskaltsis, N. & Mantalaris, A. Human embryonic and induced pluripotent stem cells maintain phenotype but alter their metabolism after exposure to ROCK inhibitor. *Sci. Rep.* **7**, (2017).

215. Heng, B. C. Effect of Rho-associated kinase (ROCK) inhibitor Y-27632 on the post-thaw viability of cryopreserved human bone marrow-derived mesenchymal stem cells. *Tissue Cell* **41**, 376–380 (2009).

216. Nakamura, K., Yoshimura, A., Kaneko, T., Sato, K. & Hara, Y. ROCK inhibitor Y-27632 maintains the proliferation of confluent human mesenchymal stem cells. *J. Periodontal Res.* **49**, 363–370 (2014).

217. Ling, L. *et al.* Effect of heparin on the biological properties and molecular signature of human mesenchymal stem cells. *Gene* **576**, 292–303 (2016).

218. Sharonov, G. V., Balatskaya, M. N. & Tkachuk, V. A. Glycosylphosphatidylinositol-anchored proteins as regulators of cortical cytoskeleton. *Biochemistry (Moscow)* vol. 81 636–650 (2016).

219. Matas, D., Juknat, A., Pietr, M., Klin, Y. & Vogel, Z. Anandamide protects from low serum-induced apoptosis via its degradation to ethanolamine. *J. Biol. Chem.* **282**, 7885–7892 (2007).

220. Sasaki, H., Kume, H., Nemoto, A., Narisawa, S. & Takahashi, N. Ethanolamine modulates the rate of rat hepatocyte proliferation in vitro and in vivo. *Proc. Natl. Acad. Sci. U. S. A.* **94**, 7320–7325 (1997).

221. Kano-Sueoka, T., Oda, D. & Kawamoto, J. K. Phosphatidylethanolamine deficiency in membrane lipids inhibits keratinocyte intercellular networks formation. *Vitr. Cell. Dev. Biol. - Anim.* **37**, 691–697 (2001).

222. Wu, R., Wolfe, R. A. & Sato, G. H. Distinctive effects of hydrocortisone on the modulation of EGF binding and cell growth in hela cells grown in defined medium. *J. Cell. Physiol.* **108**, 83–90 (1981).

223. Arpels, C., Babcock, V. I. & Southam, C. M. Effect of Steroids on Human Cell

Cultures; Sustaining Effect of Hydrocortisone. *Exp. Biol. Med.* **115**, 102–106 (1964).

224. Fujisawa, K. *et al.* Evaluation of the effects of ascorbic acid on metabolism of human mesenchymal stem cells. *Stem Cell Res. Ther.* **9**, 93 (2018).

225. Choi, K. M. *et al.* Effect of ascorbic acid on bone marrow-derived mesenchymal stem cell proliferation and differentiation. *J. Biosci. Bioeng.* **105**, 586–594 (2008).

226. Hee Kim, M., Ok Kim, M., Hee Kim, Y., Sang Kim, J. & Jae Han, H. *Linoleic Acid Induces Mouse Embryonic Stem Cell Proliferation Via Ca 2+ /PKC, PI3K/Akt, and MAPKs*. *Original Paper Cell Physiol Biochem* vol. 23 www.karger.comwww.karger.com/cpb (2009).

227. Lehrich, B. M., Liang, Y., Khosravi, P., Federoff, H. J. & Fiandaca, M. S. Fetal Bovine Serum-Derived Extracellular Vesicles Persist within Vesicle-Depleted Culture Media. *Int. J. Mol. Sci.* **19**, (2018).

228. Frank, N. D., Jones, M. E., Vang, B. & Coeshott, C. Evaluation of reagents used to coat the hollow-fiber bioreactor membrane of the Quantum® Cell Expansion System for the culture of human mesenchymal stem cells. *Mater. Sci. Eng. C* **96**, 77–85 (2019).

229. Hanley, P. J. *et al.* Efficient manufacturing of therapeutic mesenchymal stromal cells with the use of the Quantum Cell Expansion System. *Cytotherapy* **16**, 1048–1058 (2014).

230. Russell, A. L., Lefavor, R. C. & Zubair, A. C. Characterization and cost–benefit analysis of automated bioreactor-expanded mesenchymal stem cells for clinical applications. *Transfusion* **58**, 2374–2382 (2018).

231. Aebli, N. *et al.* In vivo comparison of the osseointegration of vacuum plasma sprayed titanium- and hydroxyapatite-coated implants. *J. Biomed. Mater. Res. - Part A* **66**, 356–363 (2003).

232. Chagnon, P. & Fauchais, P. Thermal spraying of ceramics. *Ceramics International* **10** 119–131 (1984).

233. Tong, W. *et al.* Effect of particle size on molten states of starting powder and degradation of the relevant plasma-sprayed hydroxyapatite coatings. *Biomaterials* **17**, 1507–1513 (1996).

234. Levingstone, T. J. *et al.* Application of response surface methodology in the design of functionally graded plasma sprayed hydroxyapatite coatings. *Surf. Coatings Technol.* **313**, 307–318 (2017).

235. Fauchais, P., Montavon, G. & Bertrand, G. From Powders to Thermally Sprayed Coatings. doi:10.1007/s11666-009-9435-x.

236. Candidato, Jr R., Sokolowski, P., Latka, L., Kozerski, S., Pawlowski, L., Denoirjean, A. Plasma spraying of hydroxyapatite coatings using powder, suspension and solution feedstocks. *Przegląd Spawalnictwa* **87** 64-71 (2015).

237. Gross, K. A. & Berndt, C. C. Thermal processing of hydroxyapatite for coating production. *J. Biomed. Mater. Res.* **39**, 580–587 (1998).

238. Rennie, R. *A Dictionary of Chemistry*. *A Dictionary of Chemistry* (Oxford University Press, 2016). doi:10.1093/acref/9780198722823.001.0001.

239. Chakravorty, N. *et al.* Pro-osteogenic topographical cues promote early activation of osteoprogenitor differentiation via enhanced TGFβ, Wnt, and Notch signaling. *Clin. Oral Implants Res.* **25**, 475–86 (2014).

240. Saleh, F., Carstairs, A., Etheridge, S. L. & Genever, P. Real-Time Analysis of Endogenous Wnt Signalling in 3D Mesenchymal Stromal Cells. *Stem Cells Int.* **2016**, (2016).

241. De Boer, J., Wang, H. J. & Van Blitterswijk, C. Effects of Wnt Signaling on Proliferation and Differentiation of Human Mesenchymal Stem Cells. in *Tissue Engineering* vol. 10 393–401 (2004).

242. Moon, J. S. *et al.* Inhibition of human mesenchymal stem cell proliferation via Wnt signaling activation. *J. Cell. Biochem.* **119**, 1670–1678 (2018).

243. Kim, J. A., Choi, H. K., Kim, T. M., Leem, S. H. & Oh, I. H. Regulation of mesenchymal stromal cells through fine tuning of canonical Wnt signaling. *Stem Cell Res.* **14**, 356–368 (2015).

244. Teo, J. L. & Kahn, M. The Wnt signaling pathway in cellular proliferation and differentiation: A tale of two coactivators. *Advanced Drug Delivery Reviews* vol. 62 1149–1155 (2010).

245. Olivares-Navarrete, R., Hyzy, S., Wieland, M., Boyan, B. D. & Schwartz, Z. The roles of Wnt signaling modulators Dickkopf-1 (Dkk1) and Dickkopf-2 (Dkk2) and cell maturation state in osteogenesis on microstructured titanium surfaces. *Biomaterials* **31**, 2015–2024 (2010).

246. Wang, W. *et al.* The role of the Wnt/β-catenin pathway in the effect of implant topography on MG63 differentiation. *Biomaterials* **33**, 7993–8002 (2012).

247. Galli, C. *et al.* Actin cytoskeleton controls activation of Wnt/β-catenin signaling in mesenchymal cells on implant surfaces with different topographies. *Acta Biomater.* **8**, 2963–2968 (2012).

248. McMurray, R. J., Wann, A. K. T., Thompson, C. L., Connelly, J. T. & Knight, M. M. Surface topography regulates wnt signaling through control of primary cilia structure in mesenchymal stem cells. *Sci. Rep.* **3**, 3545 (2013).

249. Boland, G. M., Perkins, G., Hall, D. J. & Tuan, R. S. Wnt 3a promotes proliferation and suppresses osteogenic differentiation of adult human mesenchymal stem cells. *J. Cell. Biochem.* **93**, 1210–1230 (2004).

250. Gustavsson, J., Ginebra, M. P., Engel, E. & Planell, J. Ion reactivity of calcium-deficient hydroxyapatite in standard cell culture media. *Acta Biomater.* **7**, 4242–4252 (2011).

251. Combes, C. & Rey, C. Amorphous calcium phosphates: Synthesis, properties and uses in biomaterials. *Acta Biomater.* **6**, 3362–3378 (2010).

252. Wang, L. & Nancollas, G. H. Calcium Orthophosphates: Crystallization and Dissolution. doi:10.1021/cr0782574.

253. Lu, J. *et al.* The biodegradation mechanism of calcium phosphate biomaterials in bone. *J. Biomed. Mater. Res.* **63**, 408–412 (2002).

254. Yu, S., Yerges-Armstrong, L. M., Chu, Y., Zmuda, J. M. & Zhang, Y. E2F1 effects on osteoblast differentiation and mineralization are mediated through up-

regulation of frizzled-1. *Bone* **56**, 234–241 (2013).

255. Olivares-Navarrete, R. *et al.* Role of non-canonical Wnt signaling in osteoblast maturation on microstructured titanium surfaces. *Acta Biomater.* **7**, 2740–2750 (2011).

256. MacDonald, B. T., Tamai, K. & He, X. Wnt/β-catenin signaling: components, mechanisms, and diseases. *Dev. Cell* **17**, 9–26 (2009).

257. Clevers, H. & Nusse, R. Wnt/β-catenin signaling and disease. *Cell* **149**, 1192–1205 (2012).

258. Karow, M. *et al.* Wnt signalling in mouse mesenchymal stem cells: Impact on proliferation, invasion and MMP expression. *J. Cell. Mol. Med.* **13**, 2506–2520 (2009).

259. Tagaya, M. *et al.* Protein adsorption and subsequent fibroblasts adhesion on hydroxyapatite nanocrystals. in *IOP Conference Series: Materials Science and Engineering* vol. 18 (2011).

260. Pascual, M., Plastre, O., Montdargent, B., Labarre, D. & Schifferli, J. A. Specific interactions of polystyrene biomaterials with factor D of human complement. *Biomaterials* **14**, 665–670 (1993).

261. Lee, J. S., Yu, X., Wagoner Johnson, A. J. & Murphy, W. L. Mineral binding peptides with enhanced binding stability in serum. *Biomater. Sci.* **5**, 663–668 (2017).

262. Lyle, D. B., Bushar, G. S. & Langone, J. J. Screening biomaterials for functional complement activation in serum. *J. Biomed. Mater. Res. - Part A* **92**, 205–213 (2010).

263. Tekkatte, C., Gunasingh, G. P., Cherian, K. M. & Sankaranarayanan, K. 'Humanized' stem cell culture techniques: the animal serum controversy. *Stem Cells Int.* **2011**, 504723 (2011).

264. Hodgson, J. Fetal bovine seram revisited: A year ago serum regulations were a hodgepodge. has anything changed? *Bio/Technology* vol. 11 49–53 (1993).

265. Hwang, S. K. Experience of Complications of Hip Arthroplasty. *Hip Pelvis* **26**, 207 (2014).

266. Maniatopoulos, G., Hopkins, C., Joyce, T. J. & Brittain, K. Framing the failure of medical implants: Media representations of the ASR hip replacements in the UK. *Heal. Expect.* **22**, 518–527 (2019).

267. Stevens, S. *Performance Report*. (2018).

268. McCabe, A., Pickford, M. & Shawcross, J. The History, Technical Specifications and Efficacy of Plasma Spray Coatings Applied to Joint Replacement Prostheses. *Reconstr. Rev.* **6**, (2016).

269. Bacakova, L., Filova, E., Parizek, M., Ruml, T. & Svorcik, V. Modulation of cell adhesion, proliferation and differentiation on materials designed for body implants. *Biotechnology Advances* vol. 29 739–767 (2011).

270. ISO - ISO 13779-2:2018 - Implants for surgery — Hydroxyapatite — Part 2: Thermally sprayed coatings of hydroxyapatite.

https://www.iso.org/standard/64617.html.

271. Mendicino, M., Bailey, A. M., Wonnacott, K., Puri, R. K. & Bauer, S. R. MSC-based product characterization for clinical trials: An FDA perspective. *Cell Stem Cell* vol. 14 141–145 (2014).

272. Brindley, D. A. *et al.* Peak serum: implications of serum supply for cell therapy manufacturing. *Regen. Med* **7**, 7–13 (2012).

273. Chase, L. G., Lakshmipathy, U., Solchaga, L. A., Rao, M. S. & Vemuri, M. C. A novel serum-free medium for the expansion of human mesenchymal stem cells. *Stem Cell Res. Ther.* **1**, 8 (2010).

274. Devireddy, L. R., Myers, M., Screven, R., Liu, Z. & Boxer, L. A serum-free medium formulation efficiently supports isolation and propagation of canine adipose-derived mesenchymal stem/stromal cells. *PLoS One* **14**, e0210250 (2019).

275. Radford, K., Niloperbowo, W., Reid, S. & Greenfield, P. F. Weaning of three hybridoma cell lines to serum free low protein medium. *Cytotechnology* **6**, 65–78 (1991).

276. Valk, J. Van Der *et al.* Optimization of chemically defined cell culture media. *Toxicol. Vitr.* 1053–1063 (2010) doi:10.1016/B978-0-08-054808-1.00009-0.

277. Marupanthorn, A., Tantrawatpan, C., Kheolamai, P., Tantikanlayaporn, D. & Manochantr, S. Bone morphogenetic protein-2 enhances the osteogenic differentiation capacity of mesenchymal stromal cells derived from human bone marrow and umbilical cord. *Int. J. Mol. Med.* **39**, 654–662 (2017).

278. Théry, C. *et al.* Minimal information for studies of extracellular vesicles 2018 (MISEV2018): a position statement of the International Society for Extracellular Vesicles and update of the MISEV2014 guidelines. *J. Extracell. Vesicles* **7**, (2018).

279. Watson, D. C. *et al.* Efficient production and enhanced tumor delivery of engineered extracellular vesicles. *Biomaterials* **105**, 195–205 (2016).

280. Murphy, D. E. *et al.* Extracellular vesicle-based therapeutics: natural versus engineered targeting and trafficking. *Experimental and Molecular Medicine* vol. 51 (2019).

281. Cabezas, M. D., Eichelsdoerfer, D. J., Brown, K. A., Mrksich, M. & Mirkin, C. A. Combinatorial screening of mesenchymal stem cell adhesion and differentiation using polymer pen lithography. in *Methods in Cell Biology* vol. 119 261–276 (Academic Press Inc., 2014).

282. Yang, Y. *et al.* Influence of Cell Spreading Area on the Osteogenic Commitment and Phenotype Maintenance of Mesenchymal Stem Cells. *Sci. Rep.* **9**, (2019).

283. Dawson, E. R., Suzuki, R. K., Samano, M. A. & Murphy, M. B. Increased internal porosity and surface area of hydroxyapatite accelerates healing and compensates for low bone marrow mesenchymal stem cell concentrations in critically-sized bone defects. *Appl. Sci.* **8**, (2018).

284. Jin, K. *et al.* In vivo vascularization of MSC-loaded porous hydroxyapatite constructs coated with VEGF-functionalized collagen/heparin multilayers. *Sci. Rep.* **6**, (2016).

285. Gao, J., Dong, X. & Wang, Z. Generation, purification and engineering of extracellular vesicles and their biomedical applications. *Methods* (2019) doi:10.1016/j.ymeth.2019.11.012.

Appendix A – Chemically defined medium development

Trace Elements composition

Appendix 1: List of trace element concentrations in commercial trace elements mixes B and C (Corning, 25-022-CI; 25-023-CI respectively).

Trace Elements Mix	Component	Units	Concentration
Trace Elements B	**MnSO4 • H20**	mg/L	1.70×10^{-1}
	Na2SiO3 • 9H20	mg/L	1.40×10^{-2}
	Molydbic acid, ammonium salt	mg/L	1.24
	NH4VO3	mg/L	6.50×10^{-1}
	NiSO4 • 6H2O	mg/L	1.30×10^{-1}
	SnCl2 (anhydrous)	mg/L	1.20×10^{-1}
Trace Elements C	**AlCl3 • 6H2O**	mg/L	1.20
	AgNO3	mg/L	1.70×10^{-1}
	Ba(C2H3O2)	mg/L	2.55
	KBr	mg/L	1.20×10^{-1}
	CdCl2	mg/L	2.28
	CoCl2 • 6H2O	mg/L	2.38
	CrCl3 (anhydrous)	mg/L	3.20×10^{-1}
	NaF	mg/L	4.20
	GeO2	mg/L	5.30×10^{-1}
	KI	mg/L	1.70×10^{-1}
	RbCl	mg/L	1.21
	ZrOCl2 • 8H2O	mg/L	3.22

Lipid Mix composition

Appendix 2: Lipid mixture (Sigma Aldrich, L5146) composition

	Component	Units	Concentration
Lipid Mix	**Arachidonic acid**	µg/ml	2.00
	Linoleic acid	µg/ml	1.00 x 10
	Linolenic acid	µg/ml	1.00 x 10
	Myristic acid	µg/ml	1.00 x 10
	Oleic acid	µg/ml	1.00 x 10
	Palmitic acid	µg/ml	1.00 x 10
	Stearic Acid	µg/ml	1.00 x 10
	Cholesterol (NZ Sheep's wool)	mg/ml	2.20×10^{-1}
	Tween-80	mg/ml	2.20
	Tocopherol acetate	µg/ml	7.00 x 10
	Pluronic F-68	mg/ml	1.00×10^{-2}

DoE I main effects and interactions

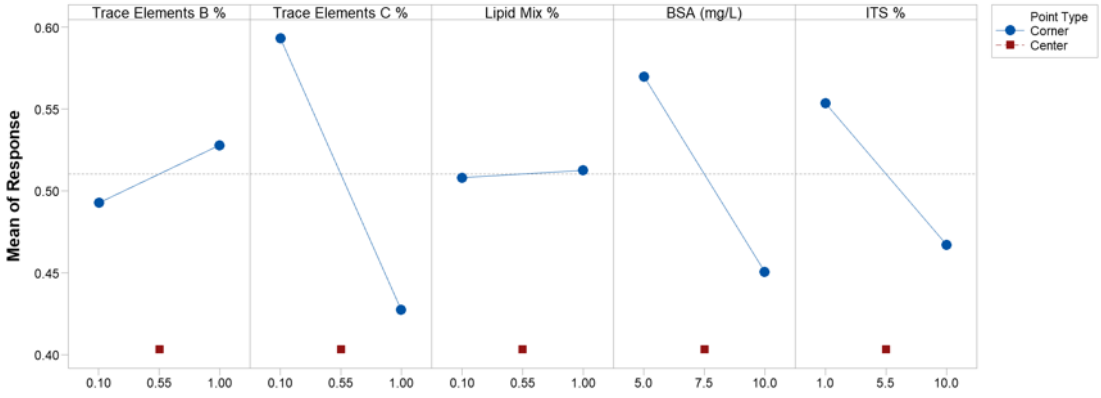

Appendix 3: Main effects plot of changes in mean Y201 viability in response to changing concentrations of CDM components as measured by Alamar blue after 10 days in culture (n = 3; α = 0.15).

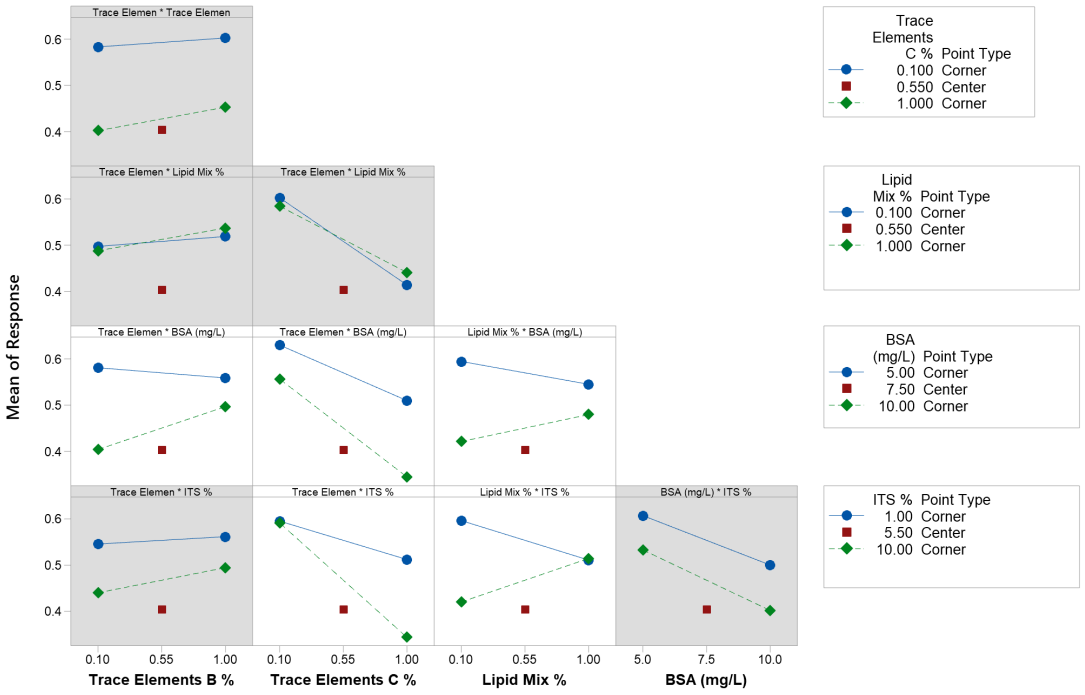

Appendix 4: Interaction plot for Y201 viability 10 days post media change as measured by Alamar blue. Grey boxes indicate non-significant interactions which have been removed from the model (n = 3; α = 0.15).

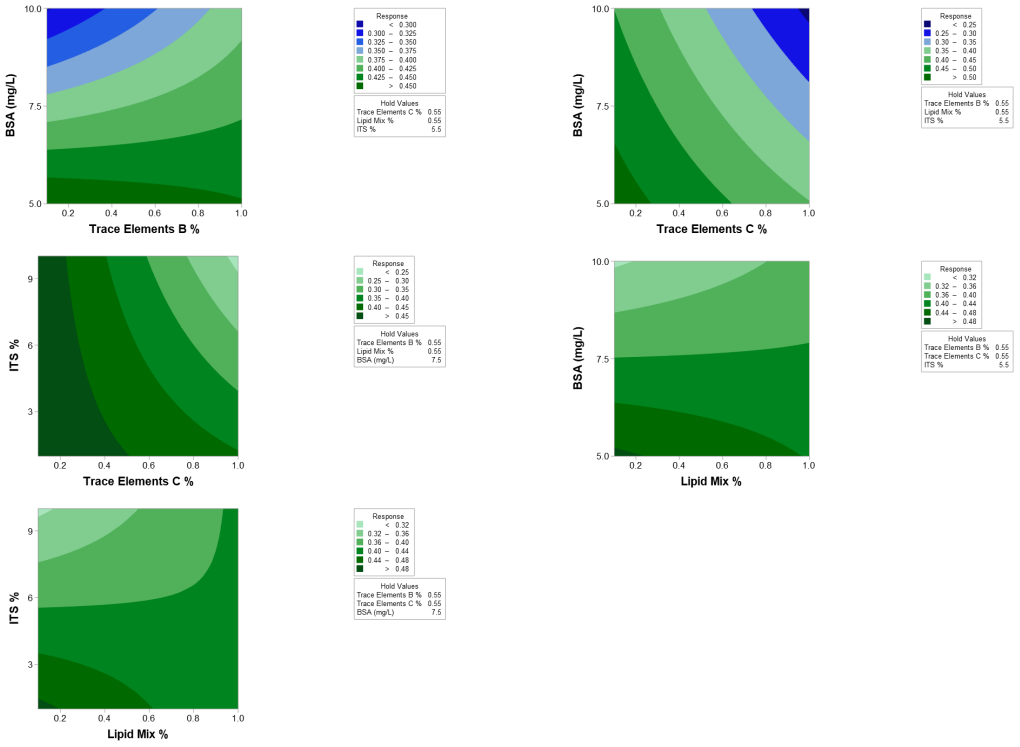

Appendix 5: Contour plots of significant interactions in Y201 viability response to changing CDM component concentrations as assessed by Alamar blue after 10 days in culture (n = 3; α = 0.15).

DoE II main effects and interactions

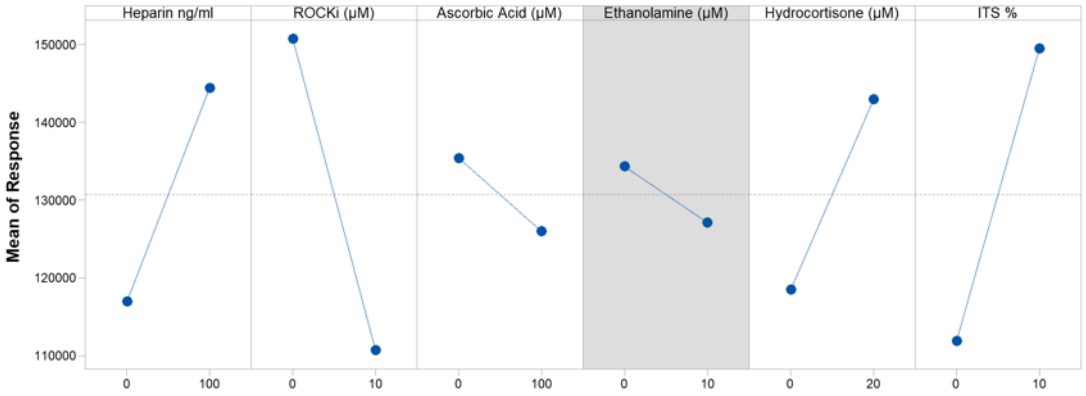

Appendix 6: Main effects plot of changes in mean Y201 viability as measured by Alamar blue after 10 days in culture in response to changing concentrations of CDM components. (n = 3; α = 0.15).

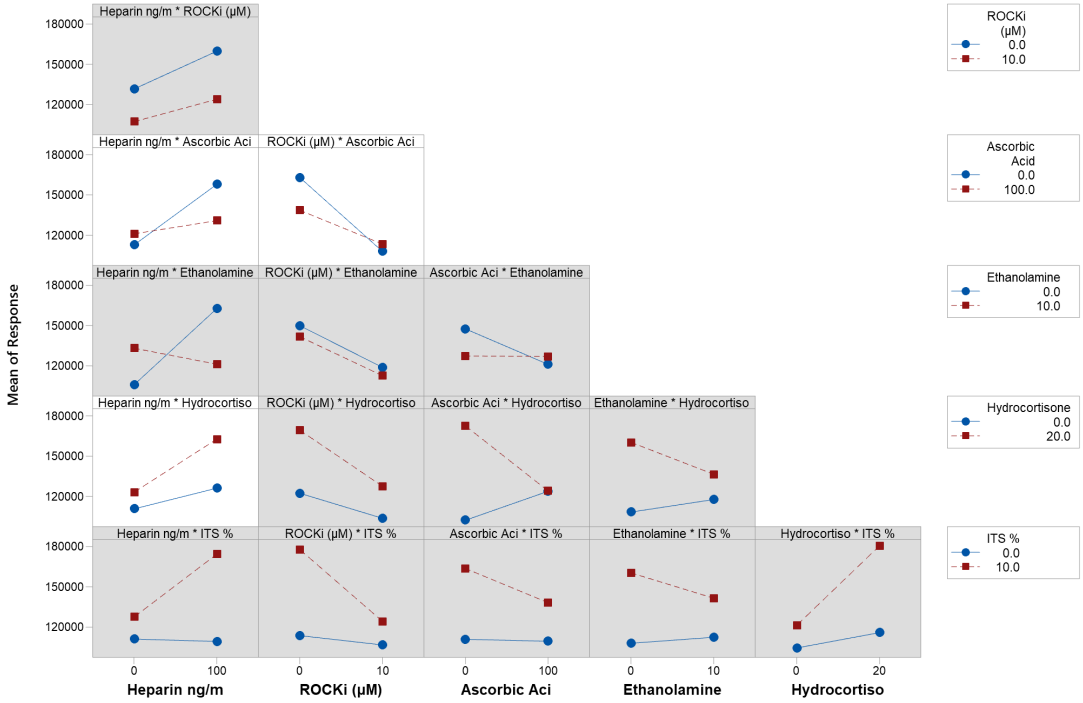

Appendix 7: Interaction plot for Y201 viability 10 days post media change as measured by Alamar blue. Grey boxes indicate non-significant interactions which have been removed from the model (n = 3; α = 0.15).

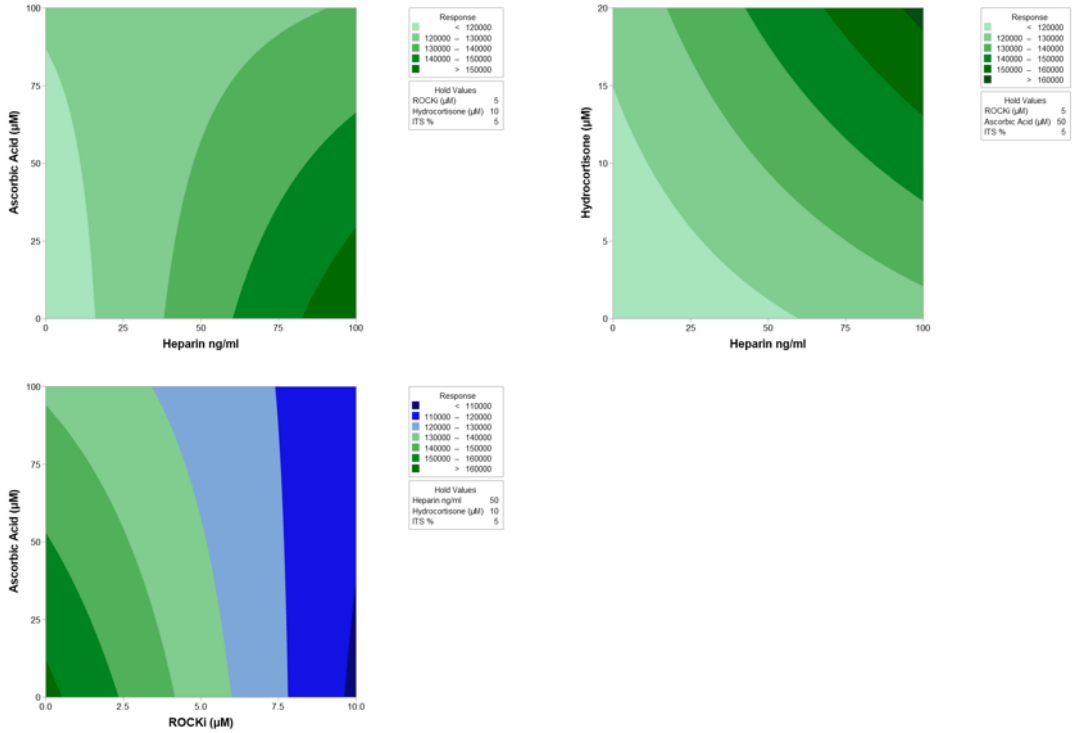

Appendix 8: Contour plots of significant interactions in Y201 viability response to changing CDM component concentrations as assessed by Alamar blue after 10 days in culture (n = 3; α = 0.15).

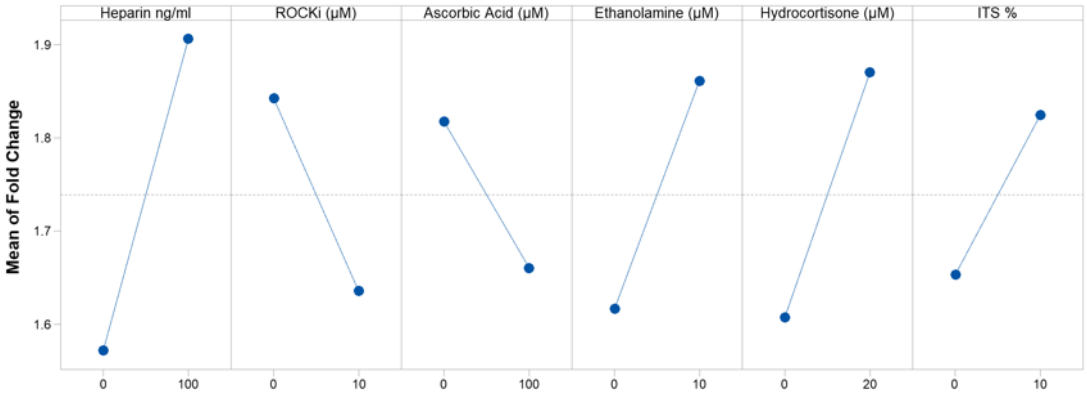

Appendix 9: Main effects plot of changes in mean Y201 cell number fold change (fold change from day 0) in response to changing concentrations of CDM components as measured by Quant-iT PicoGreen after 3 days in culture (n = 3; α = 0.15).

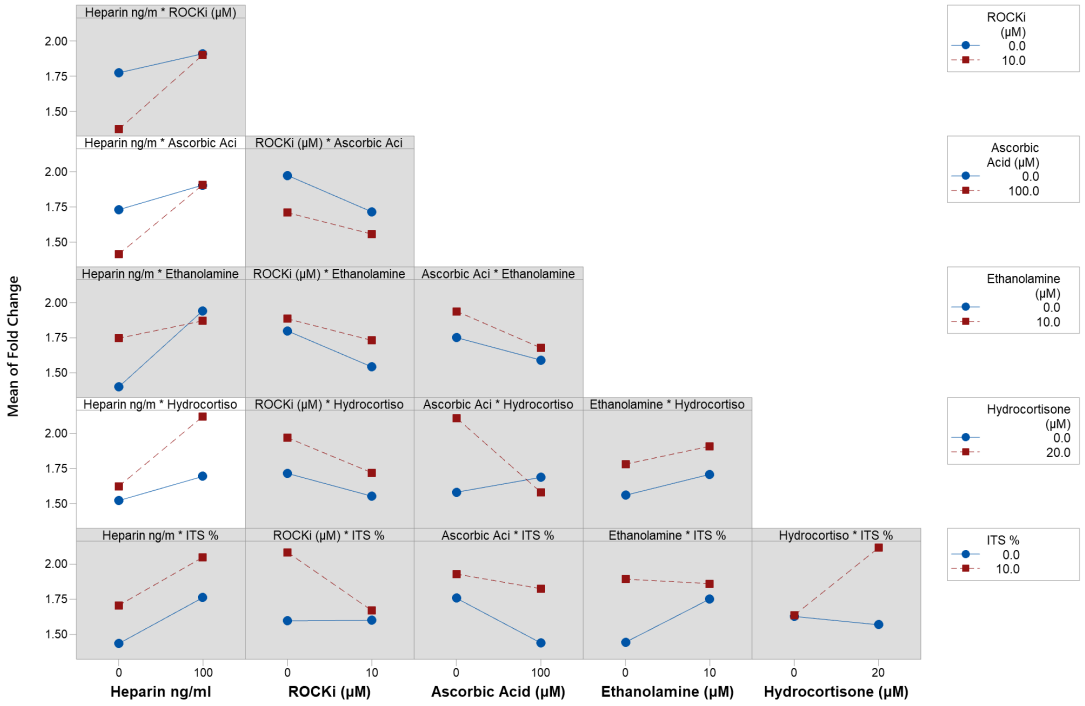

Appendix 10: Interaction plot for Y201 cell number change as assessed by Quant-iT PicoGreen after 3 days in culture (fold change from day 0). Grey boxes indicate non-significant interactions which have been removed from the model (n = 3; α = 0.15).

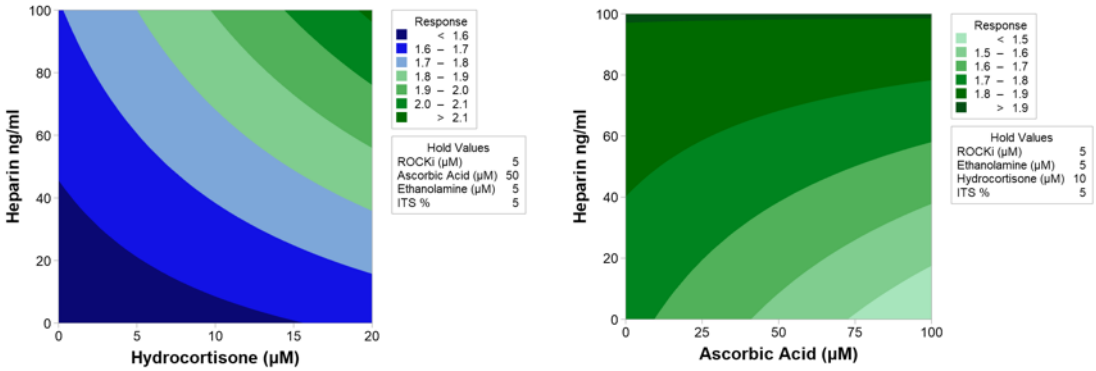

Appendix 11: Contour plots of significant interactions in Y201 viability response to changing CDM component concentrations as assessed by Alamar blue after 10 days in culture (n = 3; α = 0.15).

DoE III main effects and interactions

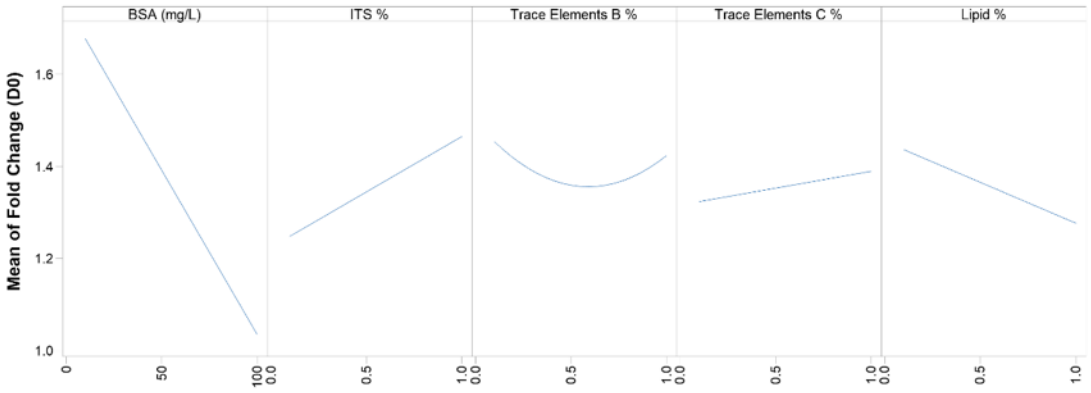

Appendix 12: Main effects plot of changes in mean Y201 cell number change (fold change from day 0) in response to changing concentrations of CDM components as measured by Quant-iT PicoGreen after 3 days in culture. Added points for better modelling of main and combined effects. (n = 5; α = 0.15).

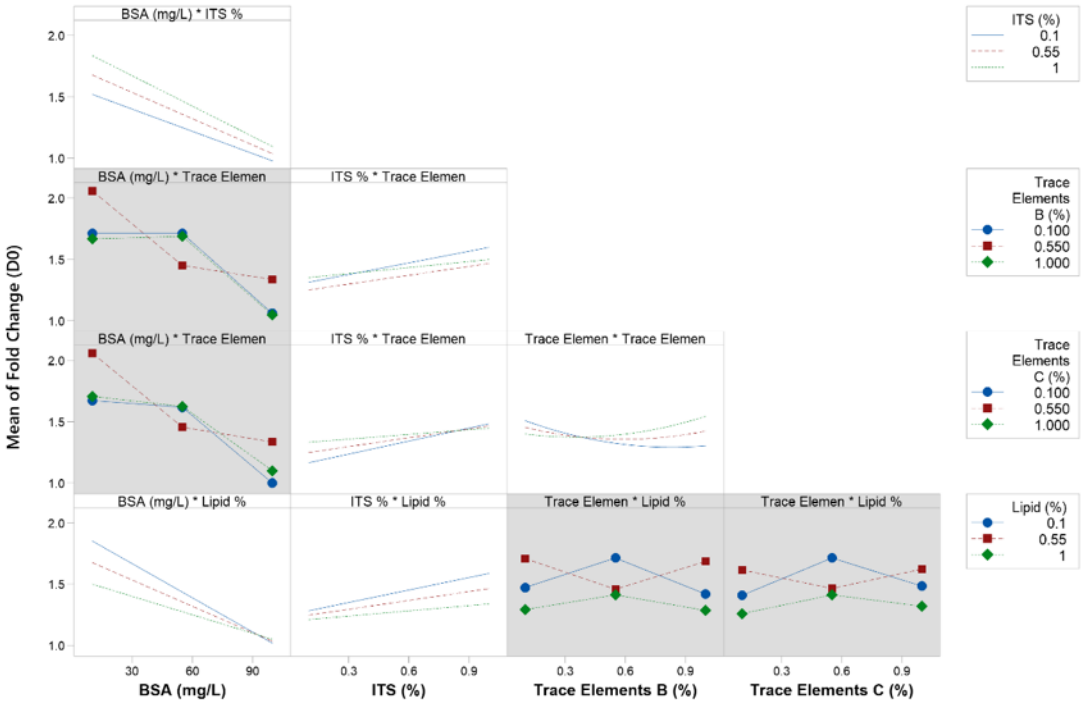

Appendix 13: Interaction plot for Y201 cell number change as assessed by Quant-iT PicoGreen after 3 days in culture (fold change from day 0). Grey boxes indicate non-significant interactions which have been removed from the model. Added points for improved modelling of main and combined effects (n = 5; α = 0.15).

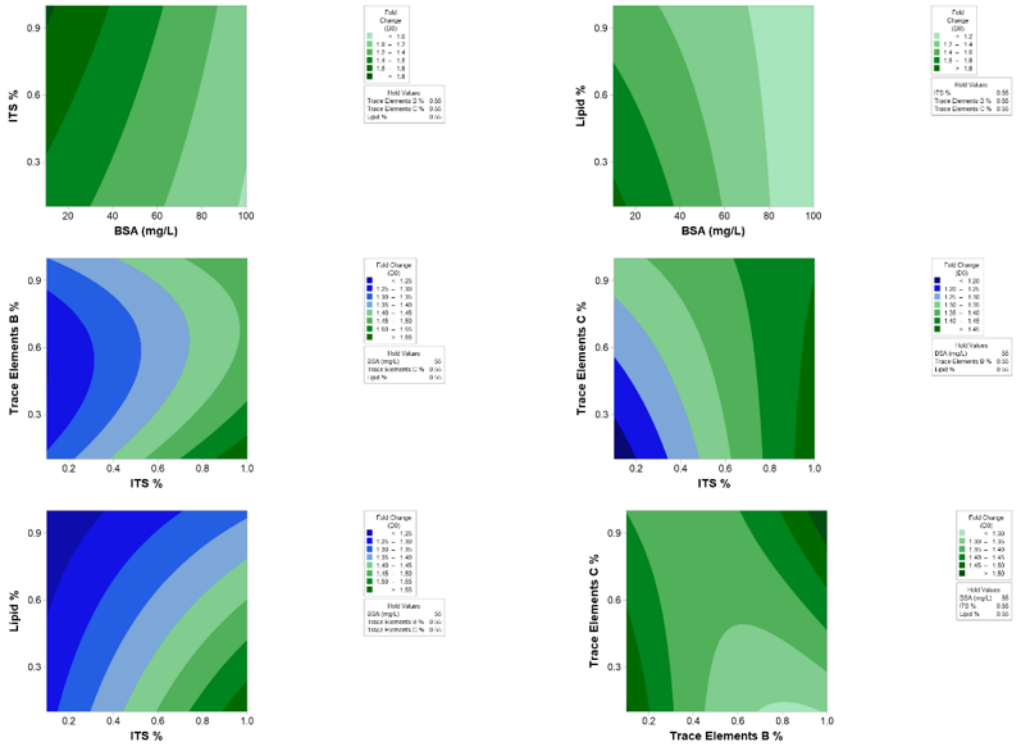

Appendix 14: Contour plots of significant interactions in Y201 cell number change as assessed by Quant-iT PicoGreen after 3 days in culture (fold change from day 0) in response to changing CDM component concentrations (n = 3; α = 0.15).

DoE IV main effects

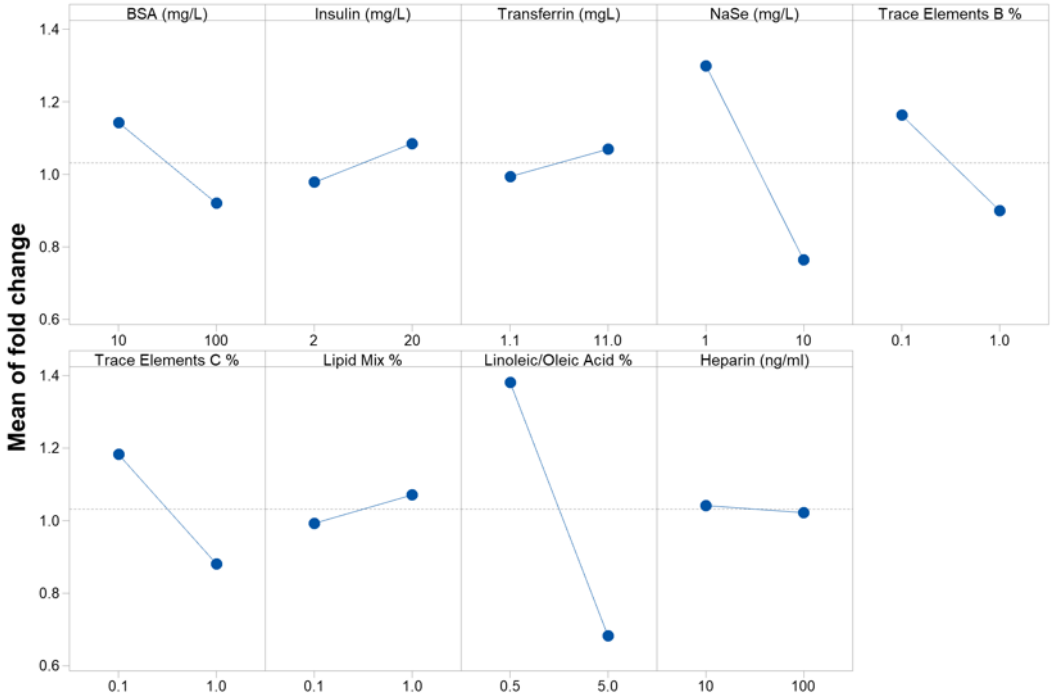

Appendix 15: Main effects plot of changes in mean Y201 cell number change (fold change from day 0) in response to changing concentrations of CDM components as measured by Quant-iT PicoGreen after 3 days in culture.

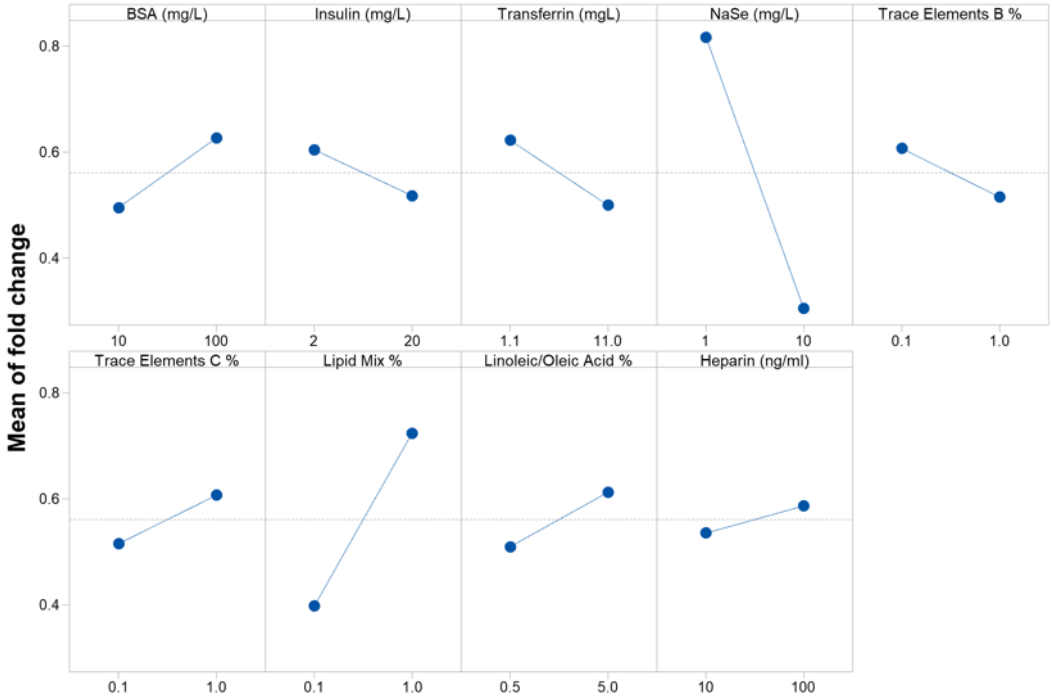

Appendix 16: Main effects plot of changes in mean Y201 cell number change (fold change from day 0) in response to changing concentrations of CDM components as measured by Quant-iT PicoGreen after 3 days in culture, using DMEM/F12 basal medium. (n = 3; α = 0.15)

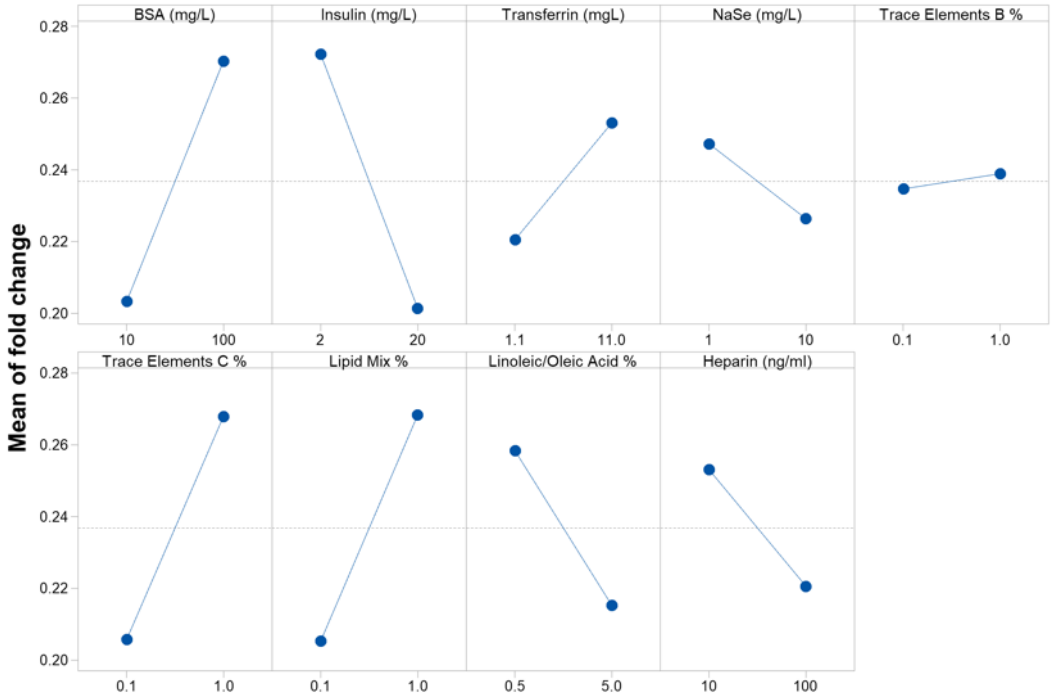

Appendix 17: Main effects plot of changes in mean Y201 cell number change (fold change from day 0) in response to changing concentrations of CDM components as measured by Quant-iT PicoGreen after 3 days in culture, using IMDM basal medium. (n = 3; α = 0.15)

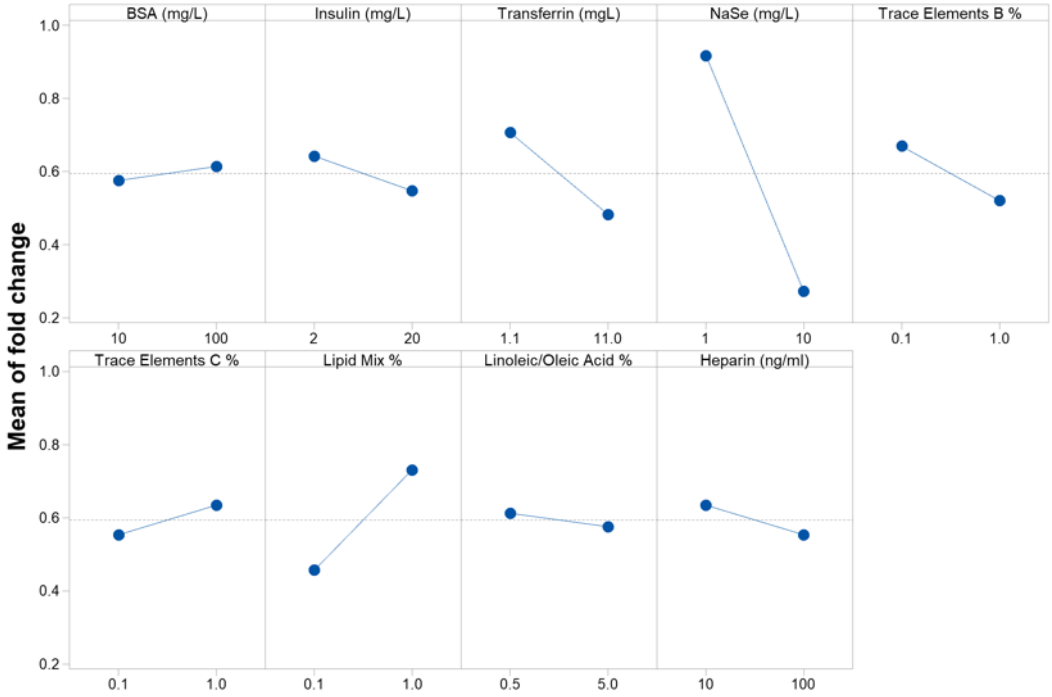

Appendix 18: Main effects plot of changes in mean Y201 cell number change (fold change from day 0) in response to changing concentrations of CDM components as measured by Quant-iT PicoGreen after 3 days in culture. (n = 3; α = 0.15).

Appendix B – Optimisation of plasma sprayed hydroxyapatite surfaces

Crystallinity – Main effects and interactions

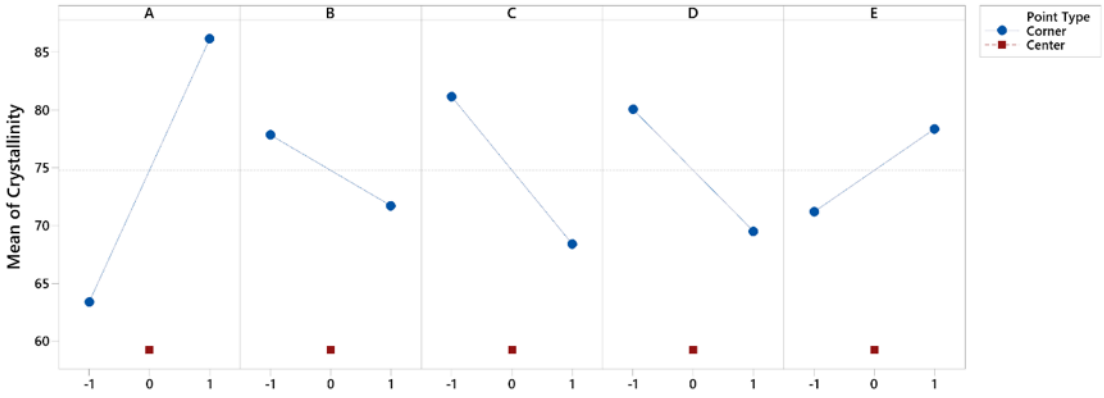

Appendix 19: Main effects plot for crystallinity. All main parameters have a significant effect on crystallinity, with increases in A and E causing an increase in crystallinity, while decreased B, C, and D cause a decrease in crystallinity. The centre point suggests a high level of curvature or higher order interactions. Plotted values are fitted means of crystallinity. Blue: Corner points; Red: Centre point.

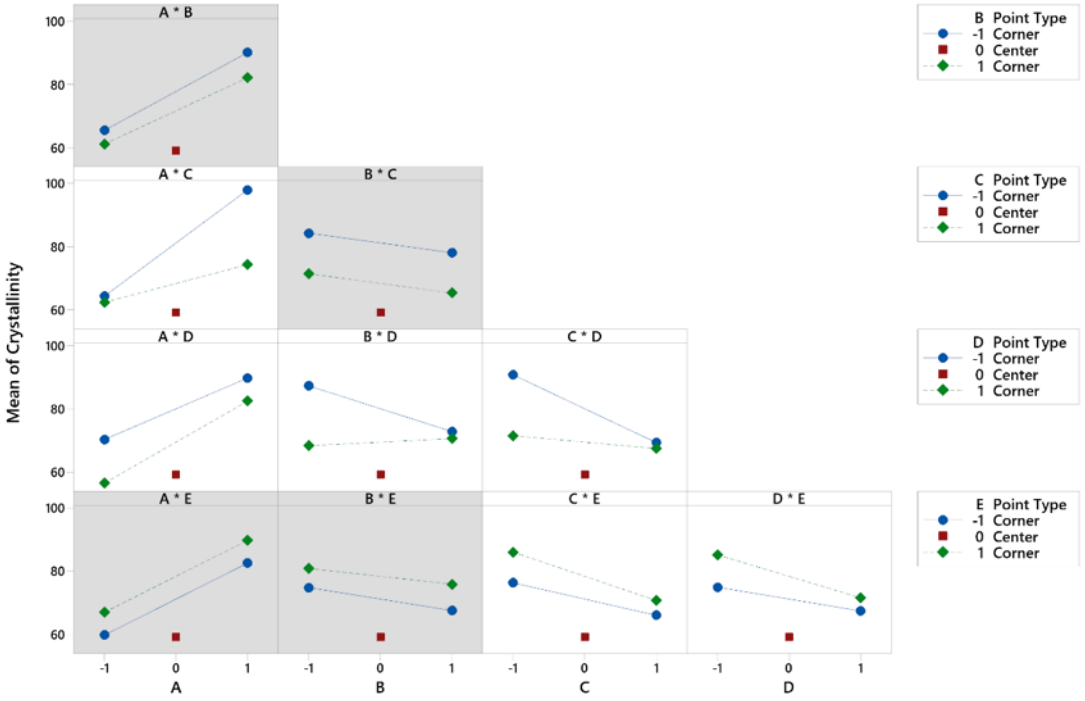

*Appendix 20: Interaction plot for crystallinity. Blue: low parameter setting; red: medium parameter setting; green: high parameter setting. Plotted values are fitted means of crystallinity. The most significant interaction is the A*C interaction, where increased C diminished A's positive effect on crystallinity. Grey boxes indicate an insignificant interaction, which has been excluded from the model, whereas white boxes indicate signifance ($p<0.15$) and inclusion in the final model.*

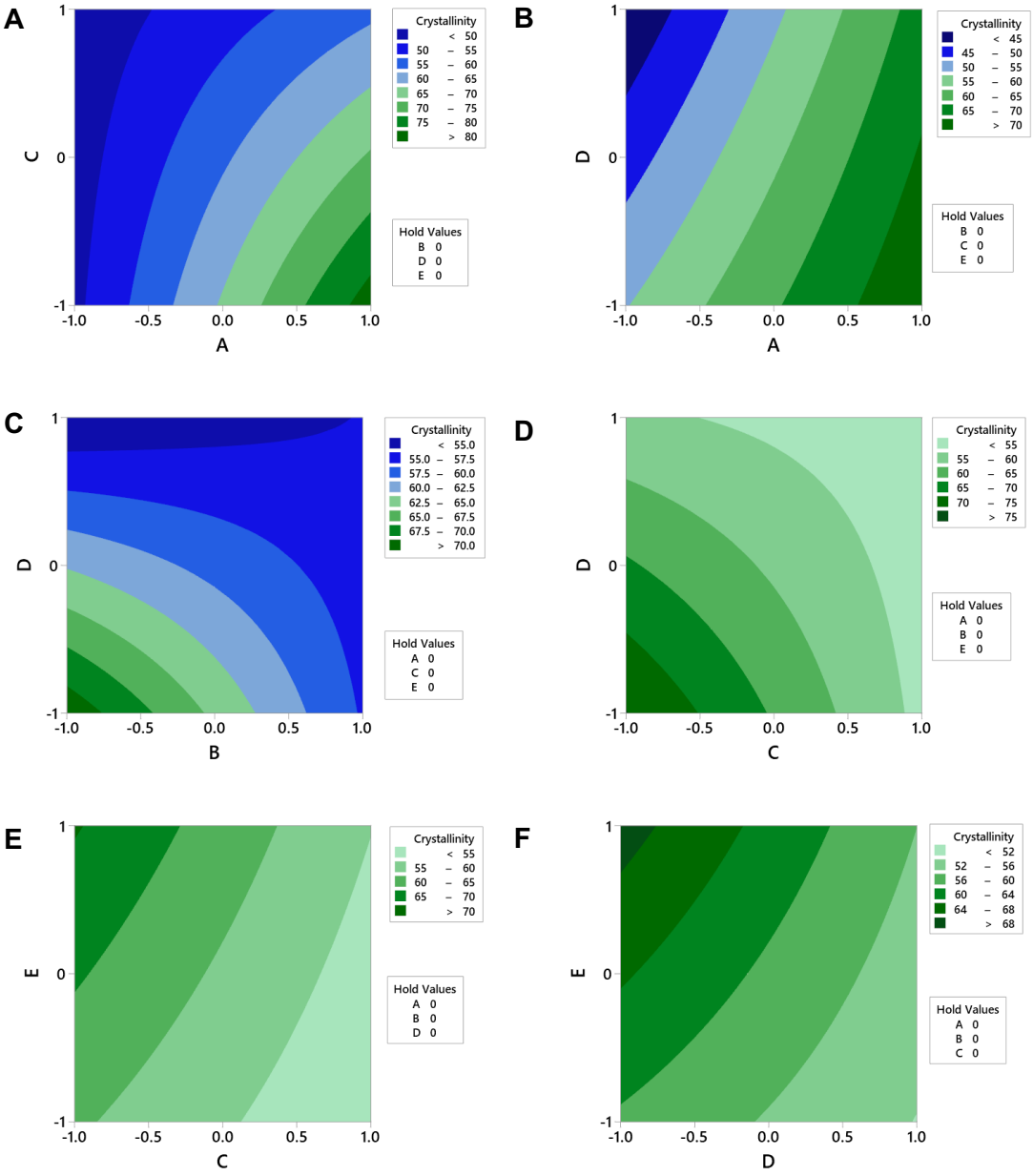

*Appendix 21: Contour plots for significant interactions in crystallinity response to changing plasma sprayer input parameter settings. A: A*C; B: A*D; C: B*D; D: C* D; E: C*E; F: D*E.*

Roughness (Sa) – Main effects and interactions

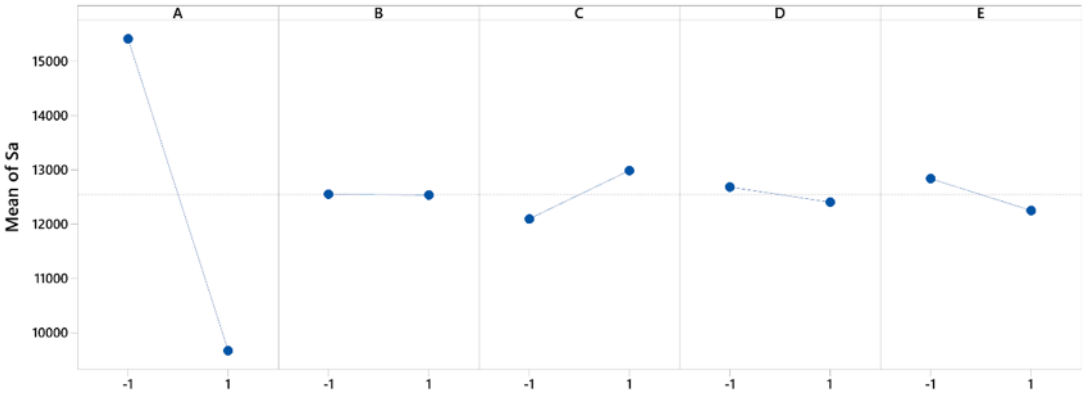

Appendix 22: Main effects plot for Sa response to changes in plasma sprayer input parameter settings. The most significant effect came from A, with increased A decreasing Sa by a factor of approximately 1.5. Note that no centre point is plotted as it was not included in the model.

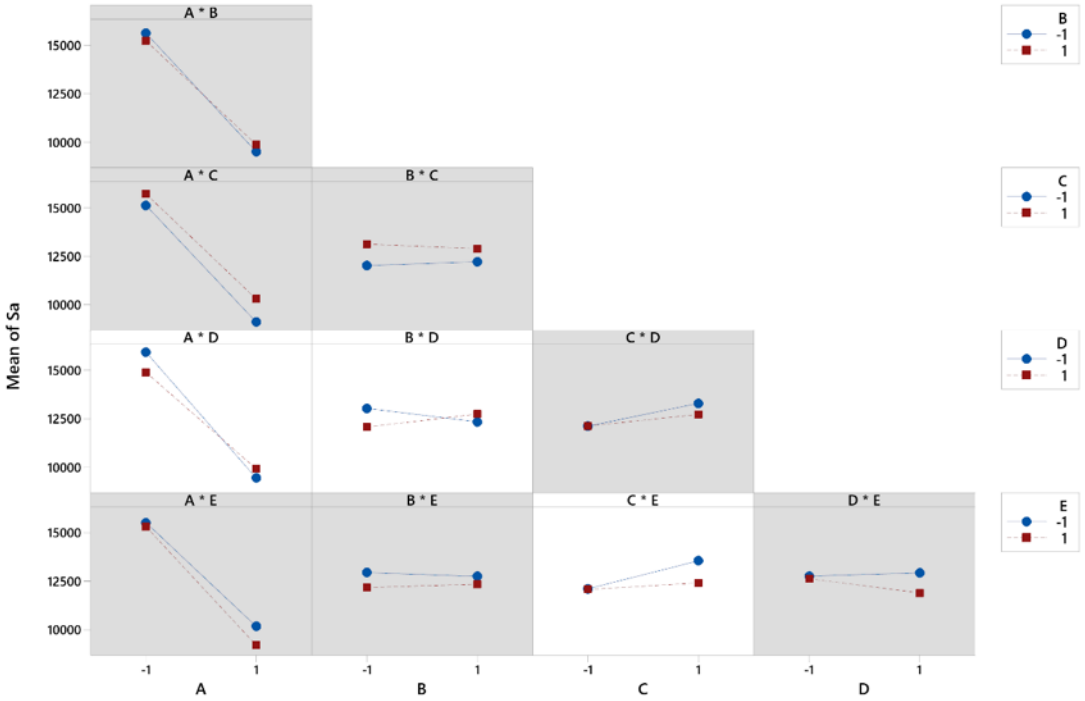

*Appendix 23: Interaction plot for Sa. Blue: low parameter setting; red: high parameter setting. Plotted values are fitted means of Sa (nm). The A*D interaction was the most significant, with an increase in D resulting in a slightly diminished Sa response to A increase. Grey boxes indicate an insignificant interaction, which has been excluded from the model, whereas white boxes indicate signifance ($p<0.15$) and inclusion in the final model.*

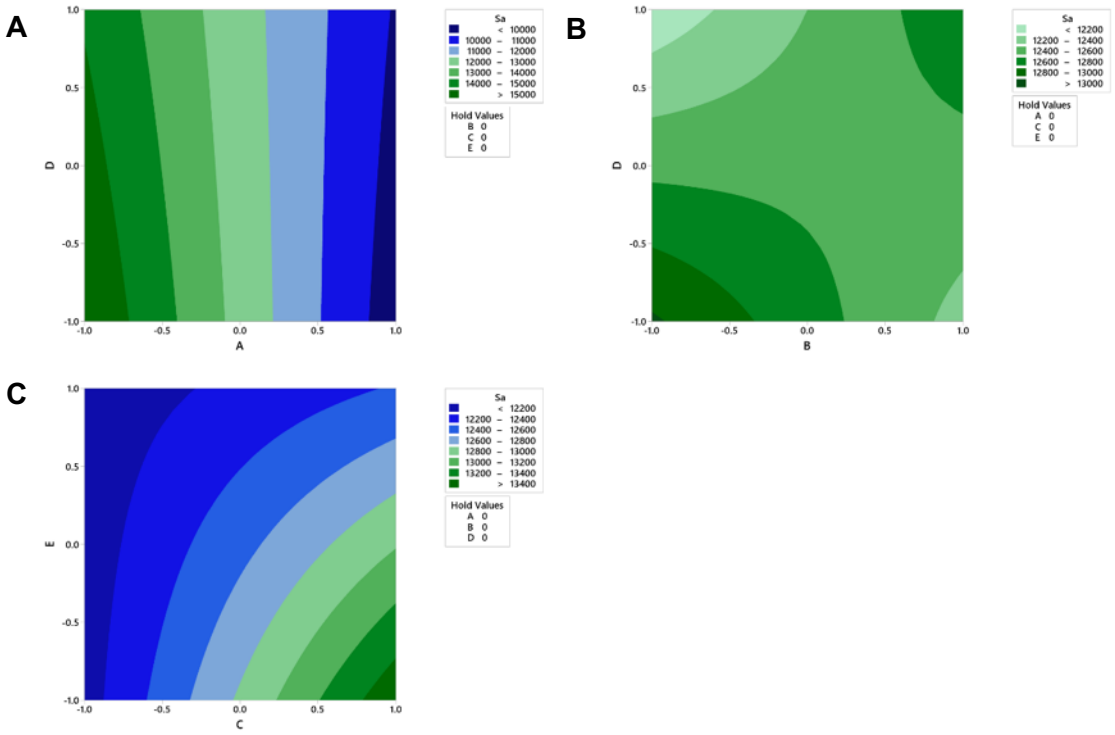

*Appendix 24: Contour plots for significant factor interactions for the Sa response to changing plasma sprayer parameter settings. A: A*D; B: B*D; C: C*E.*

Roughness (Sp) – Main effects and interactions

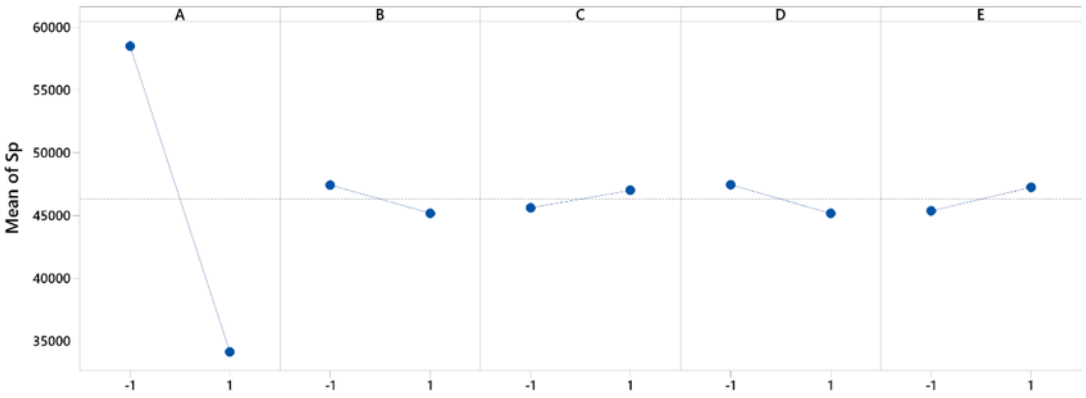

Appendix 25: Main effects plot for Sp response to changes in plasma sprayer input parameter settings. Increase in A caused the most significant effect, lowering Sp approximately 1.7-fold. Note that no centre point is plotted as it was not included in the model.

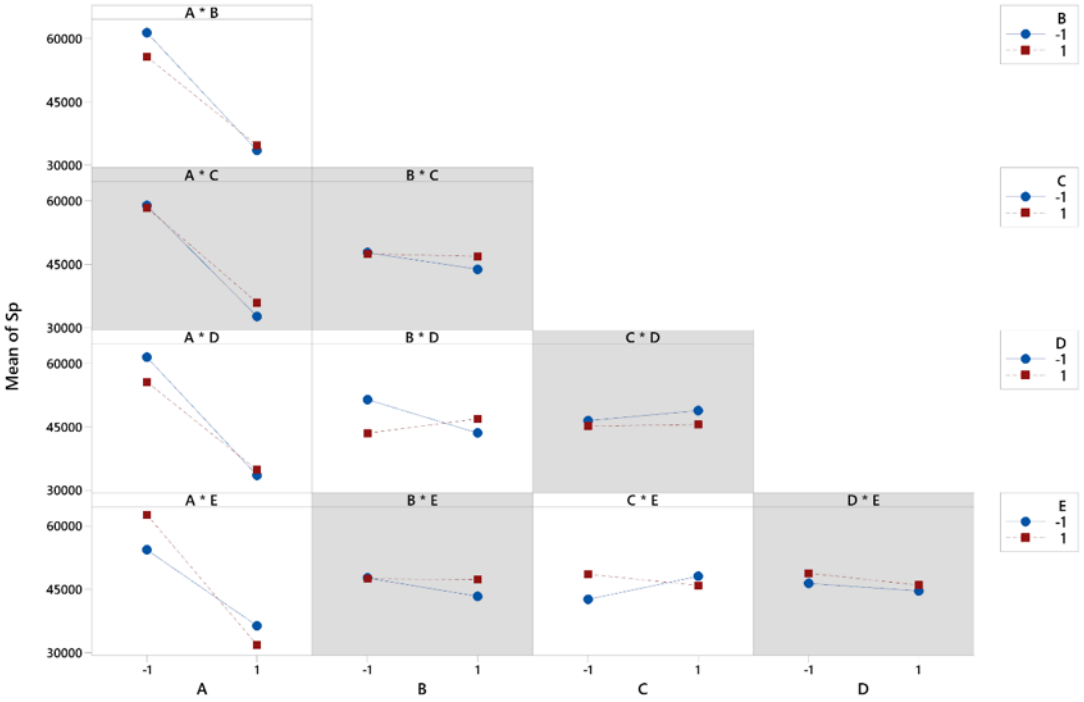

*Appendix 26: Interaction plot for Sp. Blue: low parameter setting; red: high parameter setting. Plotted values are fitted means of Sp. Several interactions in which A was involved resulted in slightly reduced responses, while others caused opposite responses (B*D; C*E). Grey boxes indicate an insignificant interaction, which has been excluded from the model, whereas white boxes indicate significant interactions included in the model ($p<0.15$).*

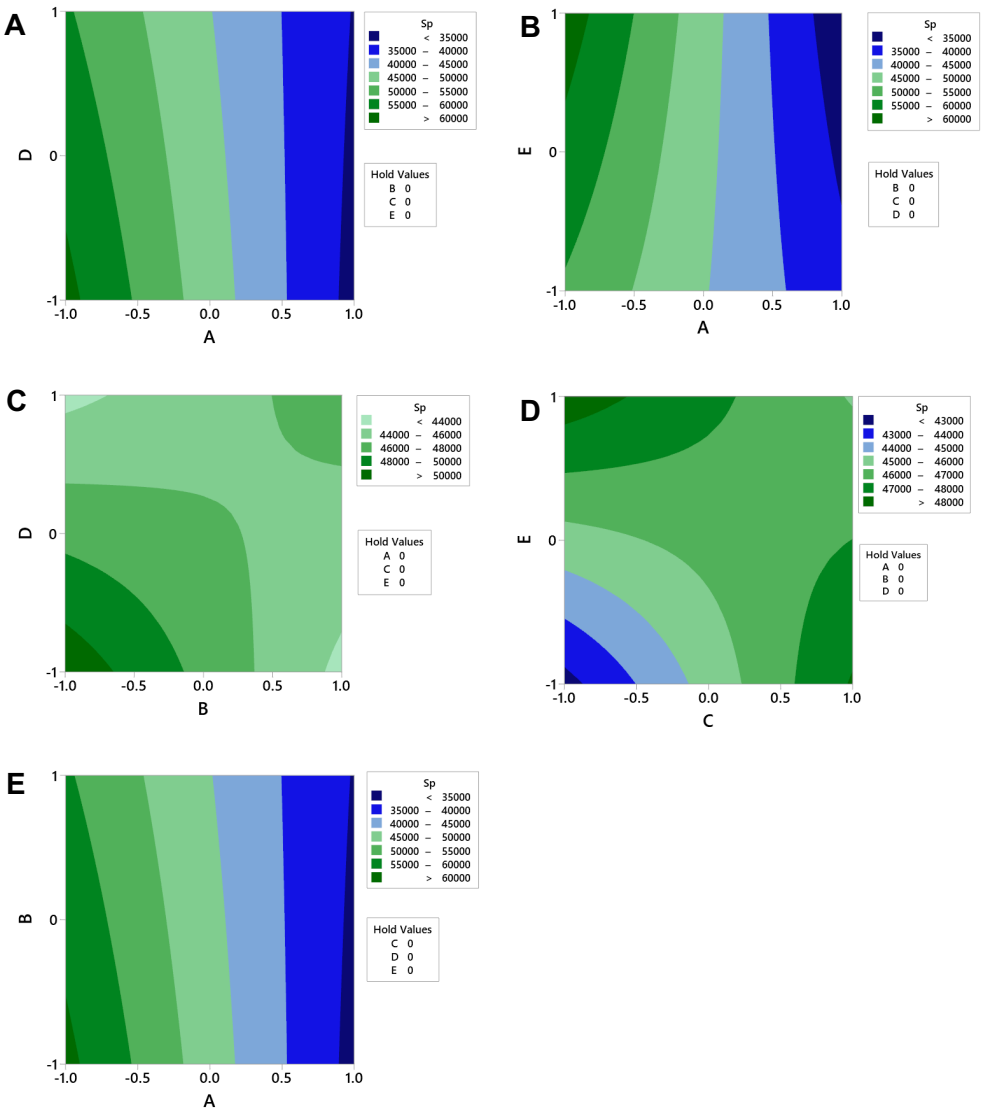

*Appendix 27: Contour plots of statistically significant interactions in the Sp response to changes in plasma spray parameter settings. A: A*D; B: A*E; C: B*D; D: C*E; E: A*B.*

Roughness (Sv) – Main effects and interactions

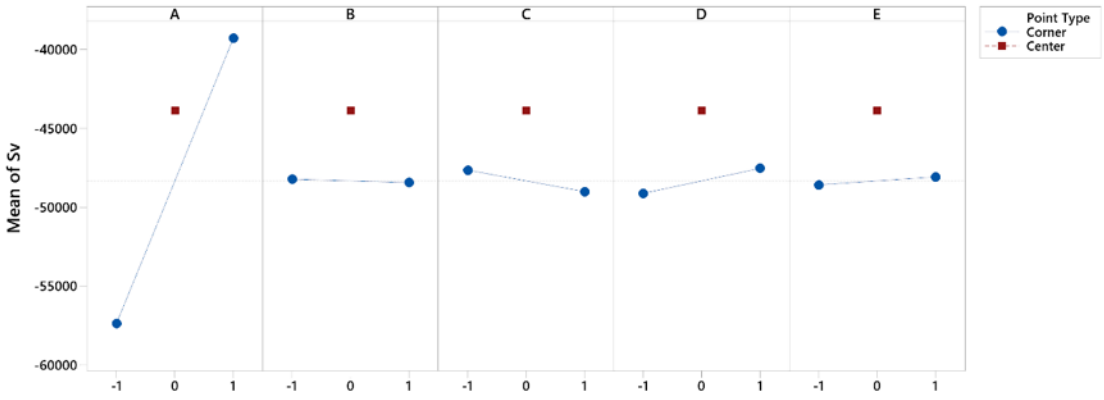

Appendix 28: Main effects plot for Sv response to changes in plasma sprayer input parameter settings. An increased A increased Sv approximately 1.5-fold, although the centre point suggests a degree of curvature in the response.

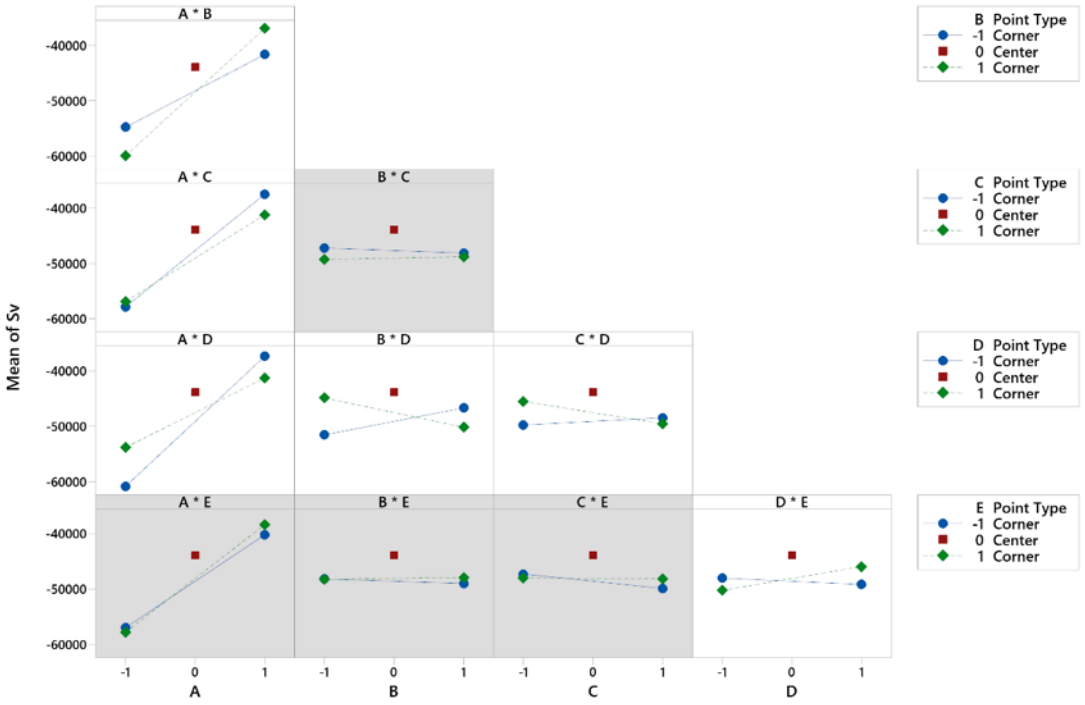

*Appendix 29: Interaction plot for Sv. Blue: low parameter setting; red: centre point; green: high parameter setting. Plotted values are fitted means of Sv. The most significant interaction, A*B, caused an increased effect on Sv by A with increased B, suggesting a synergistic effect. Grey boxes indicate an insignificant interaction, which has been excluded from the model, whereas white boxes indicate signifance (p<0.15) and inclusion in the final model.*

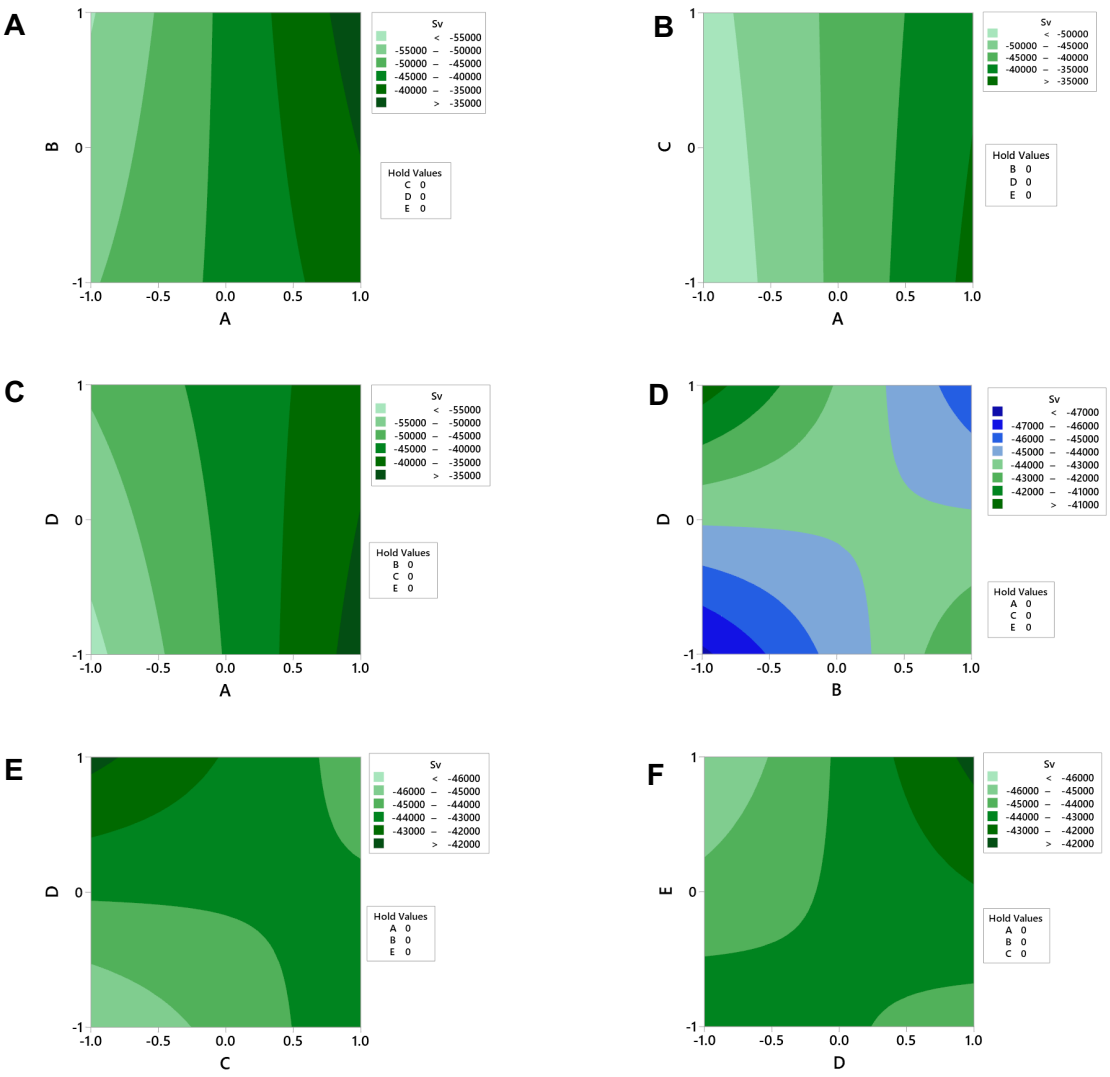

*Appendix 30: Contour plots of statistically significant interactions in the Sv response to changes in plasma spray parameter settings. A: A*B; B: A*C; C: A*D; D: B*D; E: C*D; F: D*E.*

Roughness (Sz) – Main effects and interactions

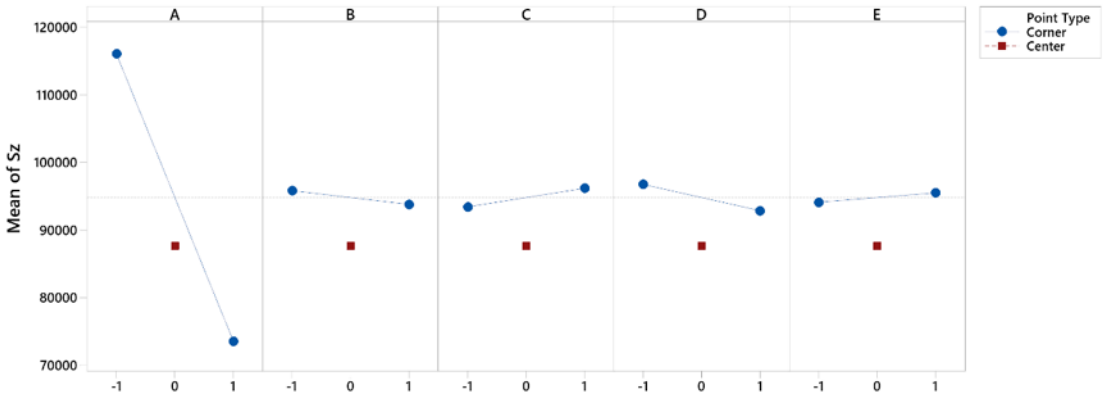

Appendix 31: Main effects plot for Sz response to changes in plasma sprayer input parameter settings. A has the most profound effect on Sz, with increases causing a steep decline in Sz. The response is not linear, with some curvature suggested due to the centre point being included in the model.

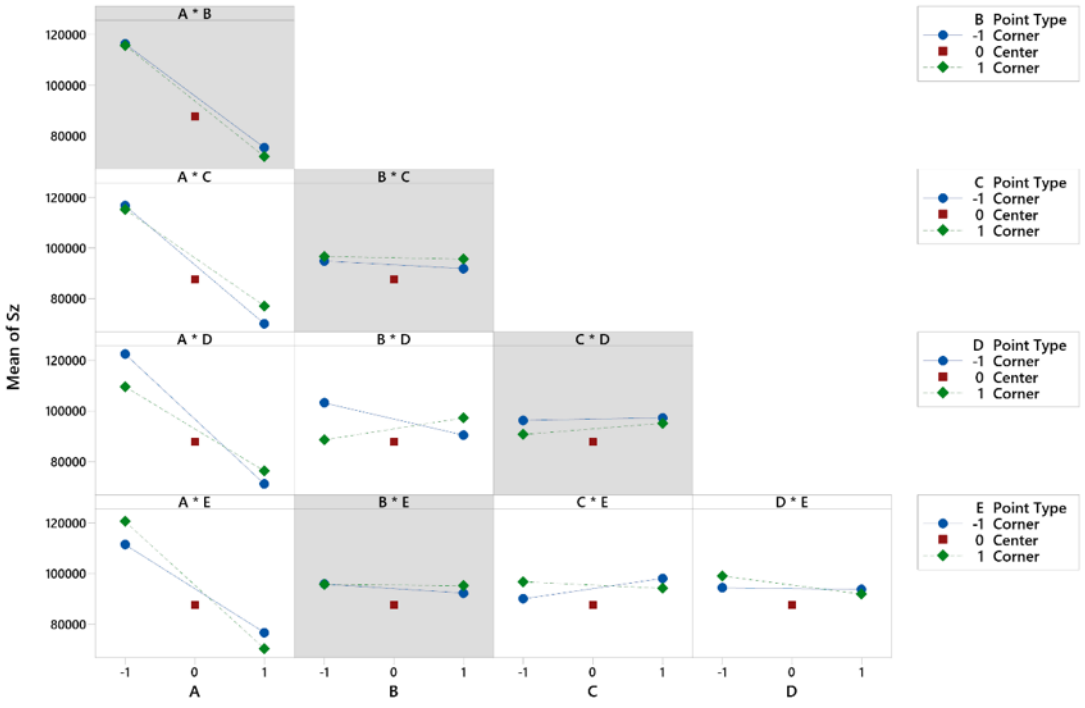

Appendix 32: Interaction plot for Sz. Blue: low parameter setting; red: centre point; green: high parameter setting. Plotted values are fitted means of Sz. Grey boxes indicate an insignificant interaction, which has been excluded from the model, whereas white boxes indicate signifance (p<0.15) and inclusion in the final model.

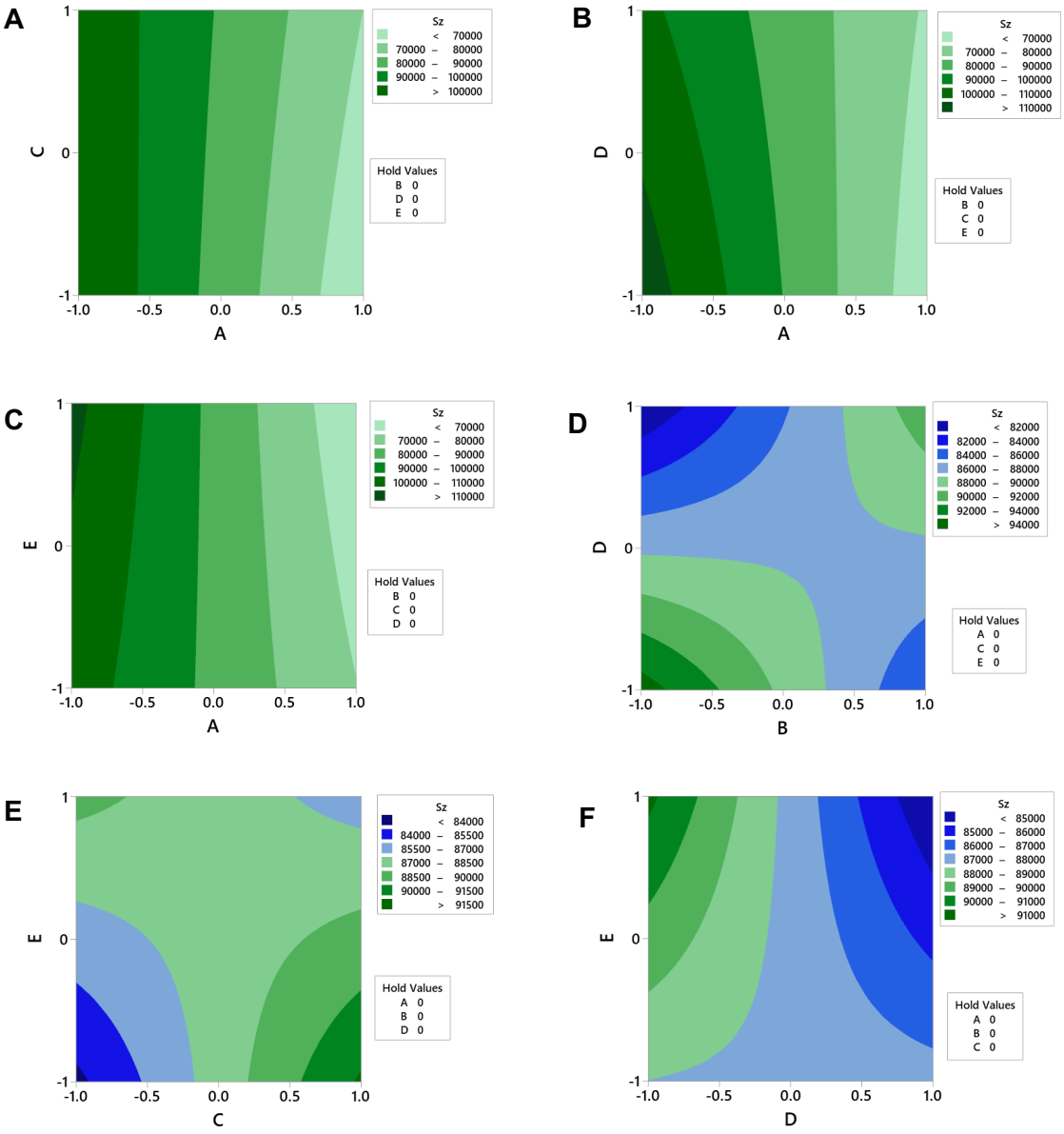

*Appendix 33: Contour plots of statistically significant interactions in the Sz response to changes in plasma spray parameter settings. A: A*C; B: A*D; C: A*E; D: B*D; E: C*E; F: D*E.*

Roughness (Sq) – Main effects and interactions

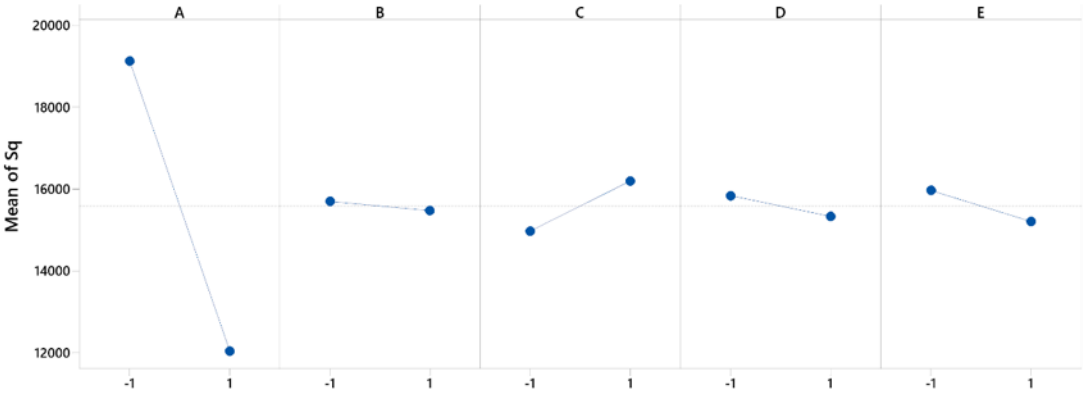

Appendix 34:Main effects plot for Sq response to changes in plasma sprayer input parameter settings. Increased A decreased Sq most significantly. Note that no centre point is plotted as it was not included in the model.

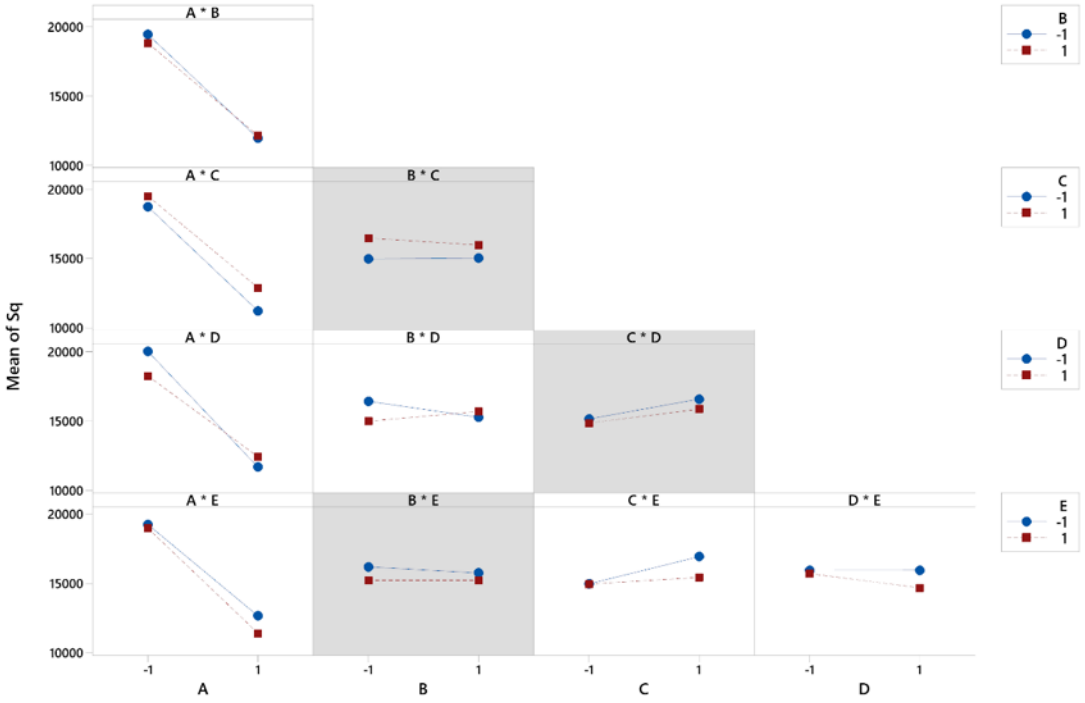

*Appendix 35: Interaction plot for Sq. Blue: low parameter setting; red: high parameter setting. Plotted values are fitted means of crystallinity. The most significant interaction was A*D, where diminished Sq response was observed at high D. Grey boxes indicate an insignificant interaction, which has been excluded from the model, whereas white boxes indicate signifance ($p<0.15$) and inclusion in the final model.*

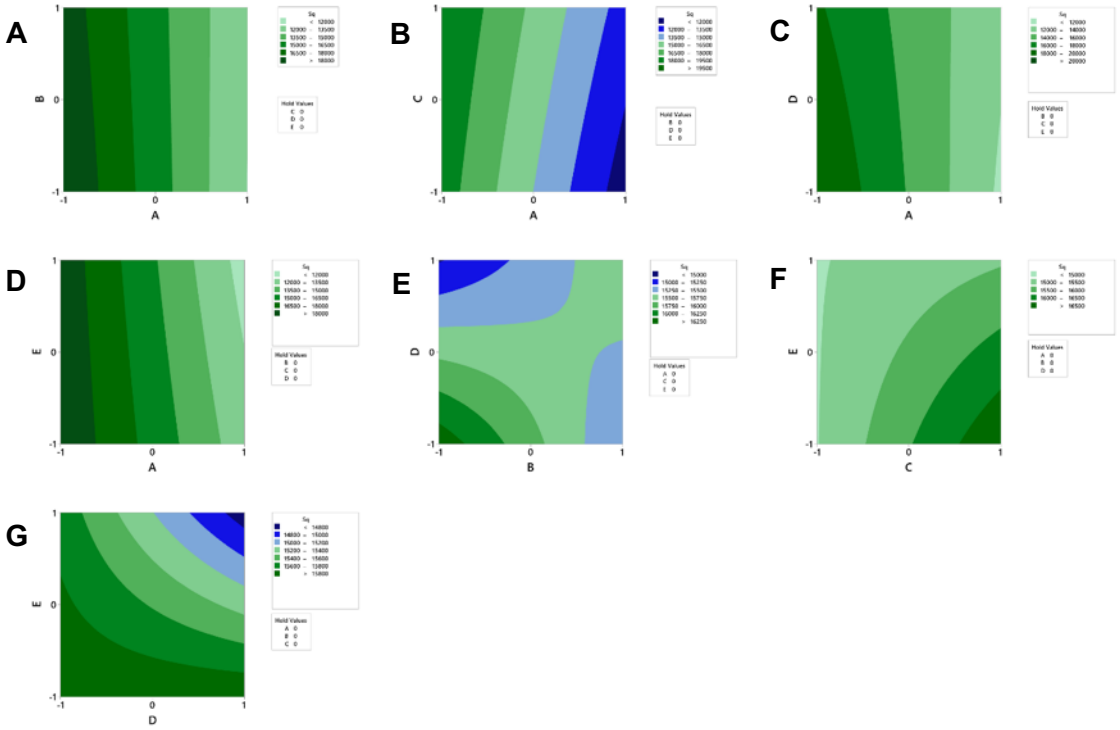

*Appendix 36: Contour plots of statistically significant interactions in the Sq response to changes in plasma spray parameter settings. A: A*B; B: A*C; C: A*D; D: A*E; E: B*D; F: C*E; G: D*E.*

Roughness (Ssk) – Main effects and interactions

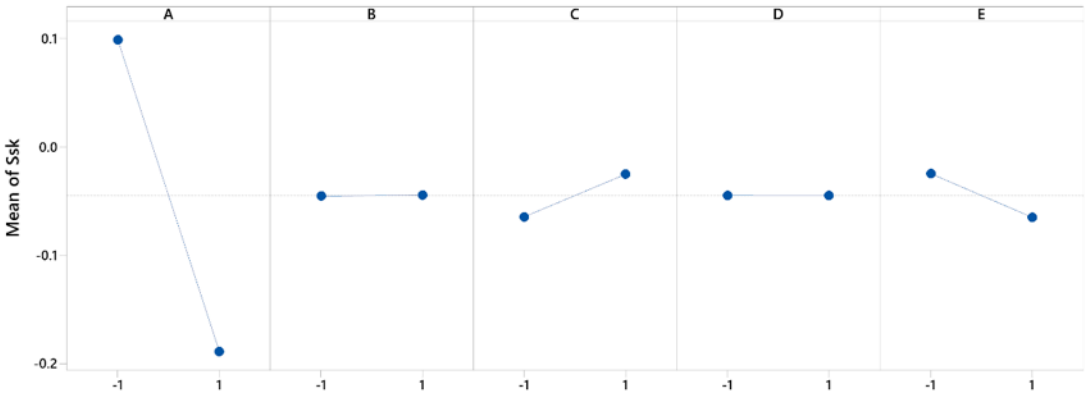

Appendix 37: Main effects plot for Ssk response to changes in plasma sprayer input parameter settings. The most pronounced effect was achieved by A. Note that no centre point is plotted as it was not included in the model.

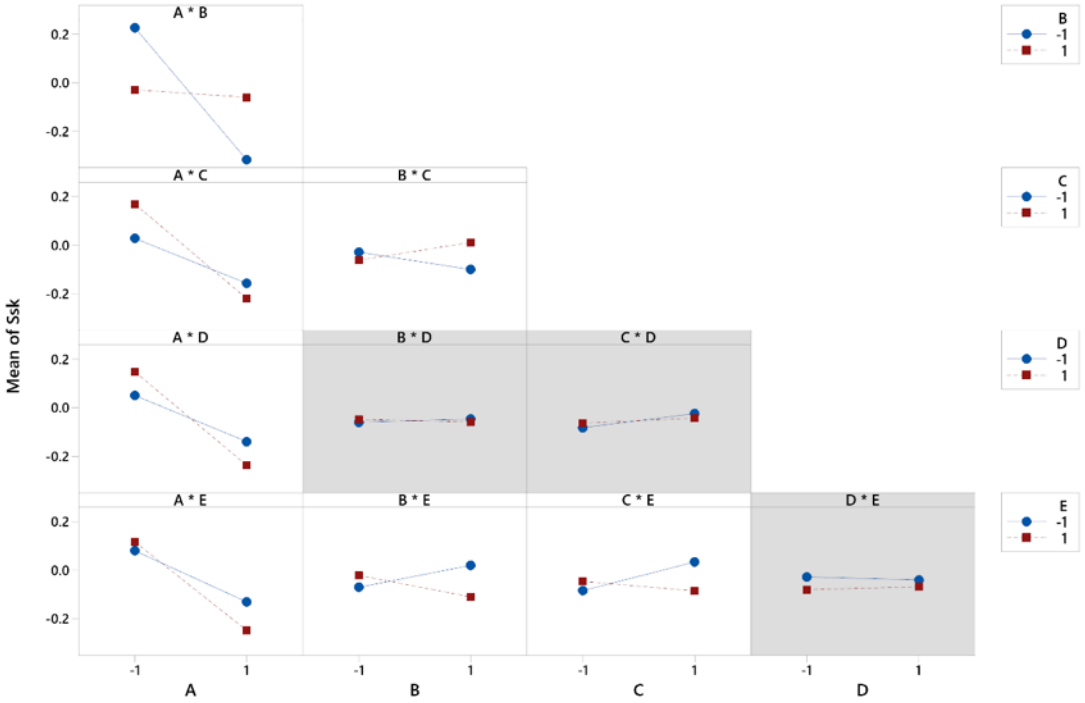

*Appendix 38: Interaction plot for Ssk. Blue: low parameter setting; red: high parameter setting. Plotted values are fitted means of Ssk. The most significant interaction is the A*B interaction, where high B essentially negate A's effect on Ssk. Grey boxes indicate an insignificant interaction, which has been excluded from the model, whereas white boxes indicate signifance ($p<0.15$) and inclusion in the final model.*

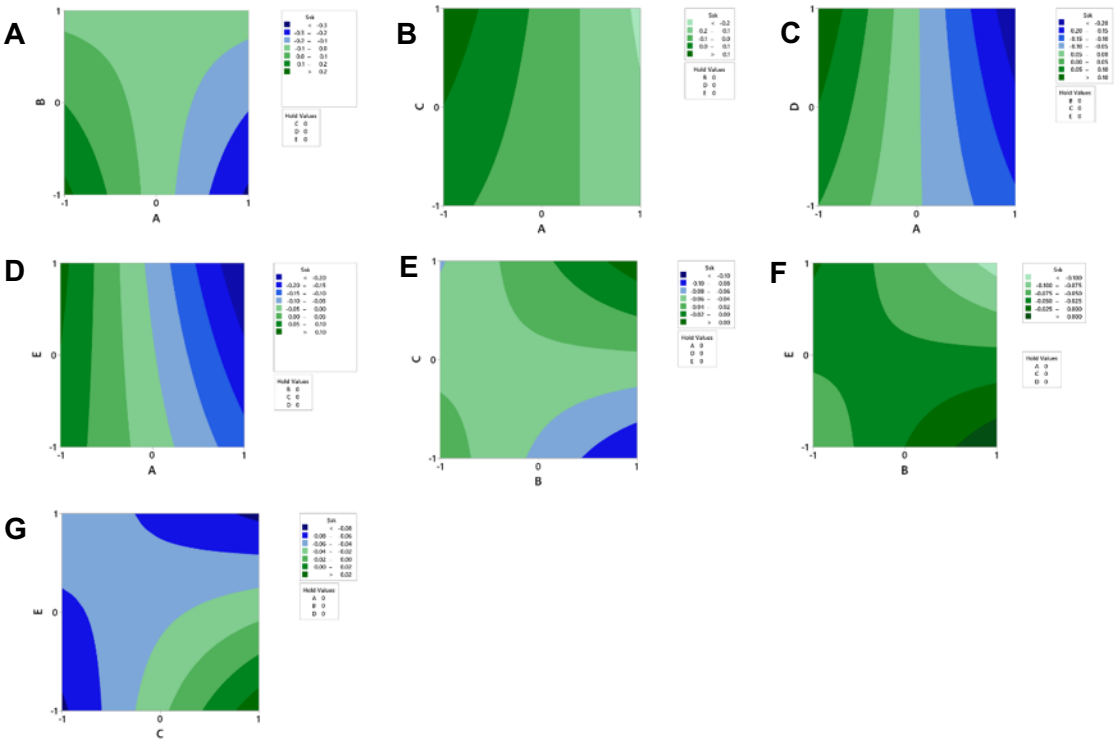

*Appendix 39: Contour plots of statistically significant interactions in the Sku response to changes in plasma spray parameter settings. A: A*B; B: A*C; C: A*D; D: A*E; E: B*C; F: B*E; G: C*E.*

Roughness (Sku) – Main effects and interactions

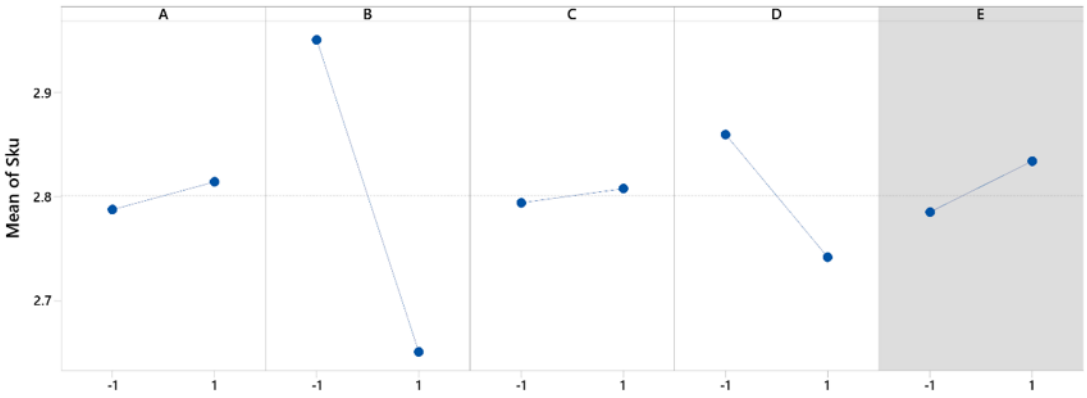

Appendix 40: Main effects plot for Sku response to changes in plasma sprayer input parameter settings. The strongest main effect was conveyed by B, where an increase in B decreased mean Sku. E was determined to have an insignificant effect and was not included in the model. Note that no centre point is plotted as it was not included in the model. White boxes indicate inclusion in the model, while a grey box indicates exclusion from the final model.

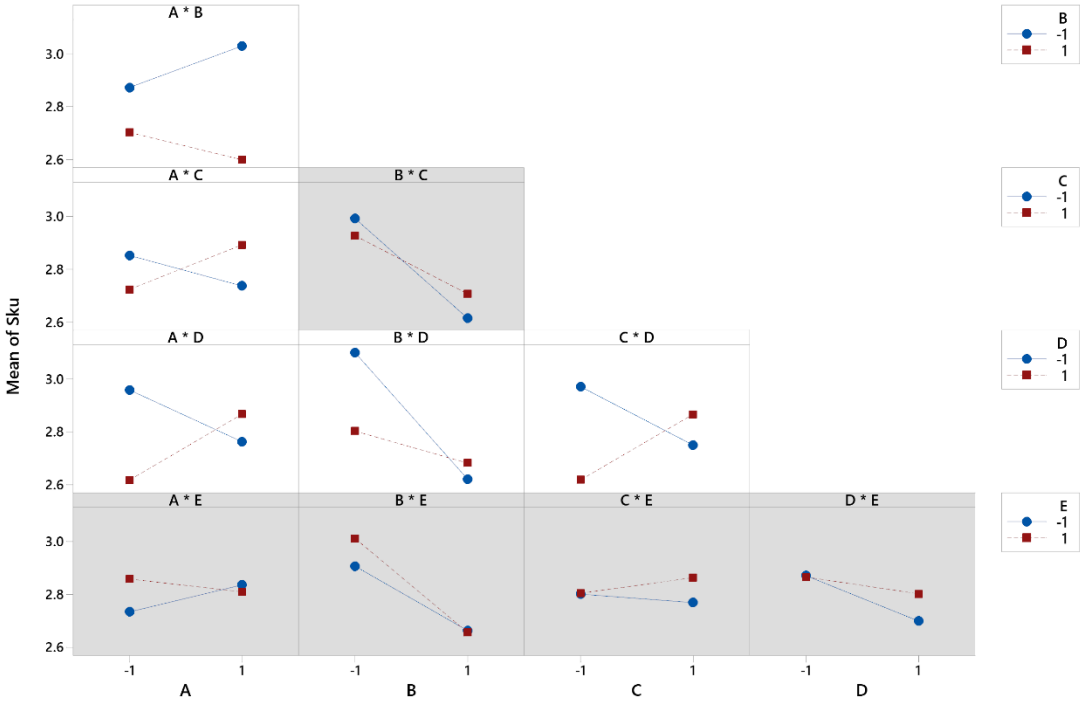

*Appendix 41: Interaction plot for Sku. Blue: low parameter setting; red: high parameter setting. Plotted values are fitted means of Sku. The strongest interaction is the C*D interaction, where a high D causes an increased Sku with increasing C, whilst a low D results in decreased Sku with increasing C. Grey boxes indicate an insignificant interaction, which has been excluded from the model, whereas white boxes indicate signifance ($p<0.15$) and inclusion in the final model.*

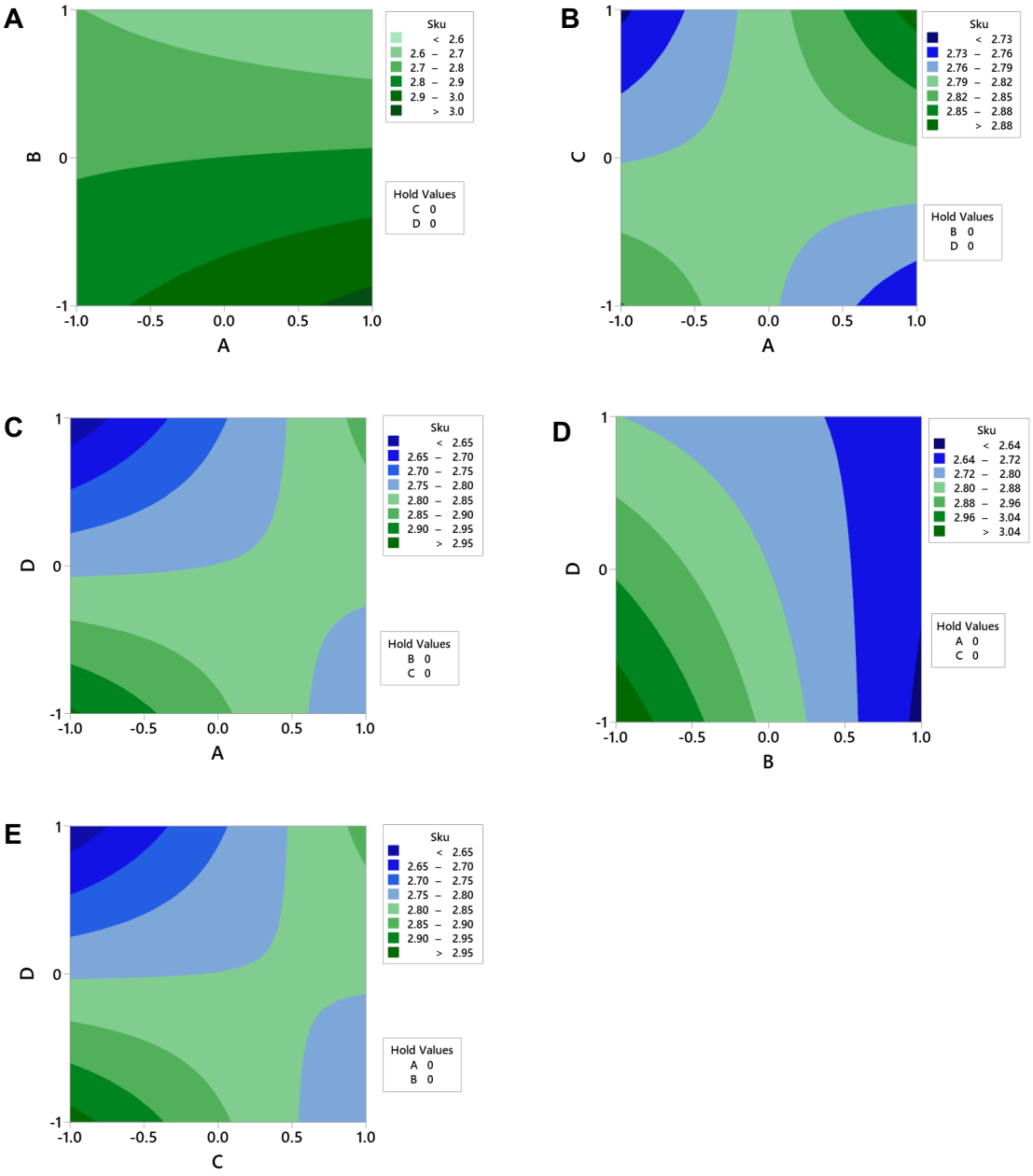

*Appendix 42: Contour plots of statistically significant interactions in the Sku response to changes in plasma spray parameter settings. A: A*B; B: A*C; C: A*D; D: B*D; E: C*D*

Endogenous Y201 Wnt response to changes in plasma sprayer settings – Main effects and interactions

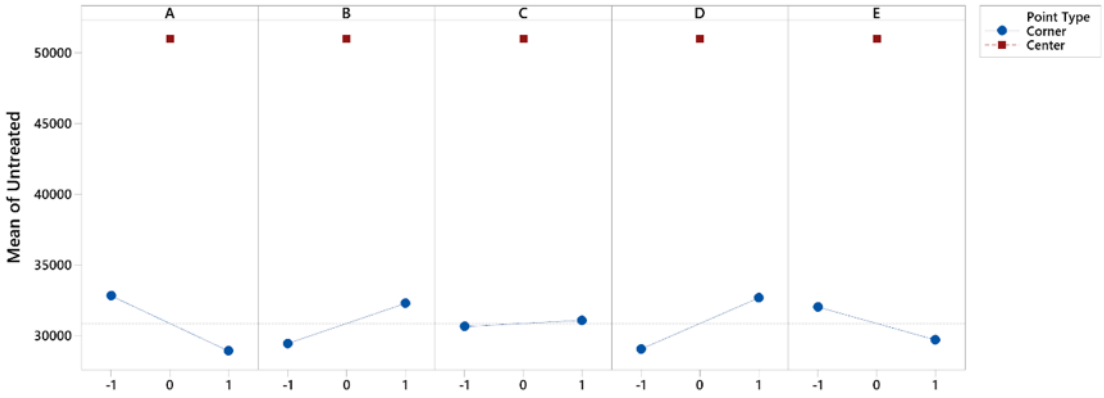

Appendix 43: Main effects plot for endogenous Wnt response to changes in plasma sprayer input parameter settings. The strongest main effect was conveyed by A, where an increase in A decreased EGFP signal. The centre point was included in the model as it suggested very strong curvature.

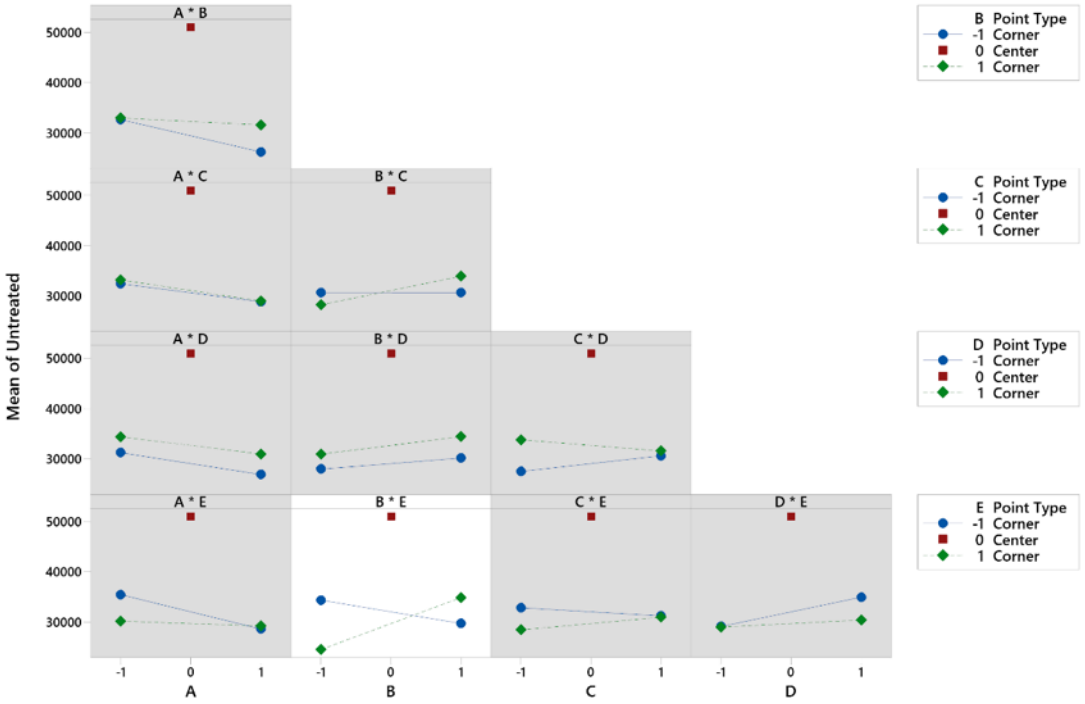

*Appendix 44: Interaction plot for endogenous Wnt signalling response to changing plasma spray parameter input settings as measured by EGFP activity. Blue: low parameter setting; red: centre point; green: high parameter setting. Plotted values are fitted means of EGFP signal. The only significant interaction is the B*E interaction, where at high E, increasing B increases EGFP signal, whereas the reverse occurs at low E. Grey boxes indicate an insignificant interaction, which has been excluded from the model, whereas white boxes indicate significance ($p<0.15$) and inclusion in the final model.*

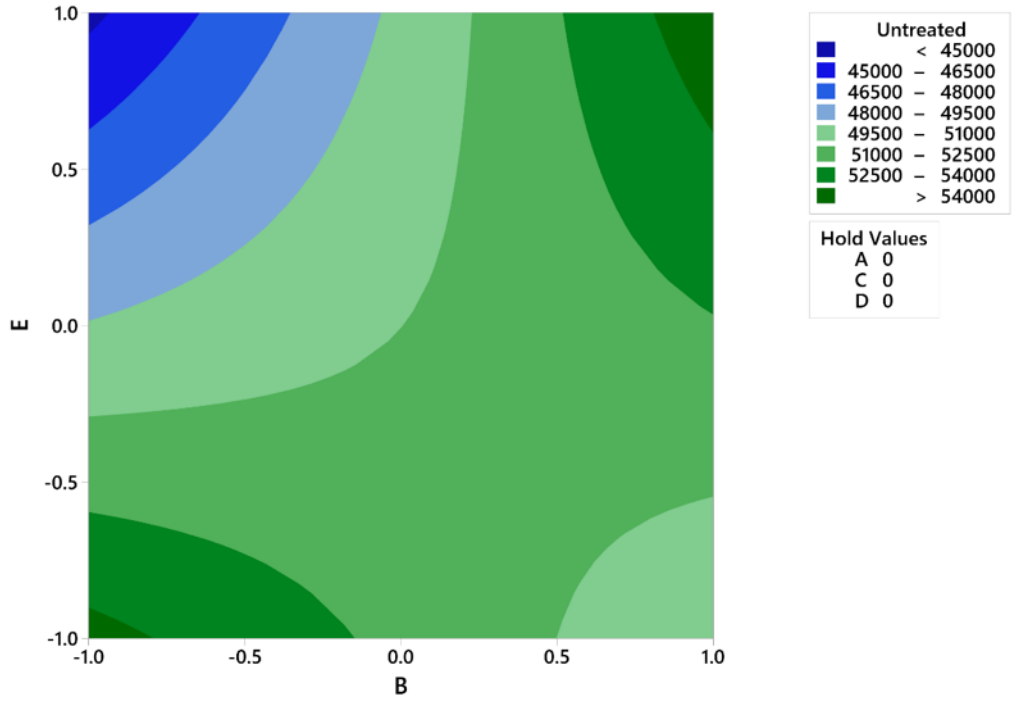

Appendix 45: Contour plot of statistically significant interaction in the endogenous response to changes in plasma spray parameter settings.

Exogenous Y201 Wnt response to changes in plasma sprayer settings – Main effects and interactions

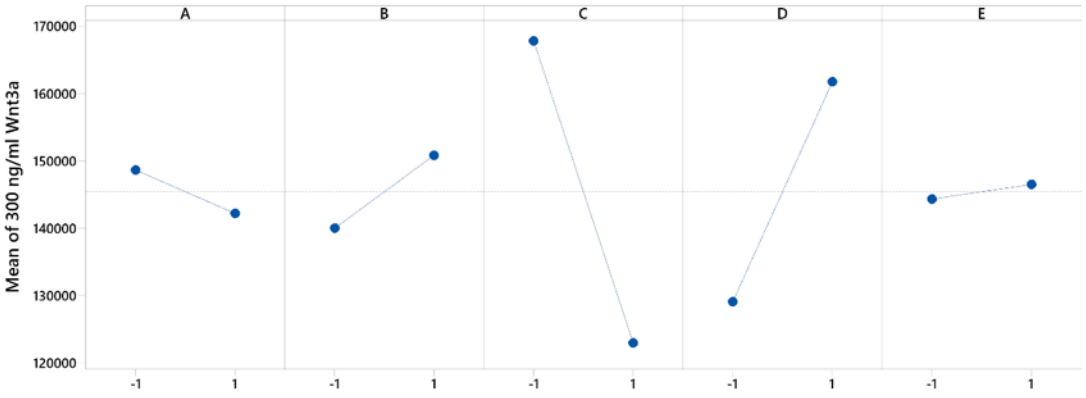

Appendix 46: Main effects plot for Y201 Wnt signalling response to changes in plasma sprayer input parameter settings in the presence of 300ng/ml Wnt3a. The strongest main effect was conveyed by C, where an increase C decreased EGFP signal. Note that no centre point is plotted as it was not included in the model.

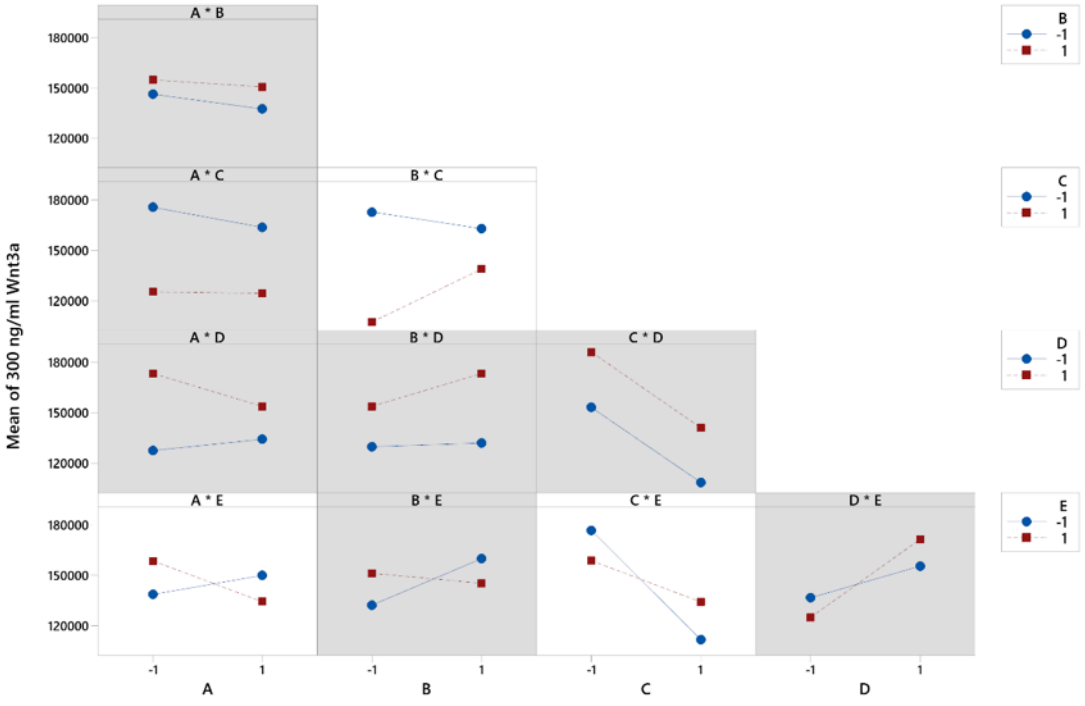

*Appendix 47: Interaction plot Wnt signalling response to changing plasma spray parameter input settings with 300 ng/ml Wnt3a treatment as measured by EGFP activity. Blue: low parameter setting; red: high parameter setting. Plotted values are fitted means of EGFP signal. The most significant interaction is the B*C interaction. Grey boxes indicate an insignificant interaction, which has been excluded from the model, whereas white boxes indicate significance (p<0.15) and inclusion in the final model.*

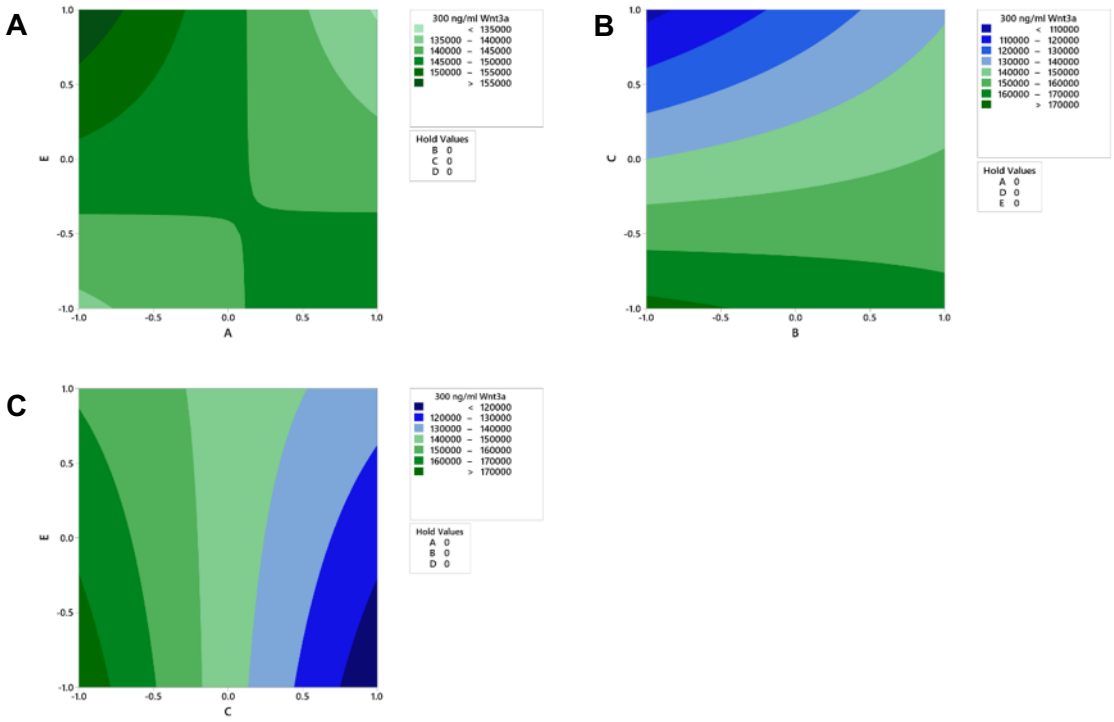

*Appendix 48: Contour plots of statistically significant interactions in the Y201 Wnt reporter response to changing plasma sprayer input settings in the presence of 300 ng/ml Wnt3a. A: A*E; B: B*C; C: C*E.*

Y201 Proliferation response to changes in plasma sprayer settings – Main effects and interactions

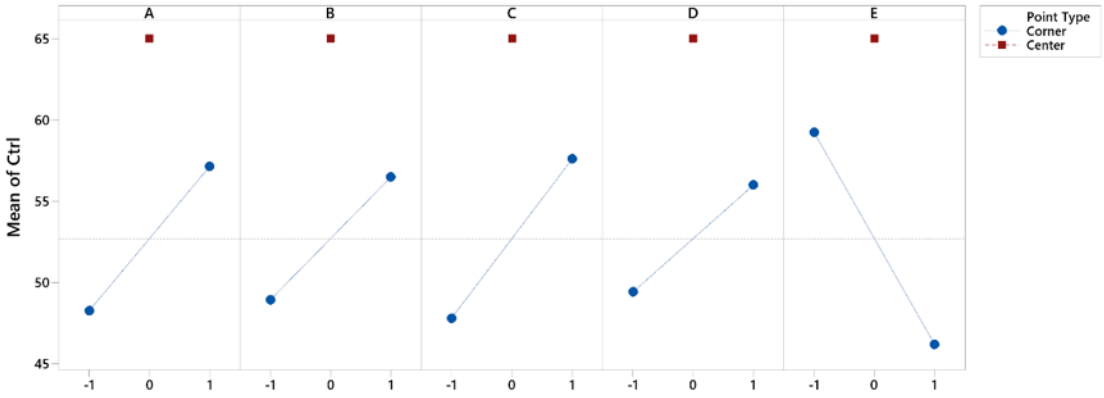

Appendix 49: Main effects plot for Y201 proliferation response to changes in plasma sprayer input parameter settings. The strongest main effect was conveyed by E, where an increase in E decreased fluorescent signal. The centre point suggested curvature in the model.

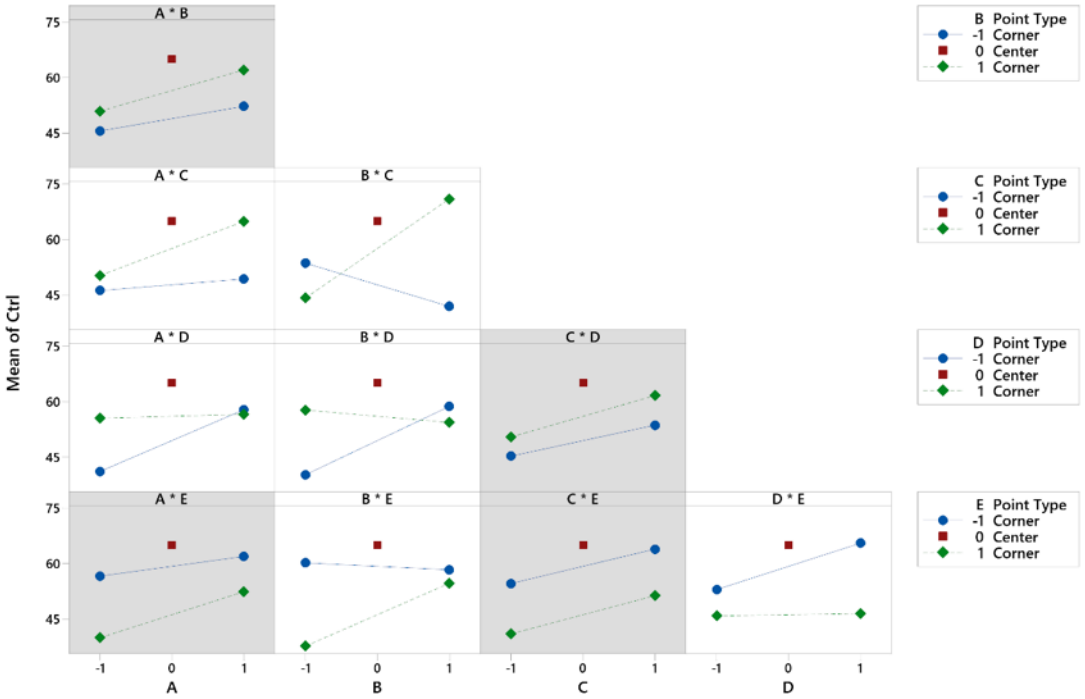

*Appendix 50: Interaction plot for Y201 proliferation response to changing plasma spray parameter input settings as measured by PicoGreen. Blue: low parameter setting; red: centre point; green: high parameter setting. Plotted values are fitted means of fluorescence fold change. The most significant interaction is the B*C interaction, where at high C, there is an increase in fluorescent signal with increasing B, while the reverse occurs at a low C. Grey boxes indicate an insignificant interaction, which has been excluded from the model, whereas white boxes indicate significance ($p<0.15$) and inclusion in the final model.*

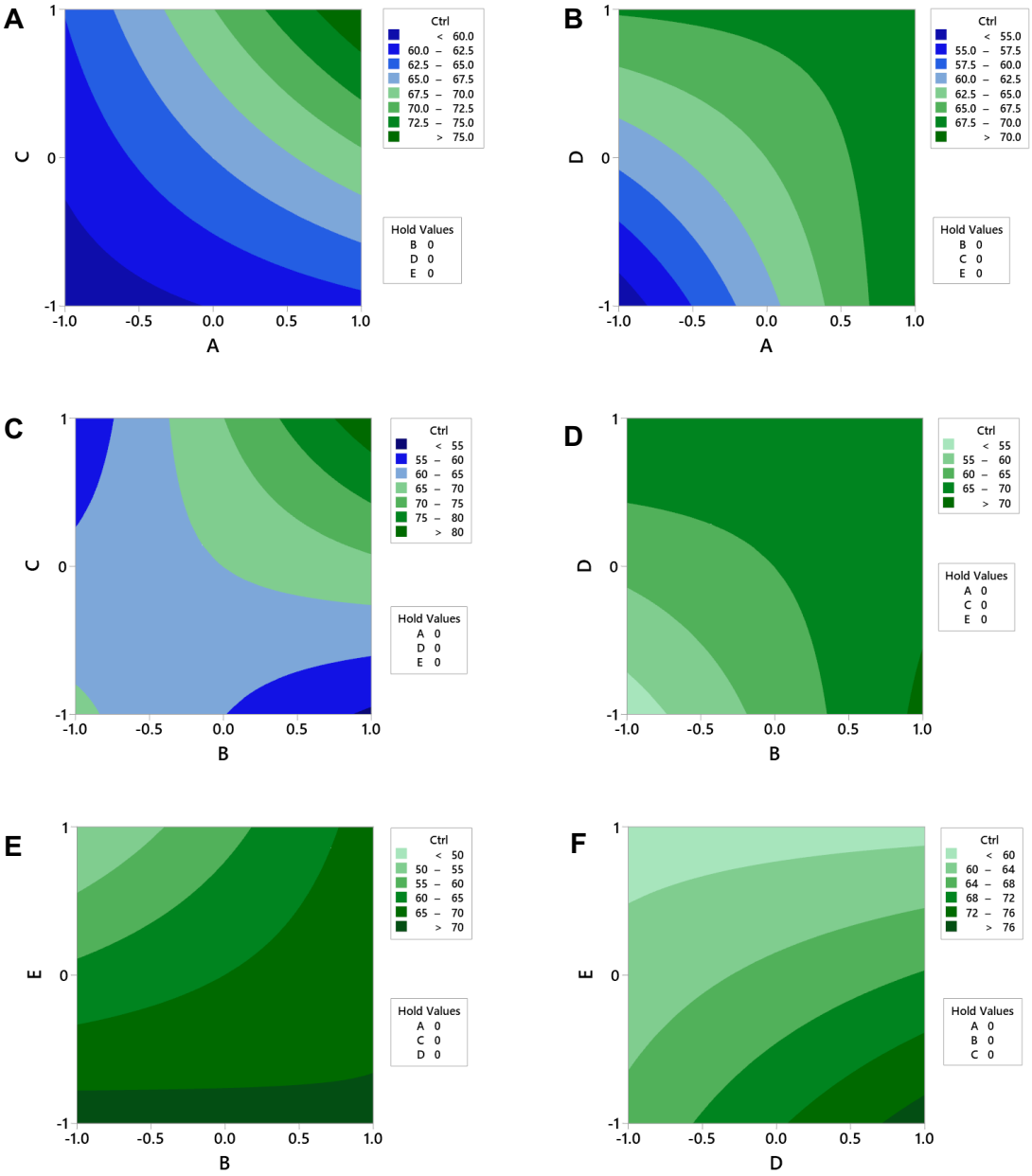

*Appendix 51: Contour plots of statistically significant interactions in proliferation response to differently sprayed HA surfaces. A: A*C; B: A*D; C: B*C; D: B*D; E: B*E; F: D*E.*

XAV939-treated Y201 Proliferation response to changes in plasma sprayer settings – Main effects and interactions

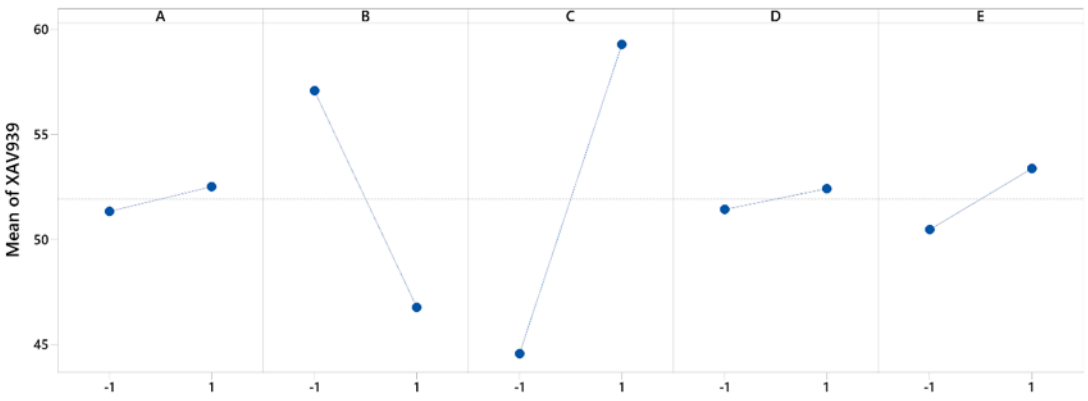

Appendix 52: Main effects plot for Y201 proliferation response to changes in plasma sprayer input parameter settings with XAV939 treatment. The strongest main effect was conveyed C, where an increase in C increased fluorescent signal. Note that no centre point is plotted as it was not included in the model.

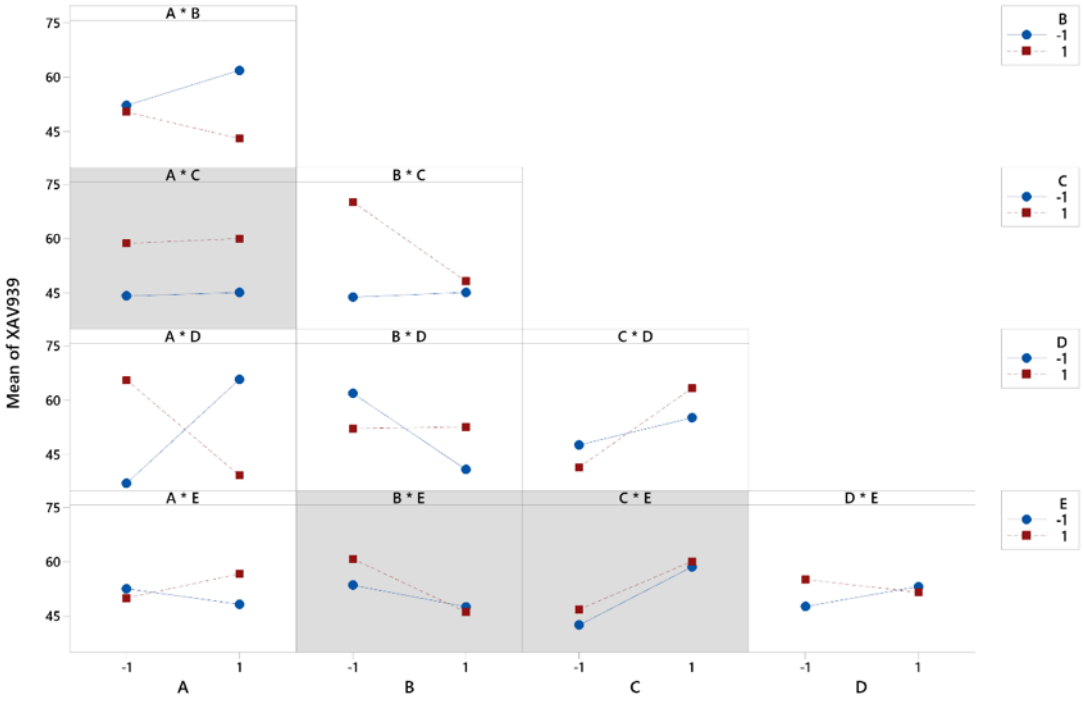

*Appendix 53: Interaction plot for Y201 proliferation response to changing plasma spray parameter input settings wit XAV939 treatment as measured by PicoGreen 3 days post-seeding. Blue: low parameter setting; red: high parameter setting. Plotted values are fitted means of fold change in fluorescence after 3 days. The most significant interaction is the A*D interaction, where at a high D, increasing A decreased fluorescent signal, whereas the reverse occurs at a low D. Grey boxes indicate an insignificant interaction, which has been excluded from the model, whereas white boxes indicate significance ($p<0.15$) and inclusion in the final model.*

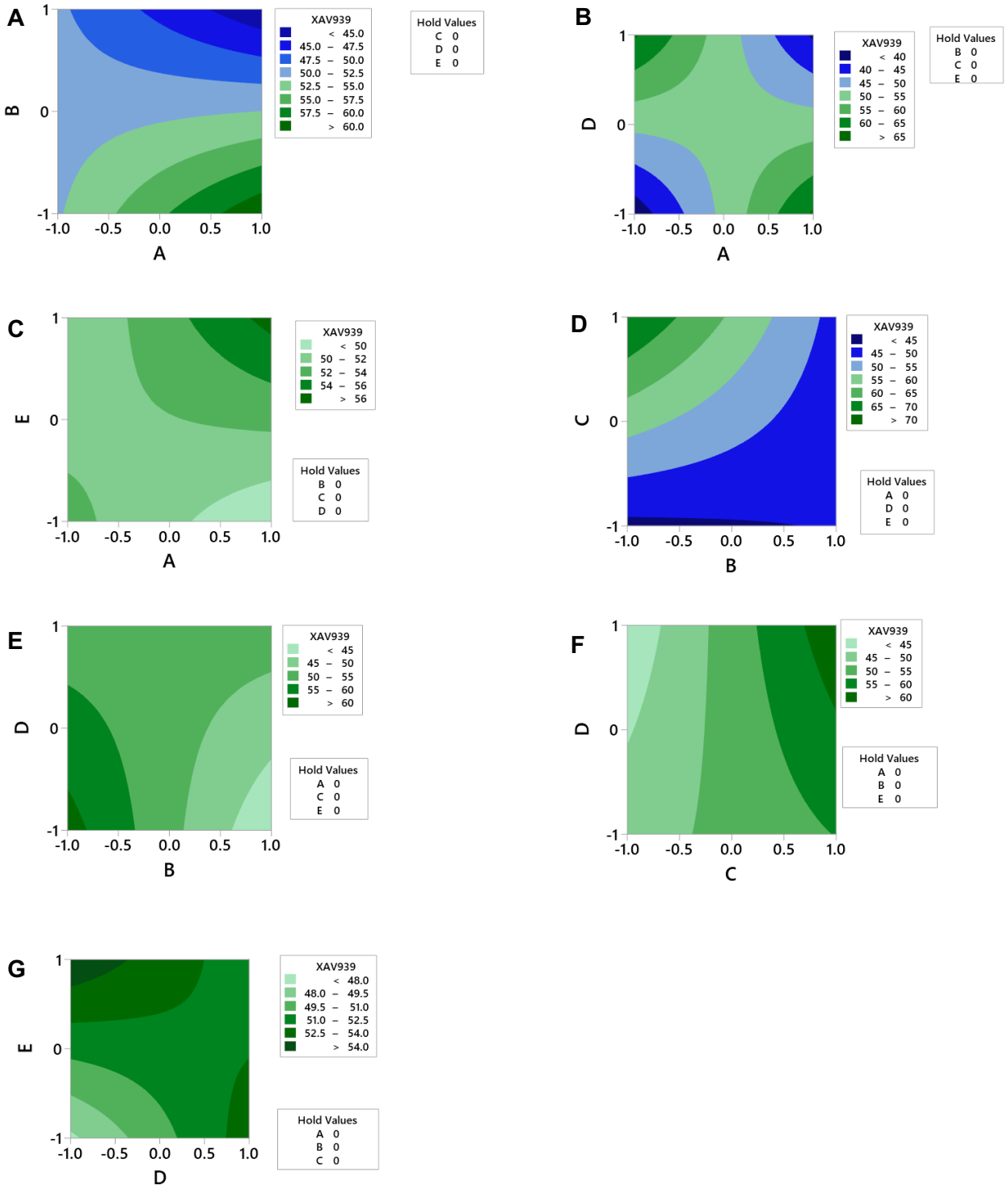

*Appendix 54: Contour plots of statistically significant interactions in Y201 proliferation response to HA parameter settings in the presence of XAV939. A: A*B; B: A*D; C: A*E; D: B*C; E: B*D; F: C*D; G: D*E.*

Y201 Osteogenic response to changes in plasma sprayer settings (basal conditions) – Main effects and interactions

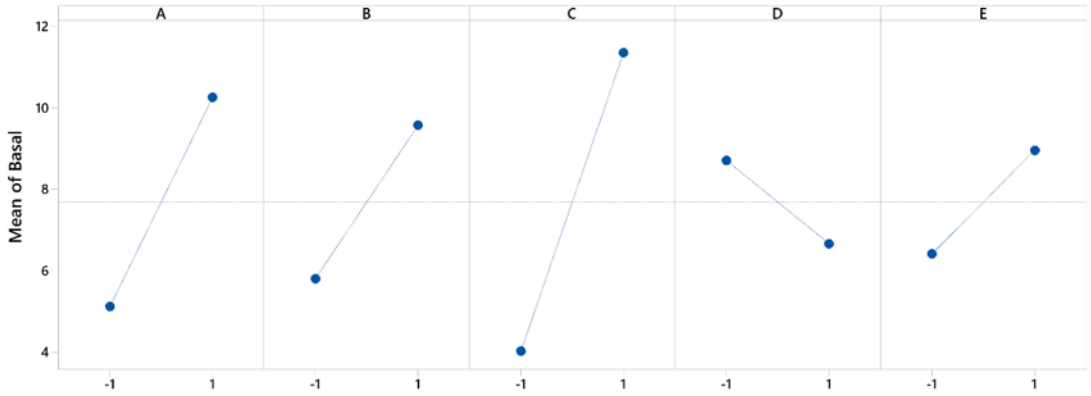

Appendix 55: Main effects plot for Y201 osteogenic response to changes in plasma sprayer input parameter settings under basal culture conditions as measured by ALP activity. The strongest main effect was conveyed by C, where an increase in C increased ALP activity. Note that no centre point is plotted as it was not included in the model.

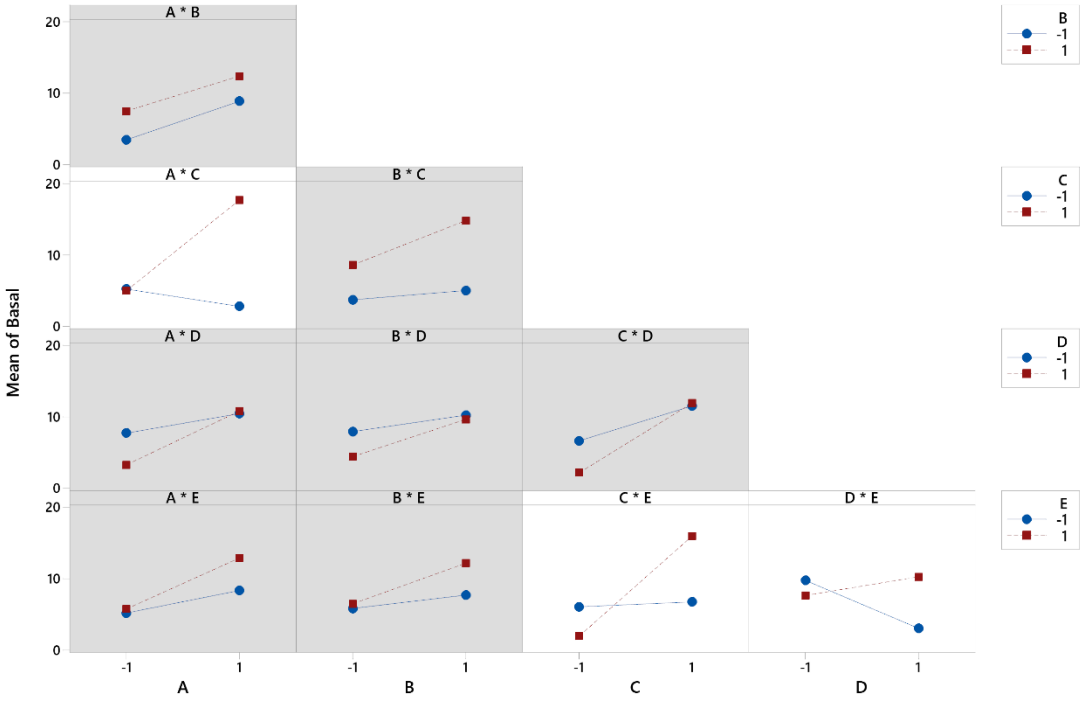

*Appendix 56: Interaction plot for Y201 osteogenic response to changing plasma spray parameter input settings under basal culture conditions as measured by ALP activity. Blue: low parameter setting; red: high parameter setting. Plotted values are fitted means of fold change in ALP activity over 9 days. The most significant interaction is the A*C interaction, where at a high C, increasing A increased ALP activity, whereas the reverse occurs at a low C. Grey boxes indicate an insignificant interaction, which has been excluded from the model, whereas white boxes indicate significance ($p<0.15$) and inclusion in the final model.*

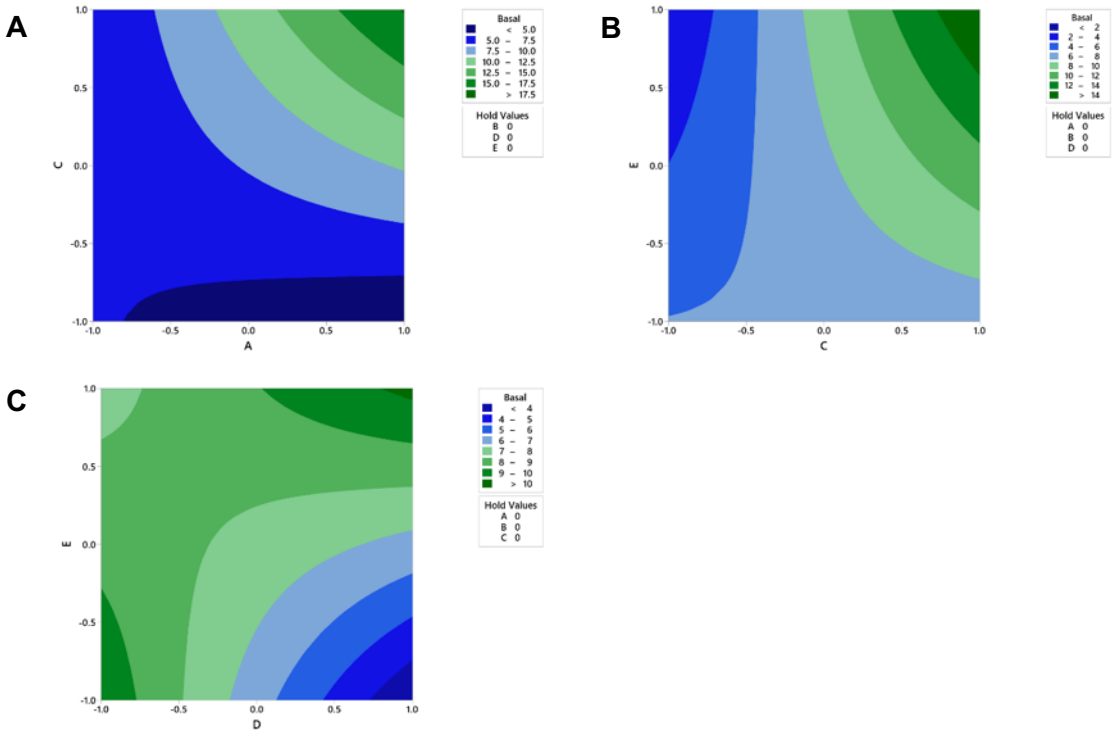

*Appendix 57: Contour plots of statistically significant interactions in the osteogenic response of Y201 MSCs under basal culture conditions to changing plasma spray parameter settings. A: A*C; B: C*E; C: D*E.*

Y201 Osteogenic response to changes in plasma sprayer settings (osteogenic conditions) – Main effects and interactions

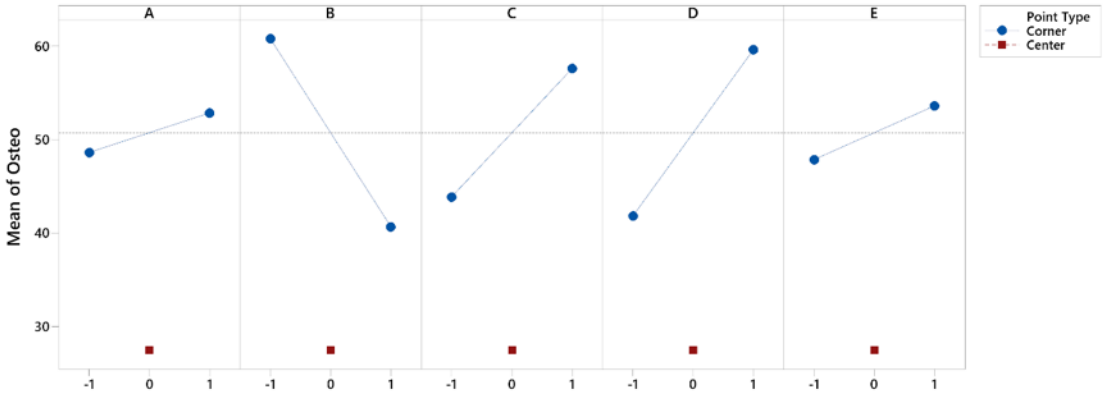

Appendix 58: Main effects plot for Y201 osteogenic response to changes in plasma sprayer input parameter settings with osteogenic supplementation. The strongest main effect was conveyed by B, where an increase in B decreased ALP activity. The centre point suggests strong curvature in the model.

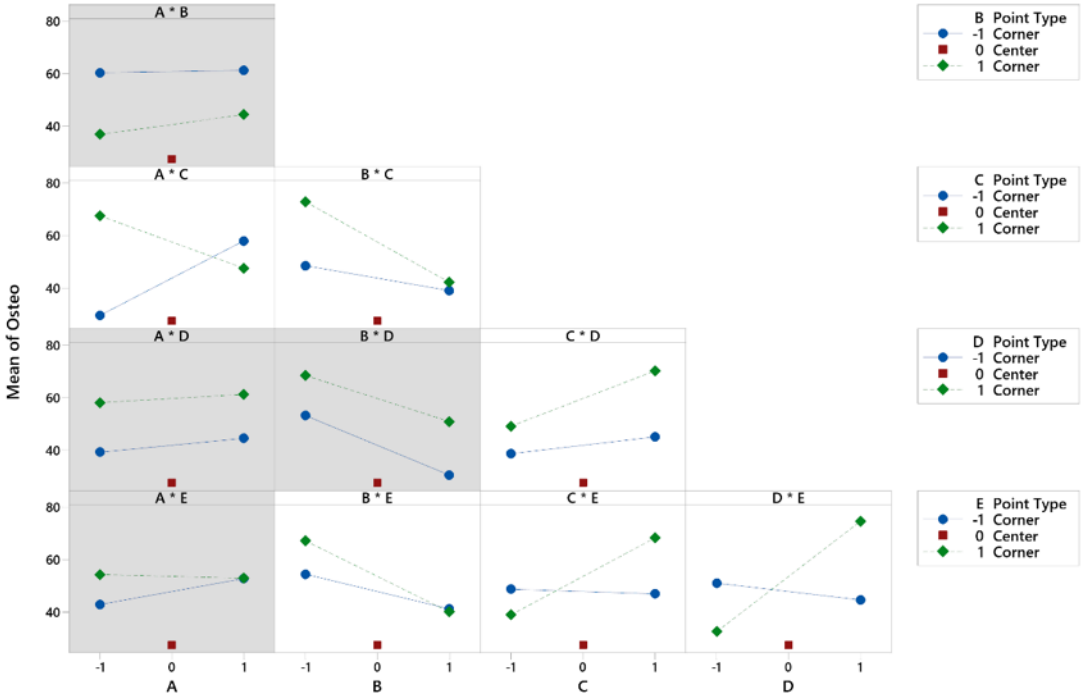

*Appendix 59: Interaction plot for Y201 osteogenic response to changing plasma spray parameter input settings under osteogenic culture conditions as measured by ALP activity. Blue: low parameter setting; red: centre point; green: high parameter setting. Plotted values are fitted means of fold change in ALP activity over 9 days. The most significant interaction is the A*C interaction, where at a low C, increasing A increased ALP activity, whereas the reverse occurs at a high C. Grey boxes indicate an insignificant interaction, which has been excluded from the model, whereas white boxes indicate significance (p<0.15) and inclusion in the final model.*

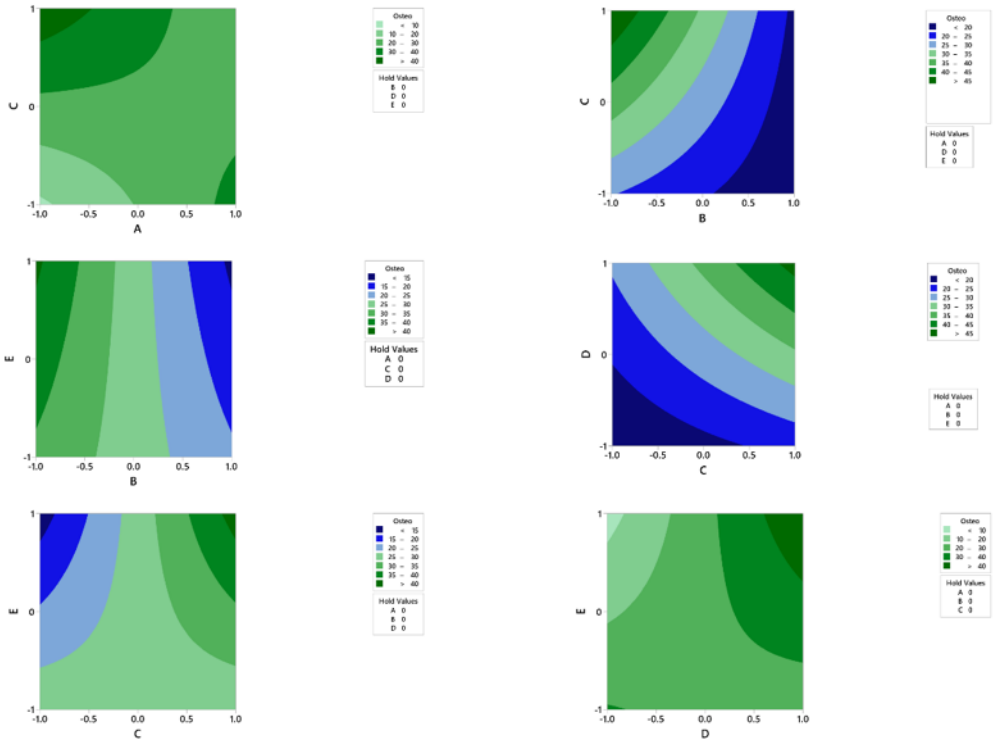

*Appendix 60: Contour plots of statistically significant interactions in the osteogenic response of Y201 MSCs under osteogenic culture conditions to changing plasma spray parameter settings. A: A*C; B: B*C; C: B*E; D: C*D; E: C*E; F: D*E.*